

JOINT INVERSION OF PRODUCTION AND TIME-LAPSE  
SEISMIC DATA: APPLICATION TO NORNE FIELD

A DISSERTATION  
SUBMITTED TO THE DEPARTMENT OF ENERGY RESOURCES  
ENGINEERING  
AND THE COMMITTEE ON GRADUATE STUDIES  
OF STANFORD UNIVERSITY  
IN PARTIAL FULFILLMENT OF THE REQUIREMENTS  
FOR THE DEGREE OF  
DOCTOR OF PHILOSOPHY

Amit Suman  
March 2013

© Copyright by Amit Suman 2013

All Rights Reserved

I certify that I have read this dissertation and that in my opinion it is fully adequate, in scope and quality, as a dissertation for the degree of Doctor of Philosophy.

---

Dr. Tapan Mukerji (Principal Adviser)

I certify that I have read this dissertation and that in my opinion it is fully adequate, in scope and quality, as a dissertation for the degree of Doctor of Philosophy.

---

Dr. Khalid Aziz

I certify that I have read this dissertation and that in my opinion it is fully adequate, in scope and quality, as a dissertation for the degree of Doctor of Philosophy.

---

Dr. Gerald Mavko

Approved for the University Committee on Graduate Studies.



# ABSTRACT

Time-lapse seismic has evolved as an important diagnostic tool in efficient reservoir characterization and monitoring. Reservoir models, optimally constrained to seismic response, as well as flow response, can provide a better description of the reservoir and thus more reliable forecast. This dissertation focuses on different aspects of joint inversion of time-lapse seismic and production data for reservoir model updating, with application to the Norne field in the Norwegian Sea. This work describes a methodology for joint inversion of production and time-lapse seismic data, analyzes sensitive parameters in the joint inversion, identifies sensitive rock physics parameters for modeling time-lapse seismic response of a field and successfully applies and compares the family of particle swarm optimizers for joint inversion of production and time-lapse seismic data of the Norne field. The contributions from this research include a systematic workflow for joint inversion of time-lapse seismic and production data that can be and has been practically applied to a real field. Better reservoir models, constrained to both data will in turn lead to better reservoir forecasts and better field management.

The first part of this thesis uses Norne field data to analyze sensitive parameters in joint inversion of production and time-lapse seismic data. An experimental design is performed on the parameters of the reservoir and seismic simulator. The results are

used to rank the parameters in terms of sensitivity to production and time-lapse seismic data. At the same time it is shown that porosity/permeability models is not the most sensitive parameter for joint inversion of production and time-lapse seismic data of the Norne field. The parameters selected for study are porosity and permeability model, relative permeability, rock physics models, pore compressibility and fluid mixing. Results show that rock physics model has the most impact on time-lapse seismic whereas relative permeability is the most important parameter for production response. The results of this study are used in selecting the most important reservoir parameters for joint inversion of time-lapse seismic and production data of the Norne field.

It is established that rock physics model is the most sensitive parameter for modeling time-lapse seismic of the Norne field, but there are rock physics parameters associated with rock physics model that impact time-lapse seismic modeling. So it is necessary to identify sensitive rock physics parameters for modeling time-lapse seismic response. Thus, the second part of this thesis identifies sensitive rock physics parameters in modeling time-lapse seismic response of Norne field. At first facies are classified based on well log data. Then sensitive parameters are investigated in the Gassmann's equation to generate the initial seismic velocities. The investigated parameters include mineral properties, water salinity, pore-pressure and gas-oil ratio (GOR). Next, parameter sensitivity for time-lapse seismic modeling of the Norne field is investigated. The investigated rock physics parameters are clay content, cement, pore-pressure and mixing. This sensitivity analysis helps to select important parameters for time-lapse (4D) seismic history matching which is an important aspect of joint inversion of production and time-lapse seismic of a field.

Joint inversion of seismic and flow data for reservoir parameter is highly non-linear and complex. Local optimization methods may fail to obtain multiple history matched models. Recently stochastic optimization based inversion has shown very good results in the integration of time-lapse seismic and production data in reservoir

history matching. Also, high dimensionality of the inverse problem makes the joint inversion of both data sets computationally expensive. High dimensionality of the inverse problem can be solved by using reduced order models. In this study, principal component bases derived from the prior is used to accomplish this. In the third part of the dissertation a family of particle swarm optimizers is used in combination with principal component bases for inversion of a synthetic data set. The performance of the different particle swarm optimizers is analyzed, both in terms of the quality of history match and convergence rate. Results show that particle swarm optimizers have very good convergence rate for a synthetic case. Also, these optimizers are used in combination with multi-dimensional scaling (MDS) to provide a set of porosity models whose simulated production and time-lapse seismic responses provide satisfactory match with the observed production and time-lapse seismic data.

The goal of the last part is to apply the results of previous parts in joint inversion of production and time-lapse seismic data of the Norne field. Time-lapse seismic and production data of the Norne field is jointly inverted by varying the sensitive parameters identified in previous chapters and using different particle swarm optimizers. At first the time-lapse seismic surveys of the Norne field acquired in 2001 and 2004 is quantitatively interpreted and analyzed. Water was injected in the oil and gas producing Norne reservoir and repeat seismic surveys were conducted to monitor the subsurface fluids. The interpreted P-wave impedance change between 2001 and 2004 is used in the joint inversion loop as time-lapse seismic data. The application of different particle swarm optimizers provides a set of parameters whose simulated responses provide a satisfactory history match with the production and time-lapse seismic data of Norne field. It is shown that particle swarm optimizers have potential to be applied for joint inversion of the production and time-lapse seismic data of a real field data set.

# ACKNOWLEDGEMENTS

I look back and find myself surprised and extremely indebted to Stanford for all I have gained throughout these years. I am surprised to see myself a totally different and a much better person. I consider myself extremely lucky to be a part of Stanford. It provided me, an excellent environment for learning, incomparable infrastructure and golden opportunity to interact with genius faculties and students. All these years of PhD studies are full of precious gifts, on professional as well as personal front. People say you may go to heaven after death, but my years in Stanford are no less than heaven. My real satisfactions are always aligned with knowledge, and since Stanford is the Mecca of knowledge, I always felt satisfied and peaceful during my journey in Stanford. I am indebted to a long list of people who played significant roles in whatever I have achieved during my PhD at Stanford.

I want first to thank my advisor Tapan Mukerji for providing me the incredible support and guidance during my research. This research would have been impossible without his consistent support and faith in me. I admire his remarkable ability to motivate and guide in the research as well as in the coursework. I can feel the optimism and energy that he puts in his efforts. His unique teaching style kept me always attentive for my purpose in the research. Tapan is very approachable, friendly

and open minded for any discussion. It helped me a lot on both professional as well as personal fronts.

I would like to thank Juan Luis Fernández Martínez for providing me guidance and feedbacks throughout my research on a family of particle swarm optimizers. Thanks Juan for being always cooperative and available for discussions. He has enriched me through his wide and extensive knowledge on stochastic optimization. I admire his never give up attitude towards research. He always motivated me during my research and taught me how to appreciate and make excellent scientific work that helps other researchers to use it.

I also thank the members of my reading committee, Khalid Aziz and Gary Mavko. I consider myself lucky to interact with Khalid on several occasions. His critical comments, feedback and ideas always helped me to shape and refine my PhD. I admire his sense of flexibility and clarity towards the research. I owe a lot of gratitude to Gary Mavko for providing me new ideas and critical comments on my research. Thanks Gary for always reminding me to maintain a clear sense of purpose in my research. Your critical comments during my proposal provided the base pillars for this research.

I wish to acknowledge the contributions of David Echeverria and Pallav Sarma for providing me valuable suggestions and feedback on my research. I also thank Mike Costello, Paul Niezguski and Robert Dombrowski for the excellent mentorship and guidance during my internships with Shell, where I got considerable help in deciding the future direction of my research.

I thank the Stanford Centre of Reservoir Forecasting (SCRF) for financial support and Smart Field Consortium at Stanford for critical comments and feedbacks on my research. Comments and feedbacks received during SCRF seminars helped me a lot in shaping up my PhD. I would like to thank Jef Caers for the comments and feedbacks on my research during SCRF seminars. I also thank Statoil and Norwegian

University of Science and Technology for providing me the Norne data set. A special note of thanks to Mohsen Dadashpour for answering my questions on the dataset very patiently. I also thank the Stanford CEES for computational support and specially Dennis Michael for always helping and solving cluster problems on short notice. I wish to acknowledge the support of Schlumberger Company for providing licenses of Petrel and Eclipse.

I met wonderful people and made good friends at Stanford. It was a pleasure to share doctoral studies and life with brilliant people like Zhe Wang, Siyao Xu, Amar Alshehri, Khalid Alnoami and my fellow SCRF members. Thanks to Nishank Saxena, Madhur Johri, Indrajit Das and Sabrina Aliyeva for incredible friendship. I am grateful to them for memorable evening parties, movie nights and outdoor trips. I am also thankful to my seniors from Indian School of Mines (ISM) and their families for always making me feel at home.

Lastly I would like to thank my family for undemanding love and selfless support. A ton of thanks to my wife Priya for being always there for me in highs and lows of my graduate study, thanks for always listening to my problems and providing pillars of strength to me. I am grateful to my parents for teaching me to respect and love everyone and worship God. Whatever is taught to me in my childhood by my parents has the biggest role to play in shaping up my professional and personal life.

I dedicate my thesis to Mummy, Papa and Priya.

Amit Suman  
Stanford University  
March, 2013

# TABLE OF CONTENTS

**ABSTRACT ..... V**

**ACKNOWLEDGEMENTS ..... VIII**

**TABLE OF CONTENTS ..... XI**

**LIST OF TABLES..... XIV**

**LIST OF FIGURES..... XV**

**CHAPTER 1: INTRODUCTION ..... 1**

    1.1 OVERVIEW ..... 1

    1.2 THESIS OUTLINE ..... 6

**CHAPTER 2: NORNE FIELD DATA AND RESERVOIR MODEL .....9**

    2.1 SEGMENT-E OF NORNE FIELD ..... 11

    2.2 AVAILABLE DATA ..... 12

    2.3 RESERVOIR MODELING WORKFLOW ..... 13

**CHAPTER 3: SENSITIVITY ANALYSIS FOR JOINT INVERSION OF TIME-LAPSE SEISMIC AND PRODUCTION DATA OF NORNE FIELD ..... 18**

    3.1 INTRODUCTION ..... 18

    3.2 SENSITIVE PARAMETERS ..... 19

        3.2.1 *Porosity and Permeability Models* ..... 19

        3.2.2 *Multi-Dimensional Scaling* ..... 20

        3.2.3 *Kernel K-Medoid Clustering* ..... 23

        3.2.4 *Relative Permeability* ..... 24

        3.2.5 *Pore compressibility* ..... 25

        3.2.6 *Rock Physics Model* ..... 27

        3.2.7 *Fluid mixing* ..... 29

    3.3 METHODOLOGY ..... 31

    3.4 FLOW SIMULATION ..... 31

    3.5 ROCK PHYSICS MODELING ..... 34

        3.5.1 *Cemented-Sand Model* ..... 34

        3.5.2 *Unconsolidated Sand Model* ..... 36

    3.6 TIME-LAPSE SEISMIC MODELING ..... 37

        3.6.1 *Change in Saturation* ..... 37

3.6.2	<i>Changes in Pore pressure</i> .....	38
3.7	RESULTS.....	38
3.8	CONCLUSIONS.....	48
<b>CHAPTER 4: SENSITIVITY STUDY OF ROCK PHYSICS PARAMETERS FOR MODELING TIME-LAPSE SEISMIC RESPONSE OF NORNE FIELD.....</b>		<b>50</b>
4.1	INTRODUCTION.....	50
4.2	ROCK PHYSICS MODELING.....	51
4.2.1	<i>Facies classification</i> .....	51
4.2.2	<i>Sensitivity to Fluid Substitution</i> .....	55
4.2.3	<i>Selection of Rock Physics Model</i> .....	58
4.2.4	<i>Constant cement model</i> .....	59
4.3	METHODOLOGY.....	62
4.3.1	<i>Flow Simulation</i> .....	63
4.3.2	<i>Time-lapse Seismic Modeling</i> .....	63
4.4	SENSITIVITY ANALYSIS RESULTS.....	65
4.5	CONCLUSIONS.....	73
<b>CHAPTER 5: JOINT INVERSION OF PRODUCTION AND TIME-LAPSE SEISMIC DATA USING A FAMILY OF PARTICLE SWARM OPTIMIZERS.....</b>		<b>74</b>
5.1	INTRODUCTION.....	74
5.2	PARTICLE SWARM OPTIMIZATION.....	76
5.3	FAMILY OF PARTICLE SWARM OPTIMIZERS.....	78
5.3.1	<i>GPSO or centred - regressive PSO (<math>t_0 = 0</math>)</i> .....	79
5.3.2	<i>CC-PSO or centred - centred PSO (<math>t_0 = 0</math>)</i> .....	79
5.3.3	<i>CP-PSO or centred -progressive PSO (<math>t_0 = \Delta t</math>)</i> .....	79
5.3.4	<i>PP-PSO or progressive-progressive PSO (<math>t_0 = 0</math>)</i> .....	80
5.3.5	<i>RR-PSO or regressive-regressive PSO (<math>t_0 = \Delta t</math>)</i> .....	80
5.4	THE CLOUD ALGORITHMS.....	80
5.5	DIMENSIONALITY REDUCTION.....	83
5.6	APPLICATION TO SYNTHETIC CASE.....	85
5.6.1	<i>Flow Simulation</i> .....	87
5.6.2	<i>Time-lapse Seismic</i> .....	87
5.6.3	<i>Dimensionality Reduction</i> .....	87
5.7	METHODOLOGY.....	92
5.8	HISTORY MATCHING RESULTS.....	94
5.9	MODEL SAMPLING.....	106
5.10	CONCLUSIONS.....	117
<b>CHAPTER 6: JOINT INVERSION OF PRODUCTION AND TIME-LAPSE SEISMIC DATA OF NORNE FIELD.....</b>		<b>118</b>
6.1	INTRODUCTION.....	118
6.2	JOINT INVERSION PROCEDURE.....	119
6.2.1	<i>Production and Time-lapse Seismic Data</i> .....	119
6.2.2	<i>Dimensionality Reduction</i> .....	131
6.2.3	<i>Sensitive Parameters</i> .....	132
6.2.4	<i>Methodology</i> .....	134
6.2.5	<i>Flow Simulations and Forward Time-lapse Seismic Modeling</i> .....	136
6.3	HISTORY MATCHING RESULTS.....	137
6.4	MODEL SAMPLING.....	158
6.5	CONCLUSIONS.....	160

<b>CHAPTER 7: CONCLUSIONS AND FUTURE RESEARCH</b> .....	<b>161</b>
FUTURE RESEARCH DIRECTIONS .....	164
<b>BIBLIOGRAPHY</b> .....	<b>167</b>

# LIST OF TABLES

Table 2.1: The details of the variograms generated using well logs. These variograms are used for generation of one thousand porosity models .....	16
Table 2.2: Porosity permeability correlation generated using the data provided by Statoil. These correlations are used for generation of permeability models.....	17
Table 3.1: Parameters and their ranges for sensitivity study.....	31
Table 4.1: Parameters used in the sensitivity study of Gassmann’s fluid substitution.....	56
Table 4.2: Values of the parameters used in this study.....	56
Table 4.3: Parameters selected for sensitivity study in modeling time-lapse seismic response of Norne field .....	62
Table 5.1: Details of the variogram used for geostatistical simulation of 1000 porosity realization. There is a geological continuity in N-E direction.....	85
Table 6.1: The parameters corresponding to initial and best models obtained using CC-PSO .....	156
Table 6.2: The parameters corresponding to initial and best models obtained using CP-PSO .....	157
Table 6.3: The parameters corresponding to initial and best models obtained using GPSO .....	157
Table 6.4: The parameters corresponding to initial and best models obtained using PP-PSO.....	157
Table 6.5: The parameters corresponding to initial and best models obtained using RR-PSO.....	157
Table 6.6: Parameters for the two history matched models after model sampling on the results of RR-PSO.....	159

# LIST OF FIGURES

Figure 1.1: Workflow of joint inversion of time-lapse seismic and production data. The blue dotted boxes indicate the flow simulator and the seismic/rock physics simulator. Often these simulators are taken as black-boxes without investigating the sensitivity of the simulator parameters on the inter-related flow and seismic response of the reservoir. ....	4
Figure 2.1: Location of the Norne field situated in the Norwegian Sea (Begum, 2009) .....	11
Figure 2.2: Top view of Norne field showing segments C, D, G and E present in the field. This study is focused on segment E of the Norne field (Begum, 2009) .....	12
Figure 2.3: Structural framework of Norne field. This framework has been used to generate 1000 realizations of Norne field.....	14
Figure 2.4: Well logs of Norne field used for generation of one thousand realizations of Norne field .....	14
Figure 2.5: Four porosity realizations of Norne field, one thousand porosity realizations are generated using SGSIM and variograms.....	15
Figure 3.1: MDS performed on 100 porosity realization and plotted in two dimensions. Red points correspond to different porosity realizations. Porosity realizations very different from each other are far away in the plot .....	22
Figure 3.2: Kernel k-medoid clustering performed on 100 porosity realizations after MDS. Green, blue and magenta color represents different clusters. Medoids of clusters are represented by squares .....	22
Figure 3.3: Three porosity realizations associated with the medoids obtained after clustering. These realizations are selected for the sensitivity study .....	23

Figure 3.4: Oil-water relative permeability curves for Norne field. Curve pairs 1 and 2 are selected for this study. Selected curves capture the uncertainty associated with relative permeability curves of Norne field..... 25

Figure 3.5: Dry rock velocities are calculated using saturated bulk rock velocities and Gassmann’s fluid substitution..... 26

Figure 3.6: Histograms of pore compressibilities present in different zones (Garn, Ile, Tofte and Tilje) of Norne field. .... 28

Figure 3.7: Crossplots of porosity and pore compressibility in different zones of Norne field (Garn, Ile, Tofte and Tilje). .... 28

Figure 3.8: Schematic of seismic velocity – porosity trend for cemented and uncemented sands (modified from Avseth et al. 2005). .... 29

Figure 3.9: P-wave velocity trends for homogeneous and patchy saturations in an oil-gas sand having a porosity of 30%..... 30

Figure 3.10: Workflow for generation of production and time-lapse seismic response associated with a set of parameters used in this study. .... 32

Figure 3.11: Top view of flow simulation model. Segment E consists of wells E-3H, E-2H, E-3AH, F1-H and F-3H. .... 33

Figure 3.12: Results of sensitivity study on time-lapse seismic response of Norne field. Box plot shows the median (red line) and interquartile range (blue box) of distribution for variations in each parameter. Rock physics model has the most impact on time-lapse seismic response of Norne field. .... 40

Figure 3.13: Effect of the rock physics model on median P-wave impedance change from 2001 to 2004. Changes are shown for three different layers (5, 7 and 10). On the right, changes in impedance for unconsolidated sand model are shown and on the left changes in impedance for cemented sand model are shown. .... 41

Figure 3.14: Effect of the relative permeability on median p-wave impedance change from 2001 to 2004. Changes are shown for three different layers (5, 7 and 10). On the right, changes in impedance for second relative permeability curve are shown and on the left changes in impedance for first relative permeability curve are shown. .... 42

Figure 3.15: Effect of the fluid mixing on median p-wave impedance change from 2001 to 2004. Changes are shown for three different layers (5, 7 and 10). On the right, changes in impedance for patchy saturation are shown and on the left changes in impedance for uniform saturation are shown. .... 43

Figure 3.16: Effect of the porosity model on median p-wave impedance change from 2001 to 2004. Changes are shown for three different layers (5, 7 and 10). From left to right, changes in impedance for Model 1, Model 2 and Model 3 are shown.....	44
Figure 3.17: Effect of the pore compressibility on median p-wave impedance change from 2001 to 2004. Changes are shown for three different layers (5, 7 and 10). From left to right, changes in impedance for pore compressibility ( $\text{Pa}^{-1}$ ) of $1.5\text{e}^{-10}$ , $3\text{e}^{-10}$ and $5\text{e}^{-10}$ are shown. ....	45
Figure 3.18: Results of sensitivity study for production response of Norne field. Box plot shows the median (red line) and interquartile range (blue box) of distribution for variations in each parameter. Relative permeability has the most impact on cumulative oil production of Norne field.....	46
Figure 3.19: Median cumulative oil production from 1997 to 2004 for two sets of relative permeability. Response of first and second relative permeability curves are shown in blue and red respectively.....	47
Figure 3.20: Median cumulative oil production from 1997 to 2004 for three porosity realizations. Response of first, second and third models are shown in blue, red and black respectively. Response of model 1 and model 3 are similar thus associated curves are identical.....	47
Figure 3.21: Median cumulative oil production from 1997 to 2004 for three different pore compressibilities. Responses of first, second and third pore compressibility are shown in blue, red and black respectively. Responses associated with pore compressibilities are almost similar thus associated curves are identical. ....	48
Figure 4.1: Workflow for generation of initial ( $t=0$ ) cube of elastic properties using well log data. Starting with well log data an appropriate rock physics model is used to establish a correlation between porosity and elastic properties. ....	52
Figure 4.2: Porosity and velocity log (generated from well logs provided by Statoil) in well E3H on the left and well F1H on the right. Both of these logs are used for the analysis .....	53
Figure 4.3: Facies classification in segment E of Norne field using well log data and based on velocity ratio, clay content and acoustic impedance. Three distinct facies are classified, namely sand, shaly sand and shale. Shaly sand and shale are limited to layer 3 in the reservoir .....	54
Figure 4.4: Result of sensitivity study for Gassmann's fluid substitution, box plot shows the median (red line) and interquartile range (blue box) of distribution for variations in each parameter.....	58

Figure 4.5: Bulk modulus obtained near the wells after fluid substitution for variations in clay content and GOR. The well log points are for nine different cases (3 clay content x 3 GOR) and colored with gamma ray values ..... 59

Figure 4.6: Variations in rock physics models by varying clay content, coordination number and cement fraction (color: Gamma Ray). The variations in rock physics parameters are successfully calibrated with the values in the well log. Blue lines are rock physics models and points are colored with gamma ray ..... 61

Figure 4.7: Workflow for generation of P-wave impedance change in four years. It consists of two parts, first is flow simulation, second is rock physics modeling and fluid substitution..... 62

Figure 4.8: Two different effective pressure models used for sensitivity study. .... 65

Figure 4.9: Results of sensitivity study of rock physics parameters for modeling the time-lapse seismic response of Norne field. Red line are median, and blue boxes are interquartile range of the distribution ..... 66

Figure 4.10: Effect of change in coordination number on the median of P-wave impedance change in four years. The median change is shown for three layers (5, 7 and 10) in the segment E of Norne field. Coordination number has the largest impact on impedance change ..... 67

Figure 4.11: Effect of change in fluid mixing (uniform or patchy) on the median of P-wave impedance change in four years. The median is shown for three layers (5, 7 and 10) in the segment E of Norne field..... 68

Figure 4.12: Effect of change in clay content on the median of P-wave impedance change in four years. The median is shown for three layers (5, 7 and 10) in the segment E of Norne field. .... 69

Figure 4.13: Effect of change cement fraction on the median of p-wave impedance change in four years. The median is shown for three layers (5, 7 and 10) in the segment E of Norne field. .... 70

Figure 4.14: Effect of change in effective pressure model on the median of p-wave impedance change in four years. The median is shown for three layers (5, 7 and 10) in the segment E of Norne field..... 71

Figure 4.15: Effect of change in field GOR on the median of p-wave impedance change in four years. The median is shown for three layers (5, 7 and 10) in the segment E of Norne field. .... 72

Figure 5.1: Logarithmic median misfit errors for the Rosenbrock function in 50 simulations (after 500 iterations) for different family members. Different family members have different

stability regions. The lines are corresponding to PSO second order trajectories (Fernández-Martínez et al. 2010d).....	82
Figure 5.2: Reference porosity realization used in this study. Porosity varies from 0 to 0.4, and there is a geological continuity in N-E direction (show positions of well data). Injector and producer locations are shown in the black circles. ....	86
Figure 5.3: Water cut over ten years for the reference porosity realization. It is considered as observed production data in this study.....	86
Figure 5.4: Normalized P-wave impedance change over ten years of production for reference porosity realization. It is considered as observed time-lapse seismic data in this study. ....	88
Figure 5.5: The change in the relative error with increase in the number of PCA coefficients. It is clear that 50 PCA coefficients are enough to reduce the relative error by 70%.....	89
Figure 5.6: Variance of the prior captured by the PCA coefficients. In this study 50 PCA coefficients are used and these coefficients are able to capture 50% of the variance present in the prior .....	89
Figure 5.7: Six porosity realizations (reservoir models) are shown out of 1000 realizations generated using sequential Gaussian simulation based on well log data and variograms.....	90
Figure 5.8: Three porosity realization shown on the left, corresponding porosity realization constructed using 50 PCA coefficients and associated vectors are shown on the right. It is clearly observed that 50 PCA coefficients are successfully capturing large scale features present in the reservoir models. ....	91
Figure 5.9: Workflow used in this study. It consists of PCA analysis, production and seismic modeling and use of particle swarm optimizers .....	93
Figure 5.10: Best porosity model (top right) and associated time-lapse seismic response (bottom right) obtained using CC-PSO. Initial guess (left), Reference porosity model and observed time-lapse seismic data (middle) are shown for comparison .....	95
Figure 5.11: Water cut over ten years of production using CC-PSO. Observed production data is shown in red, water cut for initial guess model is shown in black, water cut associated with the best model is shown in blue .....	95
Figure 5.12: Behavior of median misfit with the increase in number of iterations using CC-PSO. Red, blue and green curves are median misfits for time-lapse seismic, production and total .....	96
Figure 5.13: Best porosity model (top right) and associated time-lapse seismic response (bottom right) obtained using CP-PSO. Initial guess (left), Reference porosity model and observed time-lapse seismic data (middle) are shown for comparison .....	97

Figure 5.14: Water cut over ten years of production using CP-PSO. Observed production data is shown in red, water cut for initial guess model is shown in black, water cut associated with the best model is shown in blue..... 97

Figure 5.15: Behavior of median misfit with the increase in number of iterations using CP-PSO. Red, blue and green curves are median misfits for time-lapse seismic, production and total..... 98

Figure 5.16: Best porosity model (top right) and associated time-lapse seismic response (bottom right) obtained using GPSO. Initial guess (left), Reference porosity model and observed time-lapse seismic data (middle) are shown for comparison ..... 98

Figure 5.17: Water cut over ten years of production using GPSO. Observed production data is shown in red, water cut for initial guess model is shown in black, water cut associated with the best model is shown in blue..... 99

Figure 5.18: Behavior of median misfit with the increase in number of iterations using GPSO. Red, blue and green curves are median misfits for time-lapse seismic, production and total..... 99

Figure 5.19: Best porosity model (top right) and associated time-lapse seismic response (bottom right) obtained using PP-PSO. Initial guess (left), Reference porosity model and observed time-lapse seismic data (middle) are shown for comparison ..... 100

Figure 5.20: Water cut over ten years of production using PP-PSO. Observed production data is shown in red, water cut for initial guess model is shown in black, water cut associated with the best model is shown in blue..... 101

Figure 5.21: Behavior of median misfit with the increase in number of iterations using PP-PSO. Red, blue and green curves are median misfits for time-lapse seismic, production and total..... 101

Figure 5.22: Best porosity model (top right) and associated time-lapse seismic response (bottom right) obtained using RR-PSO. Initial guess (left), Reference porosity model and observed time-lapse seismic data (middle) are shown for comparison ..... 102

Figure 5.23: Water cut over ten years of production using RR-PSO. Observed production data is shown in red, water cut for initial guess model is shown in black, water cut associated with the best model is shown in blue..... 103

Figure 5.24: Behavior of median misfit with the increase in number of iterations using RR-PSO. Red, blue and green curves are median misfits for time-lapse seismic, production and total..... 103

Figure 5.25: Behavior of time-lapse seismic misfit with the increase in number of iterations. Red, blue, green, black and magenta curves are responses of CC-PSO, CP-PSO, GPSO, PP-PSO and RR-PSO respectively ..... 104

Figure 5.26: Behavior of production misfit with the increase in number of iterations. Red, blue, green, black and magenta curves are responses of CC-PSO, CP-PSO, GPSO, PP-PSO and RR-PSO respectively.....	104
Figure 5.27: Behavior of total misfit with the increase in number of iterations. Red, blue, green, black and magenta curves are responses of CC-PSO, CP-PSO, GPSO, PP-PSO and RR-PSO respectively .....	105
Figure 5.28: Reservoir models in a two dimensional MDS space. points on the plot represent reservoir models.....	107
Figure 5.29: Four clusters and their centers in four different colors (green, blue, yellow and magenta) using kernel k-medoid clustering on reservoir models obtained using CP-PSO .....	107
Figure 5.30: Four reservoir models obtained after kernel k-medoid clustering using CC-PSO on the Top. Time –lapse seismic response associated with reservoir models at the bottom. Reference porosity model and observed time-lapse seismic response on the left.....	109
Figure 5.31: Blue curves represent production response of four reservoir models obtained after kernel k-medoid clustering using CC-PSO. Observed production data is shown in red curve.....	110
Figure 5.32: Blue curves represent production response of four reservoir models obtained after kernel k-medoid clustering using CP-PSO. Observed production data is shown in red curve.....	110
Figure 5.33: Four reservoir models obtained after kernel k-medoid clustering using CP-PSO on the Top. Time –lapse seismic response associated with reservoir models at the bottom. Reference porosity model and observed time-lapse seismic response on the left. ....	111
Figure 5.34: Blue curves represent production response of four reservoir models obtained after kernel k-medoid clustering using GPSO. Observed production data is shown in red curve.....	112
Figure 5.35: Four reservoir models obtained after kernel k-medoid clustering using GPSO on the Top. Time –lapse seismic response associated with reservoir models at the bottom. Reference porosity model and observed time-lapse seismic response on the left. ....	113
Figure 5.36: Four reservoir models obtained after kernel k-medoid clustering using PP-PSO on the Top. Time –lapse seismic response associated with reservoir models at the bottom. Reference porosity model and observed time-lapse seismic response on the left. ....	114
Figure 5.37: Blue curves represent production response of four reservoir models obtained after kernel k-medoid clustering using PP-PSO. Observed production data is shown in the red curve.....	115

Figure 5.38: Blue curves represent production response of four reservoir models obtained after kernel k-medoid clustering using RR-PSO. Observed production data is shown in the red curve..... 115

Figure 5.39: Four reservoir models obtained after kernel k-medoid clustering using RR-PSO on the Top. Time –lapse seismic response associated with reservoir models at the bottom. Reference porosity model and observed time-lapse seismic response on the left ..... 116

Figure 6.1: Observed production data in the well E-2H from 1997 to 2004 (a) Observed water rate in the well E-2H from 1997 to 2004 (b) Observed oil rate in the well E-2H from 1997 to 2004 (c) Observed gas rate in the well E-2H from 1997 to 2004 (d) Observed bottom hole pressure in the well E-2H from 1997 to 2004 ..... 120

Figure 6.2: Observed production data in the well E-3H from 1997 to 2004 (a) Observed water rate in the well E-3H from 1997 to 2004 (b) Observed oil rate in the well E-3H from 1997 to 2004 (c) Observed gas rate in the well E-3H from 1997 to 2004 (d) Observed bottom hole pressure in the well E-3H from 1997 to 2004 ..... 121

Figure 6.3: Observed production data in the well E-3AH from 1997 to 2004 (a) Observed water rate in the well E-3AH from 1997 to 2004 (b) Observed oil rate in the well E-3AH from 1997 to 2004 (c) Observed gas rate in the well E-3AH from 1997 to 2004 (d) Observed bottom hole pressure in the well E-3AH from 1997 to 2004 ..... 122

Figure 6.4: 3D seismic survey acquired in 2001 (base line survey, provided by Statoil). Seismic amplitude at inline 1023 (generated using PETREL)..... 124

Figure 6.5: 3D seismic survey acquired in 2004 (provided by Statoil). Seismic amplitude at inline 1023 (generated using PETREL)..... 124

Figure 6.6: Seismic cross section showing well F1-H, reservoir top and bottom horizon used for the acoustic impedance inversion in Hampson-Russell. .... 125

Figure 6.7: Cross section of P-wave seismic impedance in time, obtained after the inversion of 3D seismic survey acquired in 2001 using Hampson-Russell..... 126

Figure 6.8: Cross section of P-wave seismic impedance in time, obtained after the inversion of 3D seismic survey acquired in 2004 using Hampson-Russell..... 127

Figure 6.9: Cross section of P-wave seismic impedance in depth at 2001, obtained after depth conversion of P-wave seismic impedance in time at 2001 using Hampson-Russell ..... 128

Figure 6.10: Cross section of P-wave seismic impedance in depth at 2004, obtained after depth conversion of P-wave seismic impedance in time at 2004 using Hampson-Russell ..... 129

Figure 6.11: Observed time-lapse seismic data in the Norne field (Normalized P-wave impedance change from 2001 to 2004), On the top normalized P-wave impedance change from

2001 to 2004 in layers 13,15 and 17, On the bottom normalized P-wave impedance change from 2001 to 2004 after 3% noise is removed .....	130
Figure 6.12: The ratio of cumulative sum of PCA coefficients and sum of PCA coefficients are plotted against the number of PCA coefficients. There are 22 blue curves, one for each of the 22 horizontal layers present in the reservoir model of the Norne field. Red line indicates that 70 PCA coefficients are required to capture the 60% variance present in the prior models of the Norne field.....	132
Figure 6.13: Norne reservoir porosity model and porosity models constructed using PCA are compared. On left three original porosity models for Norne field and on right three corresponding porosity models of Norne constructed using PCA coefficients. Clearly 70 PCA coefficients are successful in capturing much of the heterogeneity present in the original porosity models .....	133
Figure 6.14: Relative permeability curves present in the Norne field. On the top all of the relative permeability curves present in the Norne field (from left to right: Gas oil relative permeability curves, Oil water relative permeability curves and capillary pressure curves). At the bottom five sets of relative permeability curves selected to be used for joint inversion (These five sets capture the range of variations present in all of the relative permeability curves. ....	134
Figure 6.15: Workflow for joint inversion of production and time-lapse seismic data of Norne field. A family of particle swarm optimizers is used in combination with principal component analysis with variations in the sensitive parameters .....	135
Figure 6.16: The decrease in median of the production misfits, time-lapse seismic misfits and total misfits with increase in number of iterations while using CC-PSO. Production misfit, time-lapse seismic misfit and total misfit are shown by blue, red and green curves respectively. ....	137
Figure 6.17: History matching results for matching production data using CC-PSO. Simulated production response of initial guess model, simulated production response of best model and history are shown by black, blue and red curves respectively. Matching of water, oil, gas rates and bottom hole pressure are shown in a column for each well .....	138
Figure 6.18: History matching results for matching time-lapse seismic data using CC-PSO. History, simulated time-lapse seismic response of initial guess model and simulated time-lapse seismic response of best model are shown from top to bottom for layers 13, 15 and 17. ....	139
Figure 6.19: The decrease in median of the production misfits, time-lapse seismic misfits and total misfits with increase in number of iterations while using CP-PSO. Production misfit,	

time-lapse seismic misfit and total misfit are shown by blue, red and green curves respectively.....	141
Figure 6.20: History matching results for matching production data using CP-PSO. Simulated production response of initial guess model, simulated production response of best model and history are shown by black, blue and red curves respectively. Matching of water, oil, gas rates and bottom hole pressure are shown in a column for each well .....	142
Figure 6.21: History matching results for matching time-lapse seismic data using CP-PSO. History, simulated time-lapse seismic response of initial guess model and simulated time-lapse seismic response of best model are shown from top to bottom for layers 13, 15 and 17.....	143
Figure 6.22: The decrease in median of the production misfits, time-lapse seismic misfits and total misfits with increase in number of iterations while using GPSO. Production misfit, time-lapse seismic misfit and total misfit are shown by blue, red and green curves respectively.....	144
Figure 6.23: History matching results for matching production data using GPSO. Simulated production response of initial guess model, simulated production response of best model and history are shown by black, blue and red curves respectively. Matching of water, oil, gas rates and bottom hole pressure are shown in a column for each well .....	145
Figure 6.24: History matching results for matching time-lapse seismic data using GPSO. History, simulated time-lapse seismic response of initial guess model and simulated time-lapse seismic response of best model are shown from top to bottom for layers 13, 15 and 17.....	146
Figure 6.25: The decrease in median of the production misfits, time-lapse seismic misfits and total misfits with increase in number of iterations while using PP-PSO. Production misfit, time-lapse seismic misfit and total misfit are shown by blue, red and green curves respectively.....	147
Figure 6.26: History matching results for matching production data using PP-PSO. Simulated production response of initial guess model, simulated production response of best model and history are shown by black, blue and red curves respectively. Matching of water, oil, gas rates and bottom hole pressure are shown in a column for each well .....	148
Figure 6.27: History matching results for matching time-lapse seismic data using PP-PSO. History, simulated time-lapse seismic response of initial guess model and simulated time-lapse seismic response of best model are shown from top to bottom for layers 13, 15 and 17.....	149

Figure 6.28: The decrease in median of the production misfits, time-lapse seismic misfits and total misfits with increase in number of iterations while using RR-PSO. Production misfit, time-lapse seismic misfit and total misfit are shown by blue, red and green curves respectively. ....	150
Figure 6.29: History matching results for matching production data using RR-PSO. Simulated production response of initial guess model, simulated production response of best model and history are shown by black, blue and red curves respectively. Matching of water, oil, gas rates and bottom hole pressure are shown in a column for each well .....	151
Figure 6.30: History matching results for matching time-lapse seismic data using RR-PSO. History, simulated time-lapse seismic response of initial guess model and simulated time-lapse seismic response of best model are shown from top to bottom for layers 13, 15 and 17. ....	152
Figure 6.31: The decrease in median of the production misfits with increase in number of iterations for different PSO family members. ....	153
Figure 6.32: The decrease in median of the time-lapse seismic misfits with increase in number of iterations for different PSO family members. ....	153
Figure 6.33: The decrease in median of the total misfits with increase in number of iterations for different PSO family members.....	154
Figure 6.34: Initial and best porosity models obtained using CC-PSO, CP-PSO and GPSO. Initial and best porosity models are shown in left and right respectively. ....	155
Figure 6.35: Initial and best porosity models obtained using PP-PSO and RR-PSO. Initial and best porosity models are shown in left and right respectively. ....	156
Figure 6.36: Two history matched models are obtained after the kernel k-medoid clustering. Model sampling is applied on the results of RR-PSO. History matched models are the centroid of clusters (shown in the red and blue square), all other models are shown in red and blue circles .....	158
Figure 6.37: Two history matched porosity models obtained after model sampling using the results of RR-PSO. The differences between two models are highlighted by the black circles. ....	159



# Chapter 1

## INTRODUCTION

### 1.1 Overview

Reservoir characterization is based on building and updating a reservoir model by integration of all data available during the different stages of reservoir development. Reservoir models can be used to estimate hydrocarbon in place; design optimum well trajectories and evaluate different possible production scenarios. At first, an initial static 3D reservoir model is built by the integration of seismic data, core and log measurements, and sedimentary models using appropriate geostatistical techniques. The model consists of both the structure (horizons and faults) and the physical properties (facies, porosity, permeability) of the reservoir. Dynamic data such as production and time-lapsed 3-D seismic data (4-D seismic data) is acquired during the production phase of the reservoir. 4-D seismic data acquired during production can be used to monitor fluid property changes in the reservoir after specific processing. It can provide information on the dynamics of fluids in the reservoir based on the relation between variations of seismic signals and movement of hydrocarbons and changes in formation pressure. Movement of

fluids and changes in pore pressure, in response to pumping and injection, depend on the petrophysical properties of the reservoir rock.

This new information can be integrated in the reservoir model by the process of history matching or joint inversion. History matched models are required during the production life of the reservoir to improve forecast reliability. The general workflow for history matching of time-lapse and production data involves minimization of the objective function, which takes into account the mismatch in the observed and modeled seismic and flow response. The objective function is minimized using a proper optimization algorithm and reservoir parameters (porosity/permeability) are updated during the process.

Huang et al. (1997, 1998) formulated the simultaneous matching of production and seismic data as an optimization problem, with updating of model parameters such as porosity. Landa and Horne (1997) used gradient-based optimization to estimate the reservoir parameters. It was assumed that water saturation changes could be derived from time-lapse seismic data. Fanchi et al. (1999) developed a workflow for calculation of geophysical attributes with an integrated flow model for different reservoir management scenarios. Oliver et al. (2000) used saturation and pore pressure maps as observation data. It was shown that matching only production data is not able to provide a good estimation of pressure and saturation map and could be trapped in a local minimum. Mantica et al. (2001) have shown the advantage of chaotic sampling of parameter space with a local optimizer over a gradient-based method. Arenas et al. (2001) have used pilot point method in joint inversion of production and time lapse seismic. Van et al. (2001) used water saturation changes based on multiple seismic surveys with production data. It was used to estimate the geometric parameters of the faults such as size, position and throw. Landro (2001a) demonstrated an efficient method to distinguish the pressure and saturation changes inside the reservoir using seismic data. Vasco et al. (2003) used streamline based flow simulation in integration of flow and time-lapse seismic data. Portella and Emerick (2005) have shown the feasibility of using time-lapse seismic data in the closed loop history matching process. It was shown that time-lapse seismic improved the workflow of history matching process. Wu et al. (2005) used time lapse seismic and production data to better predict water saturation fields thus

helping to locate new wells and to monitor fluid movement. Stephen et al. (2005) have shown that a quasi-global stochastic neighborhood algorithm (NA) approach improves on gradient-based methods by avoiding entrapment in local minima and can be used for joint inversion of seismic and flow data. Rotondi et al. (2006) used stochastic sampling techniques in a Bayesian framework for the uncertainty quantification in joint inversion of production and time-lapse seismic data. Walker and Lane (2007) presented a case study that included time-lapse seismic data as a part of the production history matching process, and show how the use of seismic monitoring can improve reservoir prediction. Castro et al. (2007) used a probabilistic approach for integration of time-lapse seismic and production data. Jin et al. (2009) developed a global optimization method based on very fast simulated annealing (VFSA) and a multi-resolution model parameterization scheme in joint inversion of production and time-lapse seismic data. Dadashpour et al. (2009) used AVO (amplitude versus offset) time lapse-data to constrain the results of the inversion, that is, the use of zero-offset amplitude and AVO gradient differences in conjunction with production data. They compared several optimization methods for joint inversion of production and time-lapse seismic data.

All of the previous research works mentioned above followed a fixed workflow of minimizing an objective function containing mismatch of seismic and production data and considered only uncertainties in reservoir porosity or permeability model (See Figure 1.1). The porosity or/and permeability models are updated till a minimum mismatch between observed and modeled data is achieved. In this process the parameters for reservoir and seismic simulator are considered as fixed, but in reality there are uncertainties attached with these parameters and if ignored, it can give misleading results in the history matching process. Also, joint inversion of production and time-lapse seismic data is complex and computationally expensive. It is essential, before proceeding with large scale history matching, to investigate parameter sensitivity for both types of data. It can reduce the computational cost and rank the sensitive parameters for perturbations. Therefore, it is critical to develop a systematic workflow for joint inversion that not only update porosity or permeability model but all sensitive parameters such that it can be applied to a real field.

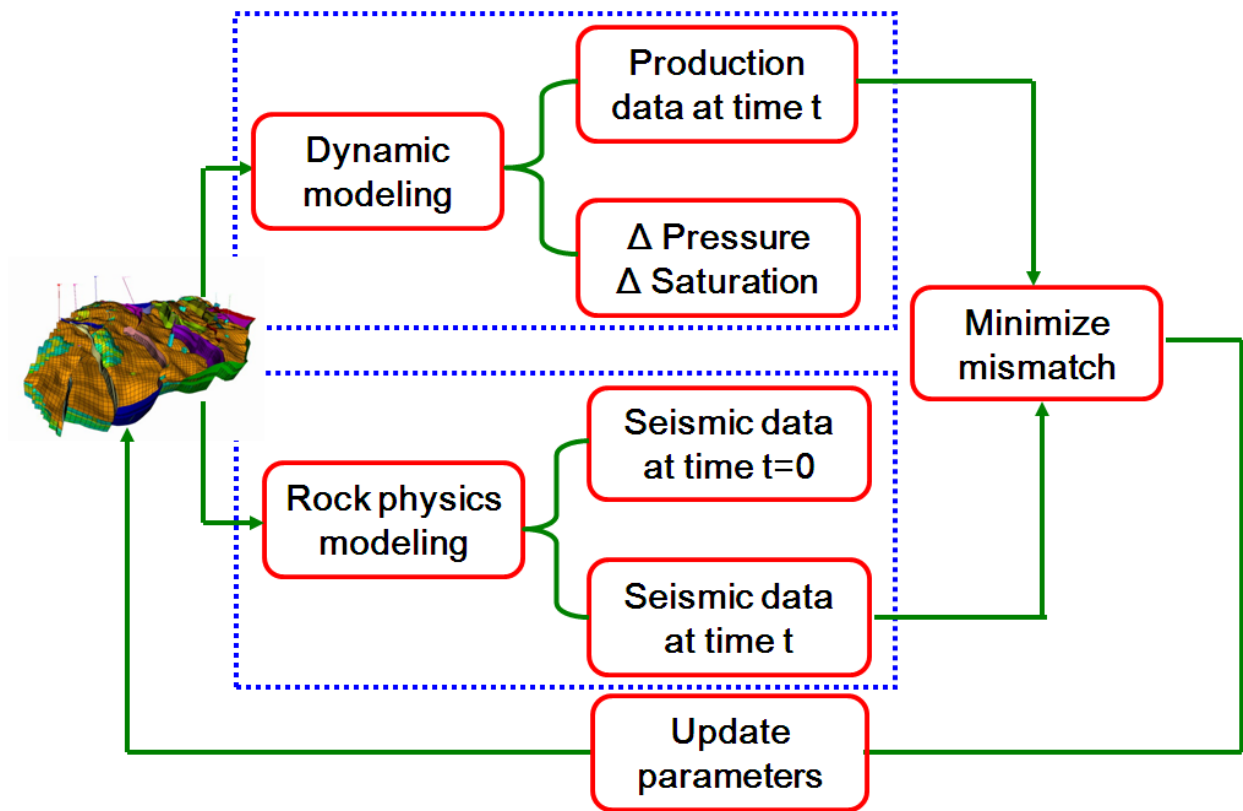


Figure 1.1: Workflow of joint inversion of time-lapse seismic and production data. The blue dotted boxes indicate the flow simulator and the seismic/rock physics simulator. Often these simulators are taken as black-boxes without investigating the sensitivity of the simulator parameters on the inter-related flow and seismic response of the reservoir.

In order to develop such a workflow, this thesis focuses on several components of the joint inversion process for production and time-lapse seismic data of the Norne field. A three-pronged approach is adopted to develop a systematic workflow. First, we identify sensitive parameters in the joint inversion loop. These sensitive parameters affect production response and/or time-lapse seismic response. Second, we analyze sensitive rock physics parameters in modeling time-lapse seismic response of a field. Third, we apply and compare different members of a family of particle swarm optimizers (Fernández-Martínez et al. 2009, García-Gonzalo and Fernández-Martínez, 2010) first on synthetic data set for joint inversion of production and time-lapse seismic data. Based on the results of the synthetic case, we include this family of particle swarm optimizers in the workflow for successful joint inversion of production and time-lapse seismic data of the Norne field, where we vary all of the sensitive parameters that have been identified previously.

The main contributions of this research are:

1. Sensitivity study for joint inversion of production and time-lapse seismic data of the Norne field; workflow can be used for joint inversion of production and time-lapse seismic data of other fields.
2. Sensitivity study of rock physics parameters in modeling the time-lapse seismic response of the Norne field; workflow can be applied for inversion of time-lapse seismic data of other fields;
3. Reservoir characterization by joint inversion of production and time-lapse seismic data using a family of particle swarm optimizers, comparison of their behavior in terms of history match and convergence;
4. Development and application of a systematic workflow for joint inversion of production and time-lapse seismic data of the Norne field using a family of particle swarm optimizers by varying the sensitive parameters identified in previous chapters;

## **1.2 Thesis outline**

This dissertation covers four main topics as described above to develop a systematic workflow for joint inversion of production and time-lapse seismic data of a field. These four topics are described in the next chapters.

### ***Chapter 2 – Norne Field Data and Reservoir Model***

Chapter 2 provides an introduction to Norne field dataset. All of the methodologies discussed in this dissertation are applied on Segment-E of the Norne field. We discuss data availability and reservoir modeling workflow to generate one thousand porosity and permeability realizations of the Norne field. These porosity and permeability realizations are used for research in the next chapters.

### ***Chapter 3 - Sensitivity Analysis for Joint Inversion of Time-lapse Seismic and Production Data of Norne Field***

Chapter 3 discusses a sensitivity study to identify and rank the sensitive parameters for joint inversion of production and time-lapse seismic data of the Norne field. We perform an experimental design on the parameters of the reservoir and seismic simulator. It is shown that reservoir model is not the most sensitive parameter in joint inversion of both the datasets. The selection of the most important reservoir parameters for joint inversion of time-lapse seismic and production data of Norne field is based on this study.

### ***Chapter 4 – Sensitivity Study of Rock Physics Parameters for Modeling Time-lapse Seismic Response of Norne Field***

Chapter 4 discusses a sensitivity study to identify sensitive rock physics parameters in modeling time-lapse seismic response of the Norne field. Rock physics analysis is the basis for modeling the time-lapse seismic signature. At first sensitive parameters are identified in the Gassmann's equation to generate the initial seismic velocities. The investigated parameters are mineral properties, water salinity, pore-pressure and gas-oil ratio (GOR). Next parameter sensitivity for time-lapse seismic modeling of Norne field is investigated. The investigated rock

physics parameters are clay content, cement, pore-pressure and mixing. This sensitivity analysis is used to select the important parameters for time-lapse (4D) seismic history matching. Sensitive rock physics parameters during the joint inversion of production and time-lapse seismic data of any real field can be identified using this method.

### ***Chapter 5 – Reservoir characterization by Joint inversion of production and time-lapse seismic data using family of particle swarm optimizers***

Chapter 5 discusses a methodology for reservoir characterization by joint inversion of production and time-lapse seismic data of a synthetic field using a family of particle swarm optimizers. High dimensionality of the inverse problem makes the joint inversion of both data sets computationally expensive. High dimensionality of the inverse problem can be solved by using principal component basis derived from the prior. In this chapter we have used a family of particle swarm optimizers in combination with principal component base for inversion of a synthetic data set. We analyze the performance of the different particle swarm optimizers, both in terms of history match and convergence. We show that particle swarm optimizers have very good convergence rate for the synthetic case. The results are promising and subsequently in the next chapter we have applied all of the particle swarm optimizers in joint inversion of production and time-lapse seismic data of the Norne field.

### ***Chapter 6 – Joint Inversion of Production and Time-lapse Seismic Data of Norne Field***

Chapter 6 discusses a systematic workflow for joint inversion of production and time-lapse seismic data of Norne field using a family of particle swarm optimizers and by varying the sensitive parameters that have been identified previously. Also, Seismic surveys of Norne field acquired in 2001 and 2004 are quantitatively interpreted and analyzed for the joint inversion. We successfully applied the proposed workflow for joint inversion of production and time-lapse seismic data of the Norne field. It is also shown that particle swarm optimizers have potential to be applied for joint inversion of a real field data set. The application of different particle swarm optimizers provided a set of parameters whose simulated responses provide satisfactory match

with production and time-lapse seismic data of Norne field. This workflow can be applied for joint inversion of production and time-lapse seismic data of other fields.

# Chapter 2

## **NORNE FIELD DATA AND RESERVOIR MODEL**

This chapter introduces the Norne field dataset and specially Segment E of this field. The Segment-E of Norne field is used as the research data set in this thesis. The chapter starts with a description of the available data. Subsequently a detailed description of reservoir modeling workflow is presented. These reservoir models are used in subsequent research studies of this thesis.

The Norne field is a large hydrocarbon reservoir located in the southern sector of Norland II area in blocks 6508/1 and 6608/10 in the Norwegian Sea, 200 km west of the mid-Norway coast (Figure 2.1). The field is 10 km long and 2 km wide and has a water depth of 380 m. Norne field was discovered in December 1991, and the development project began in 1993. The field consists of two separate structures, Norne main structure (Segment C, D and E) and Norne G-Segment (Figure 2.2).

The hydrocarbons are in sandstone rocks of lower and middle Jurassic age (Begum, 2009). It consists of a 110 m thick oil zone with 75 m thick overlying gas cap. The structure of the reservoir is flat with a trend of NE-SW. The top of the reservoir is about 2525 m below the mean sea level, and reservoir pressure is close to the hydrostatic pressure. The reservoir consists of five primary zones. Starting from the top they are Garn, Not, Ile, Tofte and Tilje.

Based on Verlo and Hetland (2008), Tilje formation was deposited in a marginal marine, tidally affected environment. Sediments deposited are mostly sand with some clay and conglomerates. There are numerous non-sealing intra reservoir faults present in the field. The Tofte formation was deposited on top of the unconformity during the Late Toracian. Mean thickness of the Tofte formation across the field is 50 m. It consists of medium to coarse grained sandstones. The Ile formation was deposited during the Aalenian, and is 32-40 m thick sandstone. The reservoir quality of the Ile formation is generally good, especially in the regressive deposition, whereas the reservoir properties are decreasing toward the top of the formation. The Not formation was also deposited during Aalenian time. It is a 7.5 m thick, dark grey to black claystone with siltstone lamina. It is almost impermeable and acts as a cap rock preventing communication between Garn and Ile formation. The Garn formation was deposited during the Late Aalenian and is 35 m thick sandstone. The depositional environment was near shore with some tidal influence. Reservoir quality is increasing upward within the formation, from pretty good in the lower parts to very good in the upper parts. The upper part is a sandstone unit which is coarsening upward from very fine to the fine grained sand.

The field has 29 producers and 10 injector wells. The oil production was started in November 1997 and gas in March 2001. The oil is produced with the support of gas and water injection. Several measures have been applied in the field to improve the hydrocarbon recovery. Time-lapse seismic monitoring is one of them. The purpose of time-lapse seismic monitoring is to identify undrained hydrocarbon areas and decide the locations of future wells. It is also being used to map the fluid movements in the reservoir and estimate the fluid and rock property for better management of the reservoir. Joint inversion or history matching of time-lapse seismic and production data can provide a better description of the reservoir and thus helps in efficient

reservoir characterization and monitoring. Reservoir models optimally constrained to both the data types can provide better reservoir forecasting.

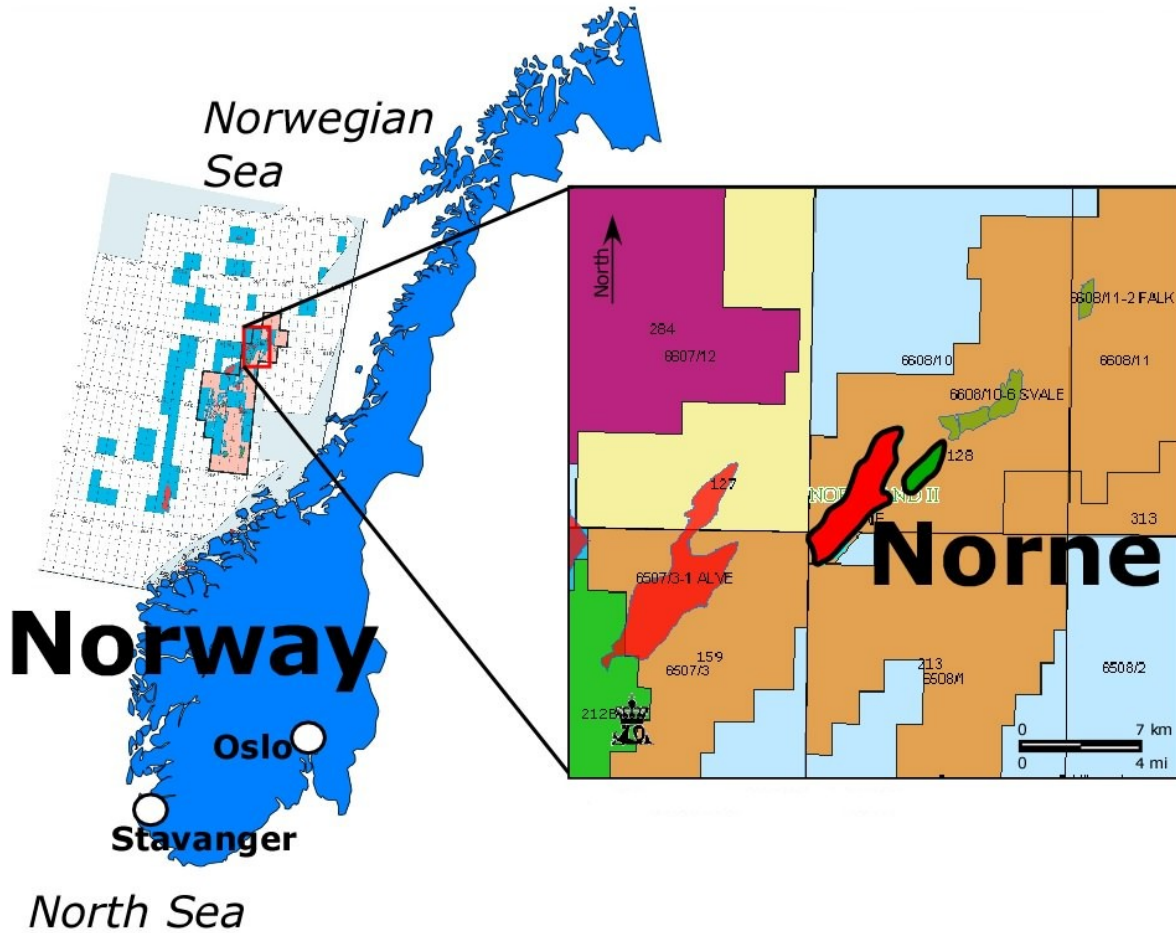


Figure 2.1: Location of the Norne field situated in the Norwegian Sea (Begum, 2009)

## 2.1 Segment-E of Norne Field

Segment-E is located on the north most part of the Norne field. It is bounded by normal faults in the north, east and west and separates segment-D of Norne field in south by a non-sealing fault. Segment-E has also five primary zones as discussed in the previous section. It is producing with five wells (3 producers and 2 injectors). Oil is mainly found in Ile and Tofte formation and free gas is in the Garn formation. The porosity is in the range of 25-30 % while permeability varies from 20 to 2500 mD (Steffensen and Karstad, 1995; Osdal et al. 2006). Since

Not formation is impermeable and acts as a cap rock, the segment E has two OWC (oil-water contact) and GOC (gas-oil contact).

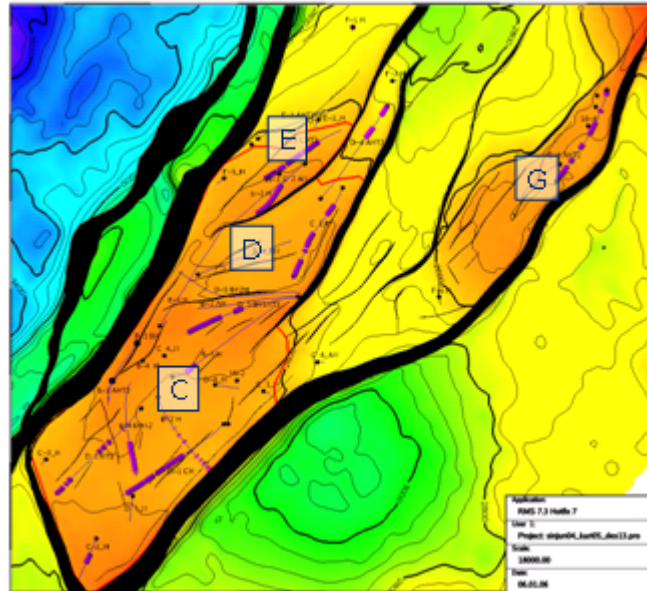


Figure 2.2: Top view of Norne field showing segments C, D, G and E present in the field. This study is focused on segment E of the Norne field (Begum, 2009)

## 2.2 Available Data

The Norne field has a wide variety of dataset, and it is maintained by a team of geologists, geophysicists and reservoir engineers working with Statoil. The dataset including well log data of 29 producer and 10 injector wells is available. These well logs include porosity, saturation, gamma ray, sonic and density logs. Only nine wells have sonic logs. Norne field has a high quality time-lapse seismic data. The baseline survey for monitoring is acquired in 2001, and monitor surveys are available in 2003, 2004 and 2006. Time-lapse seismic data has near, mid, far and full 3D stacks. Other data includes properties of the fluids in the reservoir, interpreted horizons, faults, velocity model, historical production data and a flow simulation model built in Eclipse (Copyright 2011 Schlumberger) flow simulator software.

## 2.3 Reservoir Modeling Workflow

The structural framework (structure grid) of the reservoir has been built by the team of geoscientists in Statoil based on interpreted horizons and faults (Figure 2.3). This section describes in details the process of generation of realizations for porosity and permeability based on the well data.

The 3D geocellular model has 146 X 112 X 22 number of grid blocks; each grid block has an average width of 120 m (in x and y direction) and average thickness of 8m in the z direction. The grid is populated with porosity and permeability based on the well log data (Figure 2.4) as described in the following. The porosity is distributed using variogram-based two-point geostatistics algorithm SGSIM (sequential gaussian simulation). There are 22 horizontal layers in the reservoir grid in the vertical direction. Variograms are obtained by fitting the models to the well log data for each of the 22 layers. The details of the variograms are shown in the Table 2.1. These variograms are used for the porosity simulations. 1000 porosity realizations are generated using SGSIM. Figure 2.5 shows four porosity realizations out of one thousand generated porosity realizations.

Next permeability models are obtained for each of the porosity models based on different correlations established between porosity and permeability in each of the 22 layers. These correlations are established based on the porosity and permeability data provided by Statoil. Table 2.2 shows the porosity permeability correlation used in each of the 22 layers for generation of permeability models.

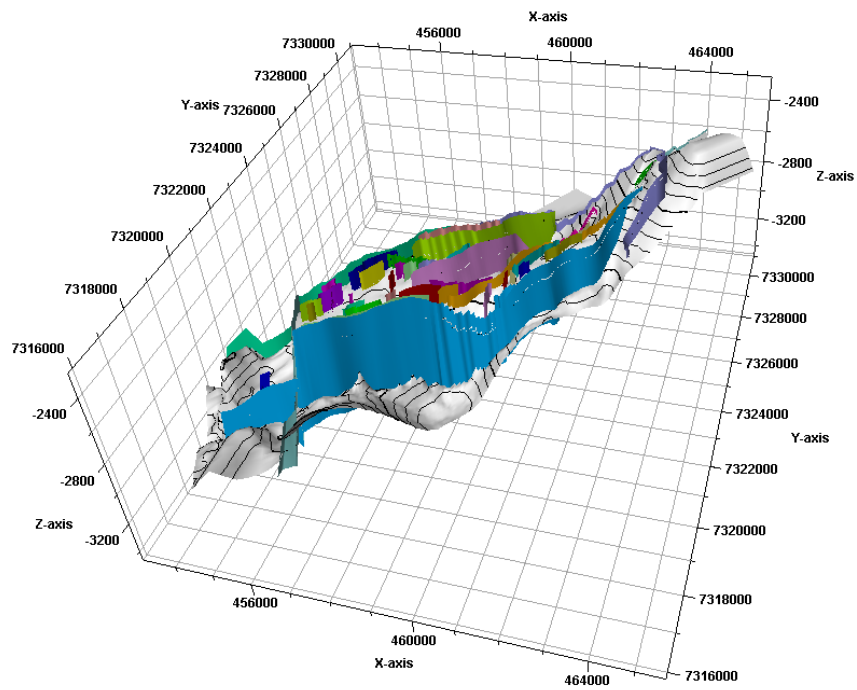


Figure 2.3: Structural framework of Norne field. This framework has been used to generate 1000 realizations of Norne field

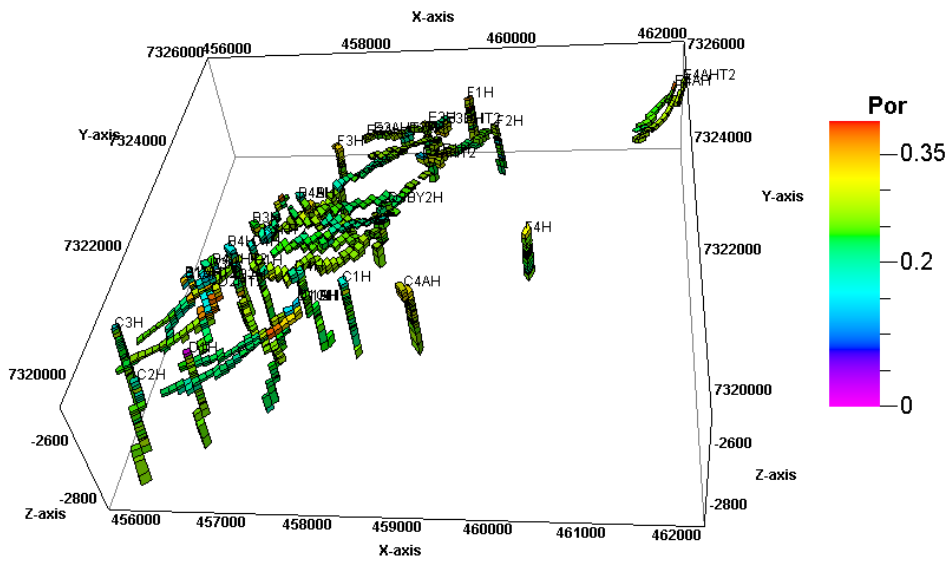


Figure 2.4: Well logs of Norne field used for generation of one thousand realizations of Norne field

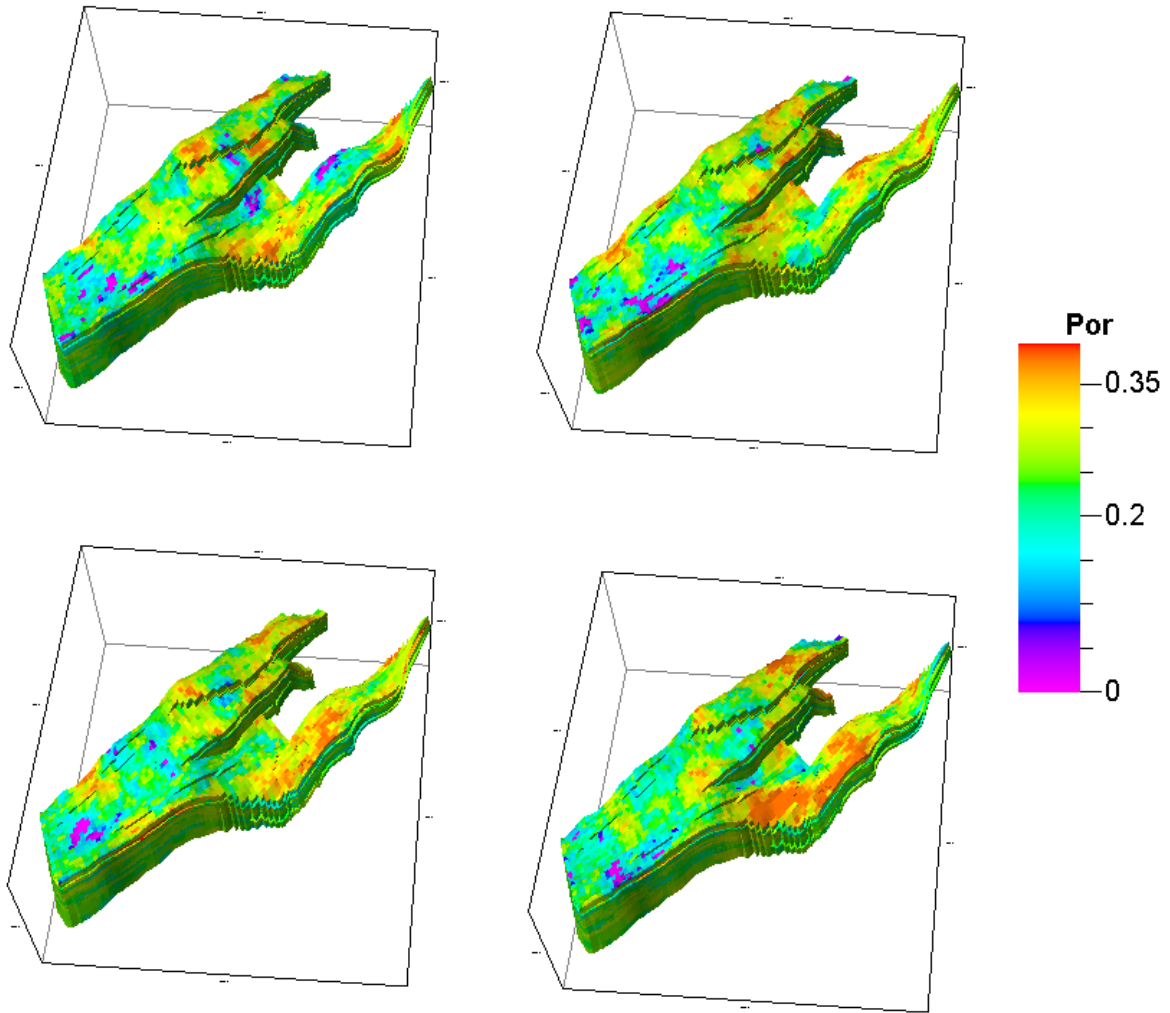


Figure 2.5: Four porosity realizations of Norne field, one thousand porosity realizations are generated using SGSIM and variograms

<b>Layers</b>	<b>Type</b>	<b>Nugget</b>	<b>Ranges</b>	<b>Angles</b>
Layer 1	Spherical	0	1231/912/0	45/135/0
Layer 2	Spherical	0.018	1584/549/0	22/112/0
Layer 3	Spherical	0.01	1081/500/0	42/132/0
Layer 4	Impermeable Layer			
Layer 5	Spherical	0.01	2506/629/0	88/178/0
Layer 6	Spherical	0.01	2574/500/0	45/135/0
Layer 7	Spherical	0.014	839/500/0	0/270/0
Layer 8	Spherical	0	1905/668/0	44/134/0
Layer 9	Spherical	0	800/674/0	135/225/0
Layer 10	Spherical	0	1527/500/0	45/135/0
Layer 11	Spherical	0	830/500/0	125/215/0
Layer 12	Spherical	0.005	2486/971/0	45/135/0
Layer 13	Spherical	0	975/500/0	135/225/0
Layer 14	Spherical	0.02	2041/775/0	45/135/0
Layer 15	Spherical	0	1256/500/0	45/135/0
Layer 16	Spherical	0.02	1644/500/0	45/135/0
Layer 17	Spherical	0.02	1809/423/0	133/223/0
Layer 18	Spherical	0.013	1004/500/0	0/270/0
Layer 19	Spherical	0.015	2136/500/0	133/223/0
Layer 20	Spherical	0	1937/755/0	45/135/0
Layer 21	Spherical	0	2175/500/0	48/138/0
Layer 22	Spherical	0.028	1571/583/0	26/116/0

Table 2.1: The details of the variograms generated using well logs. These variograms are used for generation of one thousand porosity models

Layers	Poro ( $\Phi$ ) – Perm (K) correlation
Layer 1	$K = 10^{(0.613367 \Phi + 2.3856)}$
Layer 2	$K = 10^{(41.2697 \Phi - 8.3165)}$
Layer 3	$K = 10^{(20.9242 \Phi - 2.84573)}$
Layer 4	K = Impermeable Layer
Layer 5	$K = 10^{(16.7372 \Phi - 1.89085)}$
Layer 6	$K = 10^{(16.7376 \Phi - 1.89096)}$
Layer 7	$K = 10^{(7.15568\Phi + 0.305633)}$
Layer 8	$K = 10^{(7.15594 \Phi + 0.305571)}$
Layer 9	$K = 10^{(14.0792 \Phi - 0.995441)}$
Layer 10	$K = 10^{(10.8496 \Phi + 0.0321041)}$
Layer 11	$K = 10^{(9.98624 \Phi - 0.0986752)}$
Layer 12	$K = 10^{(16.4895 \Phi - 1.89487)}$
Layer 13	$K = 10^{(11.0849 \Phi - 0.28299)}$
Layer 14	$K = 10^{(14.7974 \Phi - 1.50772)}$
Layer 15	$K = 10^{(7.26556 \Phi + 0.150546)}$
Layer 16	$K = 10^{(17.7683 \Phi - 1.45932)}$
Layer 17	$K = 10^{(21.3169 \Phi - 2.21284)}$
Layer 18	$K = 10^{(12.1738 \Phi - 0.113427)}$
Layer 19	$K = 10^{(26.8009 \Phi - 3.28972)}$
Layer 20	$K = 10^{(14.6343 \Phi - 0.924636)}$
Layer 21	$K = 10^{(20.6326 \Phi - 1.85891)}$
Layer 22	$K = 10^{(11.3666 \Phi + 0.0467612)}$

Table 2.2: Porosity permeability correlation generated using the data provided by Statoil. These correlations are used for generation of permeability models.

# Chapter 3

## **SENSITIVITY ANALYSIS FOR JOINT INVERSION OF TIME-LAPSE SEISMIC AND PRODUCTION DATA OF NORNE FIELD**

### **3.1 Introduction**

Dynamic data of the reservoir is used for efficient reservoir characterization, monitoring and forecasting. The dynamic data set includes production and time-lapse seismic data. Both of these data sets can be used in history matching process for a better description of the reservoir and thus for better reservoir forecasting. As previously mentioned, it is essential, before proceeding with large scale history matching, to investigate parameter sensitivity for both types of data. In this chapter the data set of Norne field is used to find out which reservoir rock and fluid parameters have the most impact jointly on time-lapse seismic and production data. The parameters investigated for this study include rock physics model, relative permeability, pore compressibility, fluid mixing and porosity model.

## **3.2 Sensitive Parameters**

Joint inversion of time-lapse seismic and production data consist of modeling of production data and time-lapse seismic data. Modeling of production data is done by a reservoir simulator and requires petrophysical properties of the reservoir, such as porosity, permeability and relative permeability curves. Pressure and saturation distribution of reservoir at different times, and a rock physics model are needed for modeling of time-lapse seismic data. Flow and time-lapse seismic response of a reservoir model or a set of parameters (that includes reservoir model) is compared with the observed production and time-lapse seismic data and a misfit is obtained based on an objective function. The objective function is minimized using an optimization algorithm, and in the process the varied parameters are updated. Finally, a reservoir model or a set of parameters (that includes reservoir model) is obtained which provides minimum misfit with the observed data. Based on this workflow we selected the following parameters for a sensitivity study:

- Porosity and Permeability model
- Relative permeability curves
- Pore compressibility
- Rock physics models for elastic properties of the rocks
- Spatial scales of saturation distribution

In the following sections we describe in detail the variations in these factors that were used in the sensitivity study.

### **3.2.1 Porosity and Permeability Models**

Reservoir rock properties are the basic input parameters for modeling of production and time-lapse seismic data. Reservoir rock porosities and permeabilities are used to model the flow response. Porosities, saturations, and pore pressures are linked to the seismic response through rock physics models. Thus, spatial distribution of porosity and permeability is an important

parameter to consider for this study. The generation and selection of these porosity and permeability models are described below.

The workflow to generate reservoir porosity and permeability models for segment E of the Norne field is described in Chapter 2. The structure model for segment E of Norne field is generated in PETREL (Copyright 2011 Schlumberger) based on the horizon data. The 3D geocellular model consists of 113344 (46 x 112 x 22) cells. Next variogram models are estimated for each of the 22 layers based on the well log data. These variogram models are used to generate one hundred porosity realizations using Sequential Gaussian simulation (SGSIM) (Deutsch and Journel, 1998). Permeability models are generated based on the correlation between porosity and permeability in each of the 22 layers.

All one hundred porosity and permeability models cannot be included in the experimental design due to high computational cost. Thus, a few representative models are required in the experimental design such that the computational cost is not very high, as well as selected models are able to capture the variability present in one hundred initial realizations. We selected three representative porosity models based on multi-dimensional scaling (MDS) (Borg and Groenen, 2005) and kernel k-medoid clustering (Scholkopf and Smola, 2002, Scheidt and Caers, 2009a, b).

### 3.2.2 Multi-Dimensional Scaling

Multi-dimensional scaling is a method to project high dimensional models from the metric space to a low dimensional space such that euclidean distance between models in the low dimensional space is close to the distance used to construct the initial metric space for models.

$$M = (m_1 \ m_2 \ m_3 \ m_4 \ \dots \ m_n) \quad \in R^{L \times n} \quad (3.1)$$

Let  $M$  be the ensemble of  $n$  models. Each of the models has a dimension of  $L$ . Multi-dimensional scaling on  $M$  is such that

$$d(m_i, m_j) \cong \sqrt{(m_{i,p} - m_{j,p})^T (m_{i,p} - m_{j,p})} \quad (3.2)$$

where  $p$  is the dimension of projection space. The method starts with centering of the distance matrix  $D$ .

$$A = CDC \quad (3.3)$$

$C$  is the centering matrix,

$$C = I - \frac{1}{n}QQ^T \quad (3.4)$$

$I$  is the identity matrix and  $Q$  is a column vector of  $n$  ones. The elements of distance matrix  $D$  are calculated as

$$D_{ij} = -\frac{1}{2}d_{ij}^2 \quad (3.5)$$

Where  $D_{ij}$  is the distance between  $i$ th and  $j$ th models. Next eigenvalue decomposition of the distance matrix  $D$  is done to obtain eigenvalues and eigenvectors,

$$D = V_D \Lambda_D V_D^T \quad (3.6)$$

$V_D$  is the matrix of eigenvectors and  $\Lambda_D$  is the diagonal matrix containing eigenvalues of matrix  $D$ . Now if,  $p$  largest eigenvalues and associated eigenvectors are retained, the models in the MDS space are defined as,

$$M_m = V_{D,p} \Lambda_{D,p}^{1/2} \quad (3.7)$$

The values of  $n$  and  $L$  in this study are 100 and 113344 respectively. The reservoir models are projected in a two dimensional space to select three representative reservoir porosity models (Figure 3.1). The representative models are selected as the centroid of clusters obtained after the kernel k-medoid clustering is performed on the projections in the MDS space. The distance used for initial distance matrix is euclidean.

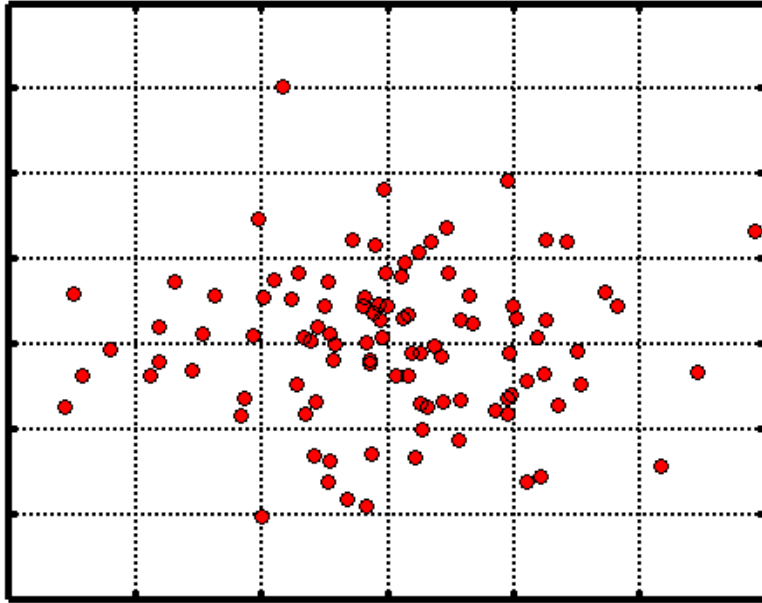


Figure 3.1: MDS performed on 100 porosity realization and plotted in two dimensions. Red points correspond to different porosity realizations. Porosity realizations very different from each other are far away in the plot

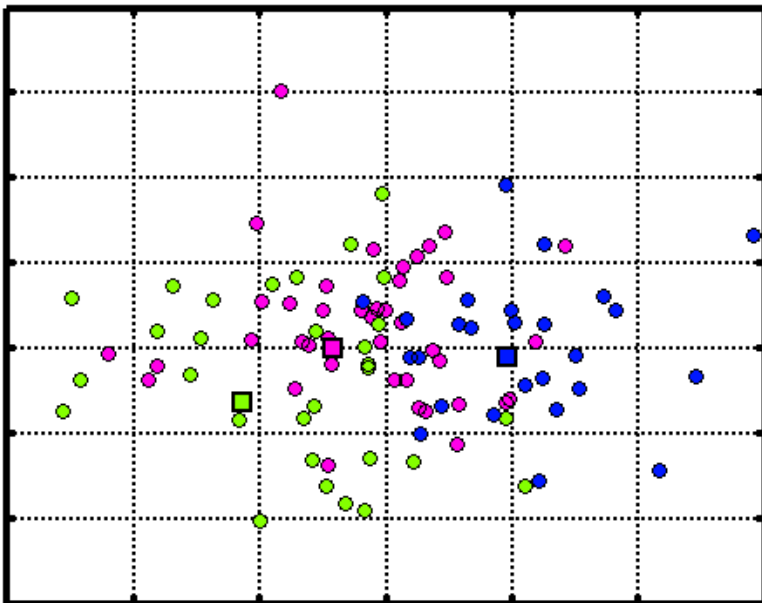


Figure 3.2: Kernel k-medoid clustering performed on 100 porosity realizations after MDS. Green, blue and magenta color represents different clusters. Medoids of clusters are represented by squares

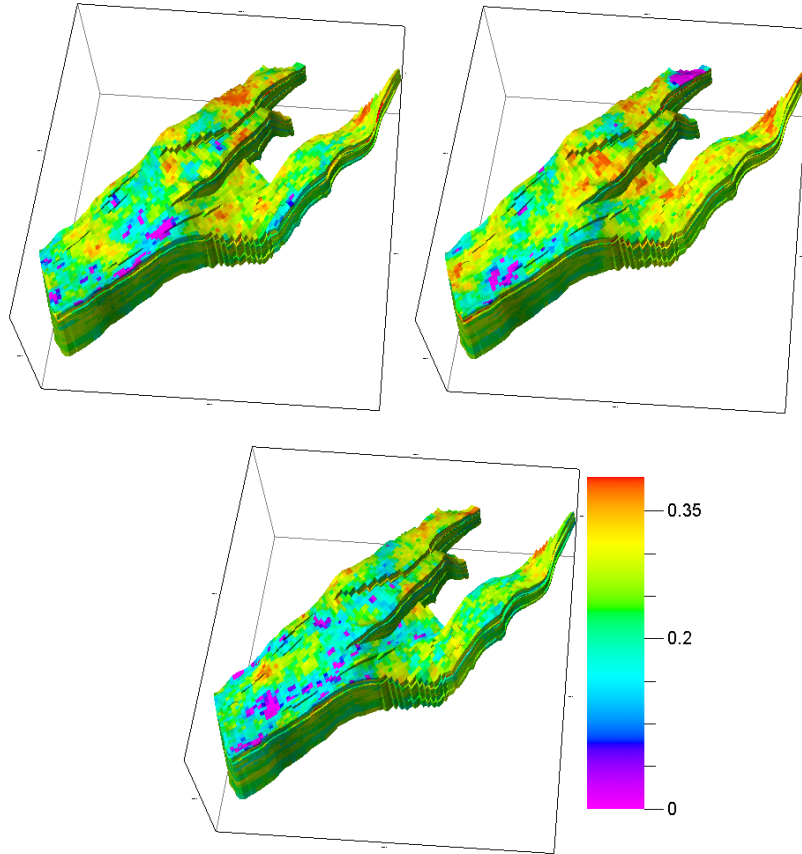


Figure 3.3: Three porosity realizations associated with the medoids obtained after clustering. These realizations are selected for the sensitivity study

### 3.2.3 Kernel K-Medoid Clustering

Clustering is an important tool to select few representative models capturing the variations present in the initial ensemble. K-medoid clustering is performed after the projection of models from the metric space to a low dimensional space since it is easy and converges fast. Kernel k-medoid clustering is k-medoid clustering in kernel space. In this method models are arranged linearly in the kernel space making clustering very effective.

K-medoid is an iterative algorithm to find the locations of the medoids such that sum of distance between models and their nearest medoid is minimized. Once the locations of medoids are identified, the models nearest to medoids are assigned the same cluster. In the kernel k-medoid clustering the very first step is the mapping of models from MDS space to kernel space. Several kernel functions are available for mapping, but Radial-Basis function (RBF) kernel is

often selected since RBF kernel is a function of distances only. Also since the distance in the kernel space is calculated using kernel function, it does not require definition of kernel feature  $\Phi$  explicitly (Scholkopf and Smola, 2002). The distance between two models is defined as

$$k(m_{i,p}, m_{j,p}) = \exp\left(-\frac{\|m_{i,p} - m_{j,p}\|^2}{2\sigma^2}\right) \quad (3.8)$$

Based on the workflow mentioned above, three porosity models and associated permeability models are selected for sensitivity study. The clusters obtained after kernel k-medoid clustering on 100 porosity realizations are shown in the Figure 3.2. Figure 3.3 shows the porosity models corresponding to these three clusters.

### 3.2.4 Relative Permeability

Relative permeability is an important part of modeling the flow response of the reservoir. It affects multiphase flow and distribution of fluids inside the reservoir during production and subsequently affects seismic response. Production response is affected by relative permeability. It has impact directly on flow as well as indirectly on time-lapse seismic response. The available data of Norne field includes eighty four combinations of oil-water relative permeability and associated gas-oil relative permeability curves (Figure 3.4). These curves have different oil relative permeability end point and critical water saturations. Two pairs of relative permeability curves are selected for sensitivity analysis (oil-water relative permeability curve and associated gas-oil relative permeability curve). These two relative permeability curves have minimum and maximum set of oil relative permeability end point and critical water saturations as shown in Figure 3.4. This study is based on the assumption that selected relative permeability curves captured the variations present in all of the relative permeability curves associated with the Norne field.

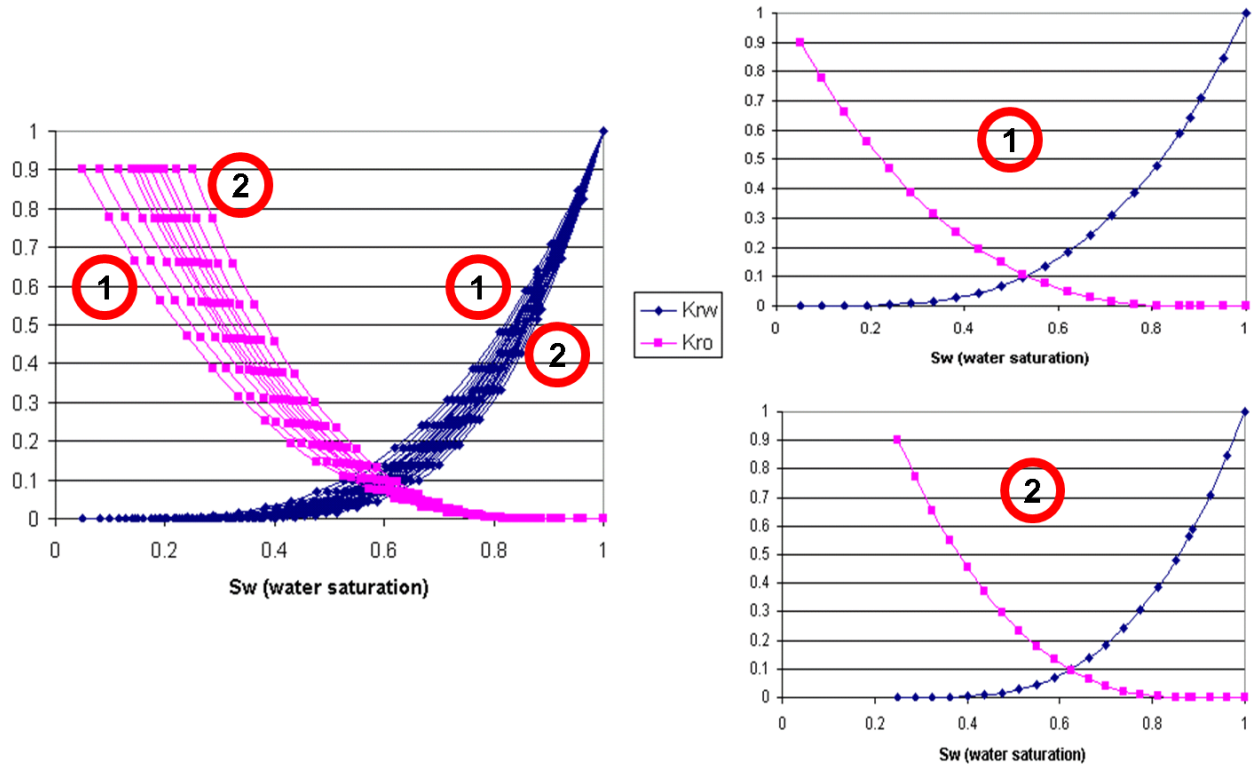


Figure 3.4: Oil-water relative permeability curves for Norne field. Curve pairs 1 and 2 are selected for this study. Selected curves capture the uncertainty associated with relative permeability curves of Norne field.

### 3.2.5 Pore compressibility

Pore compressibility is a parameter that can impact both flow, as well as elastic (and hence seismic) response of the reservoir. Compressibilities for porous media depend on two pressures (the external confining pressure,  $\sigma_c$  and the internal pore pressure  $\sigma_p$ ) and two volumes (bulk volume,  $V_b$  and pore volume,  $v_p$ ). Therefore, we can define at least four compressibilities. Following Zimmerman's (1991) notation, in which the first subscript indicates the volume change (b for bulk, p for pore) and the second subscript denotes the pressure that is varied (c for confining, p for pore), these compressibilities are

$$C_{bc} = \frac{1}{V_b} \left( \frac{\partial V_b}{\partial \sigma_c} \right)_{\sigma_p} \quad (3.9)$$

$$C_{bp} = \frac{1}{V_b} \left( \frac{\partial V_b}{\partial \sigma_p} \right)_{\sigma_c} \quad (3.10)$$

$$C_{pc} = \frac{1}{v_p} \left( \frac{\partial v_p}{\partial \sigma_c} \right)_{\sigma_p} \quad (3.11)$$

$$C_{pp} = \frac{1}{v_p} \left( \frac{\partial v_p}{\partial \sigma_p} \right)_{\sigma_c} \quad (3.12)$$

Note that the signs are chosen to ensure that the compressibilities are positive when tensional stress is taken to be positive. Thus, for instance,  $C_{bp}$  is to be interpreted as the fractional change in the bulk volume with respect to change in the pore pressure while the confining pressure is held constant. These are the dry or drained bulk and pore compressibilities. The effective dry bulk modulus is  $K_{dry} = 1/C_{bc}$ , and is related to the seismic P-wave velocity by

$$V_p = \sqrt{(K_{dry} + 4\mu/3)/\rho} \quad (3.13)$$

where  $\rho$  and  $\mu$  are the dry bulk density and shear modulus respectively. Dry rock velocities can be related to the saturated bulk rock velocity through the Gassmann's fluid substitution (Gassmann, 1951) (Figure 3.5).

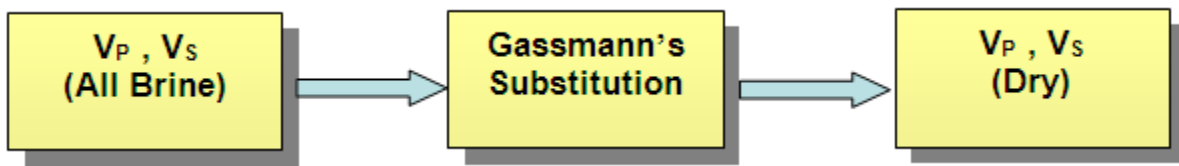


Figure 3.5: Dry rock velocities are calculated using saturated bulk rock velocities and Gassmann's fluid substitution.

The different compressibilities can be related to each other by elasticity theory using linear superposition and reciprocity. The compressibility  $C_{pp}$  appears in the fluid flow equations through the storage term, and can be related to  $C_{bc}$  (and hence to seismic velocity) by the equation (Zimmerman, 1991).

$$C_{pp} = \frac{C_{bc} - (1 + \phi) \frac{1}{K_{min}}}{\phi} \quad (3.14)$$

where  $\phi$  is the porosity and  $K_{min}$  is the solid mineral bulk modulus. To test the sensitivity of the seismic velocity and fluid flow response to variations in pore compressibility, three levels of pore compressibility were selected based on its overall range estimated from well logs. Pore compressibility for each of the zone is calculated based on the well log data and using the relation between  $C_{pp}$  and  $C_{bc}$  as described above. Figure 3.6 shows histograms of pore compressibility in each of the zones. The plots show that the pore compressibility can vary within formations by factors of 2 to 4 and by an order of magnitude across different formations. Yet, often in flow simulations (typically simulations that do not account for geomechanics) though porosity is taken to vary over every grid block, the corresponding rock pore compressibility is taken to be a constant. This leads to a clearly inconsistent model. Pore compressibility of the rock varies with porosity in each of the zones in Norne and is shown in Figure 3.7. Suman et al. (2008) showed that spatial variability in pore compressibility can play an important role in time-lapse seismic modeling. Three sets of pore compressibility values ( $1.5e^{-10} \text{ Pa}^{-1}$ ,  $3e^{-10} \text{ Pa}^{-1}$  and  $5e^{-10} \text{ Pa}^{-1}$ ) are selected for the sensitivity study. These values capture the range of pore compressibility variations observed in the Norne field.

### 3.2.6 Rock Physics Model

Rock physics modeling is used to determine the change in elastic properties of rocks due to variations in mineralogy, change in fluid type, variation in saturation and pore pressure and change in the reservoir effective stress. It can also be used to populate acoustic and elastic properties ( $V_p$  and  $V_s$  and density) inside the reservoir away from the well. The basis of our approach is to relate elastic moduli and porosity near the well (based on the well log data) and use this relation to populate away from the well. Rock physics model selection is an important step in time-lapse seismic modeling. The rock physics models can be different depending upon diagenesis, sorting, and clay content present in the reservoir (Figure 3.8). In this study two rock physics models are selected for analysis.

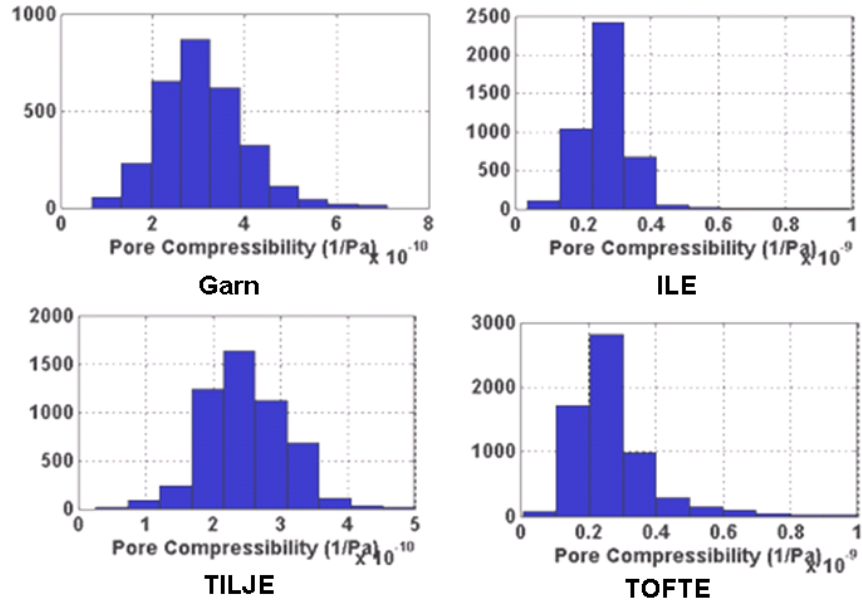


Figure 3.6: Histograms of pore compressibilities present in different zones (Garn, Ile, Tofte and Tilje) of Norne field.

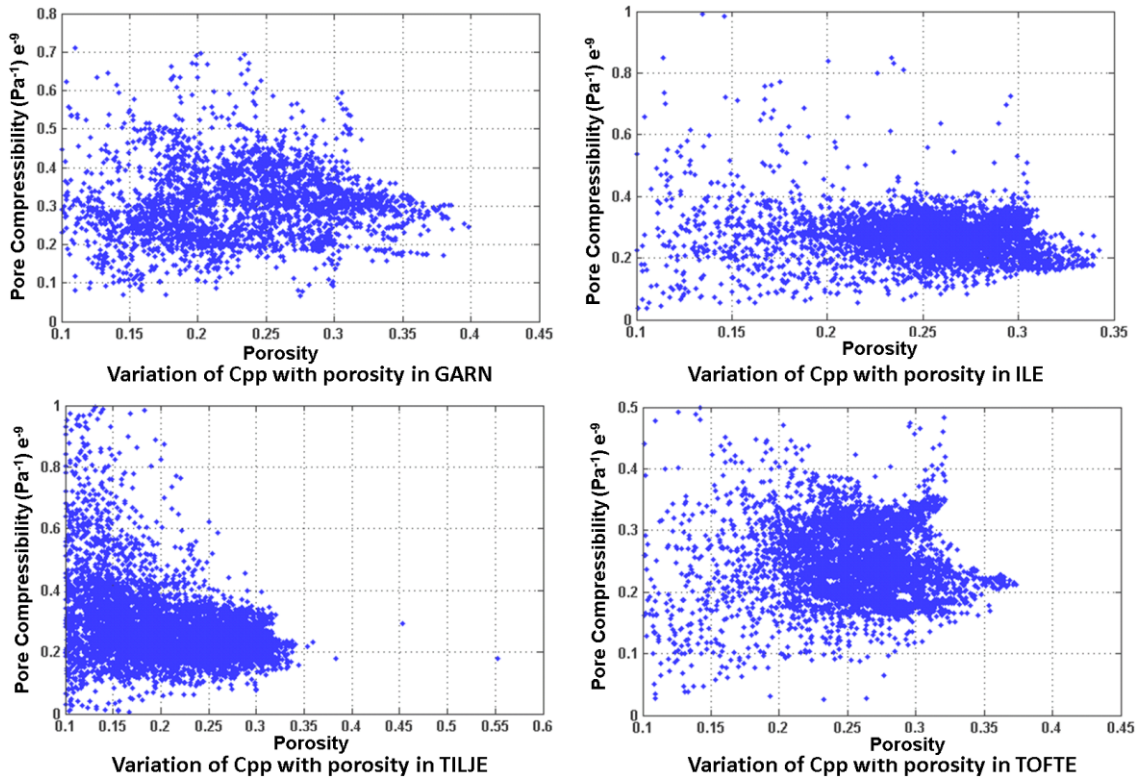


Figure 3.7: Crossplots of porosity and pore compressibility in different zones of Norne field (Garn, Ile, Tofte and Tilje).

These two rock physics models are the cemented sand model and the unconsolidated sand model. These models are described in Dvorkin and Nur (1996) and have been used before for North Sea reservoirs. Seismic velocity porosity trends can be established using well log data, but uncertainties are always present away from the wells. Therefore, it is necessary to consider the possibility of other scenarios not seen in the well.

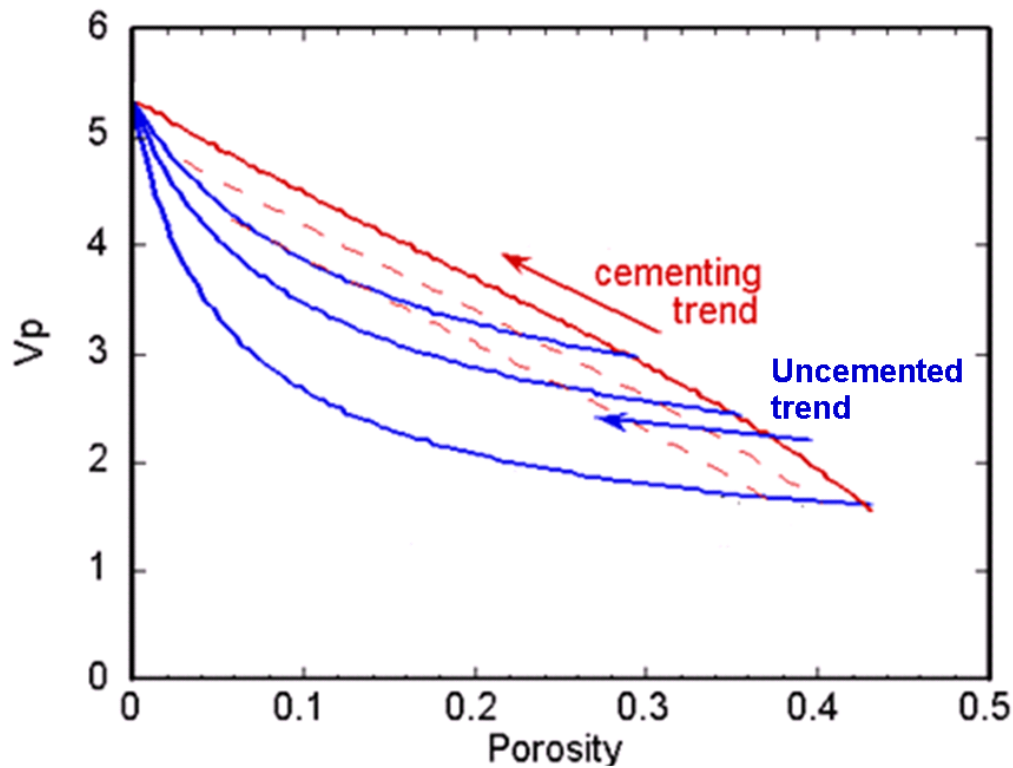


Figure 3.8: Schematic of seismic velocity – porosity trend for cemented and uncemented sands (modified from Avseth et al. 2005).

### 3.2.7 Fluid mixing

Seismic velocities depend on fluid saturations as well as spatial scales of saturation distribution. It has been pointed out by several authors that seismic velocity not only depends on fluid type and saturation but also on spatial scale of fluid mixing in the pore space (White, 1975, Dutta and Ode, 1979, Mavko and Mukerji, 1998). Uncertainties in the saturation scale lead to uncertainties in the interpretation of seismic attributes. Sengupta (2000) discussed the importance of saturation scales in modeling the changes in seismic velocity with respect to changes in the reservoir at different times. Seismic velocities are different for uniform and patchy saturation

distribution in the reservoir. For example, for an oil-gas mixture the seismic P-wave velocity can be different for the same oil saturation depending upon the type of fluid mixing. Figure 3.9 shows the effect on seismic P-wave velocity due to change in oil saturation in an oil-gas mixture for uniform and patchy saturations. Oil saturation of 0.6 could have seismic P-wave velocity of 2.09 km/s for uniform saturation or 2.16 km/s for patchy saturation, or anywhere in between.

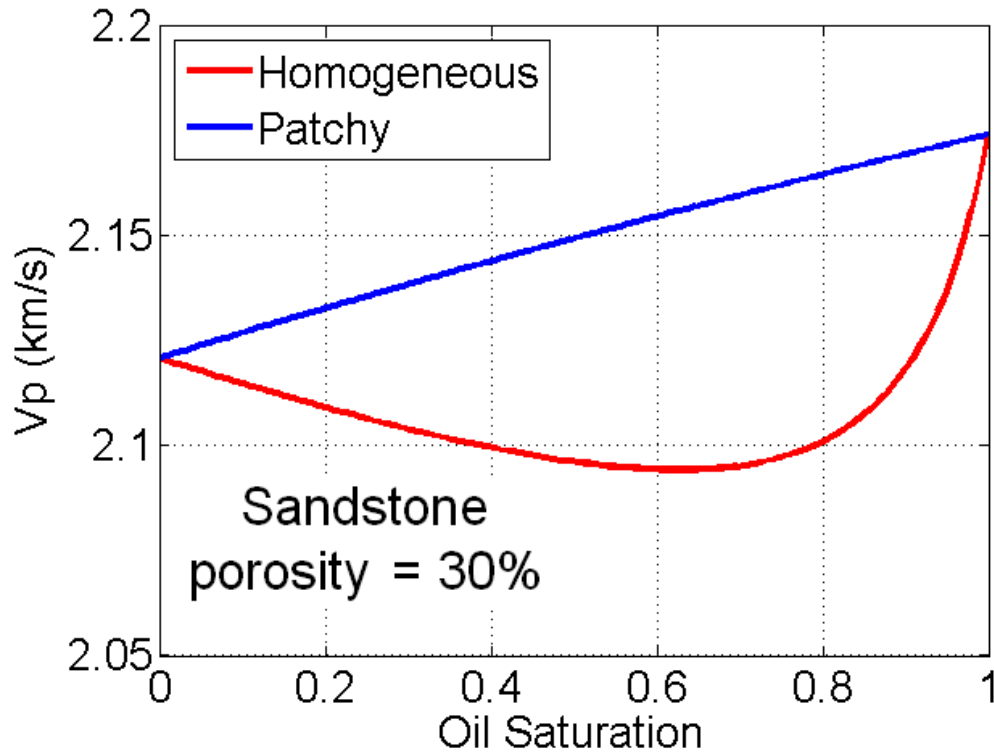


Figure 3.9: P-wave velocity trends for homogeneous and patchy saturations in an oil-gas sand having a porosity of 30%.

Thus, saturation scale is considered as a parameter for this study. Table 3.1 describes the selected parameters and their ranges for the sensitivity analysis.

We have selected experimental design for sensitivity analysis. All of the selected parameters are varied, and the response is calculated for combination of parameters values. Based on the parameters values selected for this study, 72 different cases have to be simulated with different combination of parameter values.

<b>Parameters</b>	<b>Values</b>		
Pore Compressibility (Pa <sup>-1</sup> )	1.5e-10	3e-10	5e-10
Relative Permeability	Low	High	
Rock Physics Model	Cemented	Uncemented	
Saturation Scale	Uniform	Patchy	
Porosity Model	Model 1	Model 2	Model 3

Table 3.1: Parameters and their ranges for sensitivity study

### 3.3 Methodology

Figure 3.10 describes the workflow used for this study. At first flow simulation is performed on selected reservoir porosity and associated permeability model from 1997 to 2004. Flow simulation provided production response (water cut in the field from 1997 to 2004) and change in pressure and saturation inside the reservoir over four years (from 2001 to 2004). Subsequently rock physics modeling is performed by selecting rock physics model (cemented or unconsolidated) to obtain seismic P-wave velocity at 2001. Next Gassmann's fluid substitution is used to obtain seismic P-wave velocity at 2004. We only considered the change in pore pressure and fluid saturation over three years. The change in p-wave seismic impedance for segment E is calculated for all of the 72 cases and selected as a basis for comparison of time-lapse seismic response. As the impedance change can be positive or negative, so we compare L1 norm of change in p-wave impedance. Water cut in well E-2H from 1997 to 2004 is taken as the basis for comparing production response. The sum of water cut in the field at each time step from 1997 to 2004 is compared for all of the 72 cases.

### 3.4 Flow Simulation

Flow simulation is performed for all 72 variations of the parameters, starting from the initial condition of the reservoir. This provides us the spatial distributions of fluids and variation of pore pressure in the reservoir at different times after the start of production. In order to use

Gassmann's equations, we need the saturations of each fluid (Oil, Water and Gas) at every cell at different times. The flow simulation model was provided by Statoil.

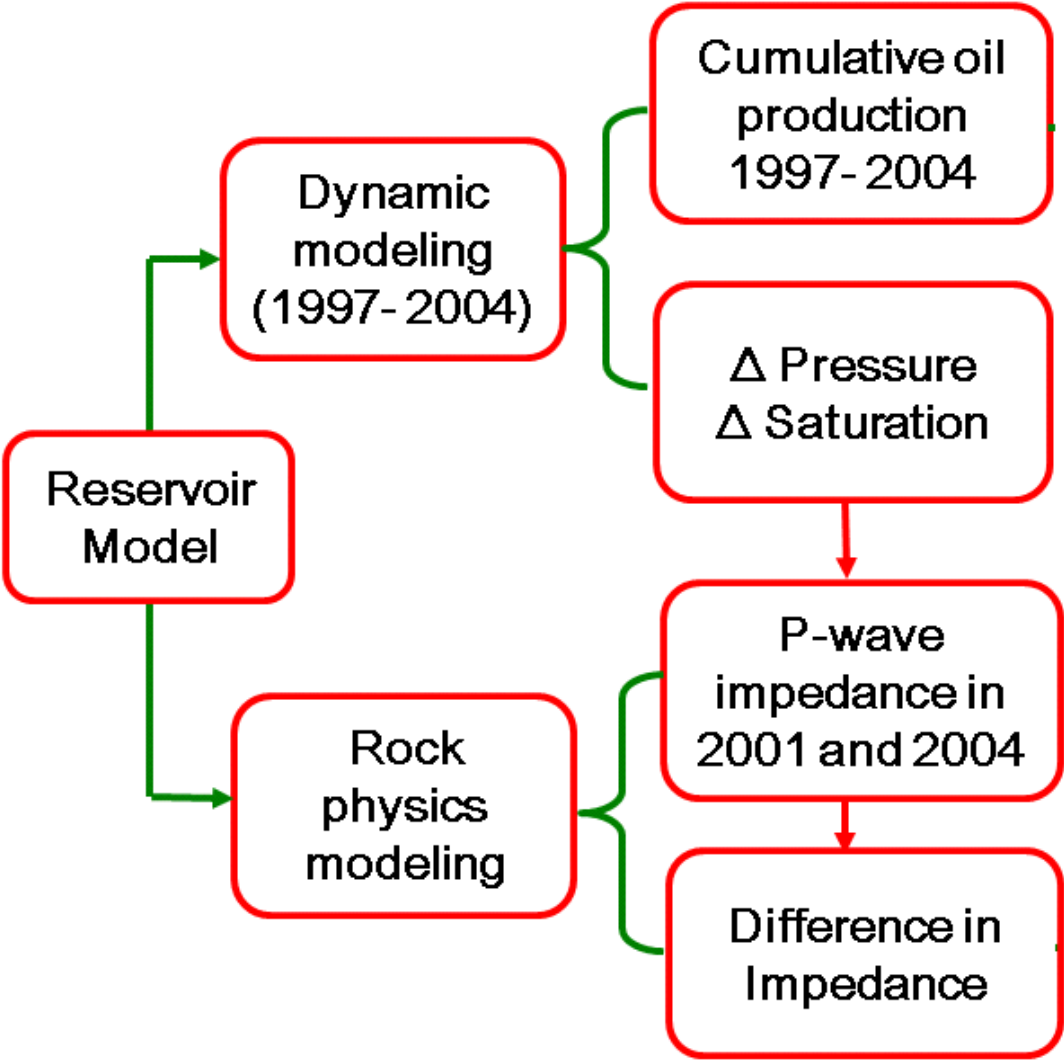


Figure 3.10: Workflow for generation of production and time-lapse seismic response associated with a set of parameters used in this study.

We observed that a fault separates segment E from other segments present in the Norne field. The simulation model consists of 113344 number of grid cells (46 x 112 x 22). The focus of this study is on segment E, but simulation model has all the segments present in the Norne field since all of the segments are separated by non-sealing faults. Segment E (Figure 3.11) has three producers (E-2H, E-3H, E-3AH) and two water injectors (F-1H and F-3H).

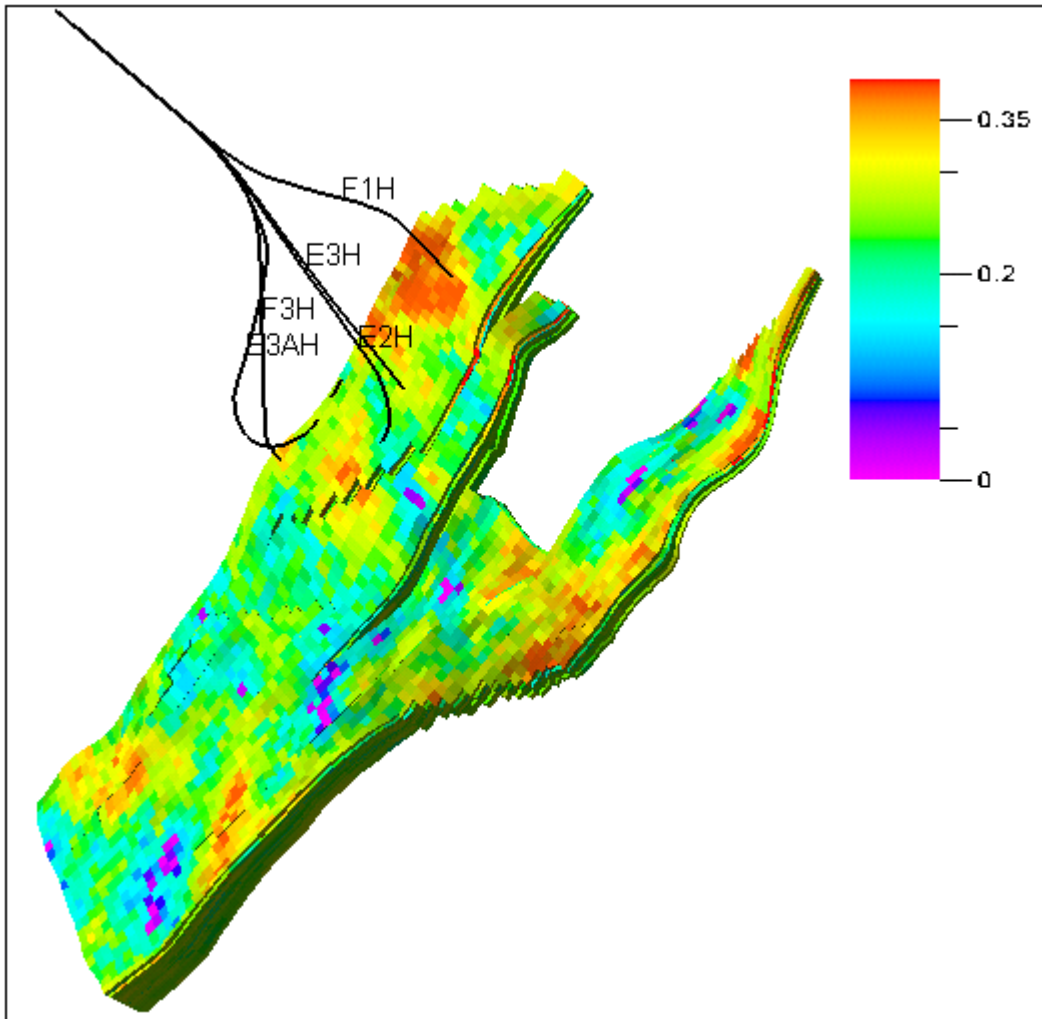


Figure 3.11: Top view of flow simulation model. Segment E consists of wells E-3H, E-2H, E-3AH, F1-H and F-3H.

Producers are controlled by reservoir fluid volume rate calculated from the observed phase flow rates, and injectors are controlled by water injection rate. Reservoir fluid volume is the volume occupied by the produced fluid at reservoir conditions. Flow simulation starts during the

year of 1997 and ends in 2004. Oil, water and gas are produced from wells E-2H, E-3H and E-3AH, while water is injected in the wells F-1H and F-3H. NOT formation is an impermeable layer (permeability is extremely low) and acts as a cap rock. It separates two formations, leading to two oil water contacts (OWC) and two gas oil contacts (GOC). The depths of GOC and OWC in the top formation are 2582 m and 2612 m respectively. Similarly depths of GOC and OWC in the bottom formation are 2585 m and 2693 m respectively.

An isothermal black-oil model is used for the flow simulation. Three phases are present in the reservoir. Gas-oil capillary pressure is assumed to be zero during the flow simulation. Flow rates and controls are set up as observed in the field. Seven years of oil production have been simulated. PVT data is taken from original Norne field simulation model (Begum, 2009). Production and injection schedule are the same as in the Norne field.

### 3.5 Rock Physics Modeling

As mentioned previously, rock physics model is used to populate acoustic and elastic properties ( $V_p$  and  $V_s$  and density) inside the reservoir away from the well. We have selected two different rock physics models for this study, namely cemented sand model and unconsolidated sand model (Dvorkin and Nur, 1996).

#### 3.5.1 Cemented-Sand Model

This model assumes that cement is deposited at grain contacts, cement is elastic and its properties may differ from those of grain spheres. Starting framework of cemented sand model is a random pack of spherical grains having a porosity of 0.36 and coordination number of 9. After addition of cement the effective dry-rock bulk and shear moduli are calculated as following (Dvorkin and Nur, 1996):

$$K_{eff} = \frac{1}{6}C(1 - \phi_0)M_c\hat{S}_n \quad (3.15)$$

$$\mu_{eff} = \frac{3}{5}K_{eff} + \frac{3}{20}C(1 - \phi_0)\mu_c\hat{S}_\tau \quad (3.16)$$

$$M_c = \rho_c V_{Pc}^2 \quad (3.17)$$

$$\mu_c = \rho_c V_{Sc}^2 \quad (3.18)$$

$\phi_0$  is 0.36 (porosity of spherical grains).  $V_{Pc}$ ,  $V_{Sc}$  and  $\rho_c$  are P-wave velocity, S-wave velocity and density of cement respectively.  $\hat{S}_n$  and  $\hat{S}_\tau$  are proportional to the normal and shear stiffnesses of a cemented two-grain combination. They are calculated as follows (Dvorkin and Nur, 1996):

$$\hat{S}_n = A_n \alpha^2 + B_n \alpha + C_n \quad (3.19)$$

$$A_n = -0.024153 \Lambda_n^{-1.3646} \quad (3.20)$$

$$B_n = 0.20405 \Lambda_n^{-0.89008} \quad (3.21)$$

$$C_n = 0.000246 \Lambda_n^{-1.9864} \quad (3.22)$$

$$\hat{S}_\tau = A_\tau \alpha^2 + B_\tau \alpha + C_\tau \quad (3.23)$$

$$A_\tau = -10^{-2} (2.26\nu^2 + 2.07\nu + 2.3) \Lambda_\tau^{0.079\nu^2 + 0.1754\nu - 1.342} \quad (3.24)$$

$$B_\tau = (0.0573\nu^2 + 0.0937\nu + 0.202) \Lambda_\tau^{0.0274\nu^2 + 0.0529\nu - 0.8765} \quad (3.25)$$

$$C_\tau = 10^{-4} (9.654\nu^2 + 4.945\nu + 3.1) \Lambda_\tau^{0.01867\nu^2 + 0.4011\nu - 1.8186} \quad (3.26)$$

$$\Lambda_n = \frac{2\mu_c (1 - \nu)(1 - \nu_c)}{\pi\mu (1 - 2\nu_c)} \quad (3.27)$$

$$\Lambda_\tau = \frac{\mu_c}{\pi\mu} \quad (3.28)$$

$$\alpha = \frac{a}{R} \quad (3.29)$$

Where  $\mu_c$  and  $\nu_c$  are the shear modulus and Poisson ratio of the cement, respectively;  $\mu$  and  $\nu$  are the shear modulus and Poisson ratio of the grain, respectively;  $R$  is the grain radius; and  $a$  is the radius of the cement layer.  $\alpha$  can be related to porosity of cemented sand as follows:

$$\alpha = 2 \left[ \frac{\phi_0 - \phi}{3C(1 - \phi_0)} \right]^{1/4} \quad (3.30)$$

### 3.5.2 Unconsolidated Sand Model

This model is based on the assumption that cement is deposited away from sand grain contacts. The starting framework of uncemented sand is a dense random pack of identical spherical grains with porosity  $\phi_0$  of about 0.36 and coordination number  $C$  varying from 5 to 9. At porosity  $\phi_0$  with a hydrostatic pressure  $P$ , the effective bulk ( $K_{HM}$ ) and shear ( $\mu_{HM}$ ) moduli of dry rock are calculated using Hertz-Mindlin theory (Mindlin, 1949).

$$K_{HM} = \left[ \frac{C^2(1 - \phi_0)^2 \mu^2}{18\pi^2(1 - \nu)^2} P \right]^{1/3} \quad (3.31)$$

$$\mu_{HM} = \frac{5 - 4\nu}{5(2 - \nu)} \left[ \frac{3C^2(1 - \phi_0)^2 \mu^2}{2\pi^2(1 - \nu)^2} P \right]^{1/3} \quad (3.32)$$

Where  $\mu$  and  $\nu$  are the grain shear modulus and Poisson ratio respectively. Effective moduli ( $K_{eff}$  and  $\mu_{eff}$ ) of a dry rock at a different porosity  $\phi$  are calculated using modified Hashin-Shtrikman lower bound (Hashin, 1965):

$$K_{eff} = \left[ \frac{\phi/\phi_0}{K_{HM} + \frac{4}{3}\mu_{HM}} + \frac{1 - \phi/\phi_0}{K + \frac{4}{3}\mu_{HM}} \right]^{-1} - \frac{4}{3}\mu_{HM} \quad (3.33)$$

$$\mu_{eff} = \left[ \frac{\phi/\phi_0}{\mu_{HM} + \frac{\mu_{HM}}{6} \left( \frac{9K_{HM} + 8\mu_{HM}}{K_{HM} + 2\mu_{HM}} \right)} + \frac{1 - \phi/\phi_0}{\mu + \frac{\mu_{HM}}{6} \left( \frac{9K_{HM} + 8\mu_{HM}}{K_{HM} + 2\mu_{HM}} \right)} \right]^{-1} - \frac{\mu_{HM}}{6} \left( \frac{9K_{HM} + 8\mu_{HM}}{K_{HM} + 2\mu_{HM}} \right) \quad (3.34)$$

Where  $K$  is the grain bulk modulus.

Once effective moduli of dry rocks are calculated, effective moduli at initial condition of the reservoir are obtained using Gassmann's fluid substitution.

### 3.6 Time-lapse Seismic Modeling

#### 3.6.1 Change in Saturation

The distribution of fluid saturations in the reservoir is obtained for seventy two different cases. These variations of saturations are responsible for change in the bulk density, effective bulk elastic moduli, and finally changes in the seismic velocities as shown below. 3-D time-lapse changes in seismic velocities are generated using initial seismic velocities, density and Gassmann's fluid substitution equation (Gassmann, 1951). Gassmann's equation (Equation 3.35) shown below is used to obtain the bulk modulus  $K_2$  of the rock saturated with fluid 2 (at year 2004), which is a mixture of oil, water and gas in this case.

$$\frac{K_2}{K_{min} - K_2} - \frac{K_{fl2}}{\phi(K_{min} - K_{fl2})} = \frac{K_1}{K_{min} - K_1} - \frac{K_{fl1}}{\phi(K_{min} - K_{fl1})} \quad (3.35)$$

$K_1$  and  $K_2$  are the rock's bulk moduli with fluids 1 (at year 2001) and 2 (at year 2004) respectively,  $K_{fl1}$  and  $K_{fl2}$  are the bulk moduli of fluids 1 and 2,  $\phi$  is the rock's porosity, and  $K_{min}$  is the bulk modulus of the mineral. The shear modulus  $G_2$  remains unchanged  $G_2 = G_1$  at low frequencies appropriate for surface seismic data, since shear stress cannot be applied to fluids. The fluid bulk moduli are a function of the oil composition, pore pressure and temperature. The fluid moduli and densities are obtained from the usual Batzle-Wang (1992) relations. The effective fluid bulk moduli are different for uniform and patchy saturation distributions. The harmonic average of the individual fluid bulk moduli is used for the case of uniform fluid distribution while the arithmetic average is used for the patchy case. The use of the arithmetic average is an approximation and gives an upper bound (Mavko and Mukerji, 1998).

$$\frac{1}{K_f^{Uniform}} = \frac{S_w}{K_w} + \frac{S_o}{K_o} + \frac{S_g}{K_g} \quad (3.36)$$

$$K_f^{Patchy} = S_w K_w + S_o K_o + S_g K_g \quad (3.37)$$

The density of the rock is also transformed and the density of the rock with the second fluid is computed as:

$$\rho_2 = \rho_1 + \phi(\rho_{f12} - \rho_{f11}) \quad (3.38)$$

Having transformed the elastic moduli and the density, the compressional and shear wave velocities of the rock with the second fluid are computed as

$$V_p = \sqrt{\frac{K_2 + \frac{4G_2}{3}}{\rho_2}} \quad (3.39)$$

$$V_s = \sqrt{\frac{G_2}{\rho_2}} \quad (3.40)$$

### 3.6.2 Changes in Pore pressure

In addition to saturation changes, the elastic moduli of the porous rock frame and hence seismic velocities are affected by pore pressure changes as well. Flow simulation provides us the variation of pore pressure and saturations with respect to time after the startup of the production. Using a proper pore pressure model seismic velocities of dry rock are first corrected for changes in pore pressure. The correction in seismic velocity of dry rock for cemented and unconsolidated reservoir rocks is different. Now corrected seismic velocities of dry rocks are used to calculate the seismic velocities by fluid substitution using Gassmann's equation as stated above. The pore pressure effect on the dry rock frame is modeled using an analytical curve fit to an empirical relation derived from dry core data for unconsolidated and cemented sands (Zimmer et al. 2002).

## 3.7 Results

P-wave seismic impedances are modeled at year 2001 and 2004. Figure 3.12 shows the results of sensitivity analysis. The results are compared based on the L1 norm of differences in

seismic P-wave impedance from 2001 to 2004; and are plotted on the y axis of the plots. The red and blue lines show the median and inter-quartile range of the distribution respectively. The plot on the left shows a clear change in the distribution due to change in the rock physics model. The shift in the median is higher as compared to the shifts of other plots in the right. This clearly shows that rock physics model is the most sensitive parameter among selected parameters of Norne field.

Figures 3.13, 3.14, 3.15, 3.16 and 3.17 are showing median change in the normalized P-wave impedance in different layers (5, 7 and 10) of segment E from 2001 to 2004. It is again clear from these figures that rock physics model has the most impact on time-lapse seismic response. It is also clear that the change in impedance is more sensitive to relative permeability end points and saturation scale as compared to changes in porosity models and pore compressibility.

Rock physics models and saturation scales only affect seismic impedance. Production data is only affected by relative permeability curves, porosity and permeability models and pore compressibility. Figures 3.18, 3.19, 3.20 and 3.21 show the effect of change in oil-water relative permeability, porosity models and pore compressibility on cumulative oil production during seven years of production. It is clear from these figures that relative permeability curves have more impact on cumulative oil production of the Norne field as compared to porosity models and pore compressibility.

One of the important findings of this chapter is that rock physics model is the most important parameter for modeling time-lapse seismic response of Norne field. The rock physics parameters are associated with rock physics model and time-lapse seismic modeling. Thus, in the next chapter we will study the sensitive rock physics parameter for modeling time-lapse seismic response of Norne field.

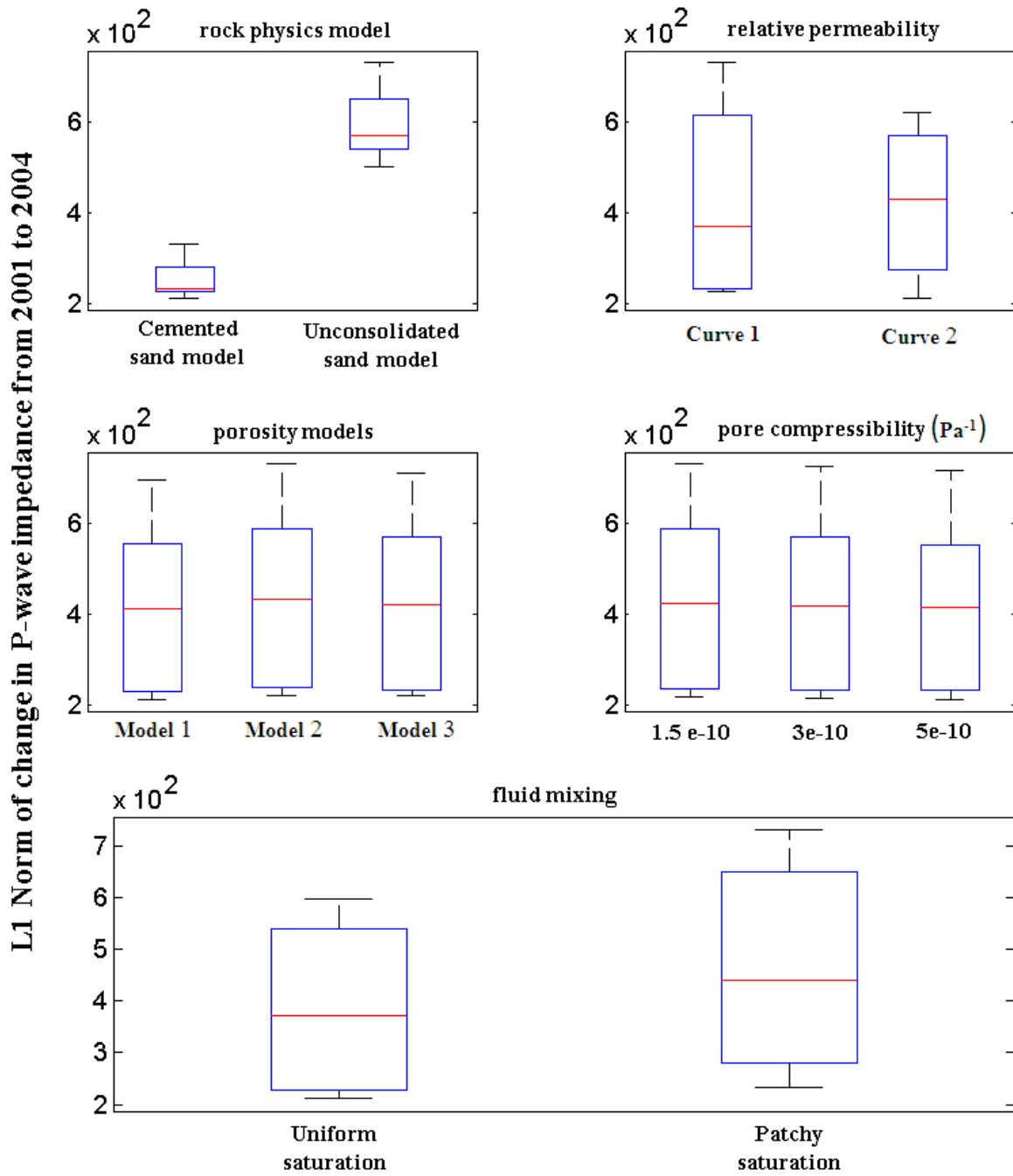


Figure 3.12: Results of sensitivity study on time-lapse seismic response of Norne field. Box plot shows the median (red line) and interquartile range (blue box) of distribution for variations in each parameter. Rock physics model has the most impact on time-lapse seismic response of Norne field.

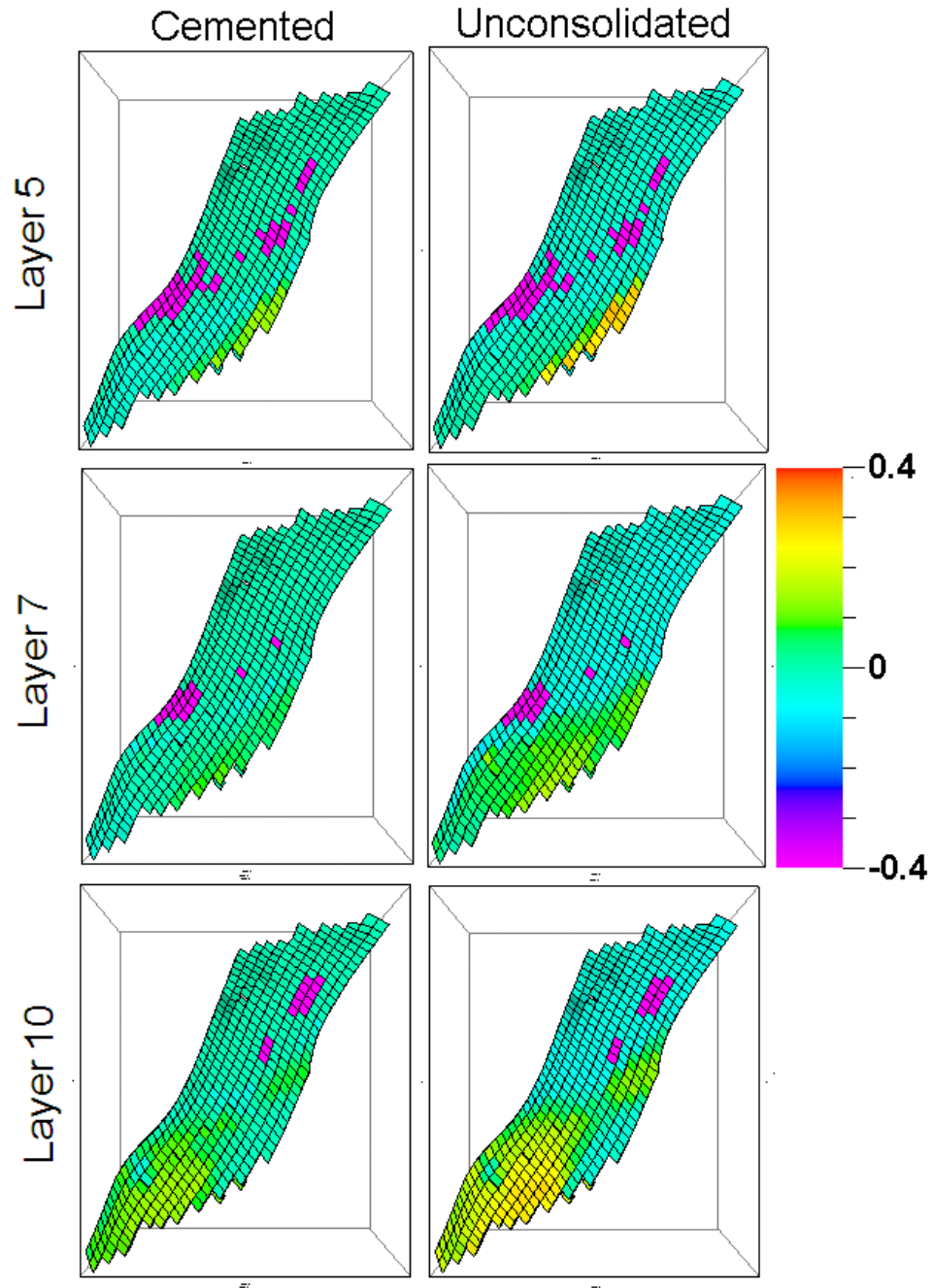


Figure 3.13: Effect of the rock physics model on median P-wave impedance change from 2001 to 2004. Changes are shown for three different layers (5, 7 and 10). On the right, changes in impedance for unconsolidated sand model are shown and on the left changes in impedance for cemented sand model are shown.

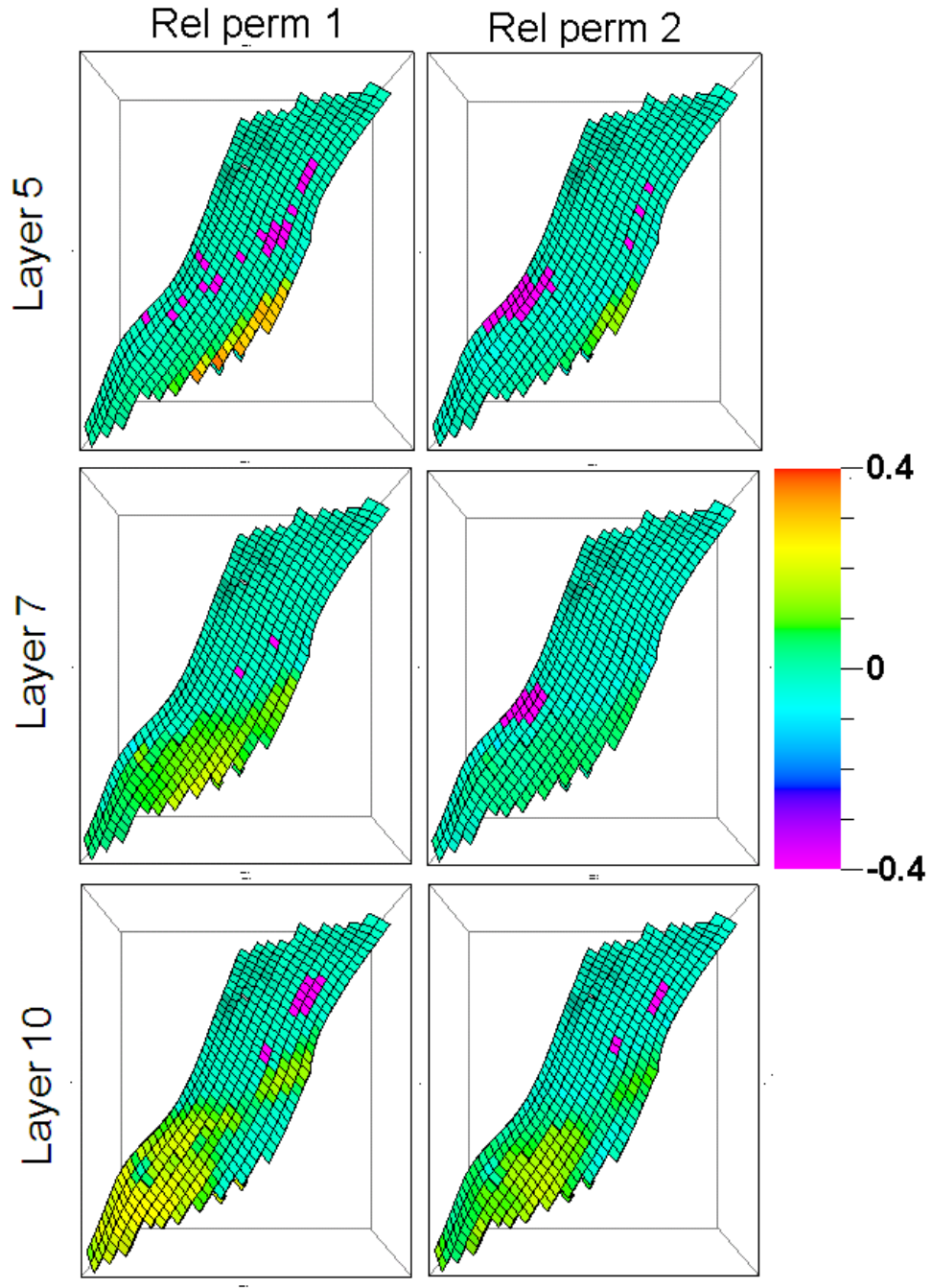


Figure 3.14: Effect of the relative permeability on median p-wave impedance change from 2001 to 2004. Changes are shown for three different layers (5, 7 and 10). On the right, changes in impedance for second relative permeability curve are shown and on the left changes in impedance for first relative permeability curve are shown.

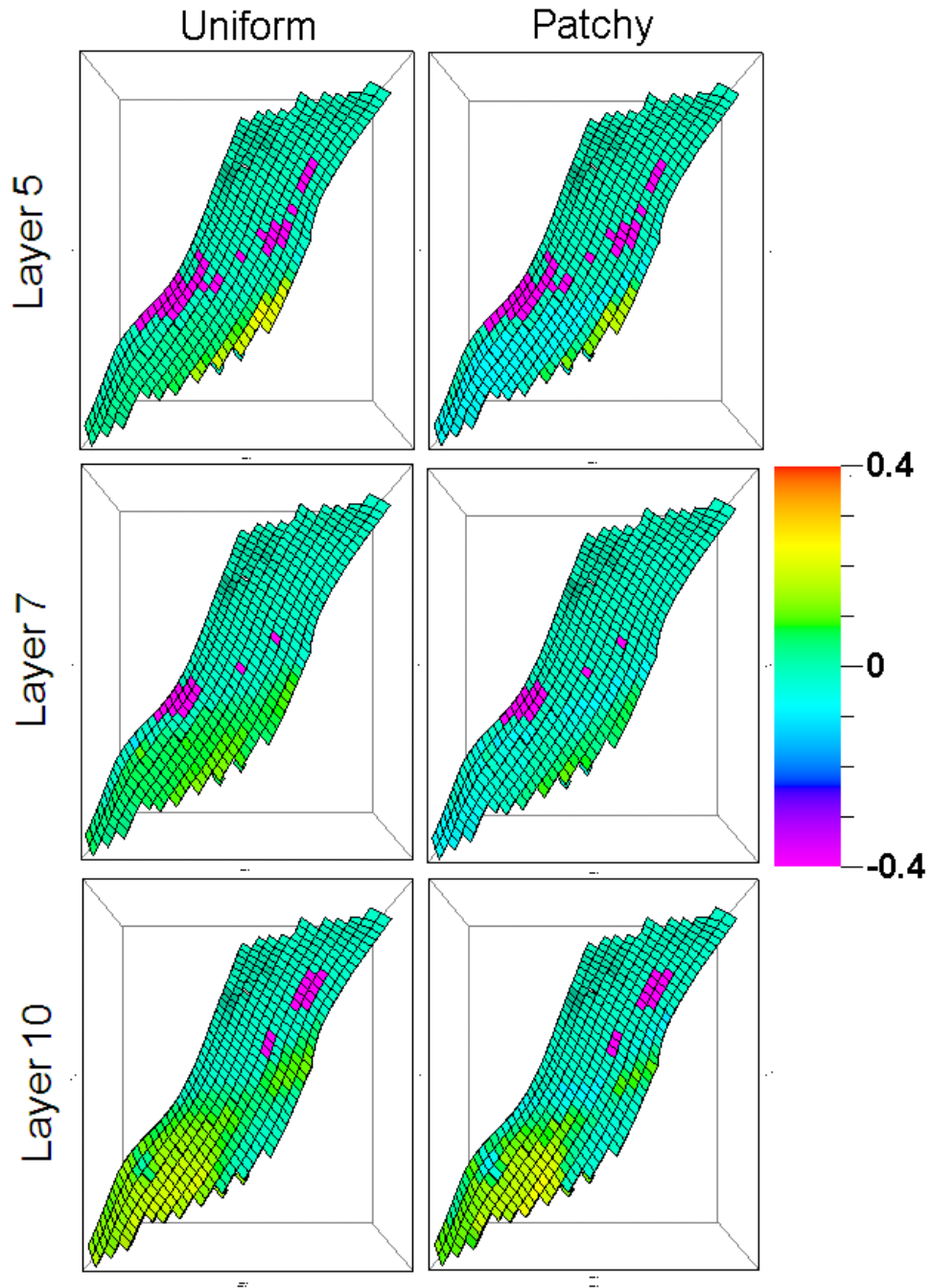


Figure 3.15: Effect of the fluid mixing on median p-wave impedance change from 2001 to 2004. Changes are shown for three different layers (5, 7 and 10). On the right, changes in impedance for patchy saturation are shown and on the left changes in impedance for uniform saturation are shown.

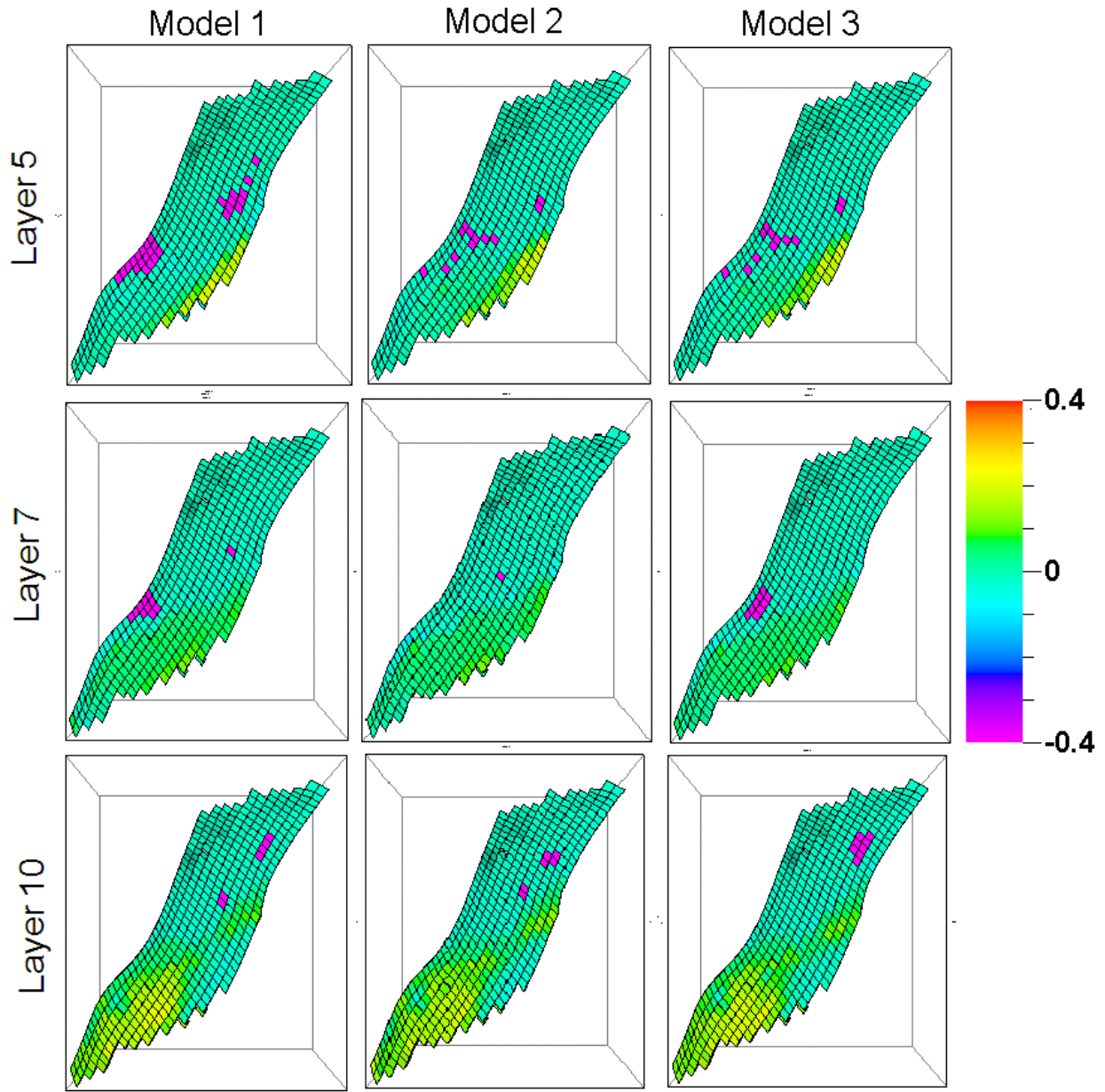


Figure 3.16: Effect of the porosity model on median p-wave impedance change from 2001 to 2004. Changes are shown for three different layers (5, 7 and 10). From left to right, changes in impedance for Model 1, Model 2 and Model 3 are shown.

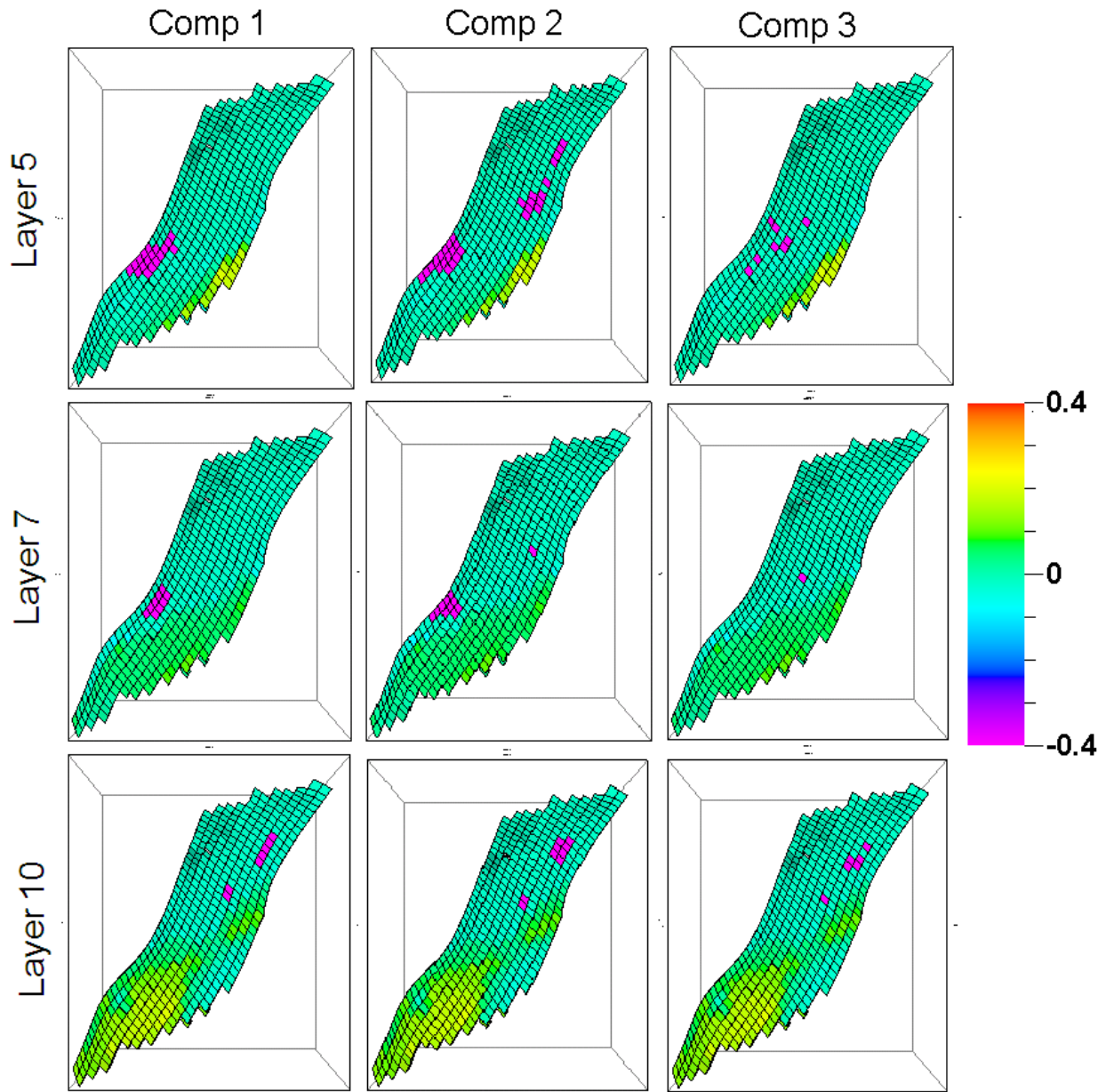


Figure 3.17: Effect of the pore compressibility on median p-wave impedance change from 2001 to 2004. Changes are shown for three different layers (5, 7 and 10). From left to right, changes in impedance for pore compressibility ( $\text{Pa}^{-1}$ ) of  $1.5e^{-10}$ ,  $3e^{-10}$  and  $5e^{-10}$  are shown.

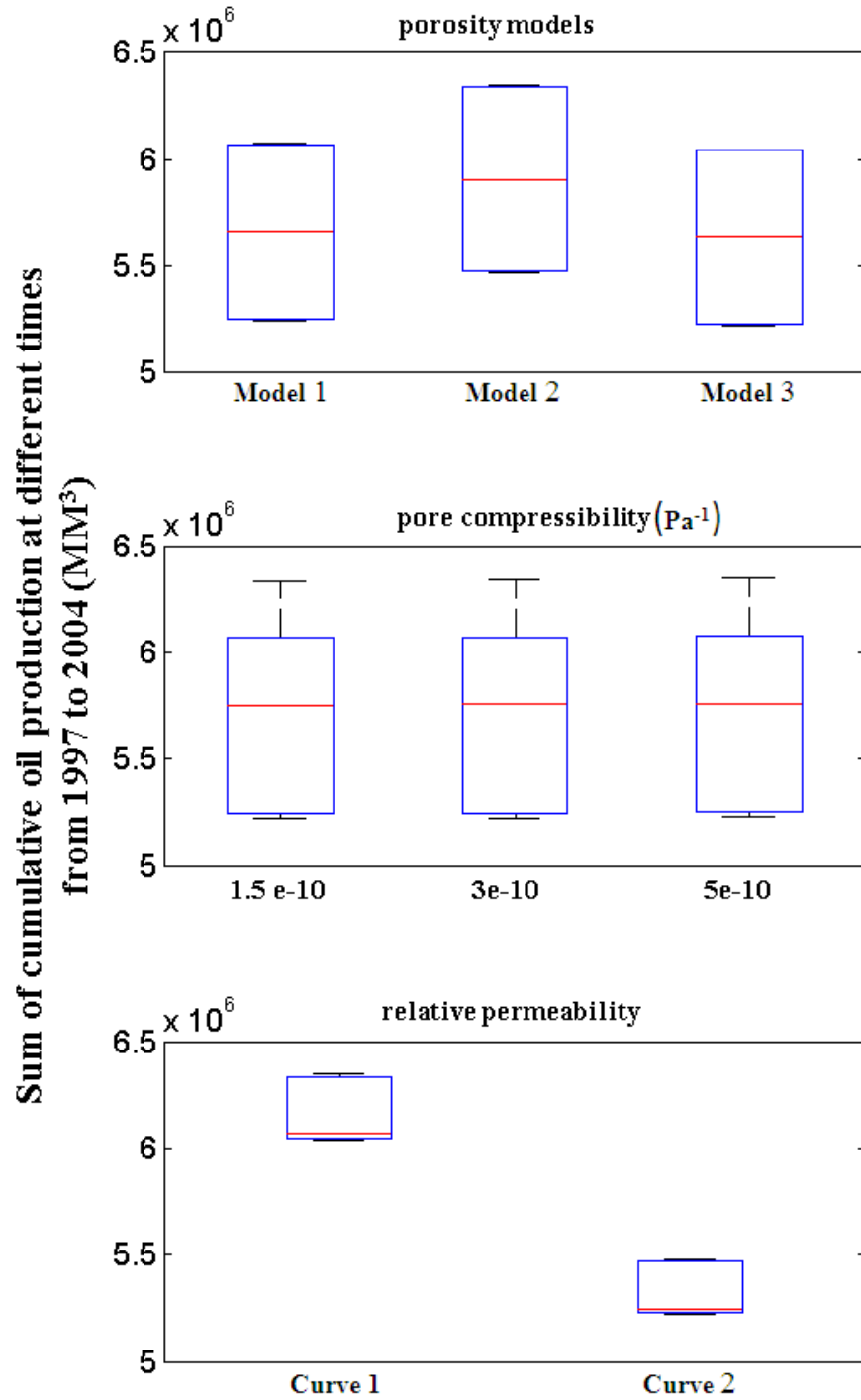


Figure 3.18: Results of sensitivity study for production response of Norne field. Box plot shows the median (red line) and interquartile range (blue box) of distribution for variations in each parameter. Relative permeability has the most impact on cumulative oil production of Norne field.

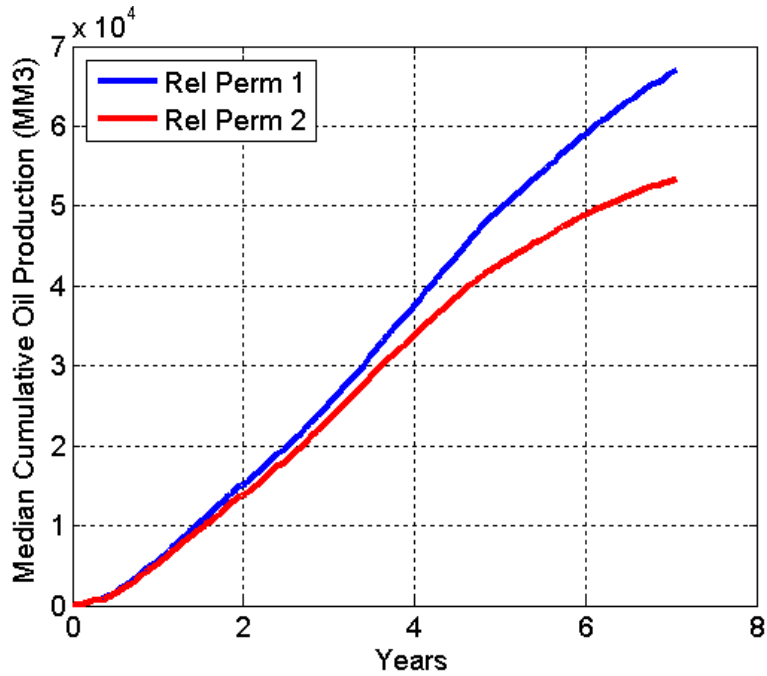


Figure 3.19: Median cumulative oil production from 1997 to 2004 for two sets of relative permeability. Response of first and second relative permeability curves are shown in blue and red respectively.

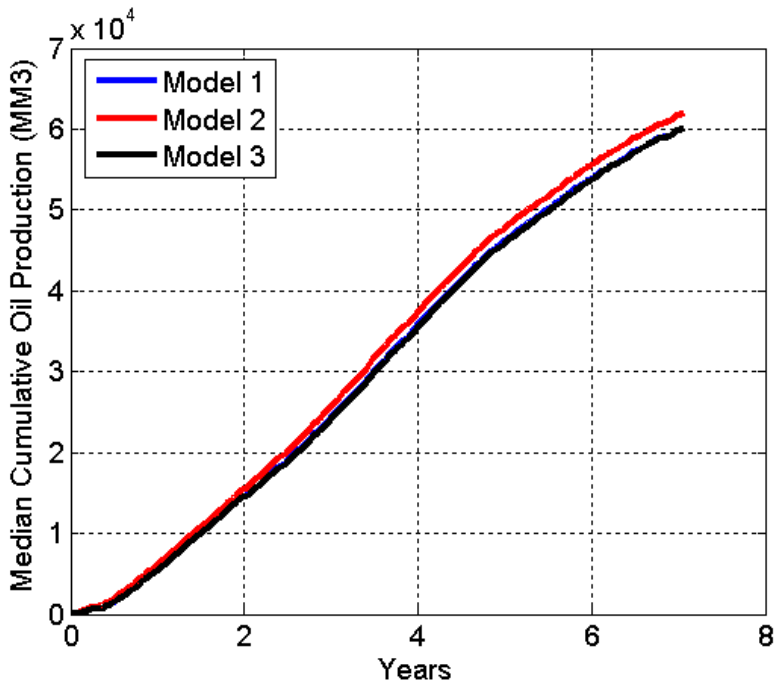


Figure 3.20: Median cumulative oil production from 1997 to 2004 for three porosity realizations. Response of first, second and third models are shown in blue, red and black respectively. Response of model 1 and model 3 are similar thus associated curves are identical

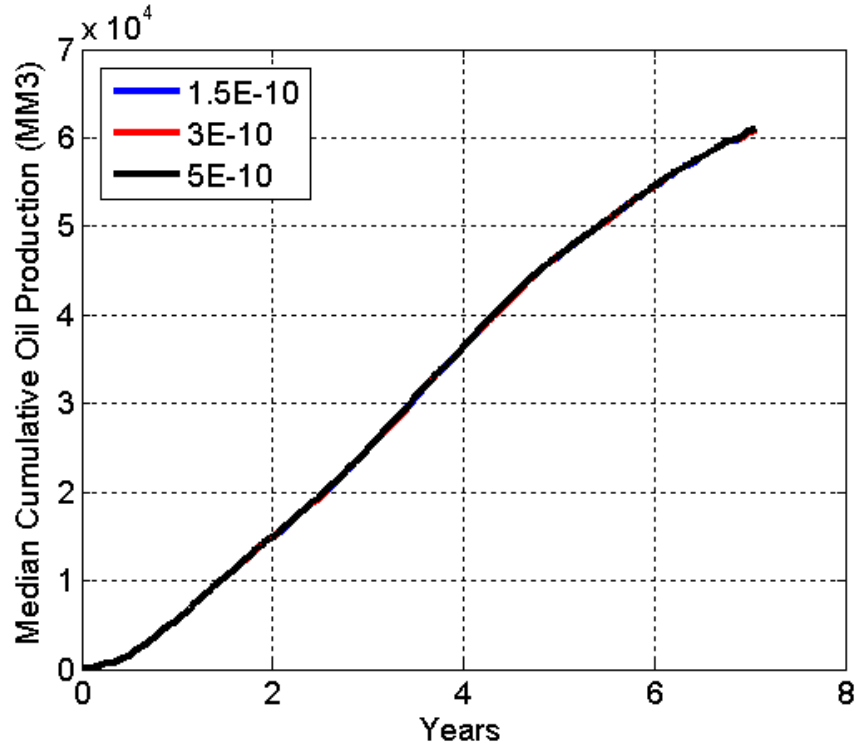


Figure 3.21: Median cumulative oil production from 1997 to 2004 for three different pore compressibilities. Responses of first, second and third pore compressibility are shown in blue, red and black respectively. Responses associated with pore compressibilities are almost similar thus associated curves are identical.

### 3.8 Conclusions

We have identified sensitive parameters and ranked them for modeling the production and time-lapse seismic response of the Norne field. This sensitivity workflow can also be applied for joint inversion of production and time-lapse seismic data of other fields. It is shown that rock physics model is the most important parameter among the parameters considered for time-lapse seismic modeling of the Norne field. Presence or absence of cement in the rock has a strong impact on the sensitivity of velocity to fluid saturation changes. Relative permeability and porosity/permeability model are the second and third most sensitivity parameters for time-lapse seismic modeling of the Norne field. Pore compressibility is the least sensitive parameter for time-lapse seismic modeling of the Norne field. We also found that relative permeability curves are the most important parameter for modeling the flow response of Norne field. Porosity/Permeability models are the second most sensitive parameter for modeling of flow

response. The result of this study will be used as inputs for parameter selection in history matching of time-lapse and production data of the Norne field. We also have shown that only porosity/permeability models are not the important parameter in joint inversion of production and time-lapse seismic data of a field.

# Chapter 4

## **SENSITIVITY STUDY OF ROCK PHYSICS PARAMETERS FOR MODELING TIME- LAPSE SEISMIC RESPONSE OF NORNE FIELD**

### **4.1 Introduction**

Time-lapse seismic modeling is an important step in joint inversion of time-lapse seismic and production data of a field. Rock physics analysis is the basis for modeling the time-lapse seismic data. In this chapter, Norne field data is used to identify and rank the sensitive rock physics parameters for the joint inversion. The sensitivity study consists of two parts. In the first part, we investigate sensitive parameters in the Gassmann's equation to generate the initial seismic velocities. The investigated parameters include mineral properties, water salinity, pore-pressure and gas-oil ratio (GOR). Next we investigate parameter sensitivity for time-lapse

seismic modeling of Norne field. The investigated rock physics parameters are clay content, cement, pore-pressure and mixing.

## **4.2 Rock Physics Modeling**

Rock physics modeling can be used to populate elastic properties inside the reservoir model away from the wells. The basis of our approach is rock physics modeling to relate elastic moduli and porosity near the well (based on the well log data) and use this relation to populate away from the wells. The rock physics relations between elastic moduli and porosity depend on factors such as clay content, diagenesis, sorting and lithofacies. Figure 4.1 describes the general workflow for modeling initial elastic properties (seismic velocity) from the well log data of a field. It starts with the well logs (porosity, saturation and sonic logs) to analyze the data near the wells.

### **4.2.1 Facies classification**

Facies classification is an important part of rock physics modeling. Lithofluid facies are classified based on available well logs. Lithofluid facies are facies having a particular type of fluid (hydrocarbon or water). Lithofluid facies of segment E of Norne field are based on the well log data of two wells E-3H and F-1H (Figure 4.2). The well log data used for analysis include porosity, saturation, clay content ( $V_{sh}$ ) and sonic logs of these two wells.

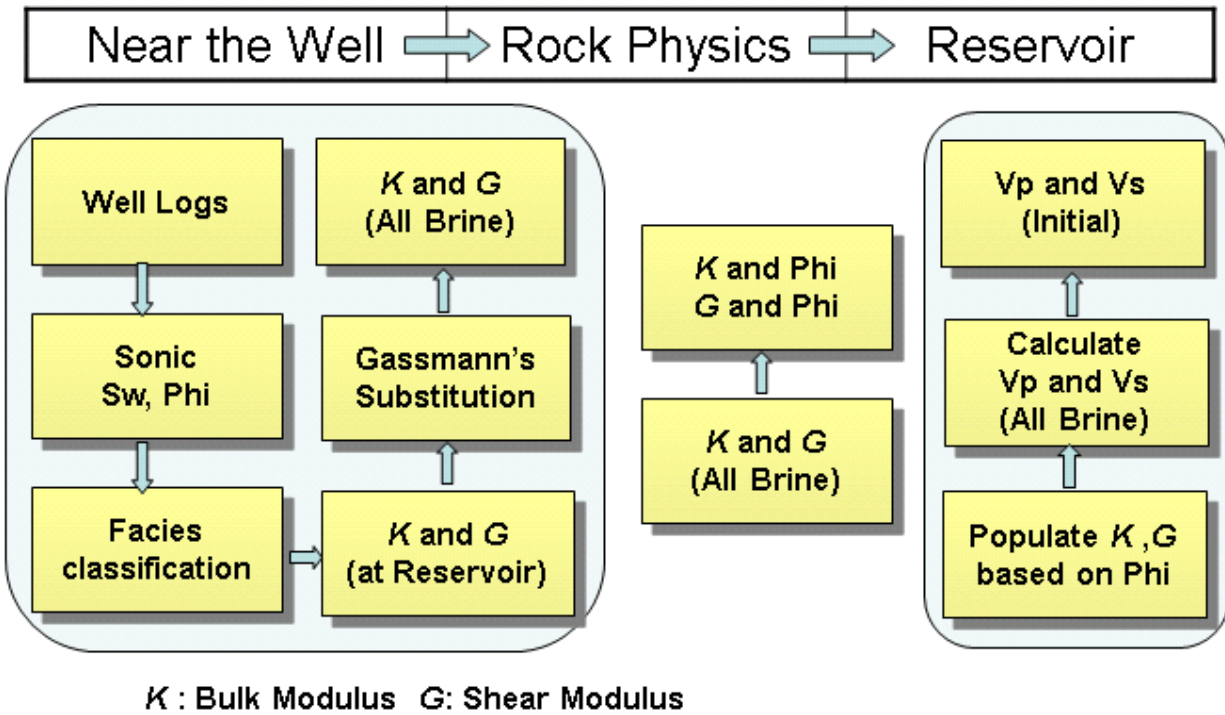


Figure 4.1: Workflow for generation of initial (t=0) cube of elastic properties using well log data. Starting with well log data an appropriate rock physics model is used to establish a correlation between porosity and elastic properties.

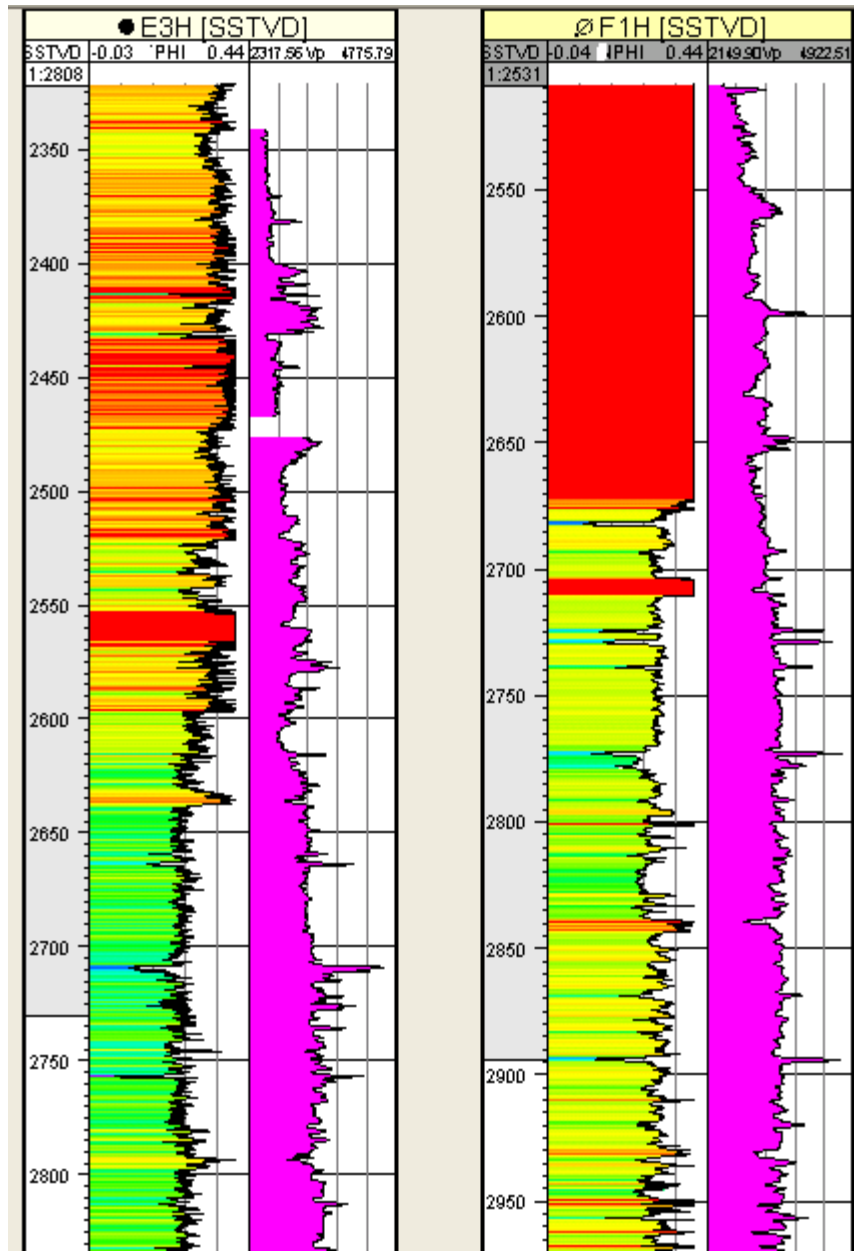


Figure 4.2: Porosity and velocity log (generated from well logs provided by Statoil) in well E3H on the left and well F1H on the right. Both of these logs are used for the analysis

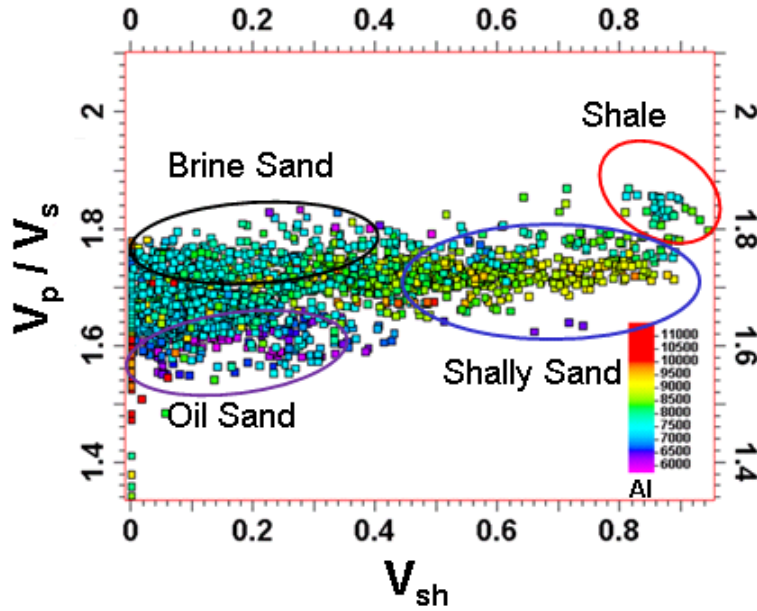


Figure 4.3: Facies classification in segment E of Norne field using well log data and based on velocity ratio, clay content and acoustic impedance. Three distinct facies are classified, namely sand, shaly sand and shale. Shaly sand and shale are limited to layer 3 in the reservoir

Seismic P-wave and S-wave velocities ( $V_p$  and  $V_s$ ) are calculated near the well based on sonic logs. Seismic P-wave impedance is established based on P-wave velocity and density log present in the well. A scatter plot between velocity ratio ( $V_p/V_s$ ) and clay content of well log data is used to classify different lithofacies. The well log data points are colored by acoustic impedance. Figure 4.3 shows clusters of different lithofluid facies in segment E of Norne field. All of the data points having shale fraction (clay content) less than 0.4 are regarded as sand. Oil sands have lower impedance than brine sands. The data points having high  $V_p/V_s$  ( $\sim 1.8$ ) and high clay content are regarded as shale. Well log data points having clay content greater than 0.4, intermediate  $V_p/V_s$  and relatively high acoustic impedance are defined as shaly sands.

Thus, segment E of Norne field is divided into three facies (sand, shaly sand and shale) for this study. In this study we have investigated sensitive rock physics parameter for time-lapse modeling of sand facies. The same workflow can be applied for the other facies present, but it has been observed that the presence of shaly sand and shale facies in the field are very limited. They are only present in the NOT formation which acts as a cap rock (permeability barrier).

Modeling and matching of time-lapse seismic response in the NOT formation is not considered in this study. Thus, Norne field is modeled as sand facies with varying clay content.

#### **4.2.2 Sensitivity to Fluid Substitution**

Facies classification provides the basis for rock physics analysis for each facies present in the field. Once the facies are established based on the method described above, next step is to fit a rock physics model based on the characteristic of plots between porosity and seismic velocity observed in the well. But to do that all of the well log data should be at the same fluid saturation which is achieved by Gassmann's fluid substitution as described in Section 3.6. There are two important steps in time-lapse seismic modeling of a field. First is the selection of an appropriate rock physics model and the second is the Gassmann's fluid substitution. The Gassmann's fluid substitution is used to capture the variation in the elastic properties of the reservoir due to changes in saturation and pore pressure. We have investigated the sensitive rock physics parameters in the both of the steps mentioned above and thus overall sensitivity for time-lapse seismic modeling. As mentioned above, after facies classification, an appropriate rock physics model is used to fit the well log data after correcting to a constant saturation (100% brine) using Gassmann's fluid substitution. Gassmann's equation (Equation 3.35) is used to obtain the bulk modulus  $K_2$  of the rock saturated with 100% brine. The fluid moduli and densities are obtained from the usual Batzle-Wang (1992) relations. Salinity, pore pressure and gas-oil ratio (GOR) effect fluid bulk moduli. Thus investigated parameters in the Gassmann's fluid substitution are clay content, gas-oil ratio (GOR), salinity and pore pressure. Again we used the approach of experimental design described in the previous chapter. Table 4.1 shows the values of different parameters used for this experimental design study. The parameters ranges are chosen based on the available data for the Norne field.

<b>Sensitive Parameters</b>	<b>Values</b>		
Clay content (%)	0	20	40
Salinity (ppm)	15000	15500	16000
GOR	175	200	225
Pressure (MPa)	25	27	30

Table 4.1: Parameters used in the sensitivity study of Gassmann's fluid substitution

<b>Reservoir parameters</b>	<b>Properties</b>
Bulk modulus of clay (GPa)	21
Shear modulus of clay (GPa)	7
Bulk modulus of quartz (GPa)	36
Shear modulus of quartz (GPa)	44
Gas gravity	0.85
API of oil	33

Table 4.2: Values of the parameters used in this study

Clay content has an impact on bulk and shear modulus of the effective mineral. The moduli of the minerals for different clay content are calculated using a Reuss average as shown in the equations below:

$$\frac{1}{K_{min}} = \frac{V_{sh}}{K_{clay}} + \frac{1 - V_{sh}}{K_{quartz}} \quad (4.1)$$

$$\frac{1}{G_{min}} = \frac{V_{sh}}{G_{clay}} + \frac{1 - V_{sh}}{G_{quartz}} \quad (4.2)$$

where  $V_{sh}$ ,  $K_{min}$  and  $G_{min}$  are clay content, bulk modulus and shear modulus of the effective mineral.  $K_{clay}$ ,  $G_{clay}$ ,  $K_{quartz}$  and  $G_{quartz}$  are the bulk and shear modulus of clay and quartz respectively.

The experimental design is based on variations of clay content, salinity, pore pressure and GOR. The range of variation of these parameters is based on the observations in the Norne field, and results in the generation of 81 cases (3 x 3 x 3 x 3). The specific gravities of fluids are measured in the laboratory. Thus, API and gas gravity are not included for sensitivity study. For each case a new set of moduli and density of rock saturated with 100% brine is obtained. The seismic P-wave velocity of the rock is calculated using the moduli and density of the rock. To study the effect of variation of designed parameters, we compared the response that is defined as the sum of seismic P-wave velocities after Gassmann's fluid substitution. Figure 4.4 shows the results of sensitivity study for fluid substitution, in which box plots are used for identifying sensitive parameters. For each value of a parameter, variation in the response (as defined above) is analyzed through a box plot which compares the median and interquartile ranges of response distribution. The sensitivity results of initial Gassmann's fluid substitution are as expected. Increasing clay content by making the rock softer, causing increased fluid sensitivity; GOR is also important while the response is not very sensitive to variations in brine salinity, within the range tested.

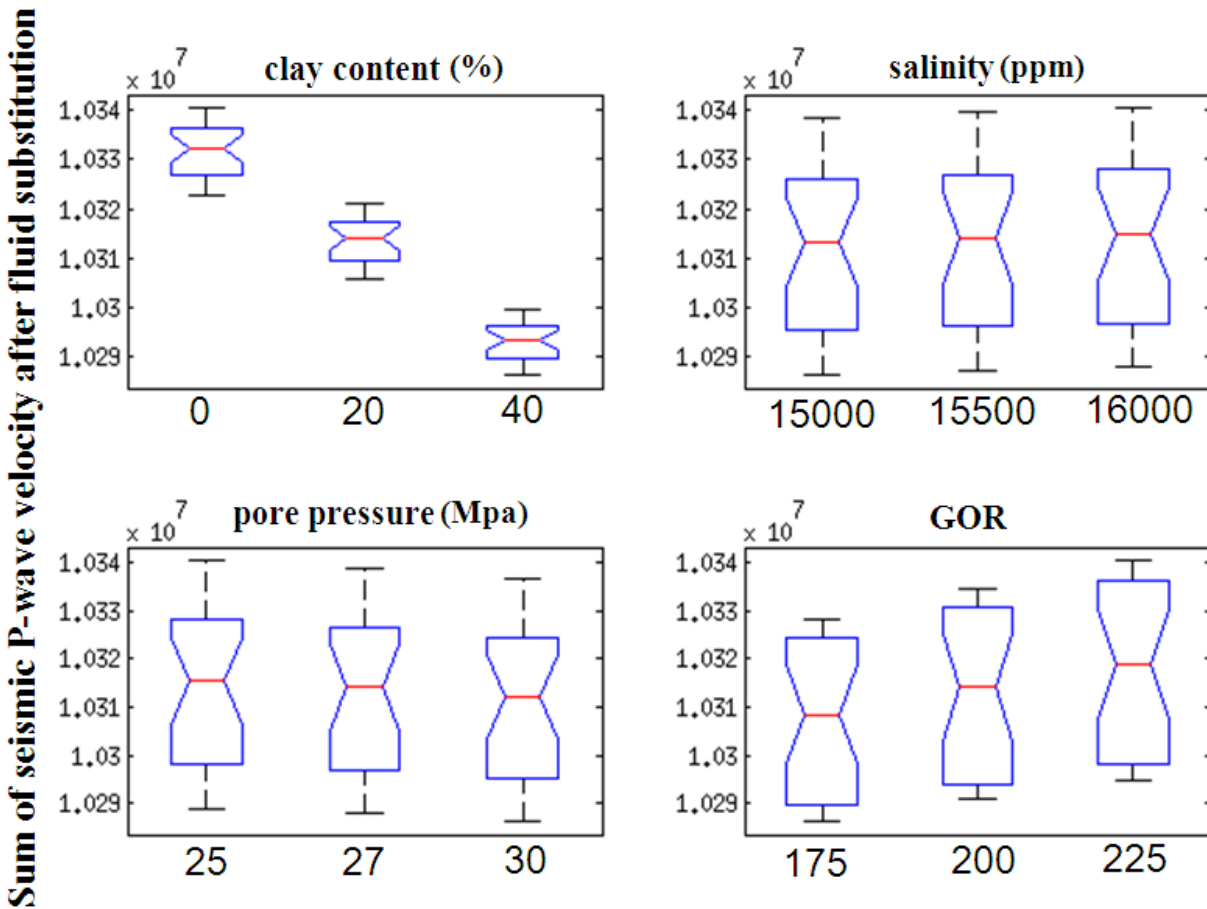


Figure 4.4: Result of sensitivity study for Gassmann’s fluid substitution, box plot shows the median (red line) and interquartile range (blue box) of distribution for variations in each parameter

Thus, clay content and GOR are kept as sensitive parameters which are varied in the overall sensitivity study of time-lapse seismic modeling. Next step in the rock physics modeling is to fit a rock physics model to the well log data modified for 100% brine saturation.

#### 4.2.3 Selection of Rock Physics Model

Nine sets (3 x 3) of bulk modulus for 100% brine saturated rock are calculated based on the variations in clay content and GOR. Figure 4.5 shows all the nine sets of bulk modulus and associated porosity colored by Gamma ray. The uncertainties in clay content and GOR lead to uncertainties in rock physics model parameters. Rock physics modeling is done to establish a model between porosity and elastic properties (bulk and shear modulus). Once a rock physics model is established based on the well log data, the correlation can be used to populate the elastic

properties away from the wells. Constant cement model (Avseth et al. 2000) is used as a rock physics model for this study based on the cross plot between bulk modulus and porosity.

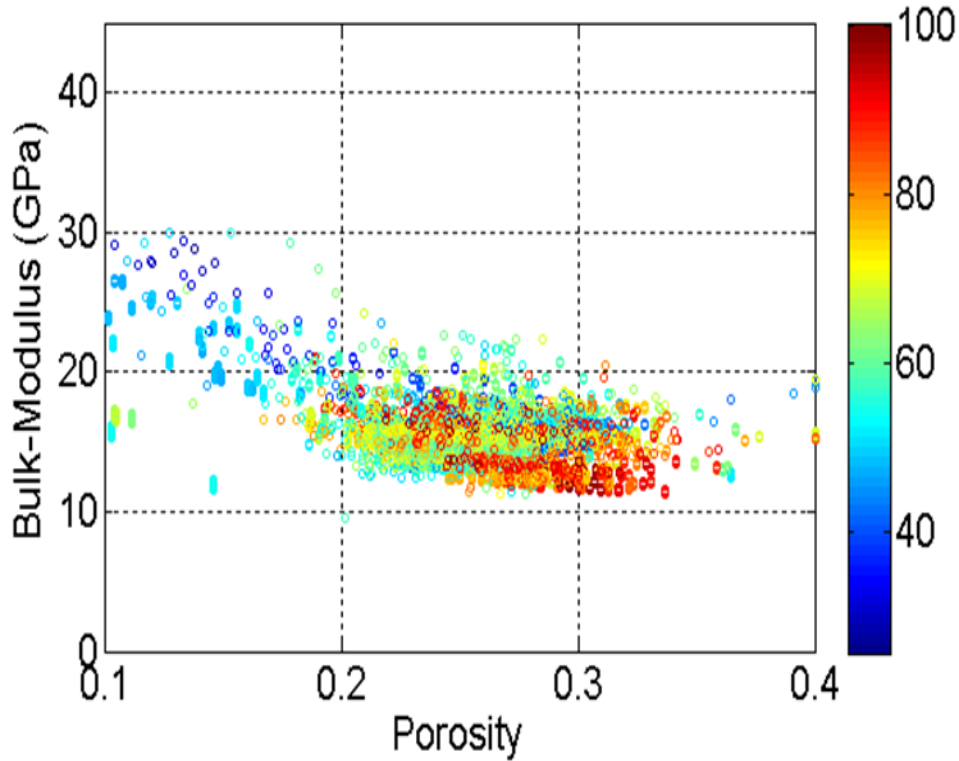


Figure 4.5: Bulk modulus obtained near the wells after fluid substitution for variations in clay content and GOR. The well log points are for nine different cases (3 clay content x 3 GOR) and colored with gamma ray values

#### 4.2.4 Constant cement model

Constant cement model is based on the assumption that sands having different porosities have the same amount of contact cement. Mathematically this model is a combination of contact cement model (Dvorkin et al. 1994) at critical porosity and friable sand model (Dvorkin et al. 1996) where porosity is lower than critical porosity. This is the most likely scenario in the reservoir since cement fraction depends on the depth and porosity variation depends on energy of the system. In this model at first dry-rock bulk ( $K_b$ ) and shear ( $\mu_b$ ) moduli are calculated at critical porosity using contact cement model and equations 3.15 - 3.30.

Next, bulk ( $K_{dry}$ ) and shear ( $\mu_{dry}$ ) moduli of the dry rock at porosities ( $\phi$ ) lower than critical porosity is obtained using the modified lower Hashin-Shtrikman bound:

$$K_{dry} = \left[ \frac{\phi/\phi_c}{K_c + \frac{4}{3}\mu_c} + \frac{1 - \phi/\phi_c}{K_s + \frac{4}{3}\mu_c} \right]^{-1} - \frac{4}{3}\mu_c \quad (4.3)$$

$$\mu_{dry} = \left[ \frac{\phi/\phi_c}{\mu_c + z} + \frac{1 - \phi/\phi_c}{\mu_s + z} \right]^{-1} - z \quad (4.4)$$

$$z = \frac{\mu_c}{6} \left( \frac{9K_c + 8\mu_c}{K_c + 2\mu_c} \right) \quad (4.5)$$

Next Bulk and shear moduli of the brine saturated rock are calculated using Gassmann's equation. The model trend varies based on the variations in clay content, coordination number and cement fractions. The variations in the rock physics model parameters are able to capture all the 9 sets of bulk moduli from well logs shown in the Figure 4.5. Figure 4.6 shows the variations in the rock physics model due to variations in clay content, coordination number and cement fractions. The range of coordination number and cement fractions are such that it successfully captures the well log data shown in the Figure 4.6. The range of clay content and coordination number is shown in the Table 4.3.

Based on the above analysis, next we investigate the sensitivity of time-lapse seismic modeling results to rock physics model parameters. The investigated parameters include clay content, GOR, coordination number, cement fraction, effective pressure model and fluid mixing. The effective pressure model defines change in elastic properties of the rock frame due to change in effective pressure.

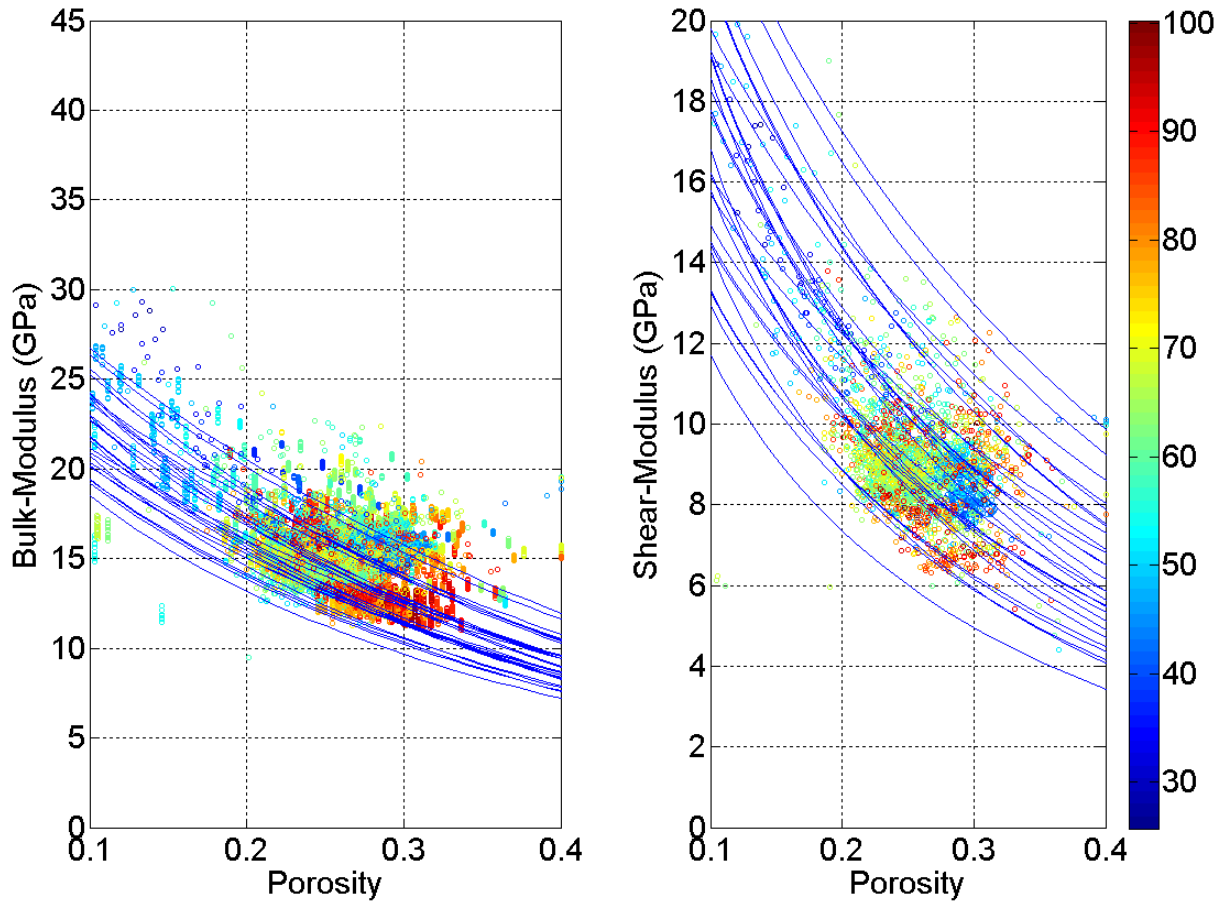


Figure 4.6: Variations in rock physics models by varying clay content, coordination number and cement fraction (color: Gamma Ray). The variations in rock physics parameters are successfully calibrated with the values in the well log. Blue lines are rock physics models and points are colored with gamma ray

The variation in elastic properties of the reservoir not only depends on changes in saturation but also on saturation scale (patchy saturation) as discussed in Section 3.2.7. This effect is more visible if there is a presence of gas in the reservoir (Sengupta, 2000). As Norne field has free gas, the scale of saturation (patchy versus uniform) is an important parameter to be considered for the sensitivity study. Thus, two types of fluid mixing are considered for sensitivity analysis. Table 4.3 shows the investigated rock physics parameters for modeling time-lapse seismic signature of Norne field.

Parameters	Values		
Clay content (%)	0	20	40
GOR	175	200	225
Coordination number	5	7	9
Cement fraction (%)	1	3	5
Effective pressure model	Model 1	Model 2	
Fluid mixing	Uniform	Patchy	

Table 4.3: Parameters selected for sensitivity study in modeling time-lapse seismic response of Norne field

### 4.3 Methodology

The methodology consists of flow and seismic simulations on reservoir property model. The output of flow simulation (change in pressure and saturation) serves as an input for time-lapse seismic modeling. The workflow for sensitivity analysis is shown in the Figure 4.7. For the sensitivity study this loop is computed for all combinations of parameters shown in Table 4.3.

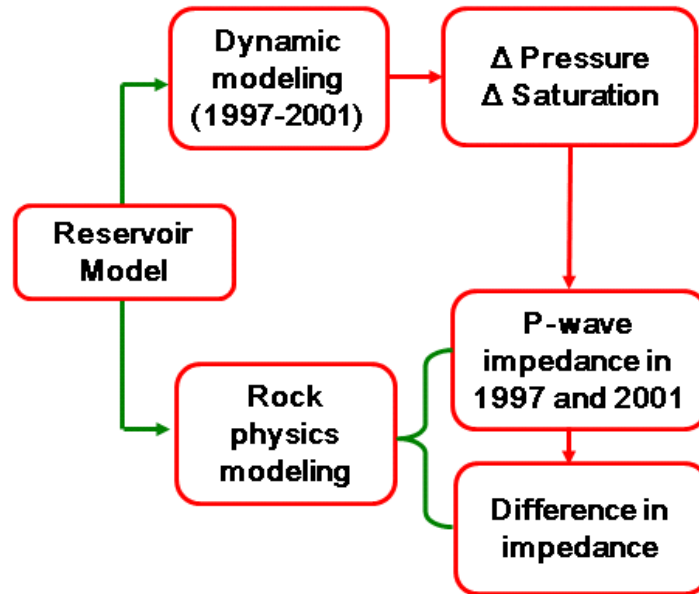


Figure 4.7: Workflow for generation of P-wave impedance change in four years. It consists of two parts, first is flow simulation, second is rock physics modeling and fluid substitution.

### 4.3.1 Flow Simulation

Flow simulation provides us the spatial distributions of fluids and variation of pore pressure in the reservoir at different times after the start of production. We need the saturations of each fluid (Oil, Water and Gas) at every cell at different times as inputs to Gassmann's equations. We have used an isothermal black-oil model and flow rates and controls are set up as observed in the field. Four years of oil production from 1997 to 2001 have been simulated. PVT and capillary pressure data are taken from the original Norne field simulation model. Production and injection schedule are the same as in the Norne field.

### 4.3.2 Time-lapse Seismic Modeling

#### *Change in Saturation*

The distribution of fluid saturations in the reservoir is obtained by dynamic modeling. These variations of saturations are responsible for changes in the bulk density, effective bulk elastic moduli, and finally changes in the seismic velocities as described below. 3-D time-lapse changes in seismic velocities are generated using initial seismic velocities, density and Gassmann's fluid substitution equation (Gassmann, 1951). Gassmann's equation (Equation 3.35) is used to obtain the bulk modulus  $K_2$  of the rock saturated with fluid 2, which is a mixture of oil, water and gas in this case.

The fluid moduli and densities are obtained from the usual Batzle-Wang (1992) relations. The effective fluid bulk moduli are different for uniform and patchy saturation distribution. The harmonic average of the individual fluid bulk moduli is used for the case of uniform fluid distribution while the arithmetic average is used for the patchy case. The use of the arithmetic average is an approximation and gives an upper bound (Mavko and Mukerji, 1998).

$$\frac{1}{K_f^{Uniform}} = \frac{S_w}{K_w} + \frac{S_o}{K_o} + \frac{S_g}{K_g} \quad (4.6)$$

$$K_f^{Patchy} = S_w K_w + S_o K_o + S_g K_g \quad (4.7)$$

The density of the rock is also transformed, and the density of the rock with the second fluid is computed as:

$$\rho_2 = \rho_1 + \phi(\rho_{fl2} - \rho_{fl1}) \quad (4.8)$$

Having transformed the elastic moduli and the density, the compressional and shear wave velocities of the rock with the second fluid are computed as

$$V_p = \sqrt{\frac{K_2 + \frac{4G_2}{3}}{\rho_2}} \quad (4.9)$$

$$V_s = \sqrt{\frac{G_2}{\rho_2}} \quad (4.10)$$

### ***Changes in Pore pressure***

In addition to saturation changes, the elastic moduli of the porous rock frame and hence seismic velocities are affected by pore pressure changes as well. Flow simulation provides us the variations of pore pressure and saturation in time during production. Using a proper pore pressure model seismic velocities of dry rock are first corrected for changes in the pore pressure. The corrected seismic velocities of dry rocks are used to calculate the seismic velocities by fluid substitution using Gassmann's equation. The pore pressure effect on the dry rock frame is modeled using an analytical curve fit to an empirical relation derived from dry core data for uncemented sands (Zimmer et al. 2002). If dry core measurements of velocities were available for the Norne field, these curves could have been also obtained by calibration to core data. Since the pressure sensitivity is an uncertain parameter, we explore the sensitivity of the pressure model on the time-lapse results by using two different effective pressure models (Figure 4.8) with large and small pressure sensitivity.

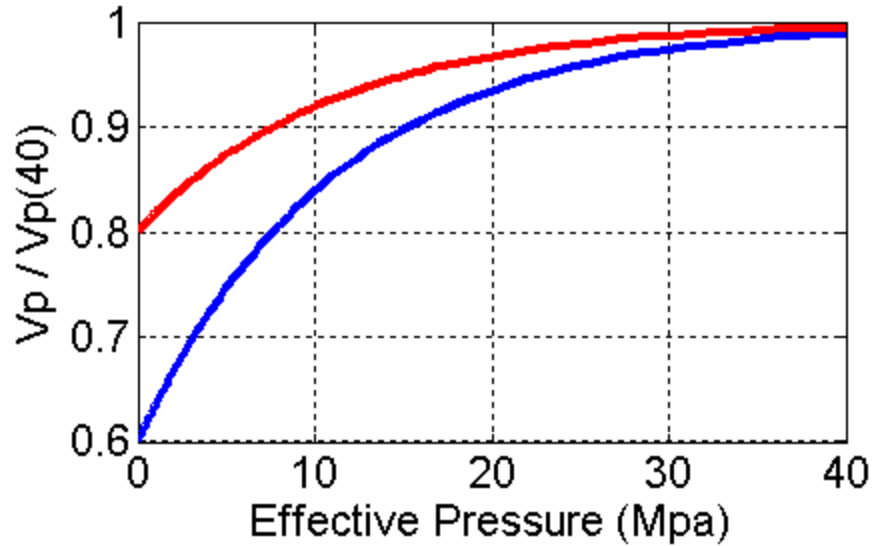


Figure 4.8: Two different effective pressure models used for sensitivity study.

#### 4.4 Sensitivity Analysis Results

Flow simulation is performed on reservoir porosity model to obtain change in saturation and pressure in four years (1997 to 2001). Now selected parameters are varied to obtain 324 (3 x 3 x 3 x 3 x 2 x 2) sets of P-wave acoustic impedance change in four years of production. To compare the results, we compared the L1 norm of differences in seismic P-wave impedance after four years of production, and are plotted on the y axis in the Figure 4.9. The red and blue lines show the median and inter-quartile range of the distribution respectively. We observe that the coordination number has the largest impact on change in impedance. Fluid mixing, clay content and cement are also important. Effective pressure model and GOR have the least impact.

We also obtained median of the distribution of the normalized P-wave impedance change for each parameter. For example, each coordination number had 108 sets of P-wave impedance change, and their median is compared. The median of P-wave impedance change for each coordination number is compared in three different layers (5, 7 and 10) of the reservoir and shown in the Figure 4.10. Similarly Figures 4.11, 4.12, 4.13, 4.14 and 4.15 show a comparison of median of P-wave impedance change for fluid mixing, clay content, cement fraction, effective pressure model and GOR. It is clear from the figures that coordination numbers have the largest

impact on change in impedance and thus in modeling time-lapse seismic response of the Norne field.

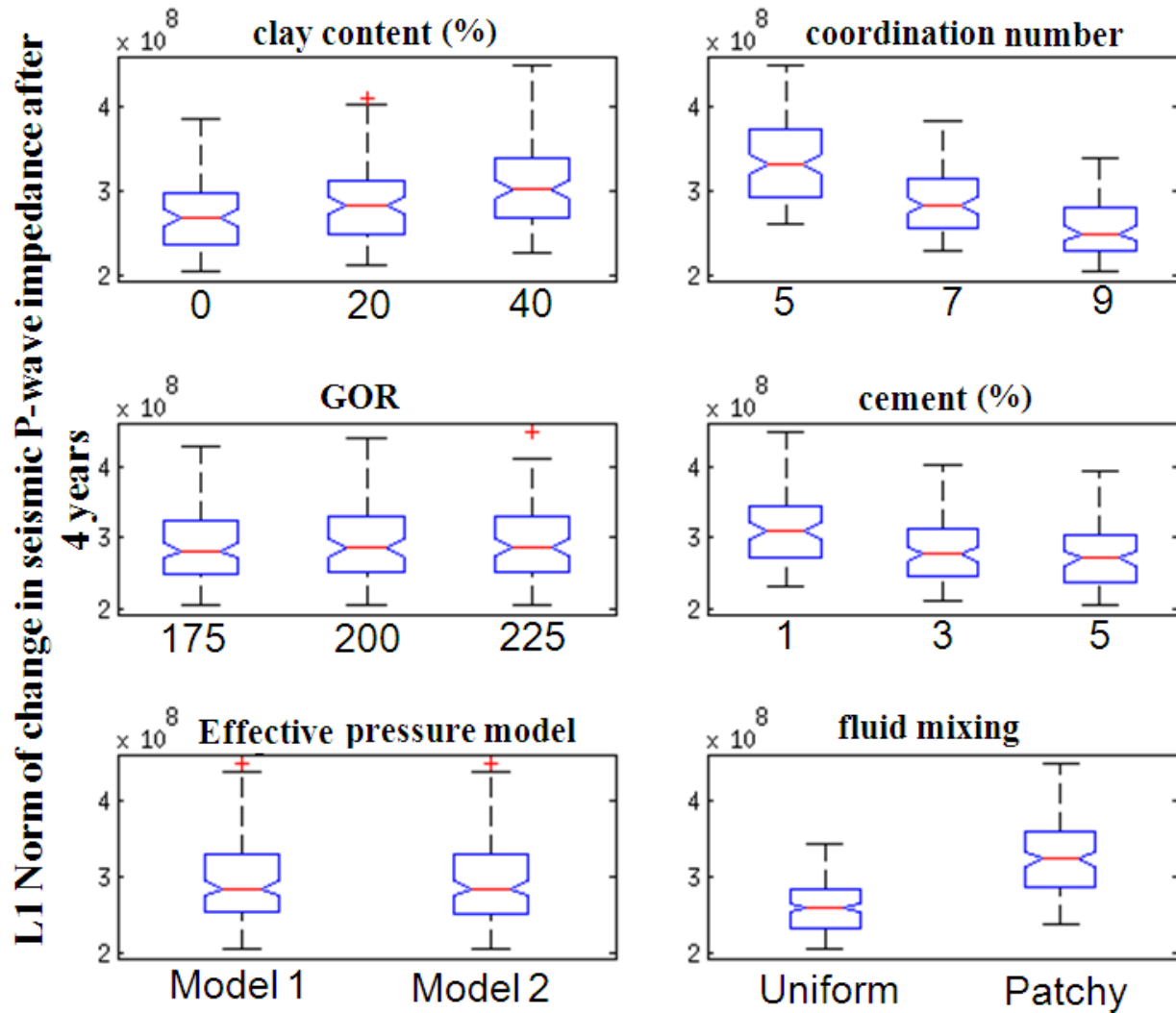


Figure 4.9: Results of sensitivity study of rock physics parameters for modeling the time-lapse seismic response of Norne field. Red line are median, and blue boxes are interquartile range of the distribution

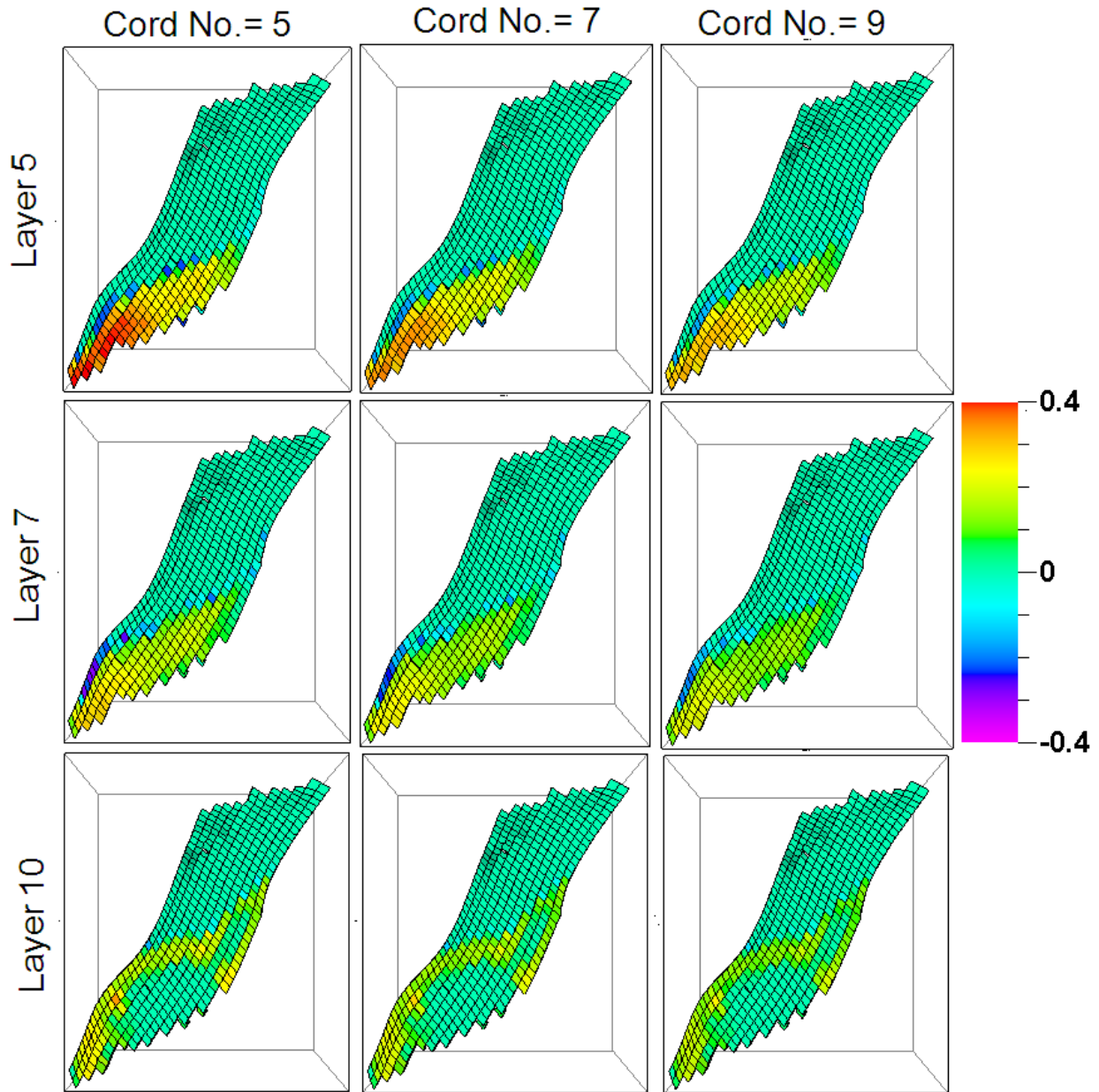


Figure 4.10: Effect of change in coordination number on the median of P-wave impedance change in four years. The median change is shown for three layers (5, 7 and 10) in the segment E of Norne field. Coordination number has the largest impact on impedance change

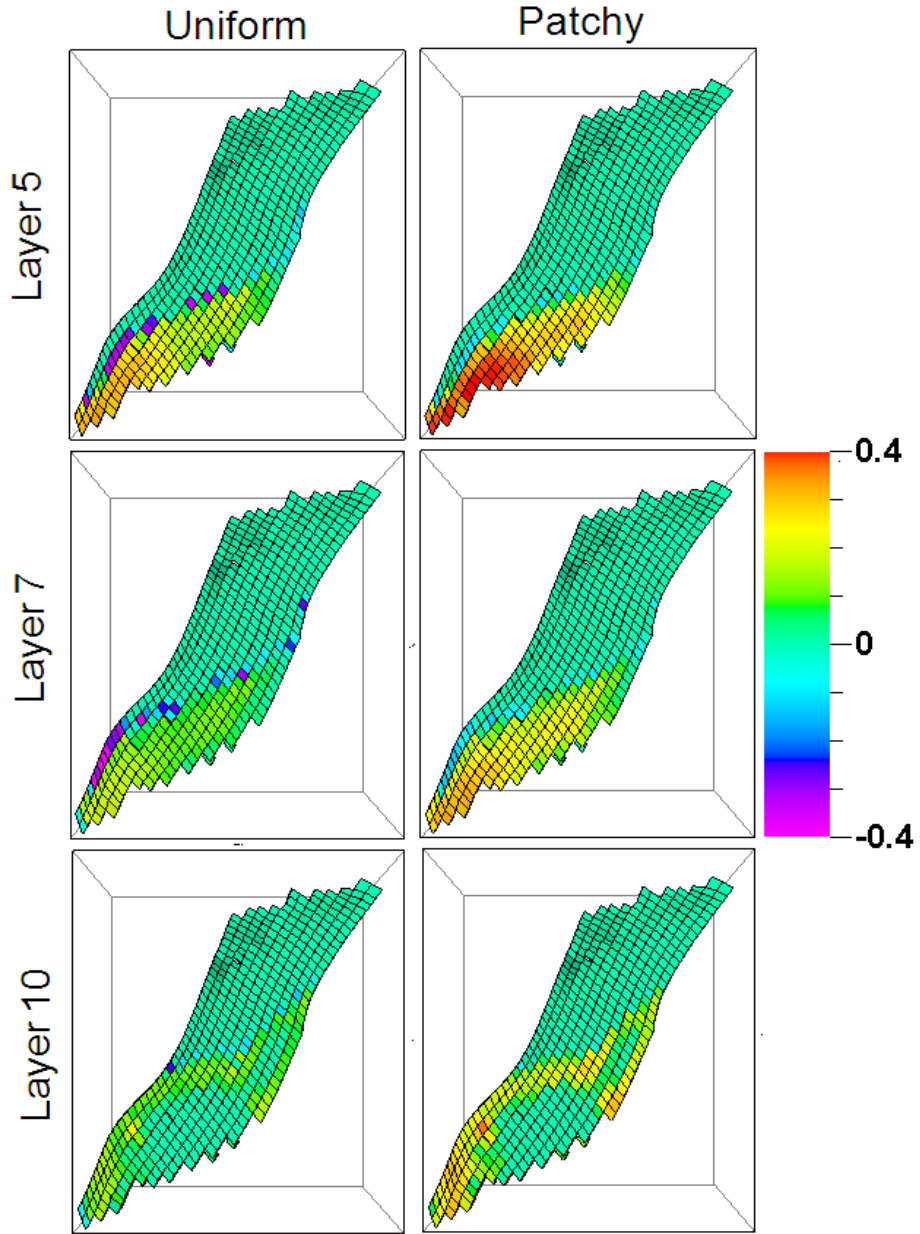


Figure 4.11: Effect of change in fluid mixing (uniform or patchy) on the median of P-wave impedance change in four years. The median is shown for three layers (5, 7 and 10) in the segment E of Norne field.

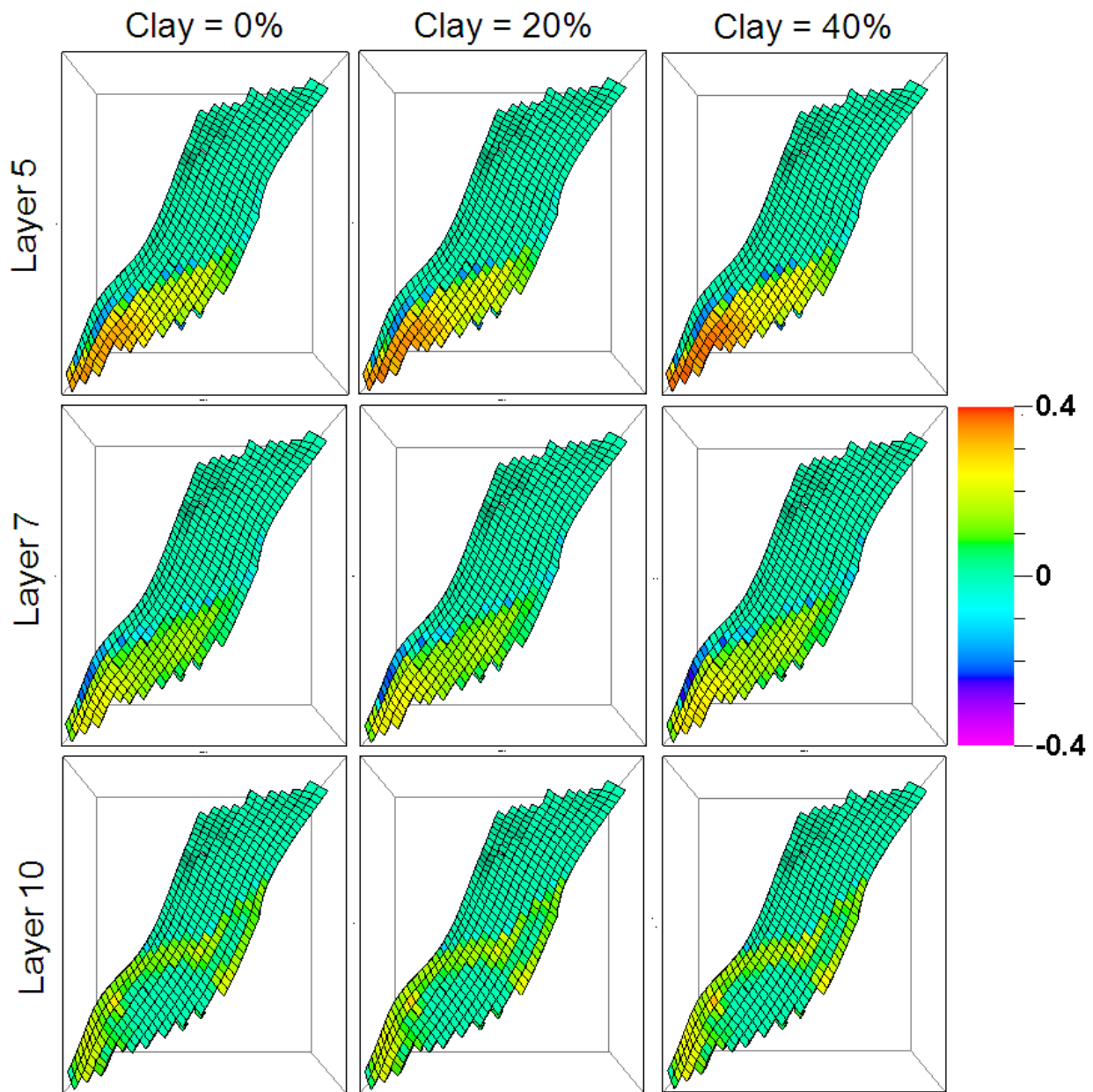


Figure 4.12: Effect of change in clay content on the median of P-wave impedance change in four years. The median is shown for three layers (5, 7 and 10) in the segment E of Norne field.

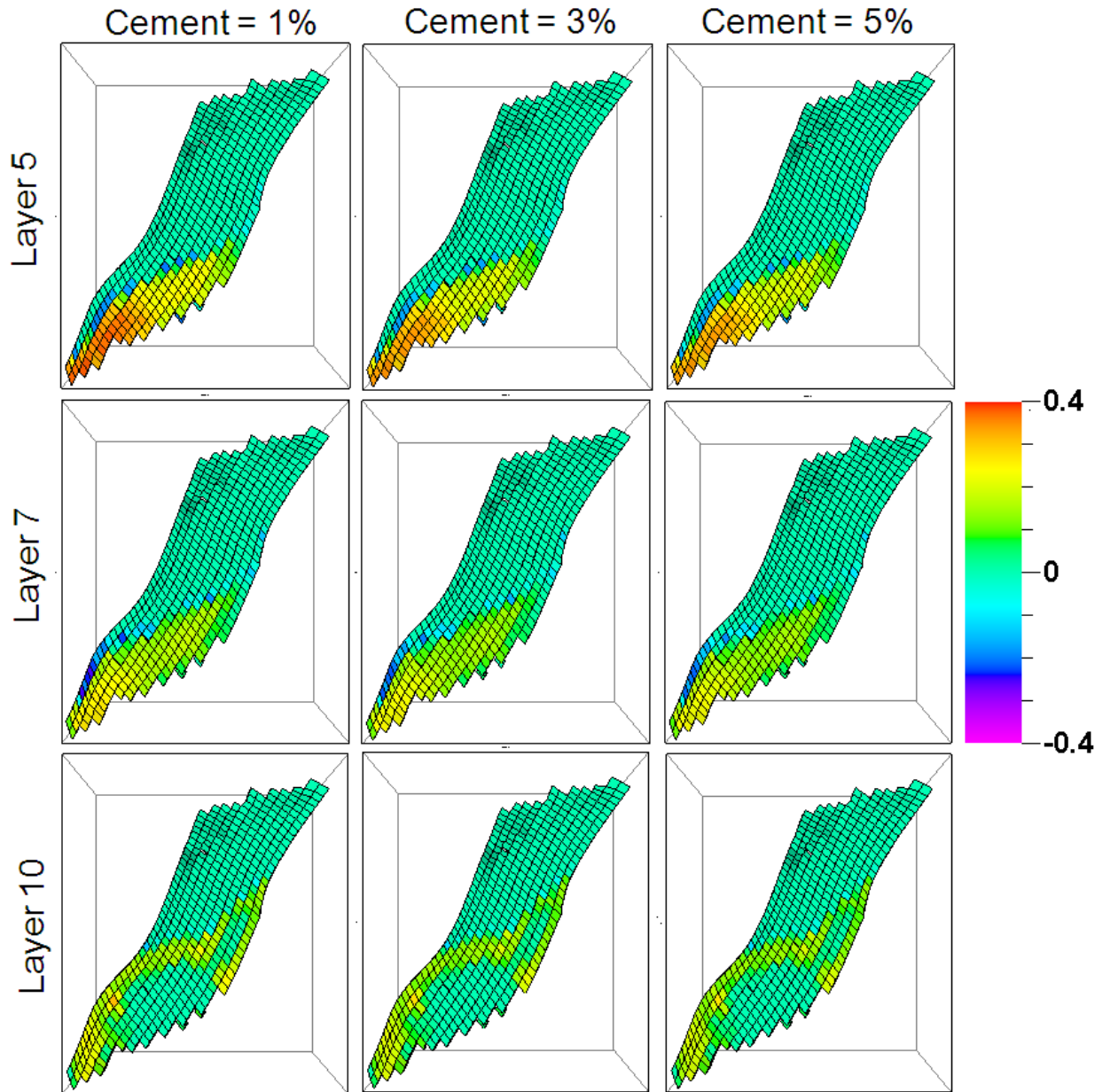


Figure 4.13: Effect of change cement fraction on the median of p-wave impedance change in four years. The median is shown for three layers (5, 7 and 10) in the segment E of Norne field.

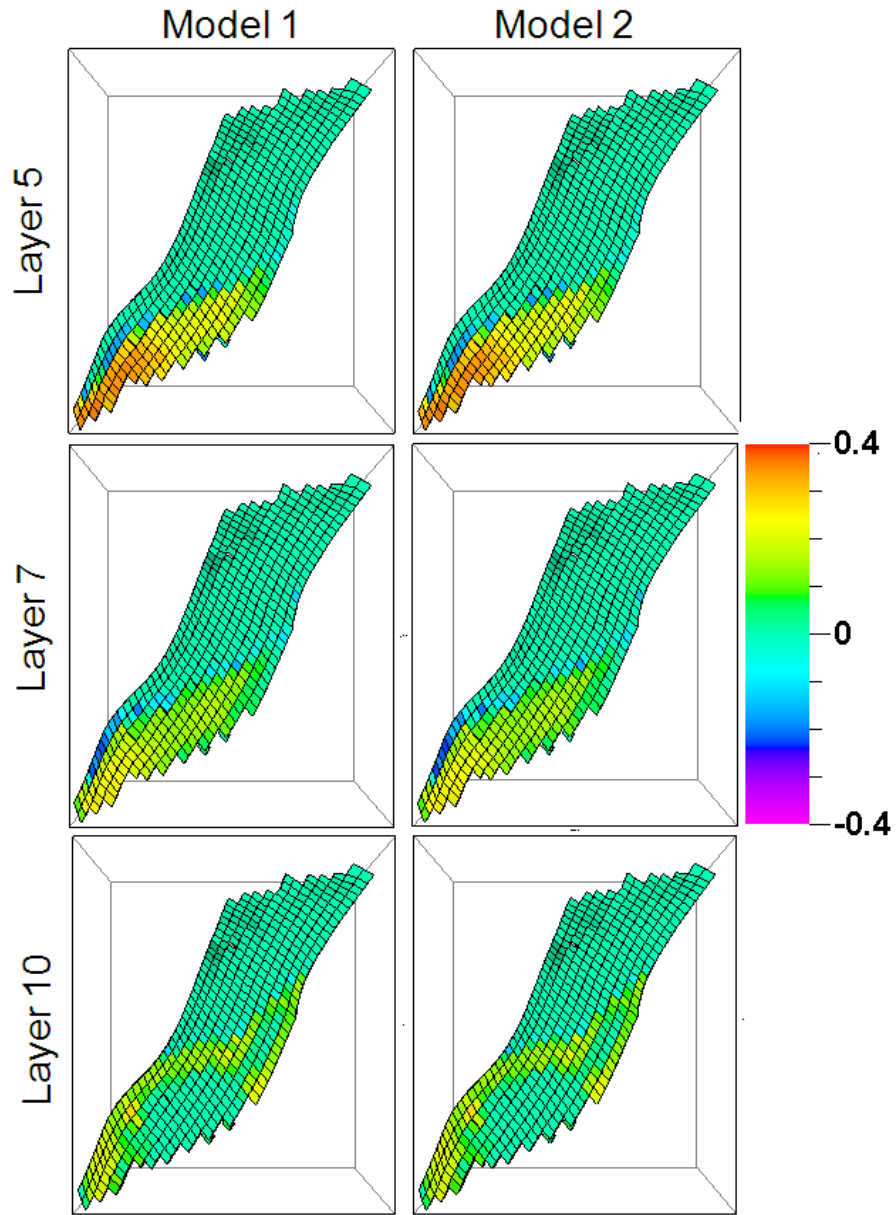


Figure 4.14: Effect of change in effective pressure model on the median of p-wave impedance change in four years. The median is shown for three layers (5, 7 and 10) in the segment E of Norne field.

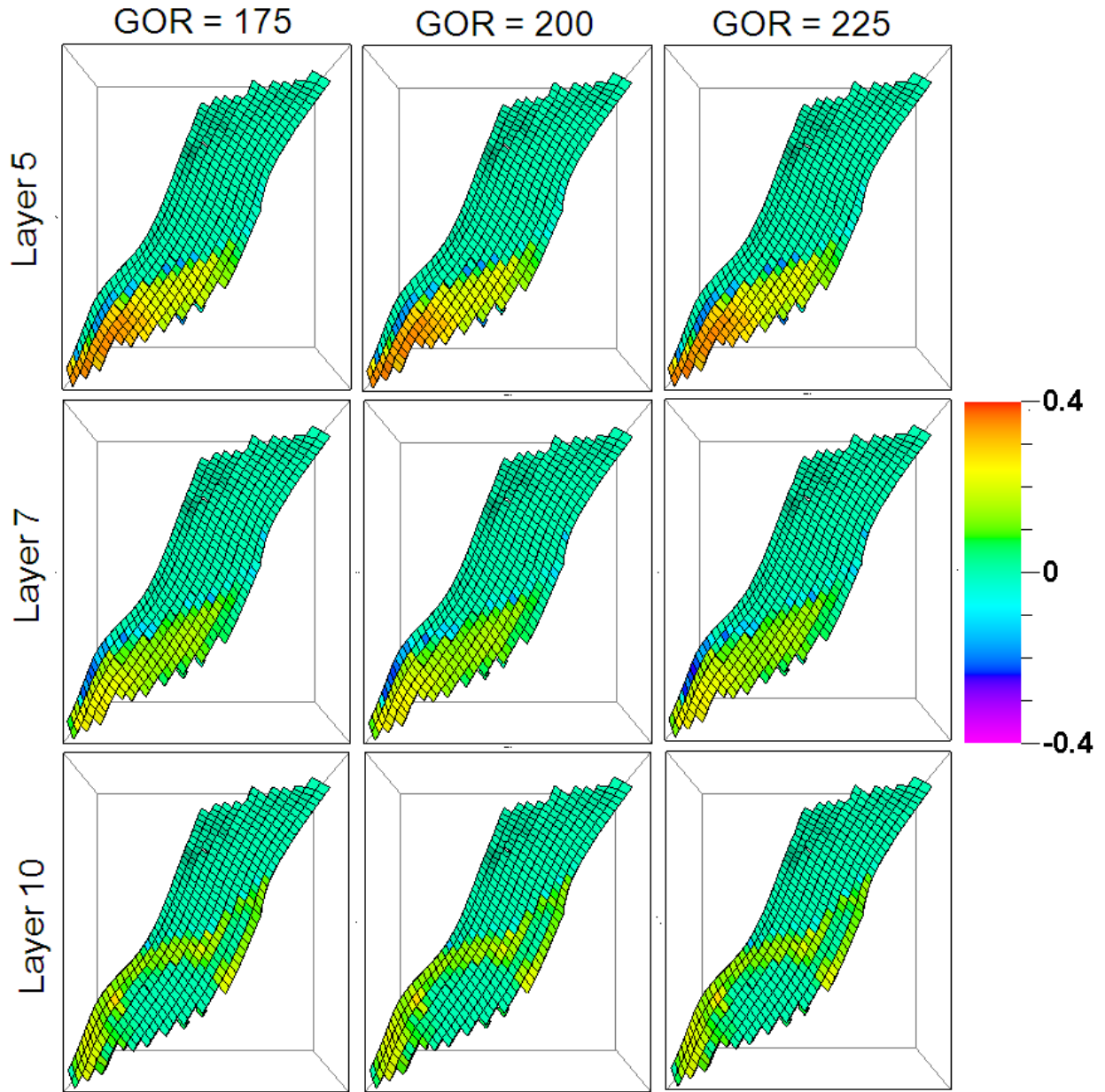


Figure 4.15: Effect of change in field GOR on the median of p-wave impedance change in four years. The median is shown for three layers (5, 7 and 10) in the segment E of Norne field.

## 4.5 Conclusions

We developed a workflow and identified sensitive rock physics parameters in modeling the time-lapse seismic response of Norne field. We also investigated sensitive parameters in the Gassmann's equation to generate the initial seismic velocity. It is found that clay content is the most sensitive parameter in fluid substitution for calculating seismic velocities in the Norne field. Salinity and pore pressure have minimal impact on fluid substitution. Coordination number is the most sensitive parameter in modeling the time-lapse seismic signature of Norne field. Clay content and fluid mixing are the second and third most sensitive parameter for modeling the time-lapse seismic signature. Results of this study will be used in joint inversion of time-lapse seismic and production data of the Norne field.

# Chapter 5

## **JOINT INVERSION OF PRODUCTION AND TIME-LAPSE SEISMIC DATA USING A FAMILY OF PARTICLE SWARM OPTIMIZERS**

### **5.1 Introduction**

In recent years people have used different methods for joint inversion of production and time-lapse seismic data. Landa et al. (1997) and Huang et al. (1997, 1998) used local optimization methods for joint inversion of seismic and production data. Castro et al. (2007) used geostatistical inversion to obtain reservoir model. The simulated production and time-lapse seismic response of the history matched reservoir model provided a satisfactory match with the observed production and time-lapse seismic data. The use of local optimization methods provides the best reservoir model that fits the observed data within a predefined tolerance. One of the disadvantages of this methodology is that no uncertainty estimation is usually performed

since it only provides the best reservoir model. In addition, local optimization methods for joint inversion are highly dependent on the initial guess which is not very robust. Also, it is difficult to obtain a global optimum match of production as well as time-lapse seismic data using conventional gradient based optimization methods (Sen and Stoffa, 1996).

Stochastic optimization based inversion methods have shown advantages in the integration of production and time-lapse seismic data in reservoir history matching (Jin et al, 2007, 2008). Stochastic optimization algorithms include simulated annealing (Kirkpatrick et al. 1983), genetic algorithms (Goldberg, 1989, Holland, 1992), particle swarm optimization (PSO) (Kennedy and Eberhart, 1995), differential evolution (Storn and Price, 1997) and Neighborhood algorithm (Sambridge, 1999). Stochastic optimization methods like genetic algorithms, simulated annealing and neighborhood algorithm are extensively used in geosciences for geophysical inversion (Sen and Stoffa, 1991, Sambridge and Drijkoningen, 1992, Sen and Stoffa, 1995, Ma, 2002, Fernández-Álvarez et al. 2008). Global optimization methods have also been used for optimization of well placement where the search space dimension is low. Global optimization algorithms have been used for inverse problems in combination with derivative-free techniques and parameter reduction techniques (Echeverría and Mukerji, 2009, Echeverría et al. 2009, Sena et al. 2009a, b, Romary, 2009a and b). Particle swarm optimization has been used in a variety of optimization and inverse problems in different branches of engineering and technology (Poli, 2008b), but its use in geosciences still remains restrained (Shaw and Srivastava, 2007, Fernández-Martínez et al. 2008b, Naudet et al. 2008, Yuan et al. 2009, Fernández-Martínez et al. 2009). Recently it has been used to optimize the well types and locations in a reservoir (Onwunalu and Durlofsky, 2009). Fernández-Martínez et al (2010) have used particle swarm optimizers to invert production data and time-lapse tomographic data using the synthetic Stanford VI reservoir. In this chapter we use the PSO family and two other novel variants of PSO (García-Gonzalo and Fernández-Martínez, 2010) as global optimizers for integration of production and time-lapse seismic data in history matching for a synthetic case. We study their convergence rate and compare their behavior. The goal of this chapter is to show the feasibility of PSO algorithms for joint inversion of production and time-lapse seismic data. We also show that use of particle swarm optimizers provide an approximate measure of uncertainty. Although

these algorithms cannot be considered exact samplers, their uncertainty information can be very useful in risk assessment (Fernández-Martínez et al. 2010a, b, and c).

The main advantage of global optimization method is that they can potentially address the inverse problem as a sampling problem. Although their use as a sampler, is limited by high computational cost attached with high number of forward simulations and high dimension of the inverse problem. The first problem can be handled by using faster approximations of the forward problem (forward surrogates) and running the forward simulation in parallel. The second problem can be handled by using parameterizations that reduce the dimensionality of the model space. In this paper we use the spatial principal component analysis as parameterization technique for dimensionality reduction (Echeverría et al. 2009, Echeverría and Mukerji ,2009) in combination with PSO family as global optimizers.

The chapter is structured as follows. First we describe the methodology in general terms; then we expand on the key components of the methodology, namely, spatial principal component analysis and family of particle swarm optimizers. Finally, we apply the different particle swarm optimizers for history matching of production and time-lapse seismic data of a synthetic data set.

## 5.2 Particle Swarm Optimization

Particle swarm optimization is a stochastic evolutionary computational technique inspired by the social behaviour of individuals (called particles) in nature, such as bird flocking and fish schooling (Kennedy and Eberhart, 1995)

Let us consider an inverse problem of the form  $F(m) = \mathbf{d}$ , where  $\mathbf{m} \in \mathbf{M} \subset \mathbf{R}^n$  are the model parameters,  $\mathbf{d} \in \mathbf{R}^n$  the discrete observed data, and

$$F(m) = (f_1(m), f_2(m), \dots, \dots, f_s(m)) \tag{5.1}$$

$F(m)$  is the vector field representing the forward operator and  $f_j(m)$  is the scalar field that accounts for the  $j$ -th data. The "classical" goal of inversion given a particular data set (often

affected by noise), is to find a set a unique set of parameters  $\mathbf{m}$ , such the data prediction error  $\|F(m) - \mathbf{d}\|$  in a certain norm  $p$ , is minimized.

A prismatic space of admissible models,  $\mathbf{M}$ , is defined:

$$l_j \leq m_{ij} \leq u_j, 1 \leq j \leq n, 1 \leq i \leq N_{size} \quad (5.2)$$

where  $l_j$  and  $u_j$  are the lower and upper limits for the  $j$ -th coordinate of each particle in the swarm,  $n$  is the number of parameters in the optimization problem and  $N_{size}$  is the swarm size. The misfit for each particle of the swarm is calculated, and then we determine for each particle its local best position found so far (called  $l_i(\mathbf{k})$ ) and the minimum of all of them is called the global best ( $\mathbf{g}(\mathbf{k})$ ). At each iteration the algorithm updates the positions ( $\mathbf{x}_i(\mathbf{k})$ ), and velocities ( $\mathbf{v}_i(\mathbf{k})$ ), of each model in the swarm. The velocity of each particle  $i$  at each iteration  $k$ , is a function of three major components. The inertia term, which consists of the old velocity of the particle, ( $\mathbf{v}_i(\mathbf{k})$ ) weighted by a real constant  $\omega$  called inertia. The social learning term, which is the difference between the global best position found so far (called  $\mathbf{g}(\mathbf{k})$ ) and the particle's current position ( $\mathbf{x}_i(\mathbf{k})$ ). The cognitive learning term, which is the difference between the particle's best position (called  $l_i(\mathbf{k})$ ) and the particle's current position ( $\mathbf{x}_i(\mathbf{k})$ ).

$$v_i(k+1) = \omega v_i(k) + \phi_1(g(k) - x_i(k)) + \phi_2(l_i(k) - x_i(k)) \quad (5.3)$$

$$x_i(k+1) = x_i(k) + v_i(k+1) \quad (5.4)$$

$$\phi_1 = r_1 a_g \quad (5.5)$$

$$\phi_2 = r_2 a_l \quad (5.6)$$

where  $\omega$ ,  $a_g$  and  $a_l$  are the PSO parameters, inertia, local, and global acceleration constants respectively.  $\phi_1$  and  $\phi_2$  are the stochastic global and local accelerations, whereas  $r_1$  and  $r_2$  are vectors of random numbers uniformly distributed in  $(0, 1)$  to weight the global and local acceleration constants. Inertia ( $\omega$ ) and total mean acceleration ( $\bar{\phi} = (a_g + a_l)/2$ ) play an important role in determining the convergence and stability of PSO algorithms. Research on PSO (Ozcan and Mohan, 1999, Carlisle and Dozier, 2001, Clerc and Kennedy, 2002, Trelea, 2003, Zheng et

al. 2003, van den Bergh and Engelbrecht, 2006, Fernández-Martínez et al. 2008a) have shown that the success of PSO depends on the values of the parameters  $\omega$ ,  $a_g$  and  $a_l$  selected for optimization. There are many variants of PSO proposed in the literature, involving a variety of heuristic mechanism for the positions and velocity updates. These fit for purpose heuristic modifications makes it impossible to approach the analysis of all of the PSO algorithms. Thus, Fernández-Martínez et al. (2009) proposed the continuous PSO model and constructed a whole family of particle swarm optimizers having different stability regions and exploration versus exploitation capabilities. These particle swarm optimizers are based on a stability analysis of the system of stochastic differential equations governing a damped mass-spring system, which is the physical analogy for the continuous PSO model.

### 5.3 Family of Particle Swarm Optimizers

The PSO algorithm can be physically interpreted as a particular discretization of a stochastic damped mass-spring system (Fernández Martínez and García Gonzalo, 2008a).

$$x_i''(t) + (1 - \omega)x_i'(t) + (\phi_1 + \phi_2)x_i(t) = \phi_1g(t - t_0) + \phi_2l_i(t - t_0) \quad (5.7)$$

This model has been addressed as the continuous PSO model since it describes (together with the initial conditions) the continuous movement of any particle coordinate in the swarm  $x_i(t)$  where  $i$  stands for the particle index, and  $g(t)$  and  $l_i(t)$  are its local and global attractors. In equation 5.7, the trajectories are allowed to be delayed a time  $t_0$  with respect to the trajectories. Using this physical analogy PSO particle trajectories were analysed (Fernández-Martínez et al. 2008a) and it explained the success in achieving convergence of some popular parameters sets found in the literature (Carlisle and Dozier, 2001 , Clerc and Kennedy, 2002), Trelea, 2003). A whole family of PSO algorithms (Fernández-Martínez and García-Gonzalo, 2009, García-Gonzalo and Fernández-Martínez, 2009) has been derived considering different differencing schemes for  $x_i''(t)$  and  $x_i'(t)$ . These family members have different properties with regard to their exploitation and exploration balance. These PSO algorithms are following:

### 5.3.1 GPSO or centred - regressive PSO ( $t_0 = 0$ )

The GPSO algorithm is the generalization of the PSO algorithm for any time step  $\Delta t$ , (PSO is the particular case for  $\Delta t = 1$ ). These expressions for the velocity and position are obtained by employing a regressive (backward) differencing scheme in velocity and a centred scheme in acceleration.

$$v(t + \Delta t) = (1 - (1 - \omega) \Delta t) v(t) + \phi_1 \Delta t (g(t) - x(t)) + \phi_2 \Delta t (l(t) - x(t)) \quad (5.8)$$

$$x(t + \Delta t) = x(t) + v(t + \Delta t) \Delta t \quad (5.9)$$

### 5.3.2 CC-PSO or centred - centred PSO ( $t_0 = 0$ )

The CC-PSO algorithm is derived from equation 5.7 by employing centred discretization in velocity as well as in acceleration. The expressions for the velocity and position obtained after discretization is shown below.

$$x(t + \Delta t) = x(t) + \left[ \frac{2 + (\omega - 1) \Delta t}{2} v(t) + \phi_1 \frac{\Delta t}{2} (g(t) - x(t)) + \phi_2 \frac{\Delta t}{2} (l(t) - x(t)) \right] \Delta t \quad (5.10)$$

$$v(t + \Delta t) = \frac{2 + (\omega - 1) \Delta t}{2 + (1 - \omega) \Delta t} v(t) + \frac{\Delta t}{2 + (1 - \omega) \Delta t} \sum_{k=0}^1 \left[ \phi_1 (l(t + k \Delta t) - x(t + k \Delta t)) + \phi_2 (g(t + k \Delta t) - x(t + k \Delta t)) \right] \quad (5.11)$$

### 5.3.3 CP-PSO or centred -progressive PSO ( $t_0 = \Delta t$ )

The CP-PSO algorithm is also derived from PSO continuous model considering centred discretization in acceleration and progressive (forward) discretization in velocity. The expressions for particle position and velocity after discretization are shown below.

$$v(t + \Delta t) = \frac{(1 - \phi \Delta t^2) v(t) + \phi_1 \Delta t (g(t) - x(t)) + \phi_2 \Delta t (l(t) - x(t))}{1 + (1 - \omega) \Delta t} \quad (5.12)$$

$$x(t + \Delta t) = x(t) + v(t) \Delta t \quad (5.13)$$

### 5.3.4 PP-PSO or progressive-progressive PSO ( $t_0 = 0$ )

PP-PSO is the member of extended PSO family and derived from PSO continuous model considering progressive discretization in both velocity and acceleration. The expressions for particle position and velocity are following:

$$v(t + \Delta t) = (1 - (1 - \omega)\Delta t)v(t) + \phi_1\Delta t(g(t) - x(t)) + \phi_2\Delta t(l(t) - x(t)) \quad (5.14)$$

$$x(t + \Delta t) = x(t) + v(t)\Delta t \quad (5.15)$$

### 5.3.5 RR-PSO or regressive-regressive PSO ( $t_0 = \Delta t$ )

The RR-PSO is obtained by regressive discretization in both acceleration and velocity to approximate the PSO continuous model. The expressions for particle position and velocity are shown below.

$$v(t + \Delta t) = \frac{v(t) + \phi_1\Delta t(g(t) - x(t)) + \phi_2\Delta t(l(t) - x(t))}{1 + (1 - \omega)\Delta t + \phi\Delta t^2} \quad (5.16)$$

$$x(t + \Delta t) = x(t) + v(t + \Delta t)\Delta t \quad (5.17)$$

All of the above algorithms are stochastic in nature and not heuristic because their convergence properties can be related to the first and second order stability of the particle trajectories, also known as stochastic processes (Fernández-Martínez and García-Gonzalo, 2009 , 2010, a ,b).

## 5.4 The Cloud Algorithms

All members of PSO family have convergence related to the first and second order stability of the particle trajectories. The stability behavior can be analyzed by examining the 2-dimensional space of  $\omega$  and  $\bar{\phi}$  . All members perform very well for a wide range of inertia ( $\omega$ ) and total mean acceleration ( $\bar{\phi}$ ). This region in the  $\omega - \bar{\phi}$  space, is close to the upper limit of the second order stability region for GPSO, CC-PSO, CP-PSO and PP-PSO. The good parameter values for RR-PSO lie along a straight line located in a zone of trajectories with medium

attenuation and high frequency. These regions are approximately the same for different kind of benchmark functions, so the same points can be used to optimize a wide variety of cost functions. Figure 5.1 shows for each family member the stability regions and the contour plots of the misfit error (in logarithmic scale) after a certain number of iterations (500) for the Rosenbrock function that has a valley shape. This numerical analysis is done for a lattice of points  $(\omega, \bar{\phi})$  located in the corresponding first order stability regions over 50 different simulations. For GPSO, CC-PSO and CP-PSO better parameter sets  $(\omega, a_g, a_l)$  are located on the first order complex region, close to the upper border of the second order stability region where the attraction from the particle oscillation center is lost, i.e. the variance becomes unbounded; and around the intersection to the median lines of the first stability regions where the temporal covariance between trajectories is close to zero (Fernández-Martínez and García-Gonzalo, 2009). The PP-PSO does not converge for  $\omega$  less than zero and the good parameter sets are in the complex region close to the limit of second order stability and to the zone of total mean acceleration equal to zero. The good parameters sets for the RR-PSO are concentrated around a line, mainly for inertia values greater than two. This line is located in a zone of medium attenuation and high frequency of trajectories (García-Gonzalo and Fernández-Martínez, 2009). Based on the above idea cloud version of PSO (García-Gonzalo and Fernández-Martínez, 2009, Fernández-Martínez et al. 2011) have been designed such that each particle in the swarm has different inertia and local and global acceleration constants, selected from within the appropriate region. In this research we have used a cloud version of the PSO. The cloud algorithm has the advantage since heuristic fine-tuning of the PSO parameters is not needed. Secondly it has potential for large explorations. Also, it does not artificially clamp the particle velocities to avoid instabilities.

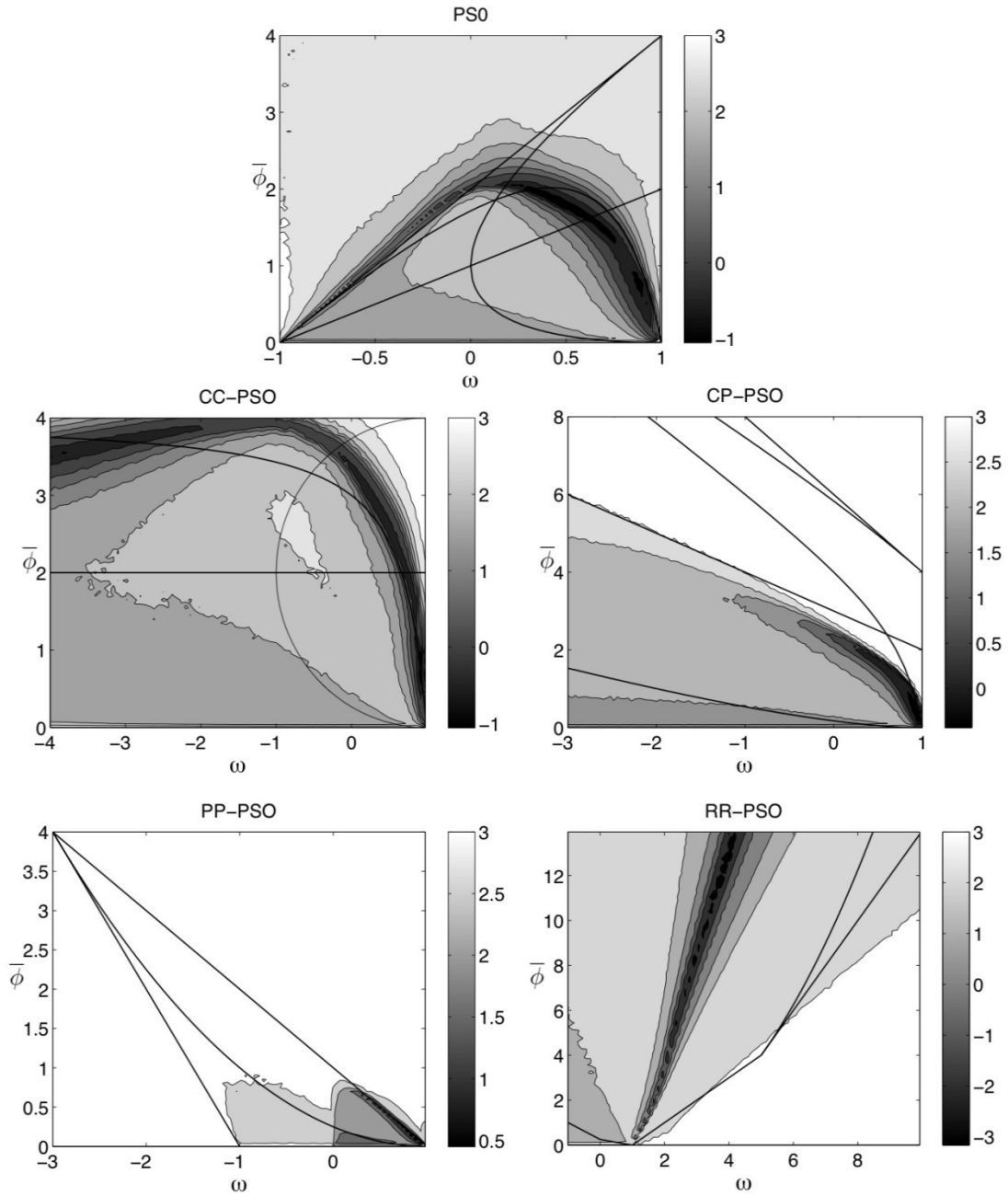


Figure 5.1: Logarithmic median misfit errors for the Rosenbrock function in 50 simulations (after 500 iterations) for different family members. Different family members have different stability regions. The lines are corresponding to PSO second order trajectories (Fernández-Martínez et al. 2010d).

## 5.5 Dimensionality Reduction

High dimensionality of the model parameters is the most challenging aspect of an inverse problem. It is associated with high computational cost and requires a large number of forward simulations. It becomes more challenging in the aspect of reservoir model updating since the reservoir petrophysical properties (optimization variables) cannot be varied independently, but have to be varied so that geology of the reservoir model is preserved. Principal component analysis (PCA) (Pearson, 1901) is a well-established method to transfer a number of correlated variables in to a smaller number of uncorrelated variables. The first principal component captures the maximum variability and variability decreases with succeeding components. PCA has been used as a model reduction technique in history matching problem by Reynolds et al. (1996), Sarma et al.(2006), Echeverría et al.(2009) and Echeverría and Mukerji,(2009).

In this study, PCA is used to reduce the dimension of model space based on the prior samples of the reservoir models that are obtained using geostatistical algorithms and conditioned to the hard (well) data. It is used to find an orthogonal basis of the covariance matrix designed from the prior reservoir models and by selecting most important eigenvalues and associated eigenvector to obtain the reduced model space.

Let  $m_i$  represents a reservoir model which is a vector containing reservoir property at each gridblock. There are  $N$  gridblocks in each reservoir model, and a total of  $L$  reservoir models are generated from the prior.  $M$  is the set of  $L$  reservoir models generated by geostatistical simulation methods (variogram based) and constrained to prior data (hard data).

$$M = (m_1 \ m_2 \ m_3 \ m_4 \ \dots \ m_i \ \dots \ m_L)^T \quad \in R^{L \times N} \quad (5.18)$$

The centered covariance matrix of ensemble  $M$  is denoted by  $C_M$

$$C_M = \frac{1}{L} \sum_{i=1}^L (m_i - \mu) (m_i - \mu)^T \quad (5.19)$$

where,  $\mu$  is the mean of the ensemble  $M$ .

The covariance matrix is centered to maintain the consistency of the data after reconstruction. Next eigenvalue decomposition is performed on the centered covariance matrix

$$C_M V_{C_M} = V_{C_M} \Lambda_{C_M} \quad (5.20)$$

Where,  $V_{C_M}$  and  $\Lambda_{C_M}$  are eigenvector and eigenvalue matrix of centered covariance matrix  $C_M$ .

A few large eigenvalues and associated eigenvectors are selected ( $d \leq L$ ) such that they capture the maximum variability of the prior reservoir models. This new set of orthogonal vectors forms the basis of the reduced model space. Now any reservoir model ( $\dot{m}_k$ ) is represented by a linear combination of the eigenvectors.

$$\dot{m}_k = \mu + \sum_{i=1}^d a_i v_i \quad (5.21)$$

$a_i$  are the coefficients (optimization variable) and  $v_i$  are the selected ( $d$ ) eigenvectors of the centered covariance matrix. The above approach is discussed in Echeverría et al. (2009) and Echeverría and Mukerji, (2009). One problem with this method is that after transformation from reduced space to model space there is a possibility of obtaining negative values for the reservoir property which is unphysical. So we propose to apply the above method, not directly on reservoir property (porosity in our case) but a particular transformation of the reservoir property. First we transfer reservoir properties using a proper transfer function and then perform the PCA analysis on transferred properties to get the reduced space. The new model is obtained by construction in the transformed space and then back transformation from transformed space to model space. The appropriate transformation function can be selected based on the reservoir property that has to be optimized. In this research we are updating porosity of the reservoir grid block based on the production and time-lapse seismic data. Logit transformation (Cramer, 2003) is an appropriate transformation for porosity field since porosities of the Norne field varies from 0 to 0.39. First porosity is normalized by dividing with 0.4 and then logit transformation is applied on normalized porosity.

$$y_i = \log \frac{p_i}{1 - p_i} \quad (5.22)$$

$p_i$  is the normalized porosity of the porosity model  $m_i$ .

PCA analysis is performed on the ensemble of  $y_i$ . The new model is obtained using back transformation after the construction in the transformed space. This removes the possibility of obtaining negative values for the reservoir properties (porosity in this case).

## 5.6 Application to synthetic case

A 2D reference porosity model (Figure 5.2) is selected on which our method will be tested. The reservoir is represented in a 2D grid of 2500 cells (50 x 50 x 1) with each grid block having a dimension of 50 m in X and Y direction and 10 m in Z direction. The model has porosity varying from 0 to 0.4. There is a spatial continuity of high porosity in the NE direction.

<b>Type</b>	Spherical
<b>Nugget</b>	0
<b>Ranges</b>	750/250/10
<b>Angles</b>	45/135/0

Table 5.1: Details of the variogram used for geostatistical simulation of 1000 porosity realization. There is a geological continuity in N-E direction

1000 realizations of porosity are generated using variograms and well log data and based on sequential Gaussian simulation. Well log data consists of porosity measured at five wells in the reference porosity model. Variograms used for the simulation are generated using reference porosity distribution. The aim is to obtain a set of history matched porosity models using the method discussed previously. The simulated response of these models should provide a satisfactory match with production and time-lapse seismic data.

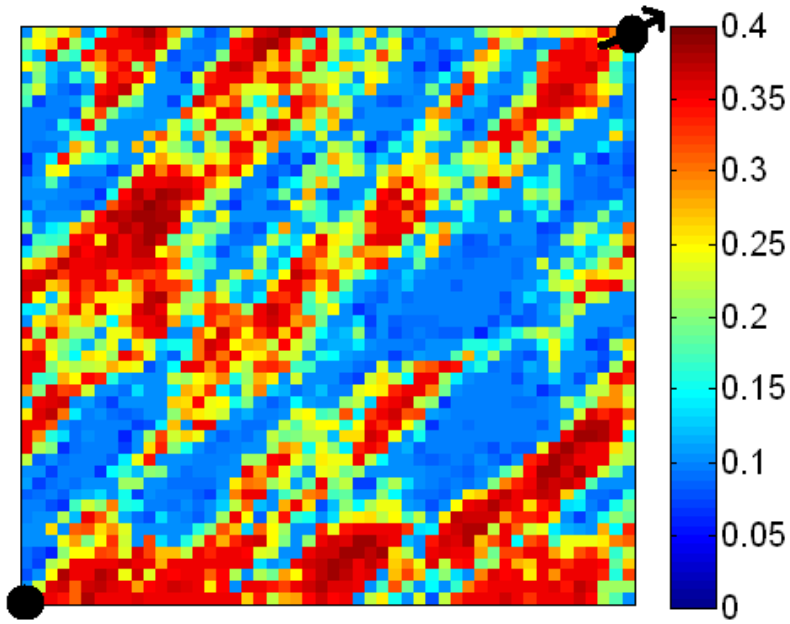


Figure 5.2: Reference porosity realization used in this study. Porosity varies from 0 to 0.4, and there is a geological continuity in N-E direction (show positions of well data). Injector and producer locations are shown in the black circles.

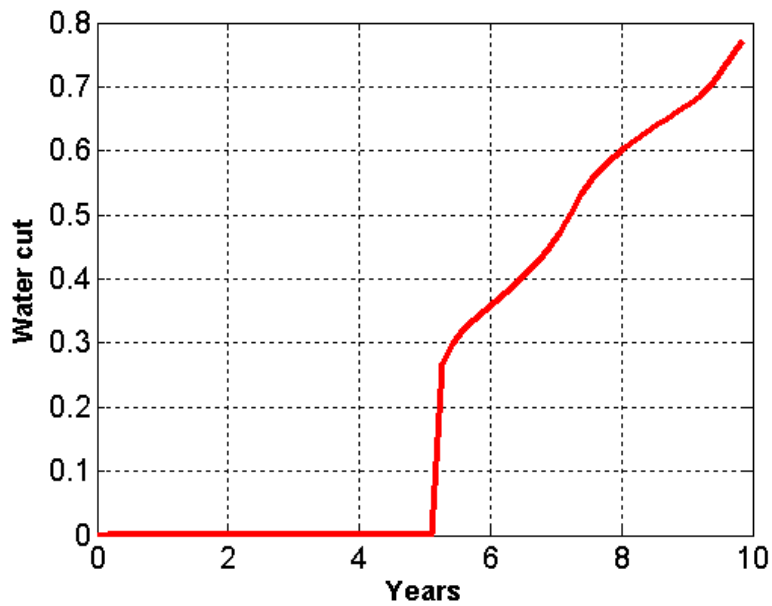


Figure 5.3: Water cut over ten years for the reference porosity realization. It is considered as observed production data in this study.

### 5.6.1 Flow Simulation

The reference reservoir is produced with one producer located at lower most left corner and one injector located at topmost right corner. Both producer and injector are operated by bottom hole pressure (BHP) of 3500 and 5500 psi respectively. Water and oil are the only fluids present in the reservoir. Thus, a two phase (oil and water) isothermal black oil model is used for dynamic modeling of the reservoir to obtain the fluid saturation distribution inside the reservoir at different times. Permeability of a model is obtained by a log normal correlation between porosity and permeability. Ten years of production have been simulated. The observed production data is the water cut of the reservoir in ten years of production (Figure 5.3). Relative permeability curves are constant in the flow simulation, and no capillary effect is considered.

### 5.6.2 Time-lapse Seismic

As the reservoir is being produced the saturation of fluid changes inside the reservoir. Seismic response of the reservoir will also change with time, due to change in the fluid saturation. In this case seismic P-wave impedance is changing with time as the reservoir is being produced. The normalized change in seismic P-wave impedance over ten years is considered as reference time-lapse seismic data (Figure 5.4).

$$S_{ref} = \frac{(AI_{t_2})_{ref} - (AI_{t_1})_{ref}}{(AI_{t_1})_{ref}} \quad (5.23)$$

The elastic properties and initial P-impedance of the reservoir rocks are modeled using Dvorkin's unconsolidated sand model (Dvorkin et al, 1996). Seismic impedance after ten years of production is obtained using Gassmann's fluid substitution considering only the effect of change in fluid saturation inside the reservoir.

### 5.6.3 Dimensionality Reduction

The reduced model space is obtained by following the methodology described in Section 5.5. Figure 5.6 shows six porosity realizations out of 1000 initial porosity realizations, used for dimensionality reduction. The number of optimization variables is an important factor in the inverse problem. The dimension of the reduced model space or number of PCA coefficient

retained for optimization is selected such that important geological features are retained as well as computational cost is reduced.

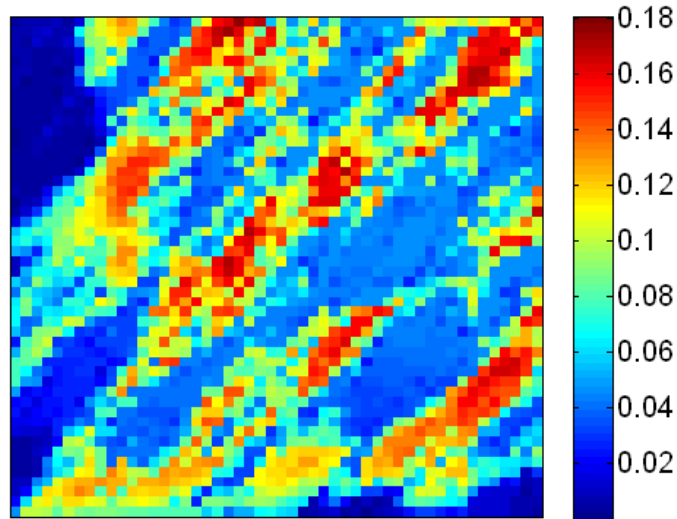


Figure 5.4: Normalized P-wave impedance change over ten years of production for reference porosity realization. It is considered as observed time-lapse seismic data in this study.

It also depends on the fact that, first PCA coefficient captures maximum variance in the prior and it decreases successively with higher coefficients. The number of PCA coefficients used for dimensionality reduction is determined by studying its impact on the production, time-lapse seismic and total misfits. The change in the production, time-lapse seismic and total misfits with increase in the number of PCA coefficients are shown in the Figure 5.5. It is observed that production misfit is more sensitive to the number of PCA coefficients. The total misfits obtained using 50 and 150 PCA coefficients are almost similar and close to the minimum total misfit. The computational cost associated with 150 PCA coefficients is higher than that of 50 PCA coefficients. Thus, 50 PCA coefficients are selected to define the dimensions of the reduced space. Normalized cumulative sum of PCA eigenvalues indicates the increase in variance with increase in the number of PCA coefficients. Figure 5.6 shows that 50 PCA coefficients are able to capture 50% of the variance of the prior. Figure 5.7 shows three actual realizations of porosity and their distribution after selecting 50 PCA coefficients and associated eigenvectors. We observed that 50 PCA coefficients are successfully capturing the large-scale features present in the actual porosity models.

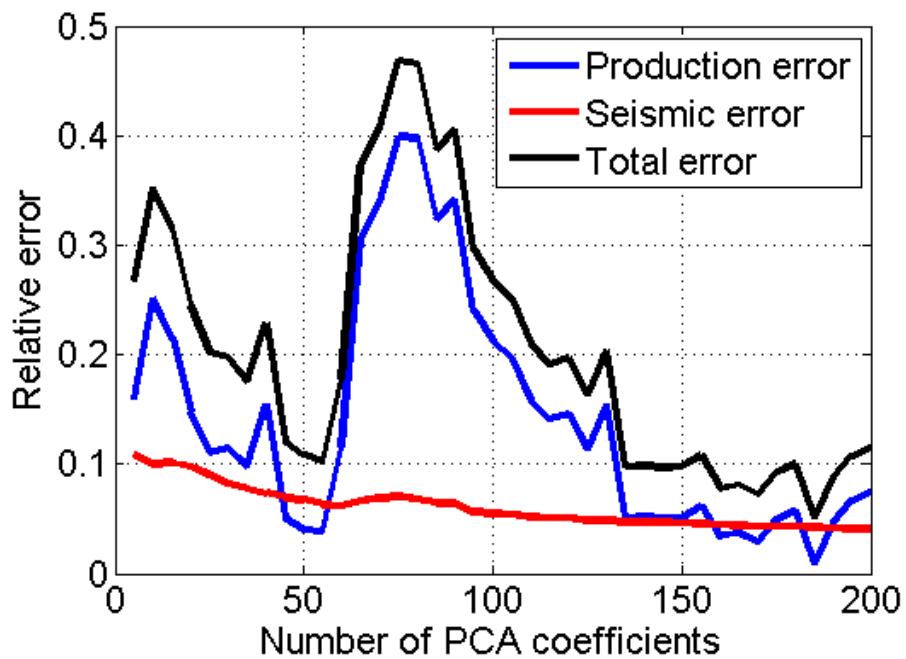


Figure 5.5: The change in the relative error with increase in the number of PCA coefficients. It is clear that 50 PCA coefficients are enough to reduce the relative error by 70%.

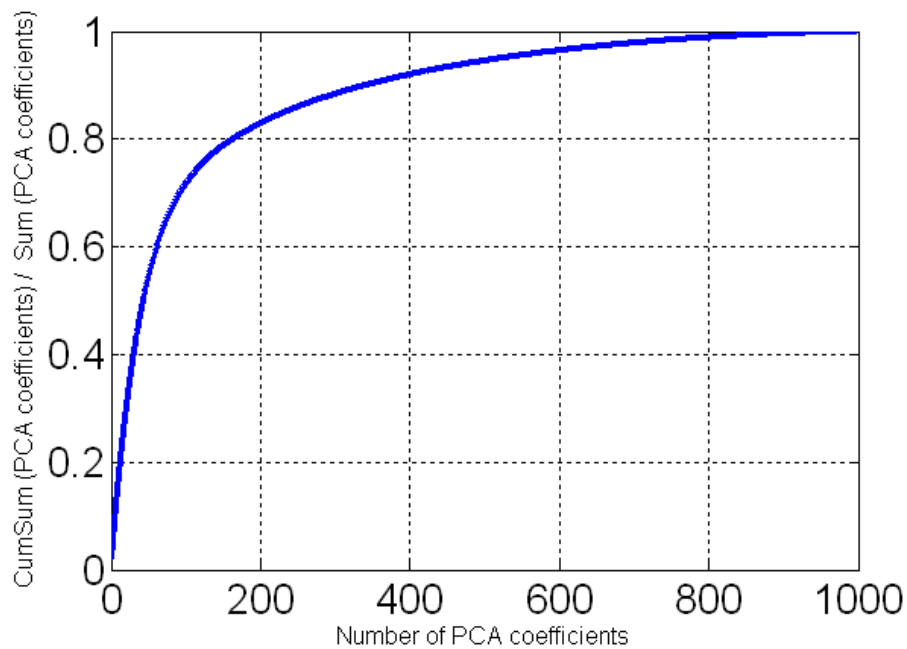


Figure 5.6: Variance of the prior captured by the PCA coefficients. In this study 50 PCA coefficients are used and these coefficients are able to capture 50% of the variance present in the prior

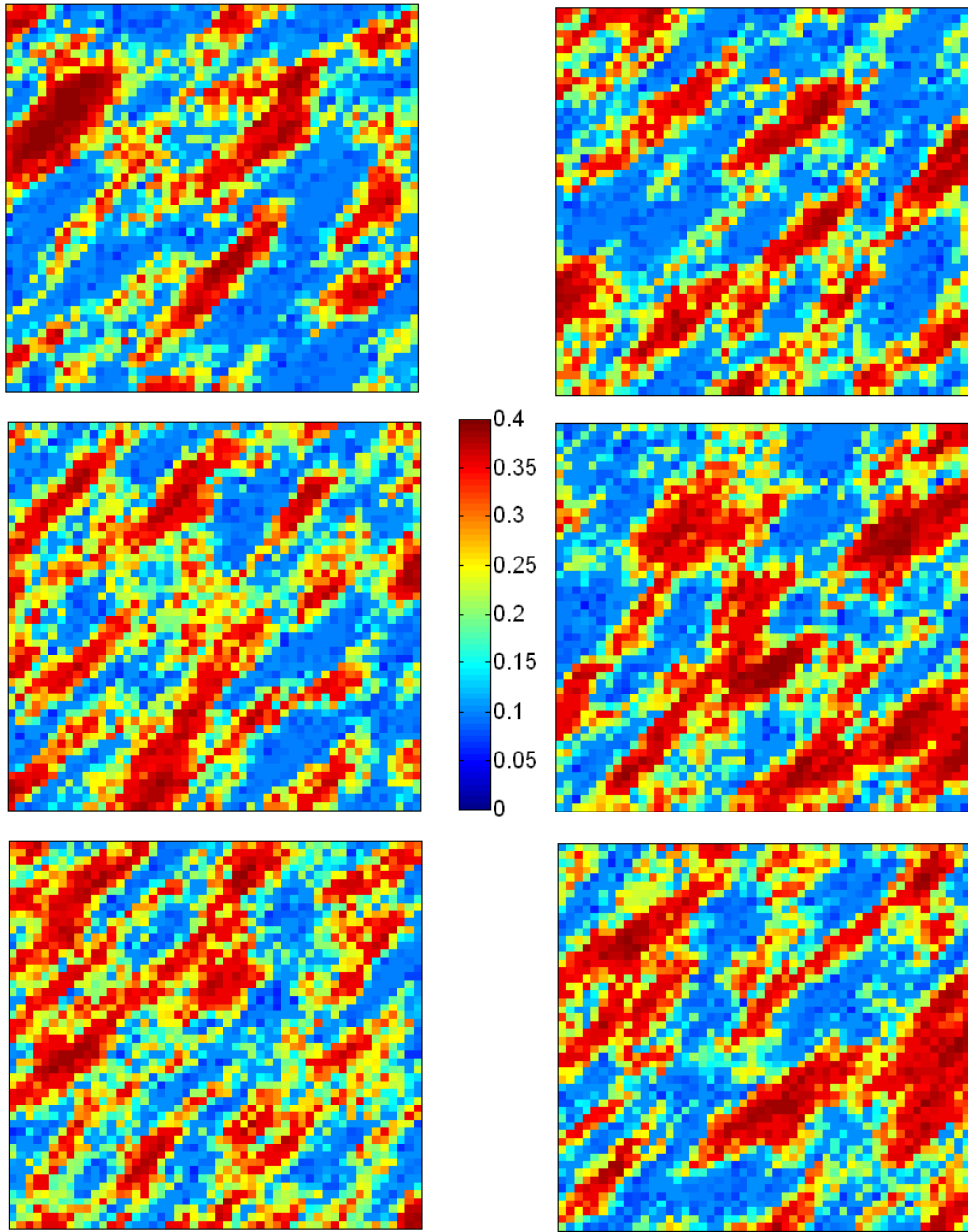


Figure 5.7: Six porosity realizations (reservoir models) are shown out of 1000 realizations generated using sequential Gaussian simulation based on well log data and variograms

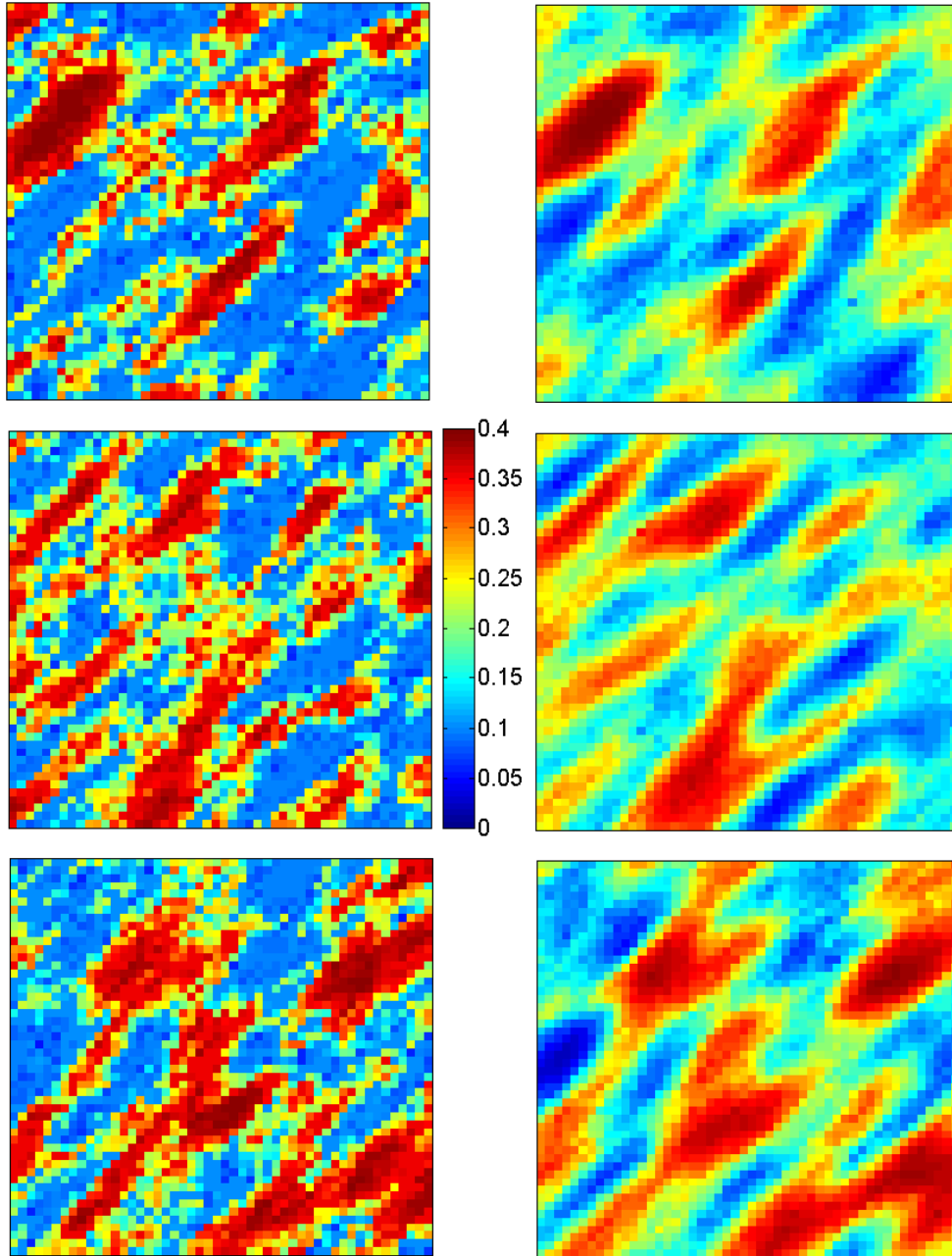


Figure 5.8: Three porosity realization shown on the left, corresponding porosity realization constructed using 50 PCA coefficients and associated vectors are shown on the right. It is clearly observed that 50 PCA coefficients are successfully capturing large scale features present in the reservoir models.

## 5.7 Methodology

Figure 5.8 describes the methodology used for this study. The coefficients for PCA vectors are optimized using different particle swarm optimizers. The objective function used in the optimization consists of two parts: production data mismatch and seismic data mismatch. The objective function  $O$  is defined in the equation below.

$$O = w_1 \frac{\|W_{ref} - W_{mod}\|_2^2}{\|W_{ref}\|_2^2} + w_2 \frac{\|S_{ref} - S_{mod}\|_2^2}{\|S_{ref}\|_2^2} \quad (5.24)$$

Where,  $W_{ref}$  and  $W_{mod}$  are reference and modeled water cut for ten years of production respectively. Similarly,  $S_{ref}$  and  $S_{mod}$  are reference normalized P-wave impedance change and modeled normalized P-wave impedance change respectively. The weights assigned to production data mismatch ( $w_1$ ) and seismic data mismatch ( $w_2$ ) are equal to 1.

We optimize 50 coefficients of PCA vectors using different particle swarm optimizers. The upper and lower ranges of 50 coefficients in optimization are obtained from the range of projections of reservoir models of the prior in the reduced space. Particle swarm optimizers start with an initial guess within this range for the swarm of 50 coefficients, and subsequently reservoir models are constructed based on the transformation (discussed in Section 5.5). Next flow simulation is performed on these reservoir models to obtain associated production response. Seismic responses of these reservoir models are also obtained using the rock physics model and Gassmann's substitution (as described in Section 5.6.2). Misfits for each of the reservoir models are calculated as defined in the objective function. Particle swarm optimizers minimize the misfit to obtain a global minimum and optimize the PCA coefficients. At the end, optimum 50 coefficients are obtained associated with the reservoir model having minimum mismatch with the observed data. In the process, not only a global minimum is obtained but at the same time several local minima are also obtained due to the exploration capability of the swarm associated with the particle swarm optimizers.

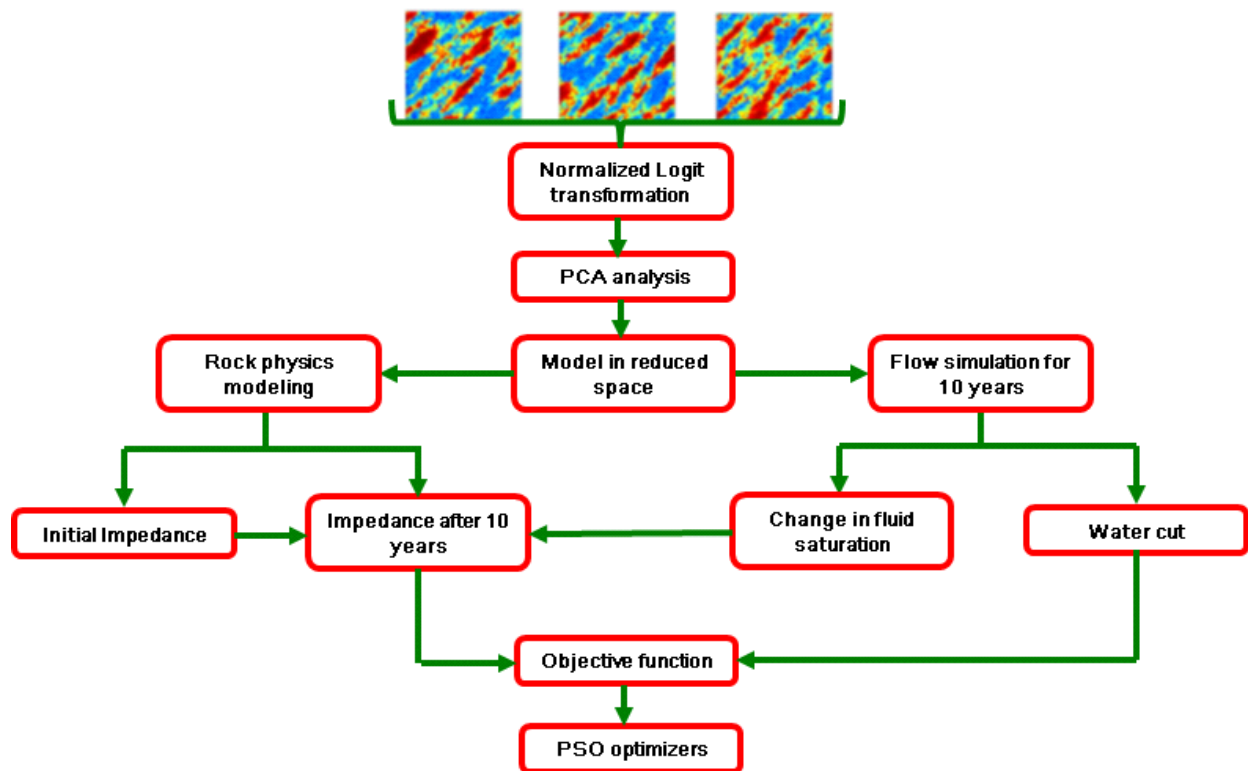


Figure 5.9: Workflow used in this study. It consists of PCA analysis, production and seismic modeling and use of particle swarm optimizers

## 5.8 History Matching Results

The proposed workflow is applied using different particle swarm optimizers, namely CC-PSO, CP-PSO, GPSO, PP-PSO and RR-PSO. Swarm size and number of iterations for particle swarm optimizers are important factors, and should be established based on computational resources available. We have used a swarm size of 20 for each of the particle swarm optimizers. Each particle swarm optimizer is run for 100 iterations, and it is observed that it is adequate for this study, since convergence is achieved for each case.

The history matching results for CC-PSO are shown in the Figure 5.9. The simulated production and time-lapse seismic response of the best model provided the minimum total misfit with the observed production and time-lapse seismic data. The simulated time-lapse seismic responses of initial guess model and best model are also shown. There is a clear improvement from the initial guess model to the best model in terms of geological continuity. It is also clear that time-lapse seismic response of the best model is very similar to the observed time-lapse seismic response as compared to time-lapse seismic response of initial guess model. Production responses (water cut) of initial guess model and best model are compared with the observed production data in the Figure 5.10. It clearly indicates the improvement of production response of initial guess model to the best model. Figure 5.11 shows the convergence behavior of CC-PSO with the increase in the number of iterations. The median of misfit of models in the swarm is plotted against the number of iterations. The decrease in production data misfit, seismic data misfit and total misfit are shown by blue, red and green curves respectively. The rate of decrease in production mismatch is higher than time-lapse seismic mismatch.

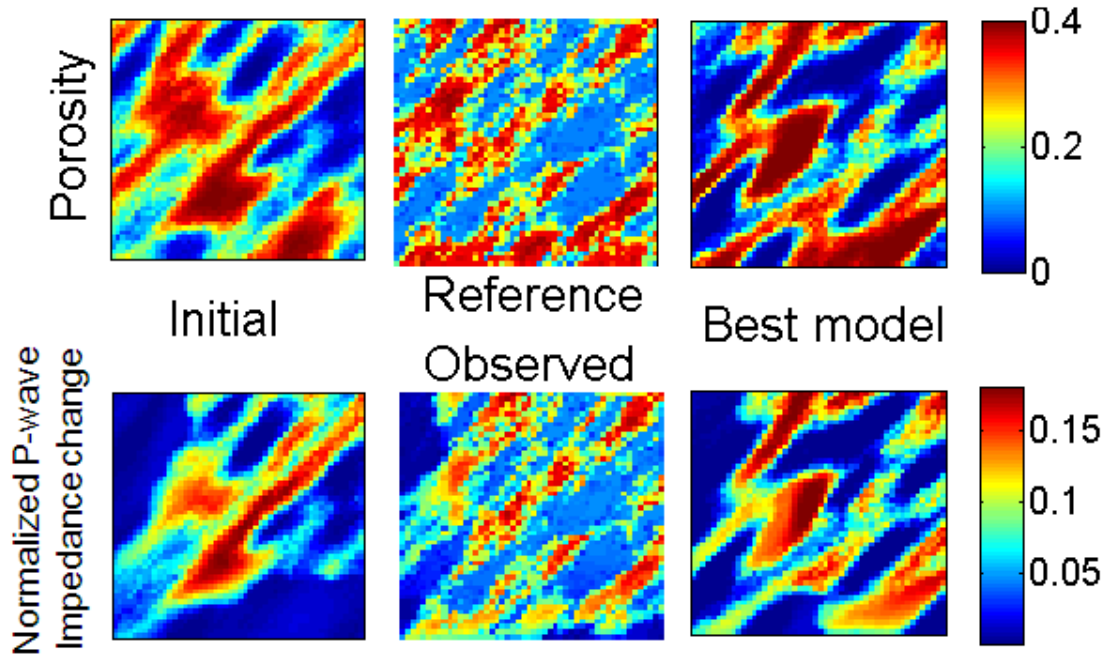


Figure 5.10: Best porosity model (top right) and associated time-lapse seismic response (bottom right) obtained using CC-PSO. Initial guess (left), Reference porosity model and observed time-lapse seismic data (middle) are shown for comparison

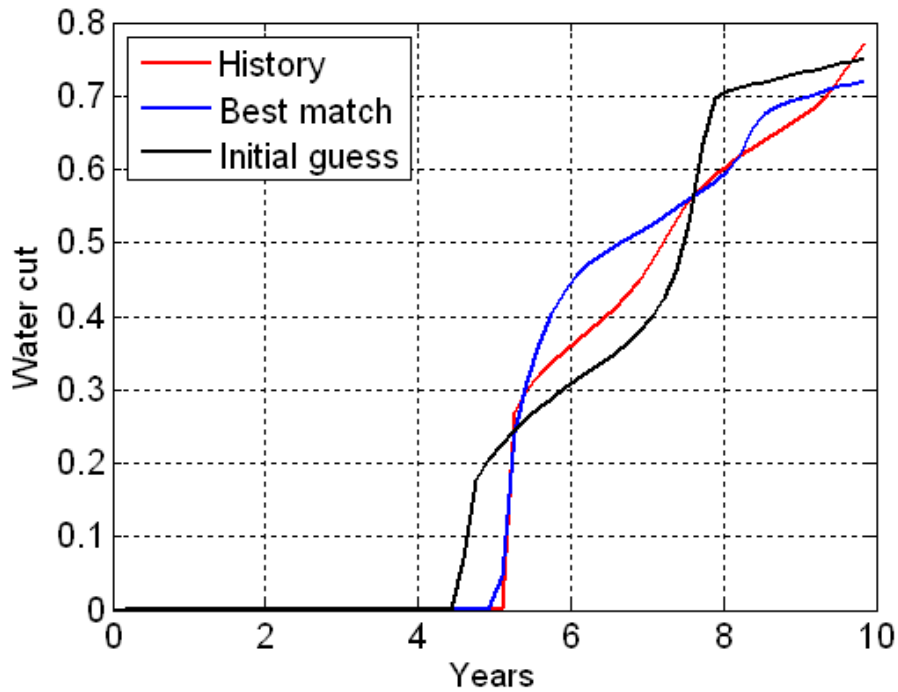


Figure 5.11: Water cut over ten years of production using CC-PSO. Observed production data is shown in red, water cut for initial guess model is shown in black, water cut associated with the best model is shown in blue

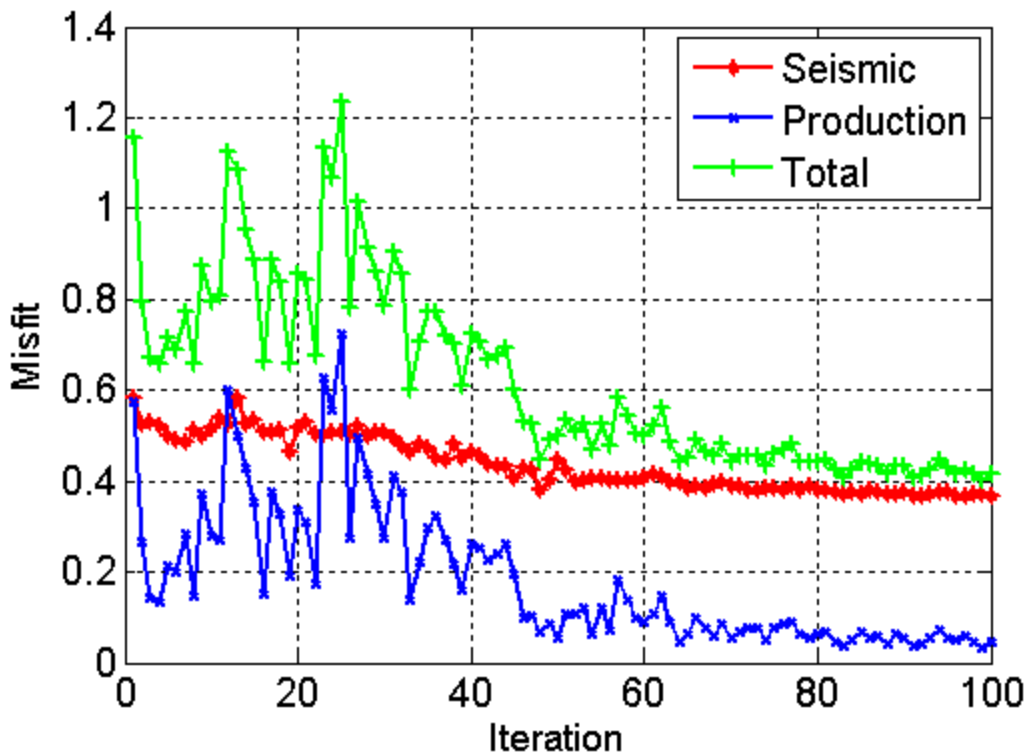


Figure 5.12: Behavior of median misfit with the increase in number of iterations using CC-PSO. Red, blue and green curves are median misfits for time-lapse seismic, production and total

History matching results for CP-PSO are shown in Figures 5.12 and 5.13. CP-PSO is designed such that  $\Delta t$  is less than 1, since CP-PSO is very explorative and it is observed that if  $\Delta t$  is greater than 1, it fails to converge and does not provide a good history match. Initial guess model, best model and associated production and seismic responses are compared with the reference model and observed data. History matched model has successfully captured the features present in the reference model. CC-PSO has failed to resolve medium porosity and history matched models have low and high porosities. CP-PSO is successful in resolving low, medium and high porosities. Also, we obtain a better history match of water cut using CP-PSO as compared to the CC-PSO. Figure 5.14 shows the decrease in production misfit, seismic misfit and total misfit with the increase in number of iterations using CP-PSO. The minimum total misfit, seismic misfit and production misfit obtained using CP-PSO are lower (almost half) than the misfits obtained using CC-PSO. Also, the decrease in the misfit is fast and smooth as compared to the results of CC-PSO.

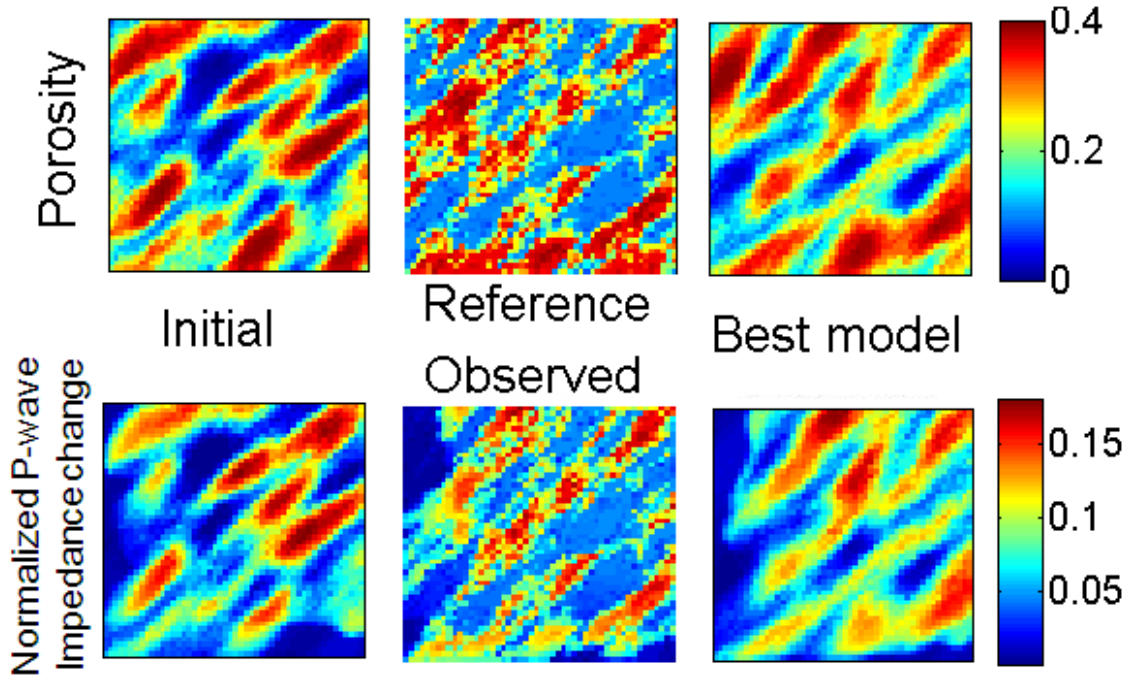


Figure 5.13: Best porosity model (top right) and associated time-lapse seismic response (bottom right) obtained using CP-PSO. Initial guess (left), Reference porosity model and observed time-lapse seismic data (middle) are shown for comparison

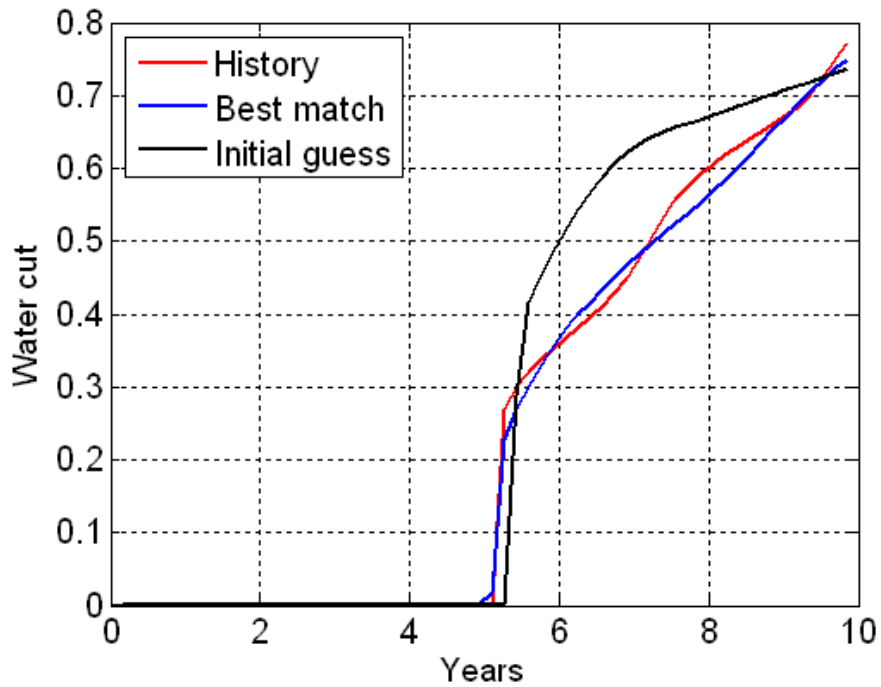


Figure 5.14: Water cut over ten years of production using CP-PSO. Observed production data is shown in red, water cut for initial guess model is shown in black, water cut associated with the best model is shown in blue

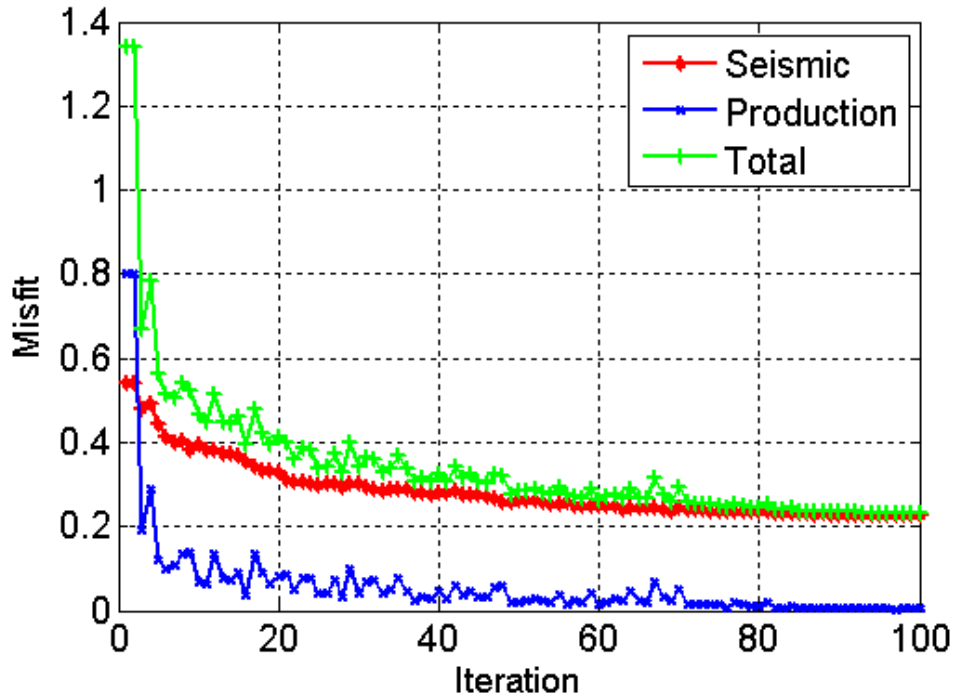


Figure 5.15: Behavior of median misfit with the increase in number of iterations using CP-PSO. Red, blue and green curves are median misfits for time-lapse seismic, production and total

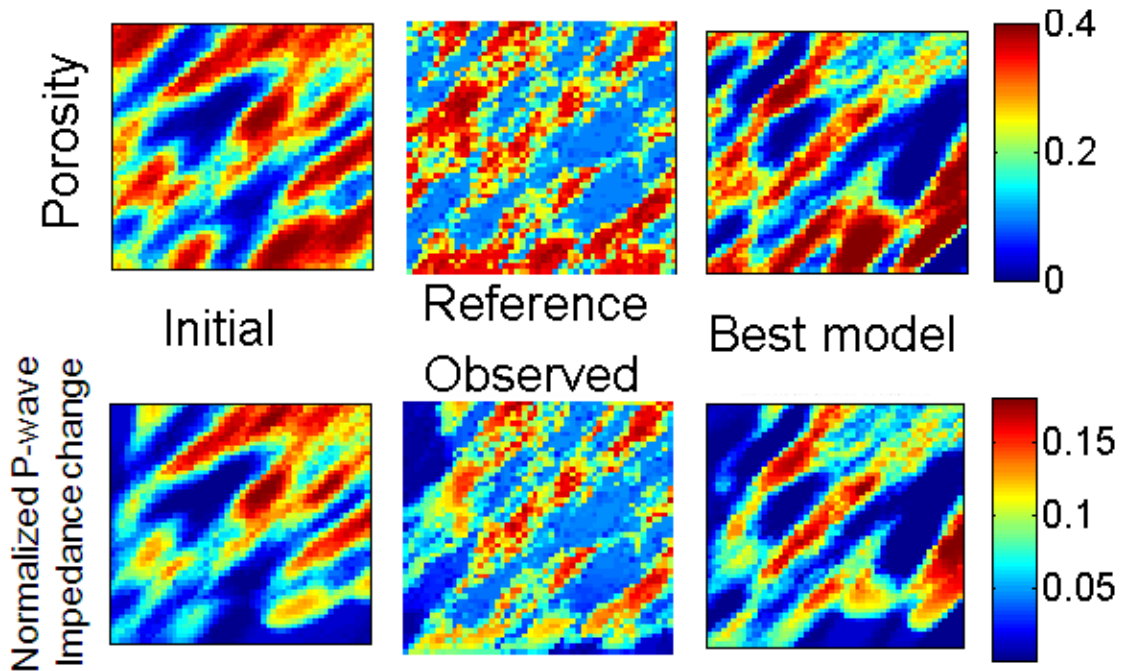


Figure 5.16: Best porosity model (top right) and associated time-lapse seismic response (bottom right) obtained using GPSO. Initial guess (left), Reference porosity model and observed time-lapse seismic data (middle) are shown for comparison

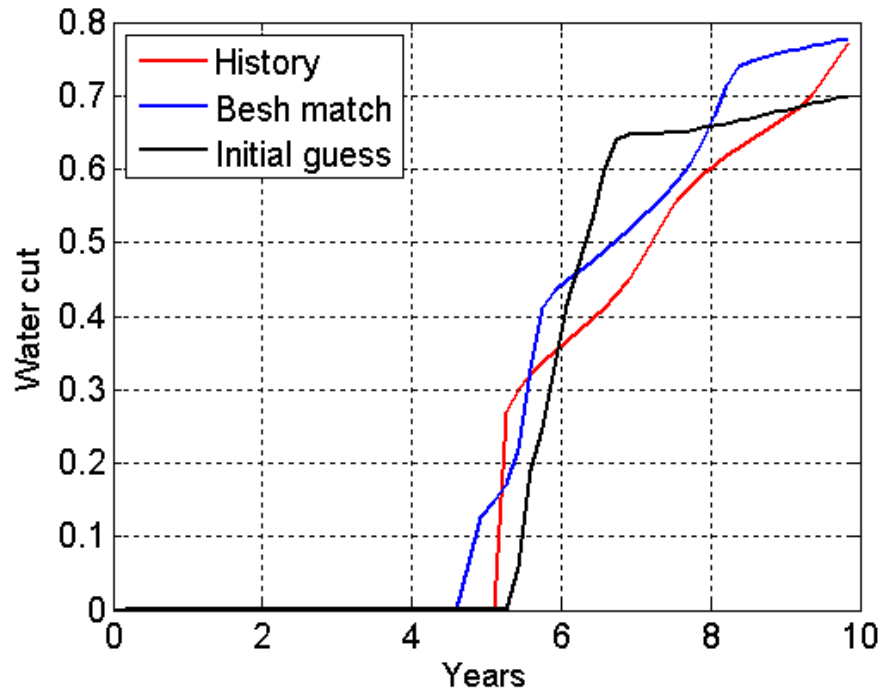


Figure 5.17: Water cut over ten years of production using GPSO. Observed production data is shown in red, water cut for initial guess model is shown in black, water cut associated with the best model is shown in blue

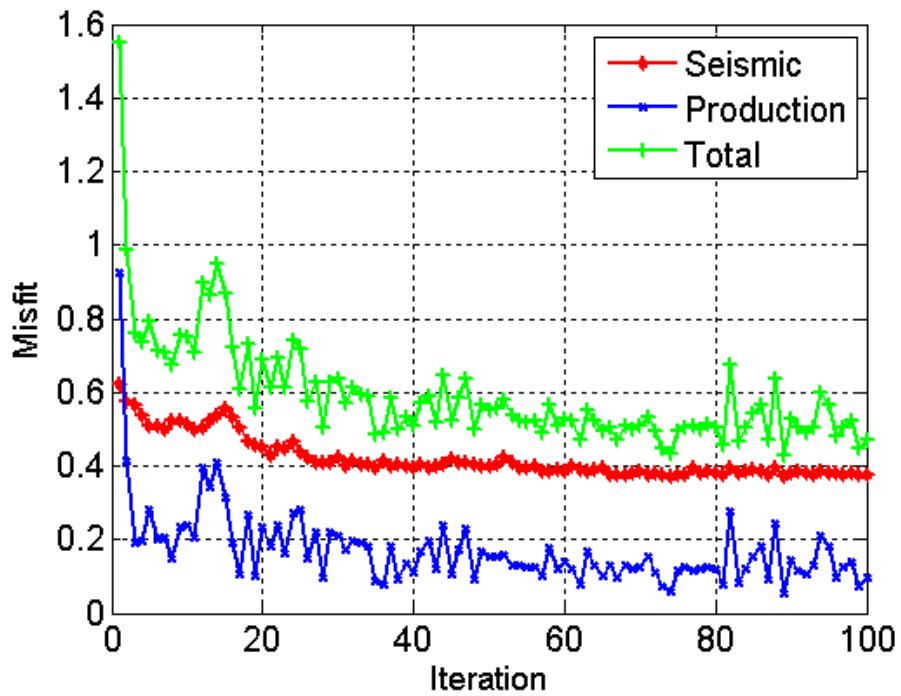


Figure 5.18: Behavior of median misfit with the increase in number of iterations using GPSO. Red, blue and green curves are median misfits for time-lapse seismic, production and total

History matching results obtained using GPSO are shown in Figures 5.15, 5.16 and 5.17 . The convergence behavior is very similar to that of CC-PSO. The best model has higher misfit as compared to best models of the CC-PSO and CP-PSO. There is an improvement in the production and seismic mismatch from the initial guess model to the best model, but the production and seismic responses of the best model are not as good as the responses of best models obtained using the CC-PSO and CP-PSO.

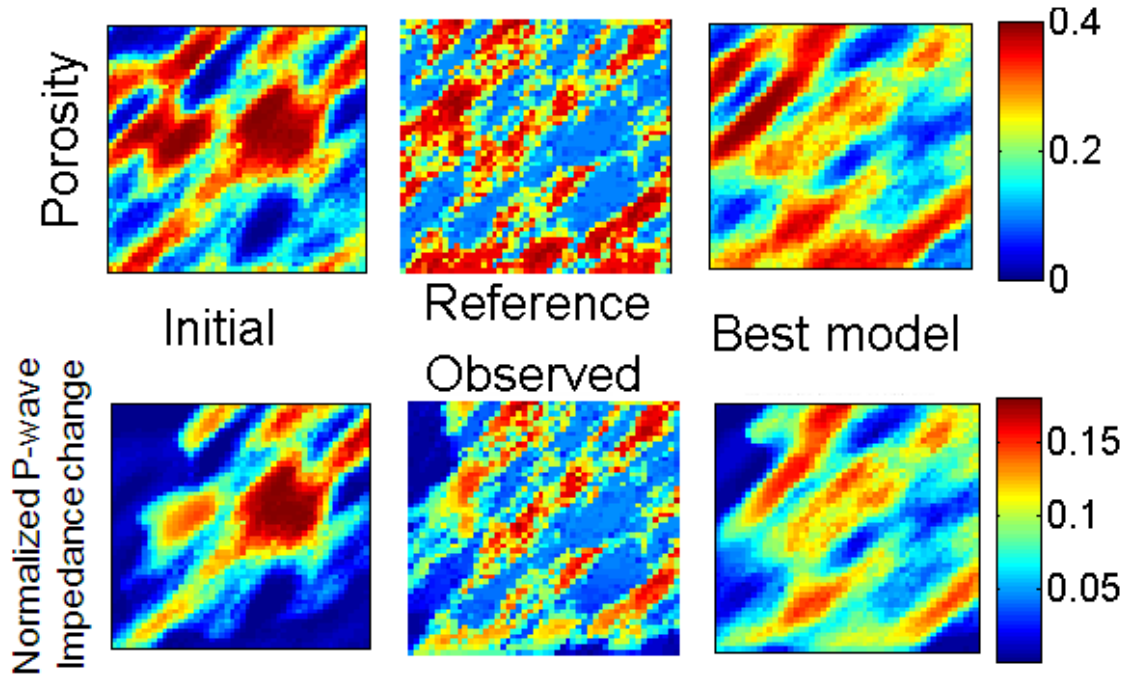


Figure 5.19: Best porosity model (top right) and associated time-lapse seismic response (bottom right) obtained using PP-PSO. Initial guess (left), Reference porosity model and observed time-lapse seismic data (middle) are shown for comparison

Figures 5.18, 5.19 and 5.20 show the history matching results obtained using PP-PSO. The best model provides a very good match with the observed production and time-lapse seismic data. The history match is better than the match obtained using the GPSO and comparable to the results of the CP-PSO. The convergence behavior of PP-PSO is shown in the Figure 5.20. The minimum misfit obtained is lower than the misfit obtained using CP-PSO, but higher than the misfits obtained using CC-PSO and GPSO.

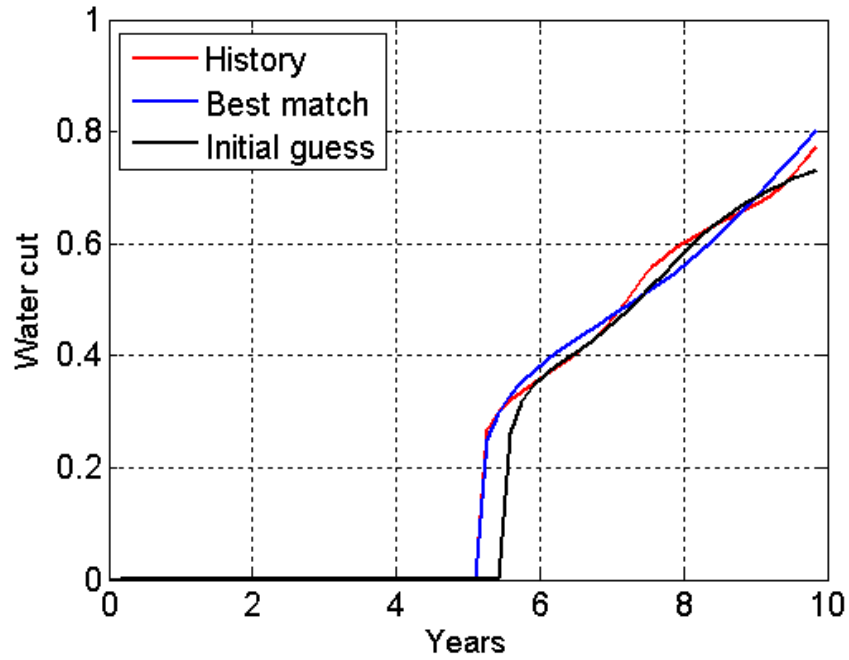


Figure 5.20: Water cut over ten years of production using PP-PSO. Observed production data is shown in red, water cut for initial guess model is shown in black, water cut associated with the best model is shown in blue

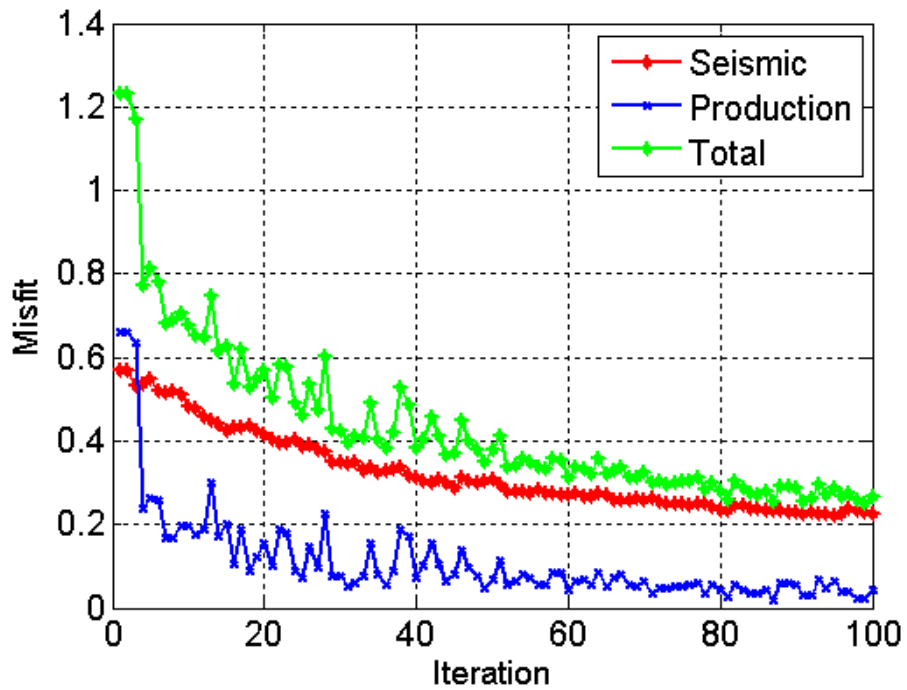


Figure 5.21: Behavior of median misfit with the increase in number of iterations using PP-PSO. Red, blue and green curves are median misfits for time-lapse seismic, production and total

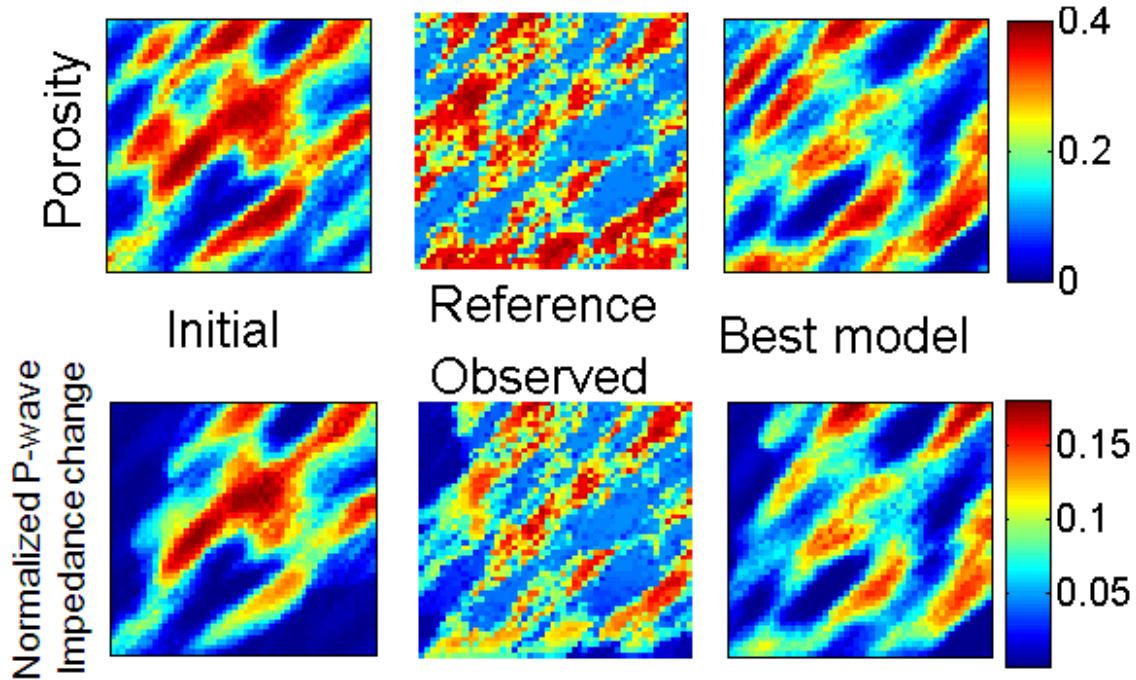


Figure 5.22: Best porosity model (top right) and associated time-lapse seismic response (bottom right) obtained using RR-PSO. Initial guess (left), Reference porosity model and observed time-lapse seismic data (middle) are shown for comparison

Figures 5.21 and 5.22 show the history matching results of RR-PSO. The simulated production and time-lapse seismic responses of the best model, obtained using RR-PSO provided a satisfactory history match to the observed production and time-lapse seismic data. The best model successfully captured features present in the reference model. The convergence behavior of RR-PSO is shown in the Figure 5.23. The rate of convergence for RR-PSO is highest among all of the PSO algorithms. The algorithm is converged in 30 iterations, whereas other particle swarm optimizers have converged in more than 50 iterations.

The performance of different particle swarm optimizers in terms of matching observed production data are shown in the Figure 5.25. The median of production responses associated with the reservoir models present in the swarm are compared for CC-PSO, CP-PSO, GPSO, PP-PSO and RR-PSO. It is clear that RR-PSO, CP-PSO and PP-PSO have performed better than CC-PSO and GPSO, since associated misfits are much lower. The rate of convergence of RR-PSO and CP-PSO ( $\Delta t < 1$ ) are also faster than CC-PSO, GPSO and PP-PSO.

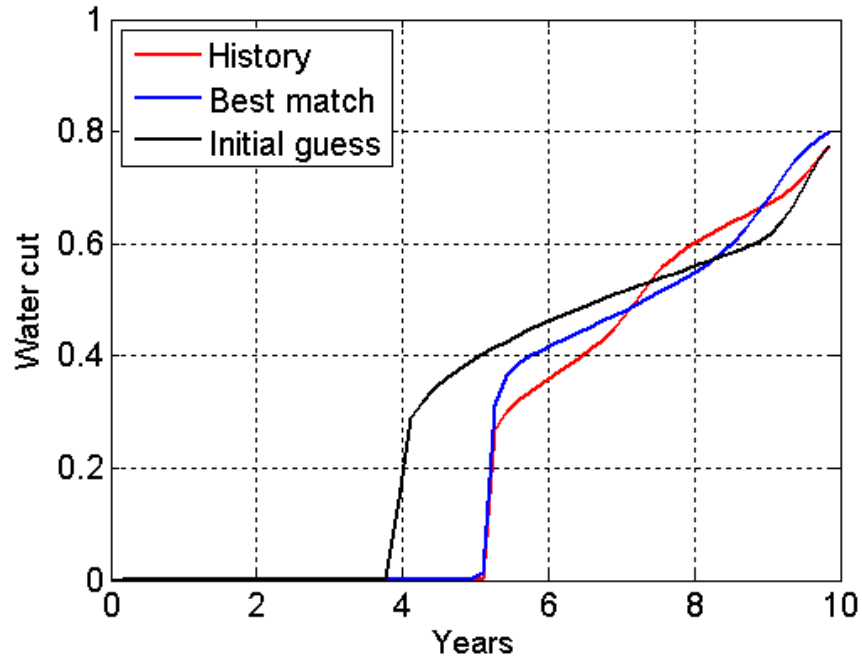


Figure 5.23: Water cut over ten years of production using RR-PSO. Observed production data is shown in red, water cut for initial guess model is shown in black, water cut associated with the best model is shown in blue

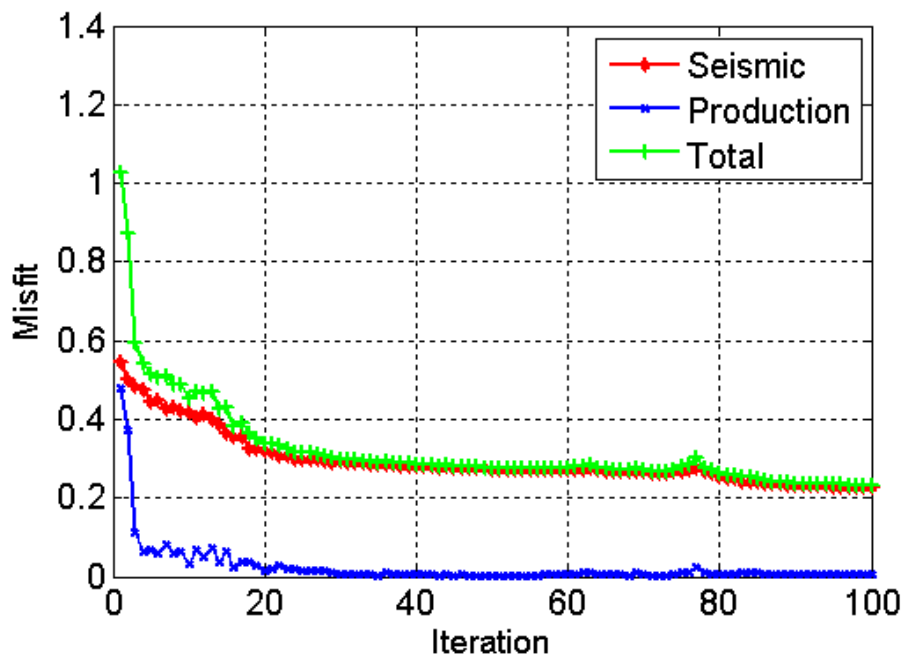


Figure 5.24: Behavior of median misfit with the increase in number of iterations using RR-PSO. Red, blue and green curves are median misfits for time-lapse seismic, production and total

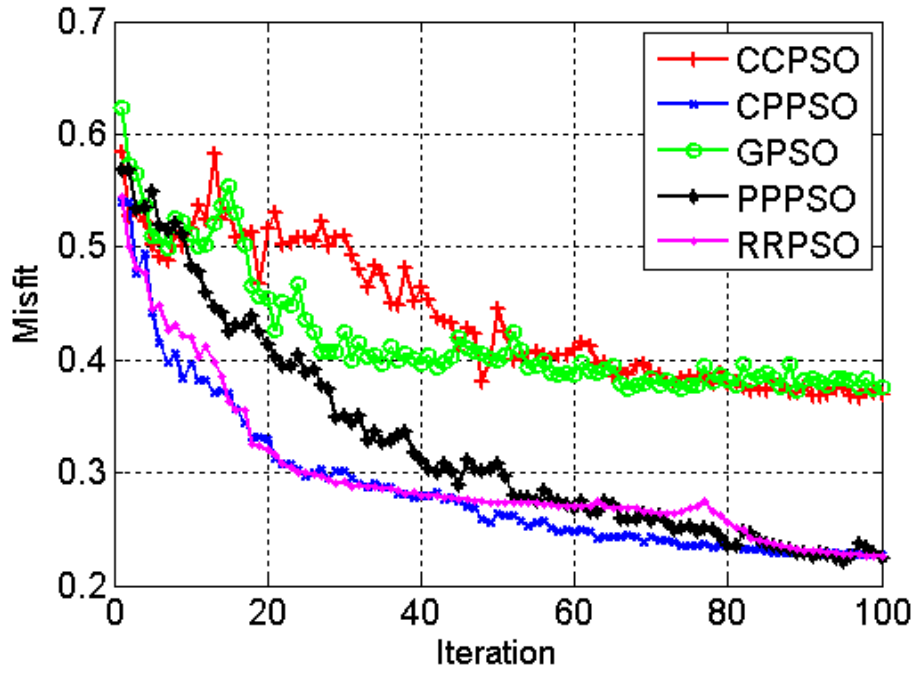


Figure 5.25: Behavior of time-lapse seismic misfit with the increase in number of iterations. Red, blue, green, black and magenta curves are responses of CC-PSO, CP-PSO, GPSO, PP-PSO and RR-PSO respectively

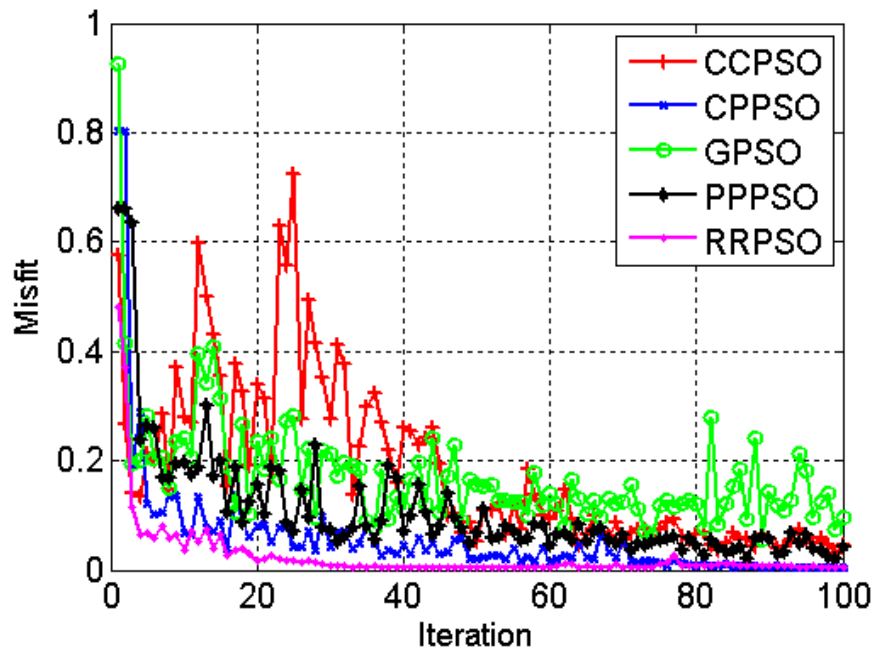


Figure 5.26: Behavior of production misfit with the increase in number of iterations. Red, blue, green, black and magenta curves are responses of CC-PSO, CP-PSO, GPSO, PP-PSO and RR-PSO respectively.

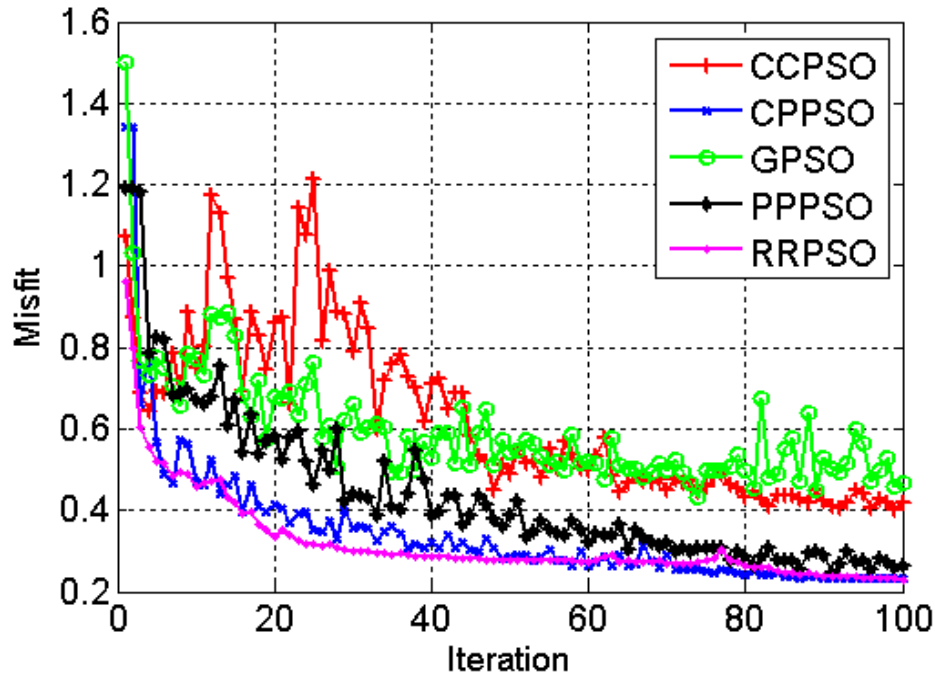


Figure 5.27: Behavior of total misfit with the increase in number of iterations. Red, blue, green, black and magenta curves are responses of CC-PSO, CP-PSO, GPSO, PP-PSO and RR-PSO respectively

Figures 5.24, 5.25 and 5.26 compare the performance of different particle swarm optimizers in terms of matching time-lapse seismic data, production data and total (sum of production and time-lapse seismic data) misfit respectively. RR-PSO, CP-PSO and PP-PSO have provided lower production, time-lapse seismic and total misfits as compared to CC-PSO and GPSO.

Overall RR-PSO, CP-PSO and PP-PSO have performed better (having lower misfit) in the history matching as compared to CC-PSO and GPSO. This fact is also supported by the comparison of best porosity model and reference porosity model for each particle swarm optimizer. Best porosity models (history matched models) obtained using RR-PSO, CP-PSO and PP-PSO are much closer to reference porosity model as compared to best porosity models obtained using CC-PSO and GPSO. Secondly, RR-PSO has performed best among RR-PSO, CP-PSO and PP-PSO, since it has the highest convergence rate. It is clear from the Figure 5.26 that RR-PSO has achieved lowest total misfit just after 20 iterations.

## 5.9 Model Sampling

All of the particle swarm optimizers have the capability to explore and thus provide the best model in the process of history matching. The exploration characteristics of the optimizers make it an efficient algorithm to obtain a number of models which fit the observed data within a specified tolerance. The misfits of reservoir models decrease with the increase in number of iterations and the swarm collapses to the global best. A number of history matched reservoir models can be selected after the iterations. These models provide a satisfactory match to the observed data within a specified tolerance. Now by the nature of particle swarm optimizers, some of these reservoir models may be different or may be identical. So it is necessary to select a number of reservoir models which are not identical and at the same time they match the observed data within a specified tolerance. We proposed to use multi-dimensional scaling in association with kernel k-medoid clustering to select the required number of history matched models. The method is already been discussed in the Sections 3.2.2 and 3.2.3. The selection of tolerance is an important step in the model sampling. It is selected based on the convergence behavior of particle swarm optimizer. The tolerance is the total misfit, selected between lowest and highest total misfit obtained during optimization. It is closer to the lowest total misfit as compared to highest total misfit. A very high value of tolerance can sample models having unsatisfactory history match. Similarly, a very low value of tolerance will provide similar history match models which are not different from each other. Both of the above scenarios are avoided, and the tolerance is selected such that there is a balance between successful history match and dissimilarity of models. We selected a tolerance of 0.5 based on the performance of CC-PSO and GPSO, since CC-PSO and GPSO have the highest total misfit (less than 0.5 but greater than total misfit obtained using CP-PSO, PP-PSO and RR-PSO). Next, reservoir models having total misfits less than 0.5 are selected. Multi-dimensional scaling (MDS) is performed on these reservoir models using euclidean distance. A plot of reservoir models after MDS in two dimensions are shown in Figure 5.27. As previously mentioned, the plot should only be inferred in the sense of closeness of two point (reservoir models) in the MDS space. If two points are close in the MDS space that means associated reservoir models are not much different. Similarly, points far apart from each other indicate that associated reservoir models are different.

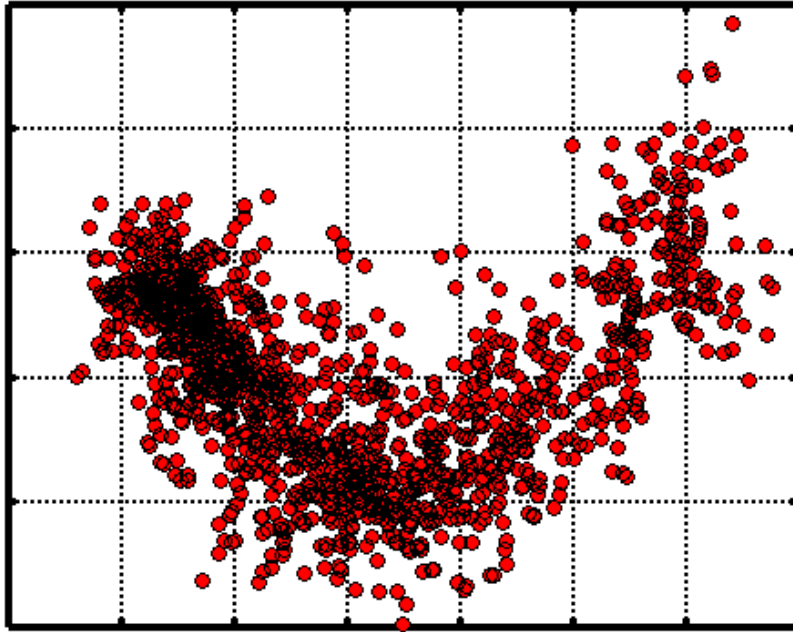


Figure 5.28: Reservoir models in a two dimensional MDS space. points on the plot represent reservoir models

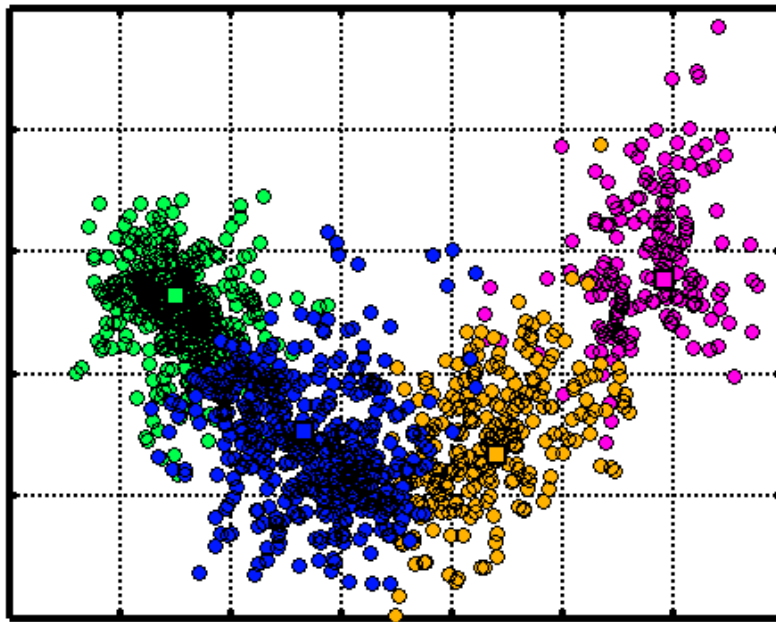


Figure 5.29: Four clusters and their centers in four different colors (green, blue, yellow and magenta) using kernel k-medoid clustering on reservoir models obtained using CP-PSO

Kernel k-mediod clustering is performed after MDS to obtain a representative number of history matched reservoir models which are different from each other. These representative reservoir models are cluster centres obtained after kernel k-mediod clustering. Figure 5.28 shows the reservoir models obtained using CP-PSO in MDS space and clustered using kernel k-mediod. Four colors are for four different clusters. Four cluster centres are obtained to represent four different reservoir models, and these reservoir models match the observed data within an acceptable tolerance. The number of representative reservoir models (number of clusters) has to be decided by the user and can vary based on the requirement.

In this study we have applied the proposed method on the results of different particle swarm optimizers to obtain four history matched reservoir models. The simulated production and time-lapse seismic responses of these different reservoir models match the observed production and time-lapse seismic data within a specified tolerance (0.5 in this case). The four reservoir models obtained using the results of CC-PSO are shown the Figure 5.29. The simulated time-lapse seismic responses of these four reservoir models are also shown. We observed that reservoir models are different, but their simulated time-lapse seismic responses provide an acceptable match to the observed time-lapse seismic response. The production responses of these four reservoir models are shown in the Figure 5.30. Again all of them provide an acceptable match to the observed production data.

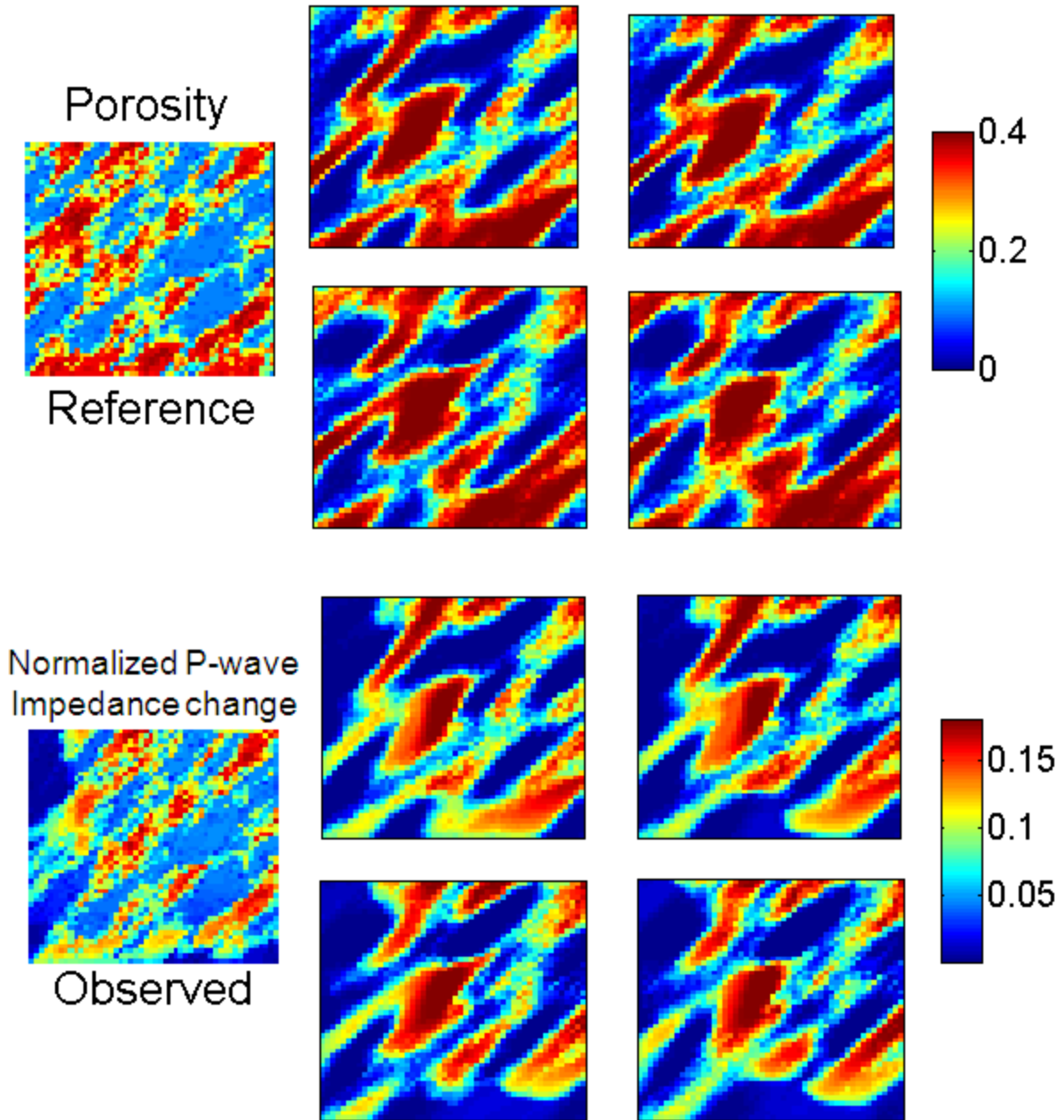


Figure 5.30: Four reservoir models obtained after kernel k-medoid clustering using CC-PSO on the Top. Time –lapse seismic response associated with reservoir models at the bottom. Reference porosity model and observed time-lapse seismic response on the left

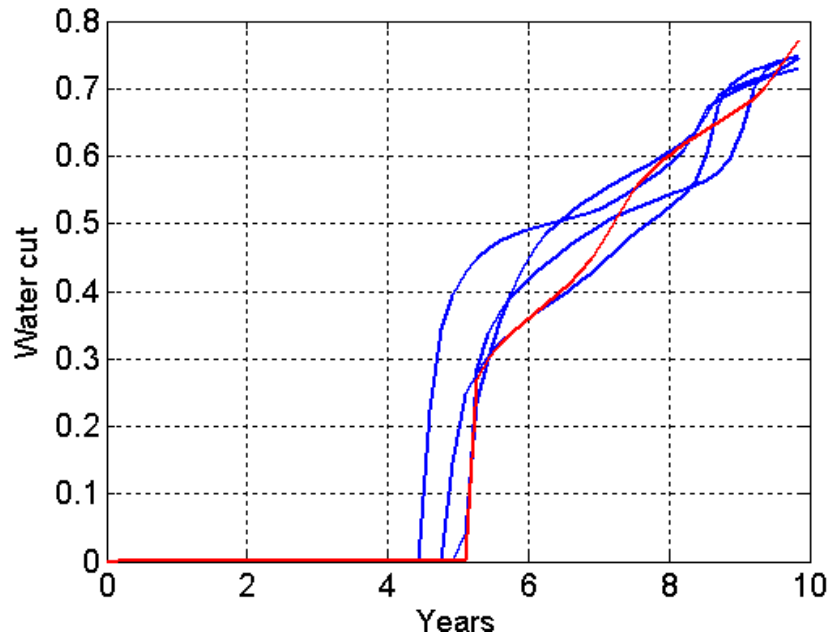


Figure 5.31: Blue curves represent production response of four reservoir models obtained after kernel k-medoid clustering using CC-PSO. Observed production data is shown in red curve

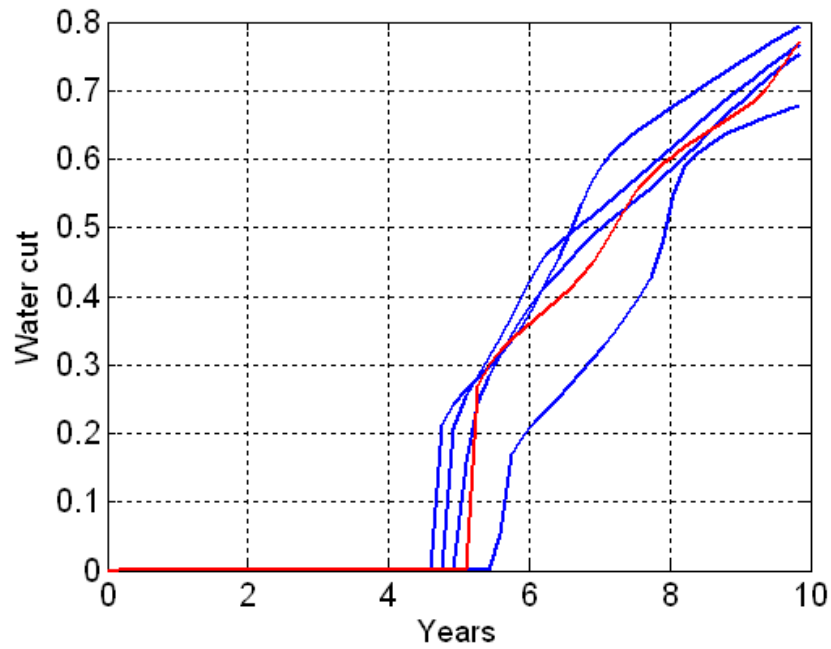


Figure 5.32: Blue curves represent production response of four reservoir models obtained after kernel k-medoid clustering using CP-PSO. Observed production data is shown in red curve

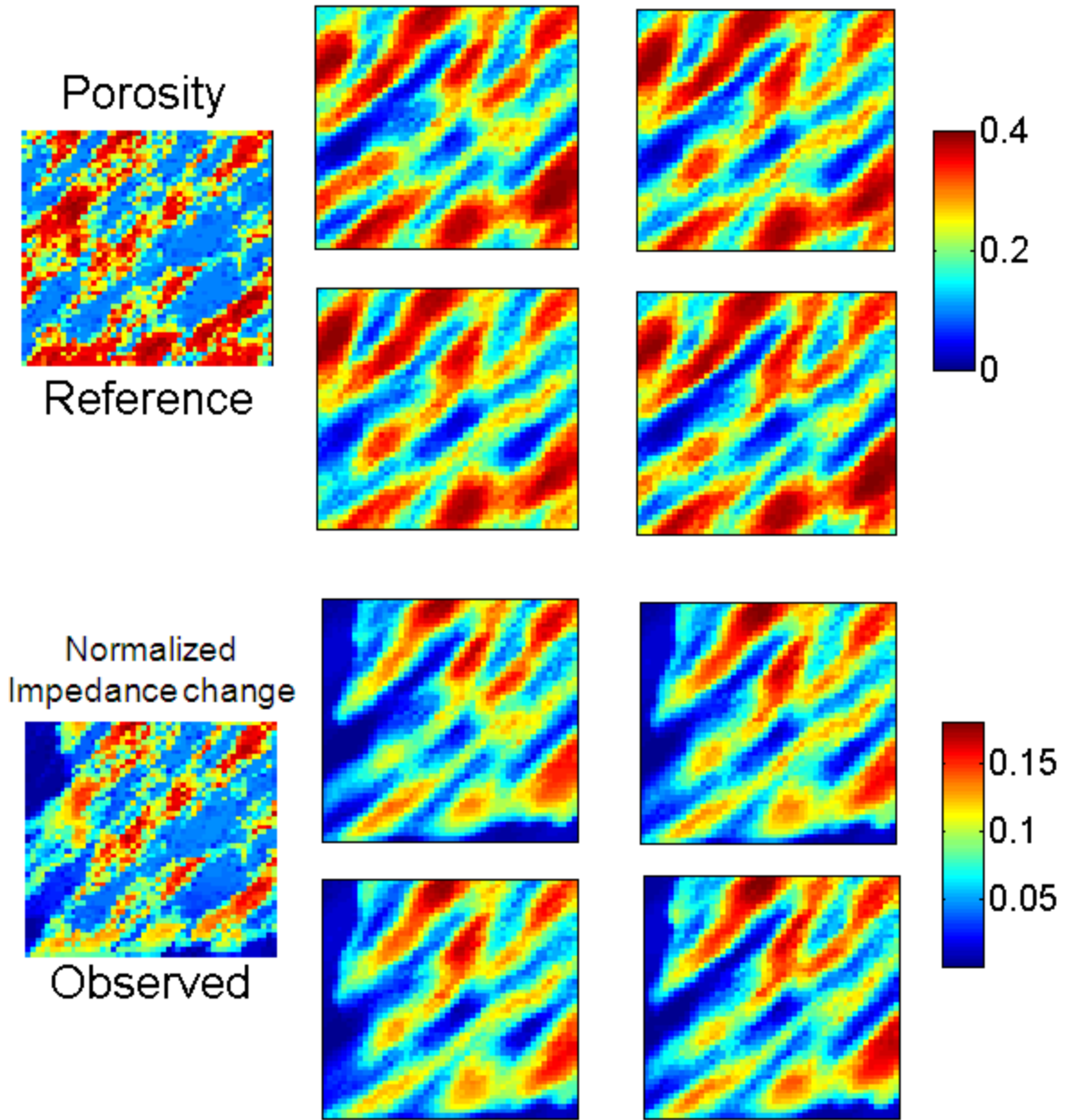


Figure 5.33: Four reservoir models obtained after kernel k-medoid clustering using CP-PSO on the Top. Time –lapse seismic response associated with reservoir models at the bottom. Reference porosity model and observed time-lapse seismic response on the left.

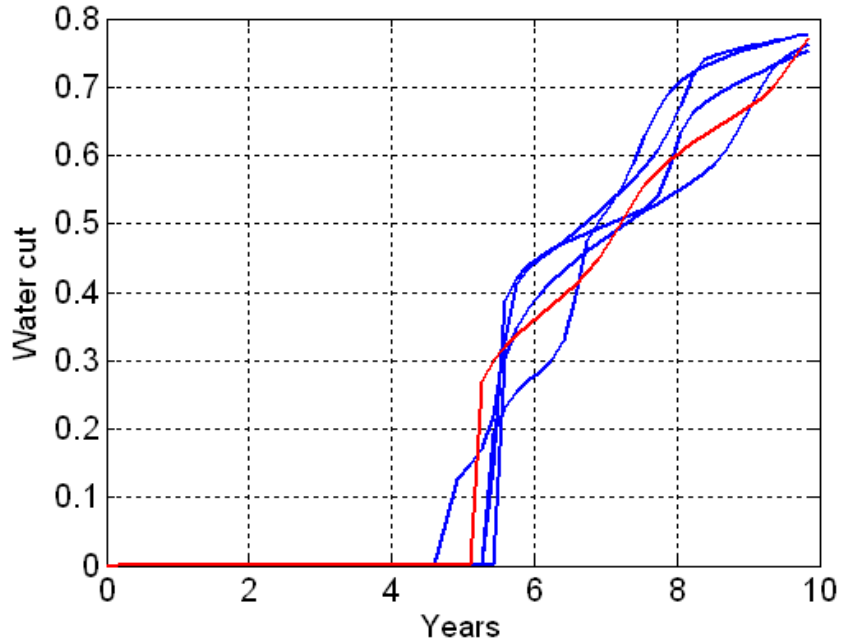


Figure 5.34: Blue curves represent production response of four reservoir models obtained after kernel k-medoid clustering using GPSO. Observed production data is shown in red curve

Figures 5.31 and 5.32 show the history matched models and associated production and time-lapse seismic response obtained using CP-PSO. These reservoir models are more successful in terms of capturing the medium porosities as compared to the models obtained using CC-PSO. The history matched models and associated production and time-lapse seismic responses obtained using GPSO are shown in Figures 5.33 and 5.34. The history matched models obtained using GPSO have also high and low porosities as observed in the history matched models obtained using CC-PSO, but the history matched models are different for CC-PSO and GPSO. Figures 5.35 and 5.36 show the history matched models and associated production and time-lapses seismic responses obtained using PP-PSO. Again the reservoir models are different from the models obtained using other particle swarm optimizers. Similarly, the results of RR-PSO are shown in Figures 5.37 and 5.38.

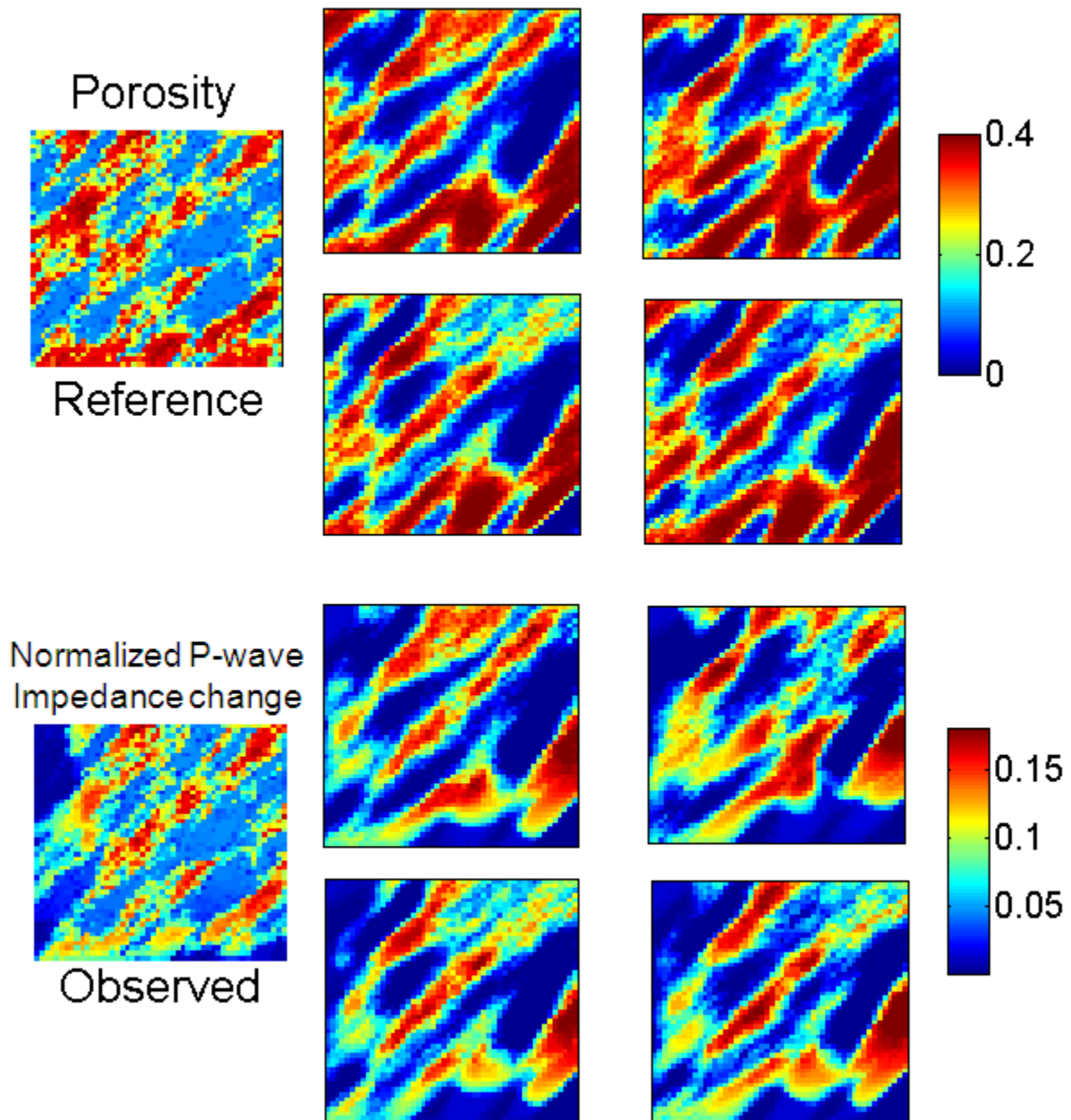


Figure 5.35: Four reservoir models obtained after kernel k-medoid clustering using GPSO on the Top. Time-lapse seismic response associated with reservoir models at the bottom. Reference porosity model and observed time-lapse seismic response on the left.

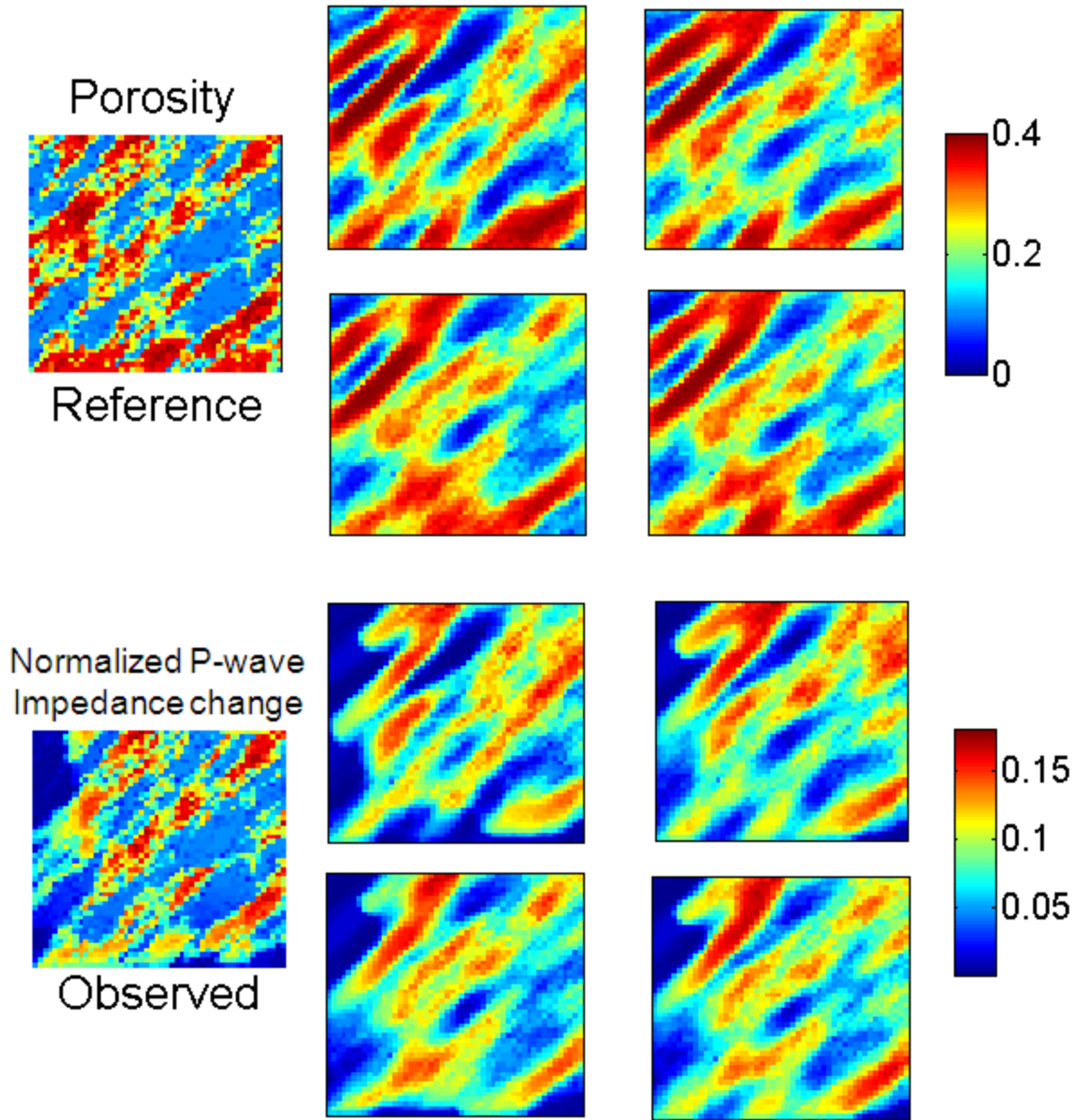


Figure 5.36: Four reservoir models obtained after kernel k-medoid clustering using PP-PSO on the Top. Time-lapse seismic response associated with reservoir models at the bottom. Reference porosity model and observed time-lapse seismic response on the left.

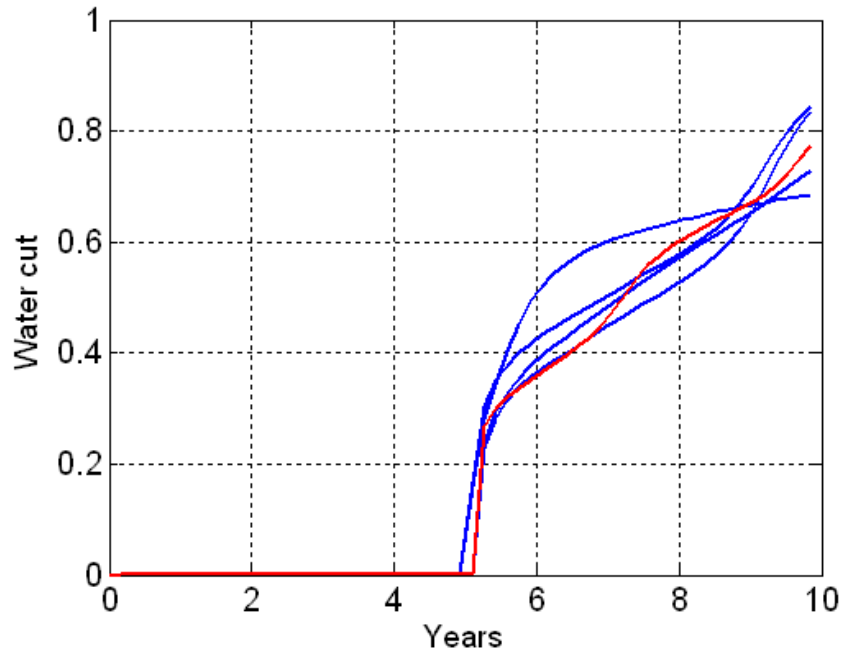


Figure 5.37: Blue curves represent production response of four reservoir models obtained after kernel k-medoid clustering using PP-PSO. Observed production data is shown in the red curve.

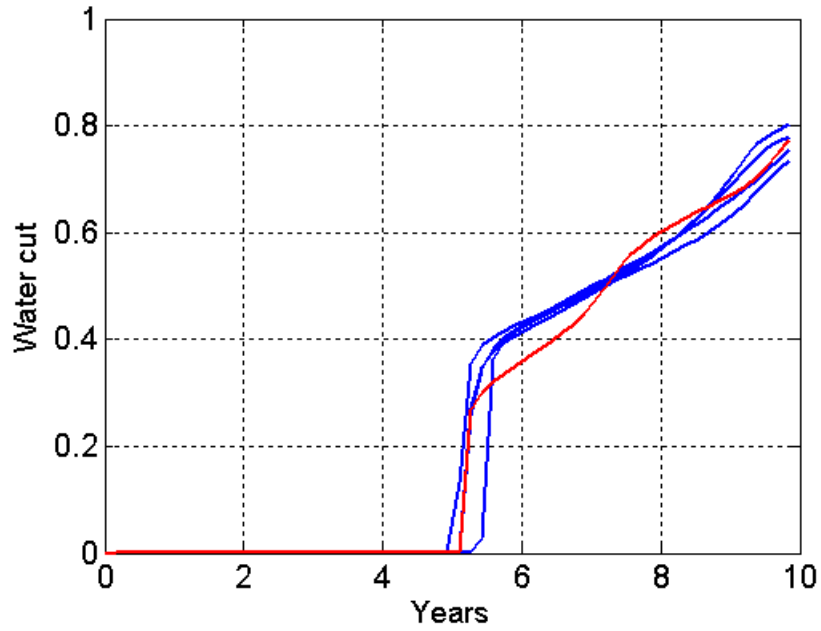


Figure 5.38: Blue curves represent production response of four reservoir models obtained after kernel k-medoid clustering using RR-PSO. Observed production data is shown in the red curve.

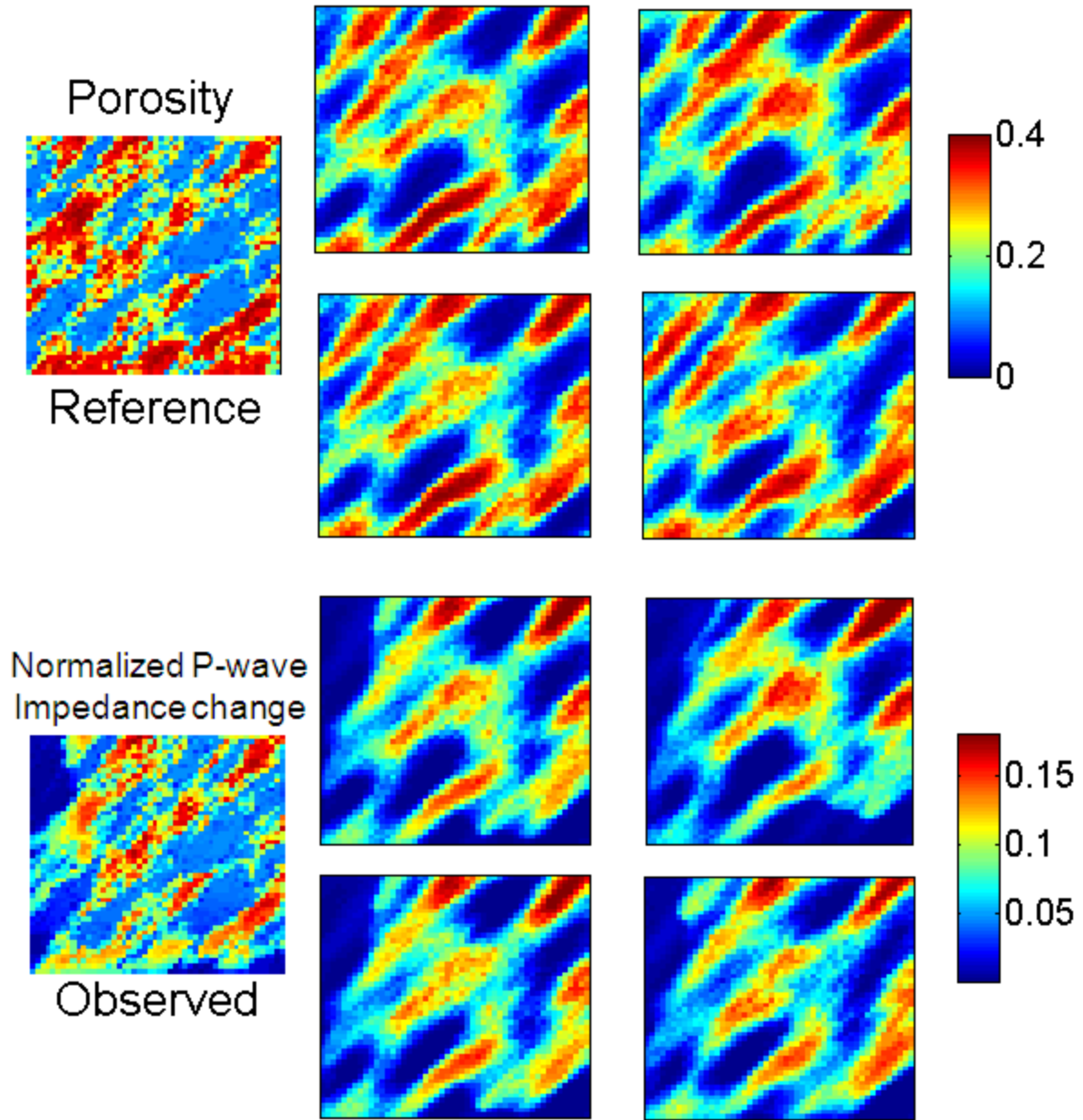


Figure 5.39: Four reservoir models obtained after kernel k-medoid clustering using RR-PSO on the Top. Time –lapse seismic response associated with reservoir models at the bottom. Reference porosity model and observed time-lapse seismic response on the left

## 5.10 Conclusions

We demonstrated that all of the members of PSO family performed well in joint inversion of production and time-lapse seismic data of a synthetic field. It is observed that RR-PSO, CP-PSO and PP-PSO have performed better than CC-PSO and GPSO in matching production and time-lapse seismic data. RR-PSO has performed best among all of the PSO family members in lowering the production misfit, time-lapse seismic misfit and total misfit. It also has the highest convergence rate as compared to all of the other PSO family members. Thus, the most important outcome of this study is that RR-PSO has the potential to provide good results for joint inversion of production and time-lapse seismic data of a field. It is shown that all of the members of PSO family can be used in combination to obtain sets of history matched models. The history matched models obtained using members of PSO family are different from each other. We also successfully applied principal component analysis to reduce the model space, as well as honoring geology during the joint inversion process. It is shown that, for each PSO family member a set of different history matched models can be obtained using multi-dimensional scaling and kernel k-medoid clustering. In the next chapter we will use the PSO family members for joint inversion of production and time-lapse seismic data of the Norne field.

# Chapter 6

## **JOINT INVERSION OF PRODUCTION AND TIME-LAPSE SEISMIC DATA OF NORNE FIELD**

### **6.1 Introduction**

It is shown in the previous chapters that porosity model is not the only sensitive parameters in the joint inversion. In the first chapter, we observed that rock physics model and relative permeability are more important parameters than porosity for joint inversion of production and time-lapse seismic data of the Norne field. In the second chapter, it is established that coordination number, clay content and fluid mixing have the most impact on modeling the time-lapse seismic response of Norne field. Based on the results of these chapters, we found that coordination number, clay content, porosity model, relative permeability and fluid mixing should be varied in the joint inversion of production and time-lapse seismic data of Norne field. We also showed that particle swarm optimizers in combination with principal component analysis (PCA) provided promising results in joint inversion of production and time-lapse seismic data of a

synthetic field. In this chapter, we apply the results of previous chapters by varying sensitive parameters and using particle swarm optimizers in combination with PCA for the joint inversion of production and time-lapse seismic data of the Norne field.

## **6.2 Joint Inversion Procedure**

Joint inversion of production and time-lapse seismic data for Norne field consists of several components. It involves the definition of production and time-lapse seismic data to be matched, selection of parameters and their ranges for variations in the joint inversion loop, selection of an appropriate number of PCA components, selection of particle swarm optimizers and definition of an objective function.

The goal of the history matching process is to perturb the sensitive parameters identified in the previous chapters. These parameters are porosity, relative permeability curve, coordination number, clay content, fluid mixing and pore compressibility. As discussed in Chapter 5, our workflow uses particle swarm optimizers in combination with principal component analysis. We perturb the selected parameters such that the simulated responses of these parameters provide a satisfactory match with the observed production and time-lapse seismic data. At the end of the joint inversion, we obtain a set of parameters that when used in the forward model give an acceptable match with the observed production and time-lapse seismic data of the Norne field.

### **6.2.1 Production and Time-lapse Seismic Data**

The production in the segment E of Norne field started in 1997 from well E-3H. Two more producers E-2H and E-3AH are added later. Water injectors F1-H and F-2H are added during the course of time to increase the hydrocarbon production from the segment E. The historical production data of producer wells E-3H, E-2H and E-3AH are shown in figures 6.10, 6.20, 6.30. The historical production data include oil, water and gas production rates from each well. The goal of joint inversion is to match the oil, gas and water production rates and bottom hole pressure (BHP) from each producer present in the segment E.

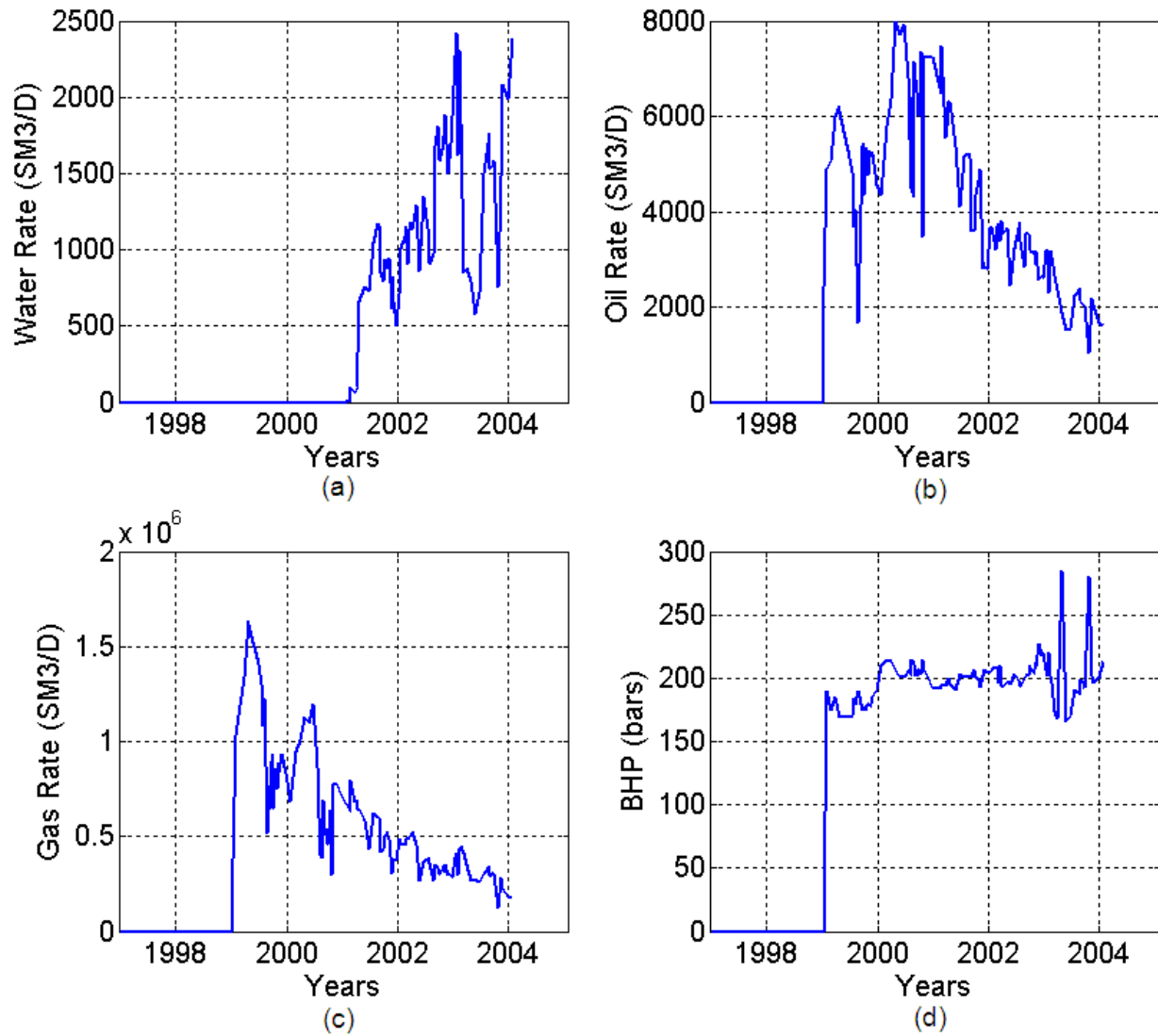


Figure 6.1: Observed production data in the well E-2H from 1997 to 2004 (a) Observed water rate in the well E-2H from 1997 to 2004 (b) Observed oil rate in the well E-2H from 1997 to 2004 (c) Observed gas rate in the well E-2H from 1997 to 2004 (d) Observed bottom hole pressure in the well E-2H from 1997 to 2004

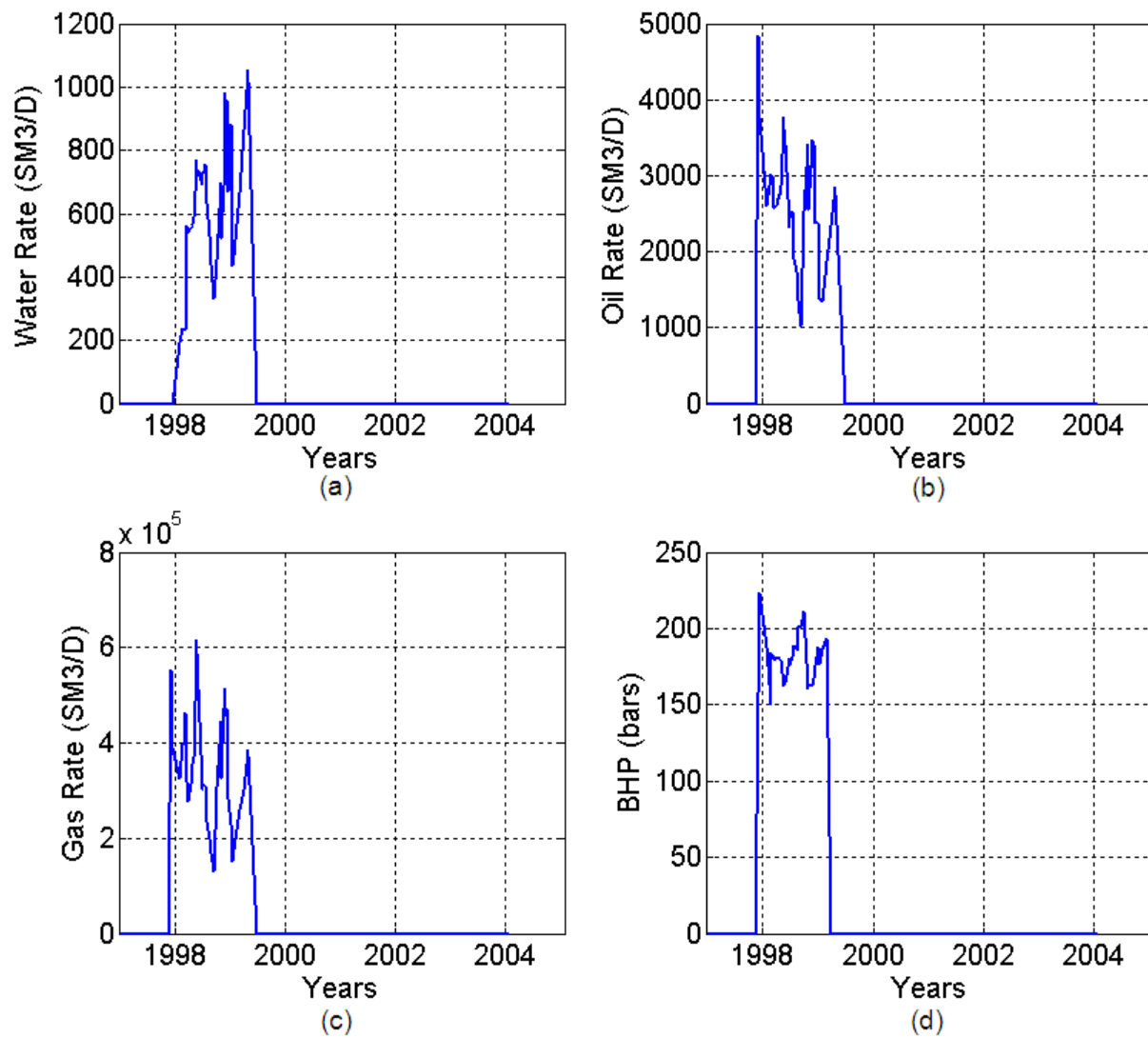


Figure 6.2: Observed production data in the well E-3H from 1997 to 2004 (a) Observed water rate in the well E-3H from 1997 to 2004 (b) Observed oil rate in the well E-3H from 1997 to 2004 (c) Observed gas rate in the well E-3H from 1997 to 2004 (d) Observed bottom hole pressure in the well E-3H from 1997 to 2004

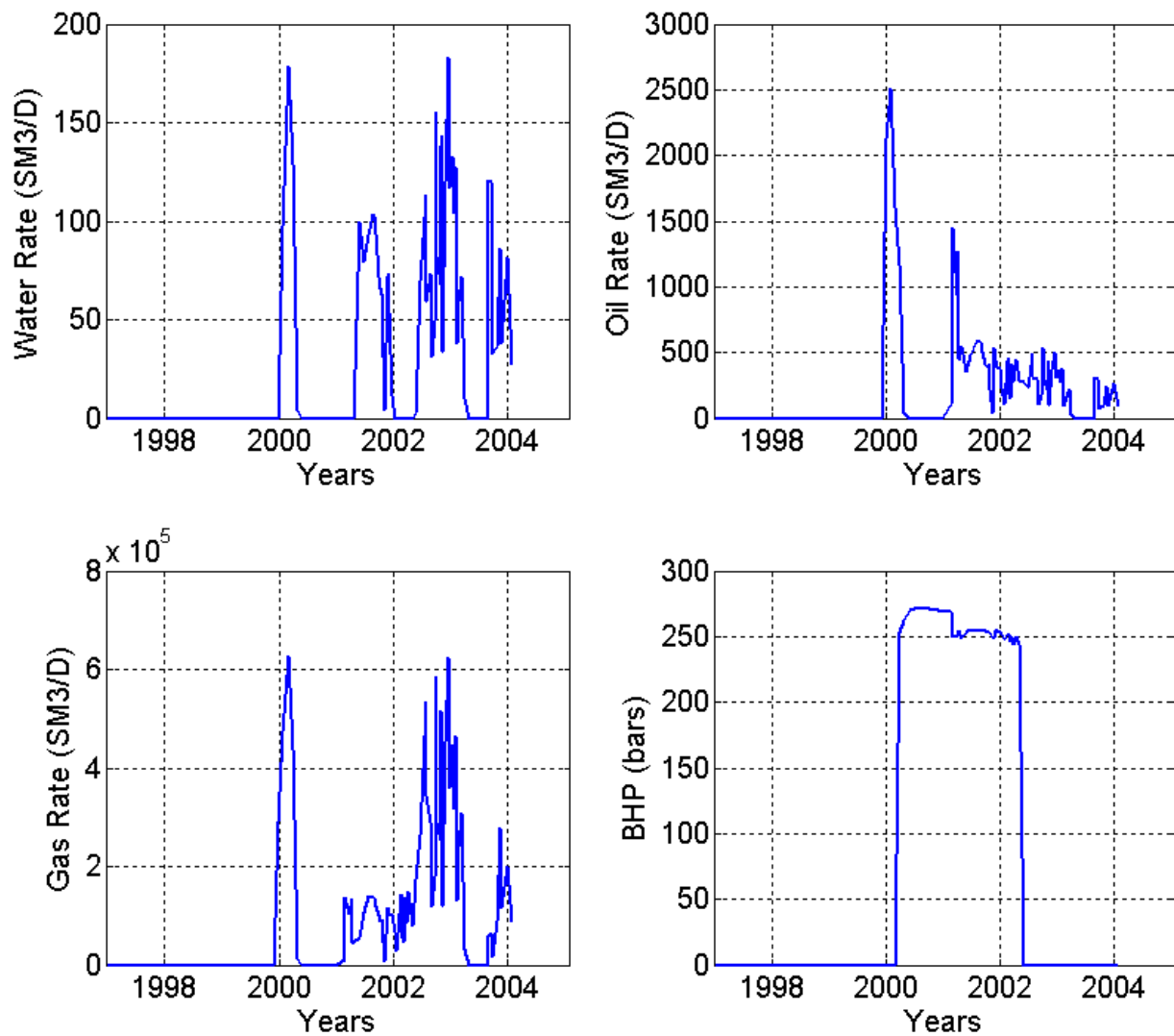


Figure 6.3: Observed production data in the well E-3AH from 1997 to 2004 (a) Observed water rate in the well E-3AH from 1997 to 2004 (b) Observed oil rate in the well E-3AH from 1997 to 2004 (c) Observed gas rate in the well E-3AH from 1997 to 2004 (d) Observed bottom hole pressure in the well E-3AH from 1997 to 2004

The base line 3D seismic survey of Norne field is acquired in 2001 and repeated 3D time-lapse survey is acquired in 2004. The goal of acquiring time-lapse seismic survey in the Norne field was to approximate the fluid distribution in the reservoir with time for better reservoir management. Water was continuously injected in the Norne reservoir; at the same time oil and gas were being produced. During this process oil and gas was being replaced by water in the reservoir and reservoir pressure is increased.

Time-lapse seismic data of Norne field consist of 3D seismic full stack surveys acquired in 2001 and 2004. 3D seismic survey acquired in 2001 is the base line survey. The repeated survey was acquired in 2004 to track the fluid saturation change inside the reservoir due to water injection. Figures 6.40 and 6.50 show the seismic amplitude for inline 1023 at 2001 and 2004 respectively. The dominant frequency and wavelength of the seismic surveys are at 30 Hz and 80 m respectively. These seismic surveys are corrected for the time shifts.

A post stack seismic inversion of seismic surveys is performed using standard software Hampson-Russell (Copyright 2010 CGG) to obtain P-wave acoustic impedance at 2001 and 2004. The data used for inversion is well logs of nine wells having sonic data and three horizons (top, bottom and intermediate). Based on the horizons, wells are correlated to improve the correlation between events on the synthetic traces and events on the seismic data (Figure 6.6). A wavelet is extracted using all the wells, and it is fine tuned to improve the correlation for each well. Next an initial model for P-wave impedance is obtained and this model is used for the inversion of 3D seismic survey. The procedure mentioned above is applied in the software suite Hampson-Russell to obtain the P-wave impedance in time at 2001 and 2004 (Figures 6.70 and 6.80). P-wave impedance in time at 2001 and 2004 are converted to P-wave impedance in depth at 2001 and 2004 respectively by using interval velocity cube (provided by Statoil) in the software suite Hampson-Russell (Figures 6.90 and 6.10).

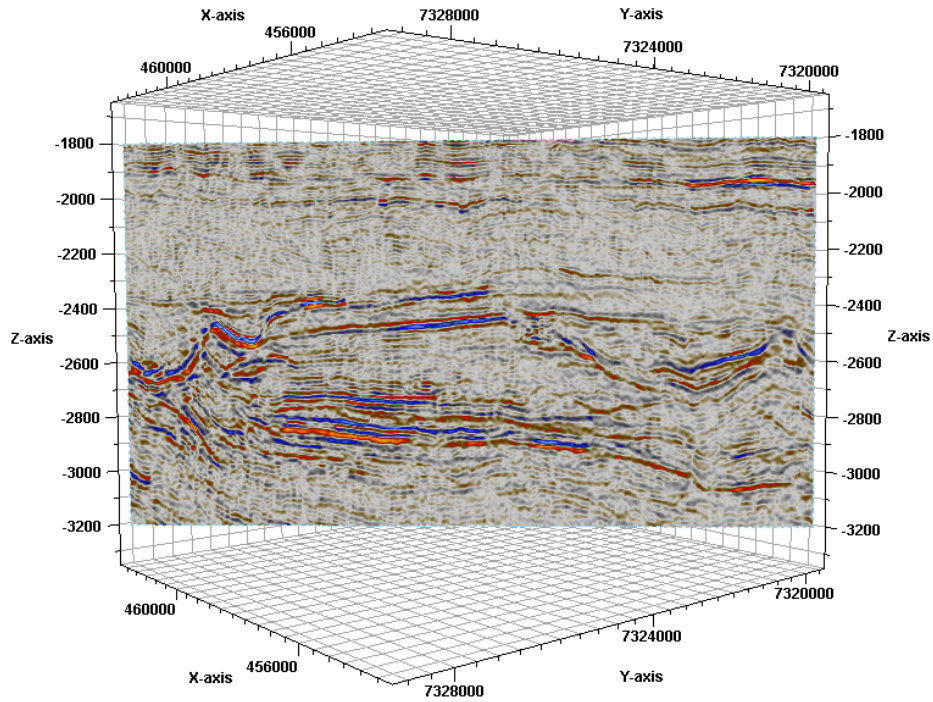


Figure 6.4: 3D seismic survey acquired in 2001 (base line survey, provided by Statoil). Seismic amplitude at inline 1023 (generated using PETREL).

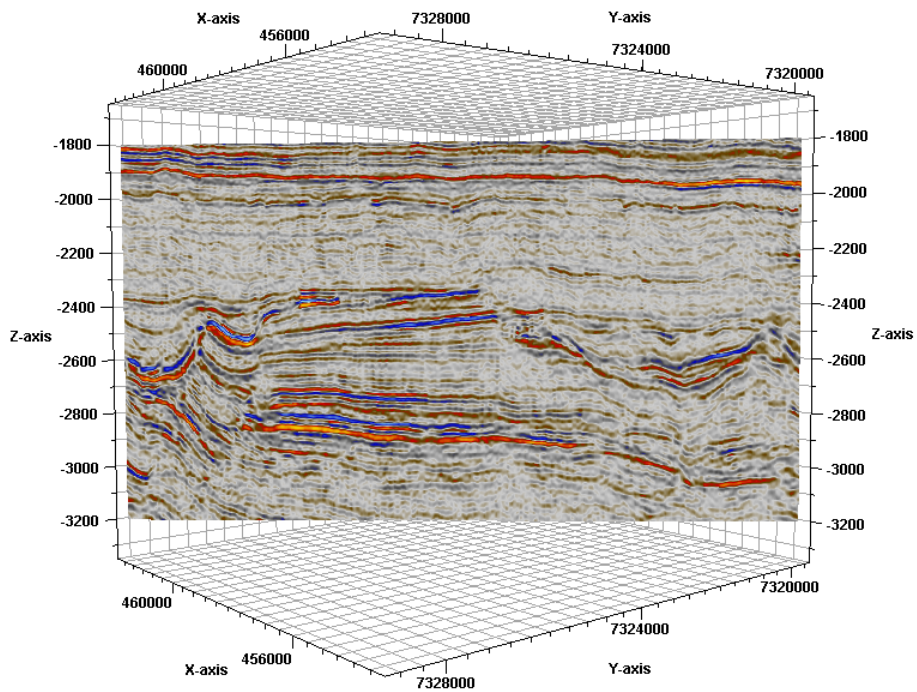


Figure 6.5: 3D seismic survey acquired in 2004 (provided by Statoil). Seismic amplitude at inline 1023 (generated using PETREL).

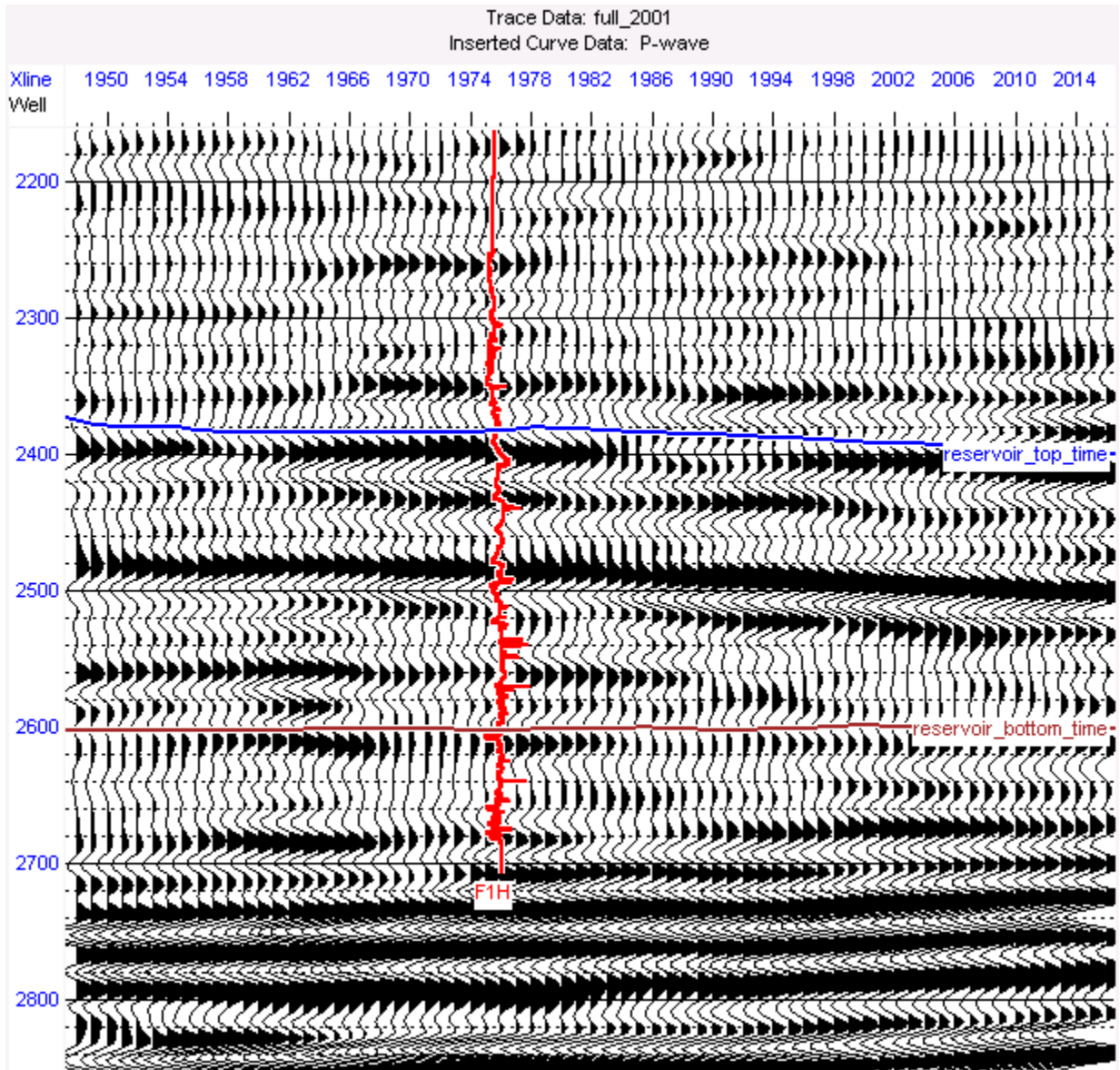


Figure 6.6: Seismic cross section showing well F1-H, reservoir top and bottom horizon used for the acoustic impedance inversion in Hampson-Russell.

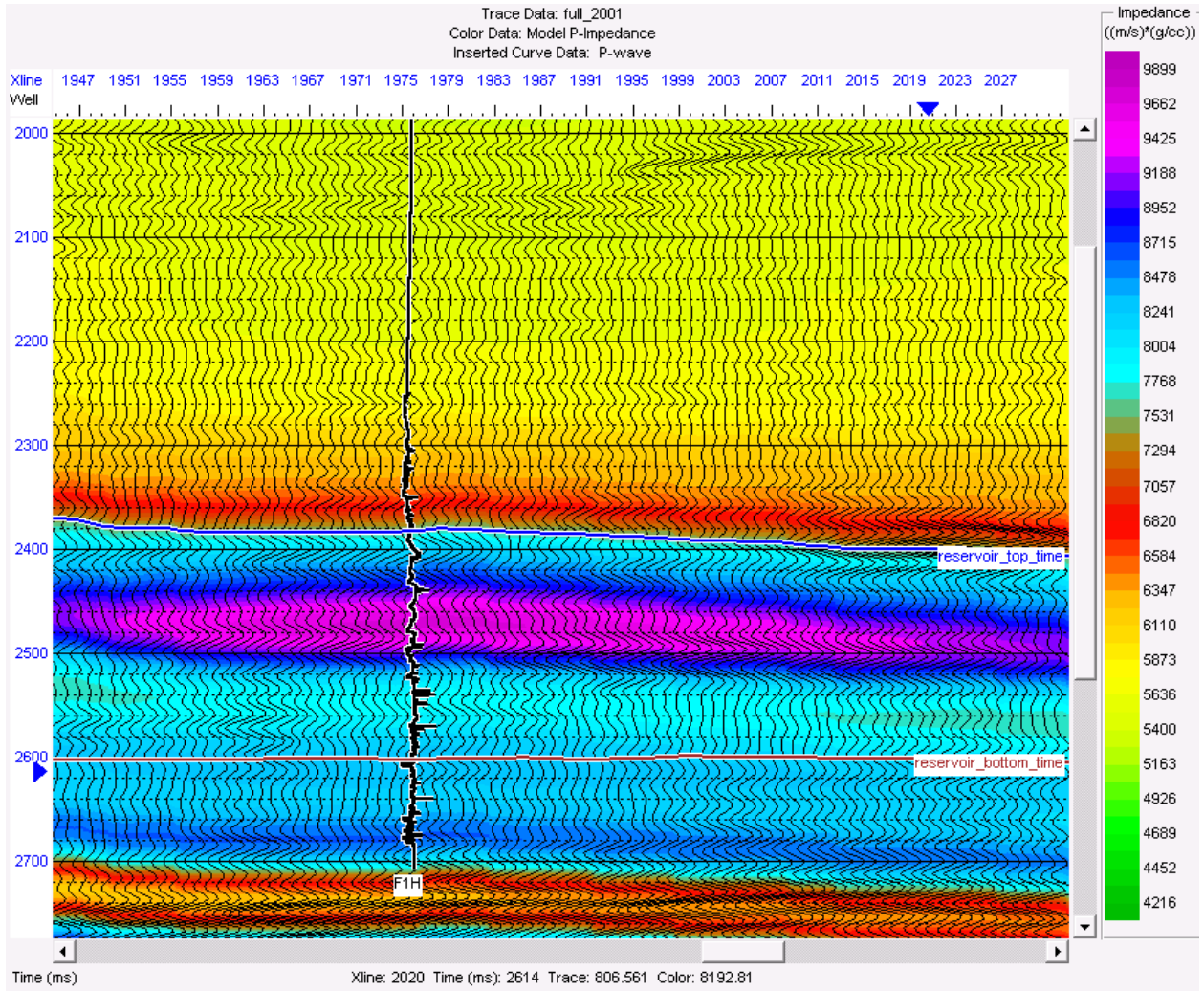


Figure 6.7: Cross section of P-wave seismic impedance in time, obtained after the inversion of 3D seismic survey acquired in 2001 using Hampson-Russell.

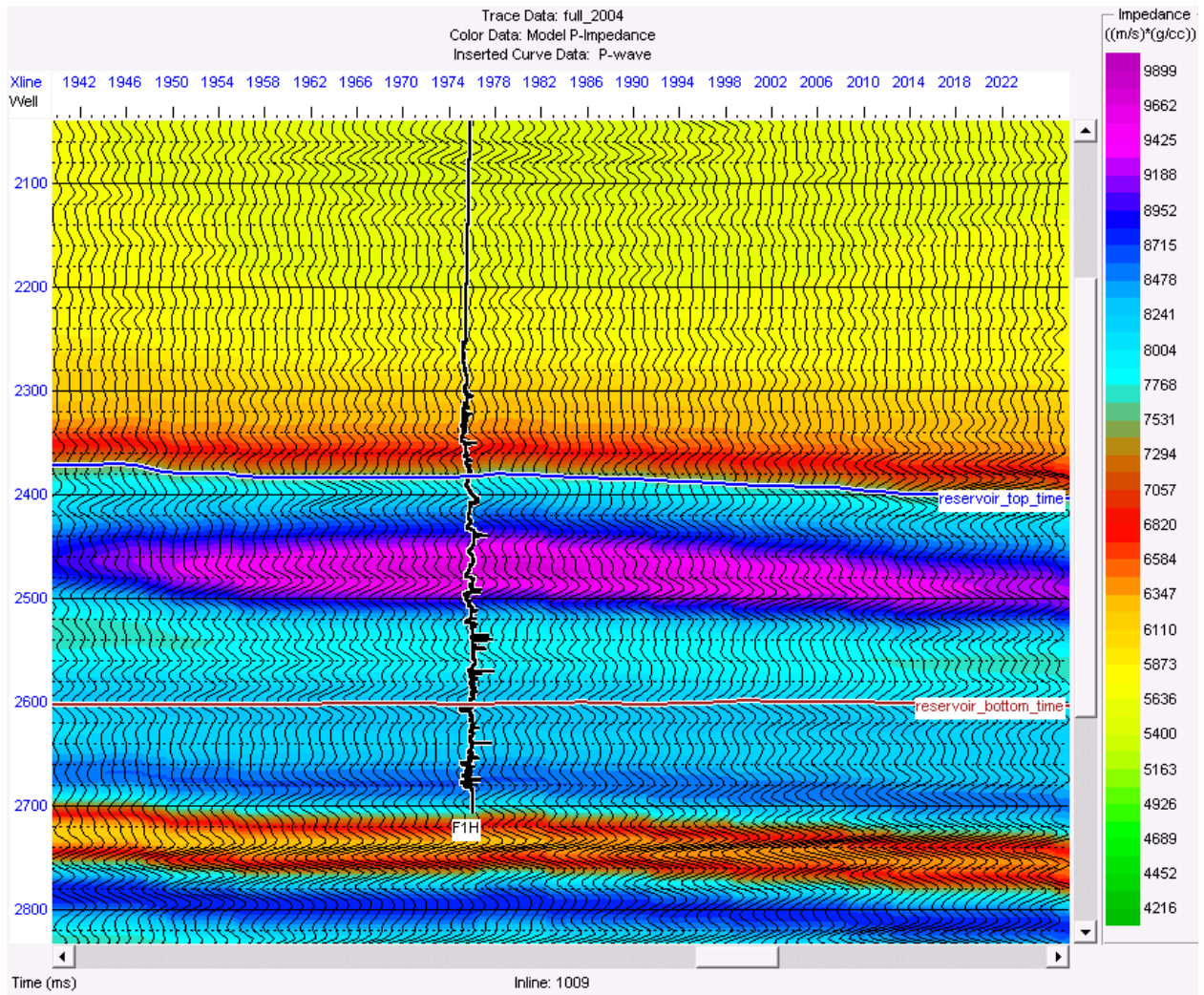


Figure 6.8: Cross section of P-wave seismic impedance in time, obtained after the inversion of 3D seismic survey acquired in 2004 using Hampson-Russell.

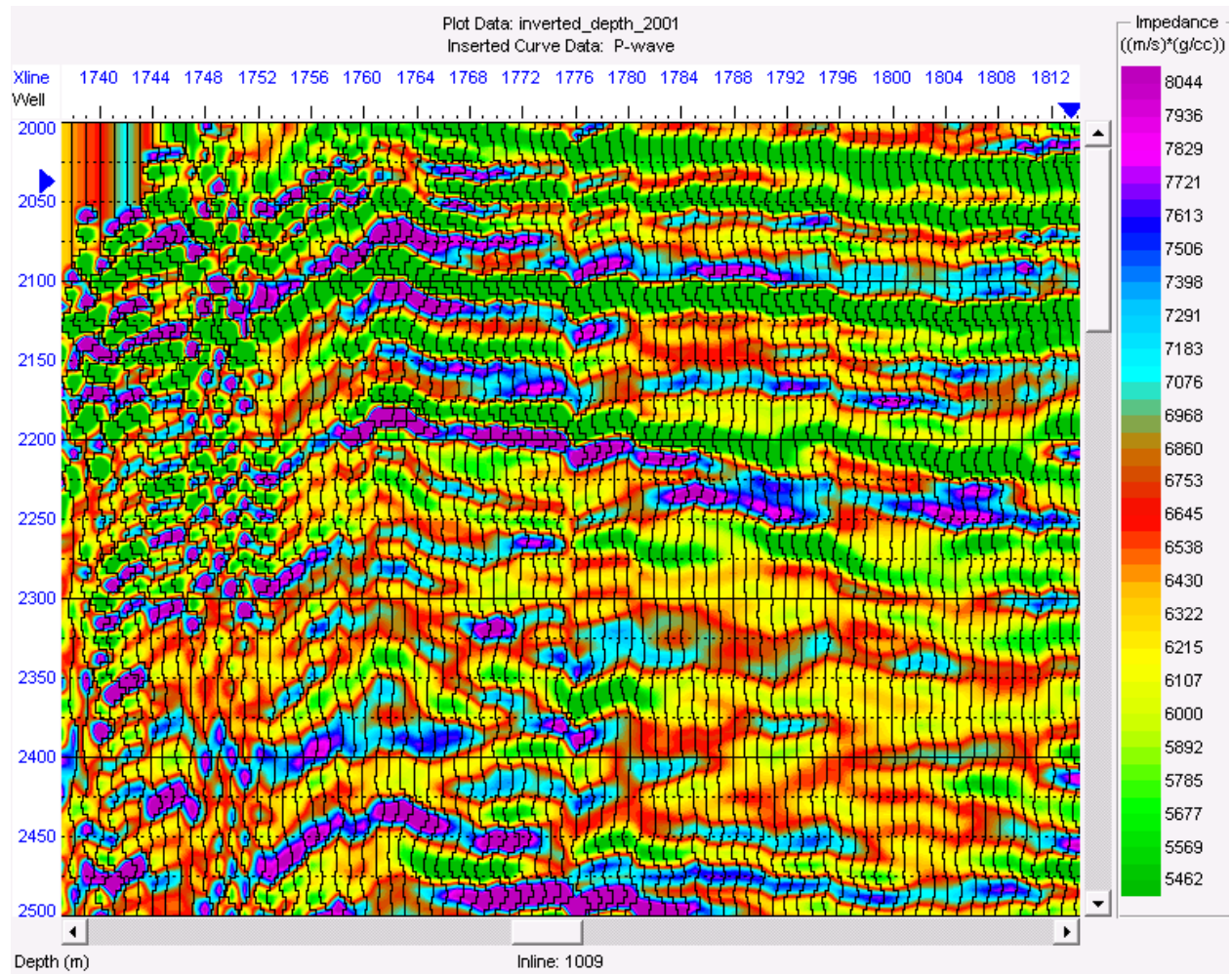


Figure 6.9: Cross section of P-wave seismic impedance in depth at 2001, obtained after depth conversion of P-wave seismic impedance in time at 2001 using Hampson-Russell

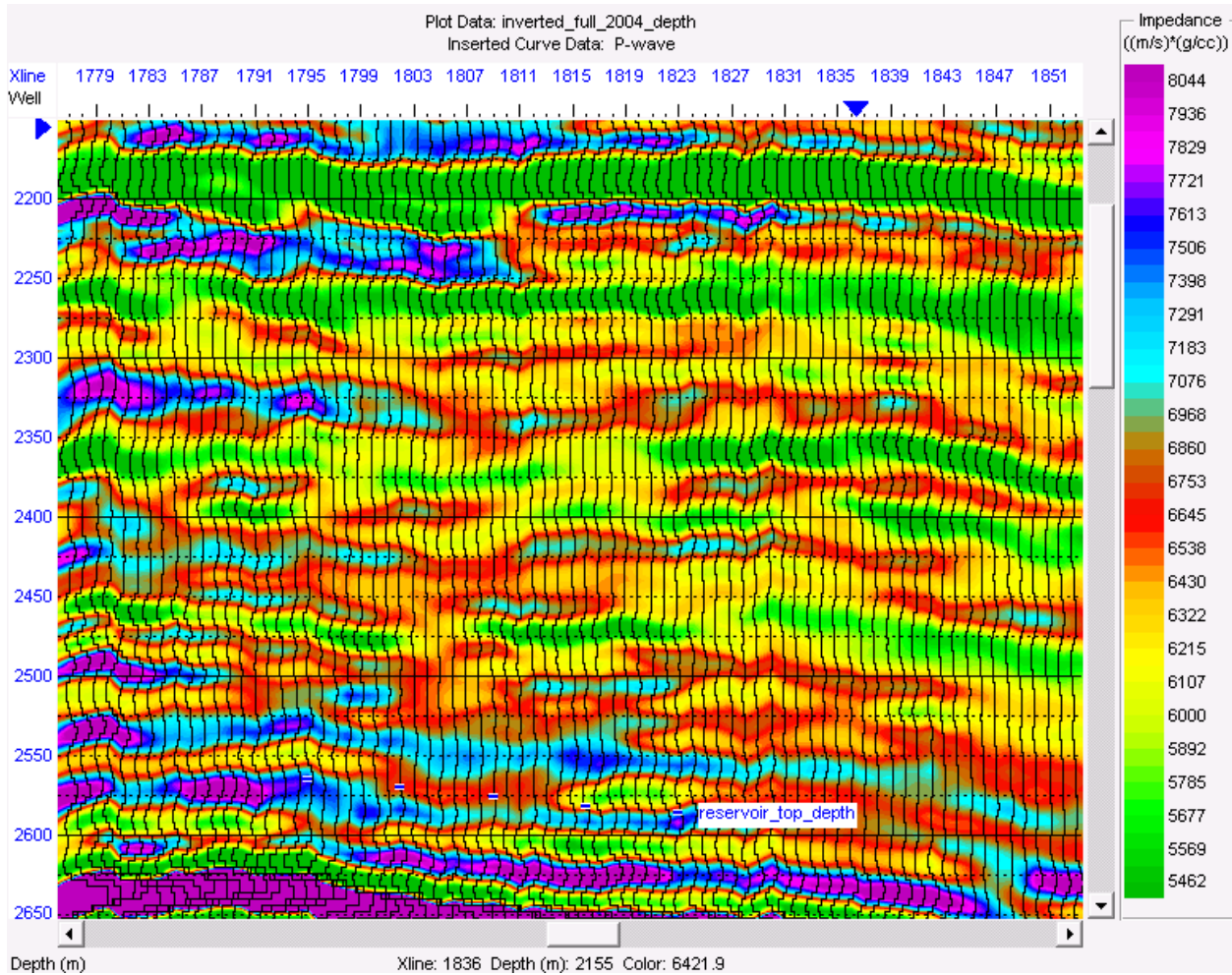


Figure 6.10: Cross section of P-wave seismic impedance in depth at 2004, obtained after depth conversion of P-wave seismic impedance in time at 2004 using Hampson-Russell

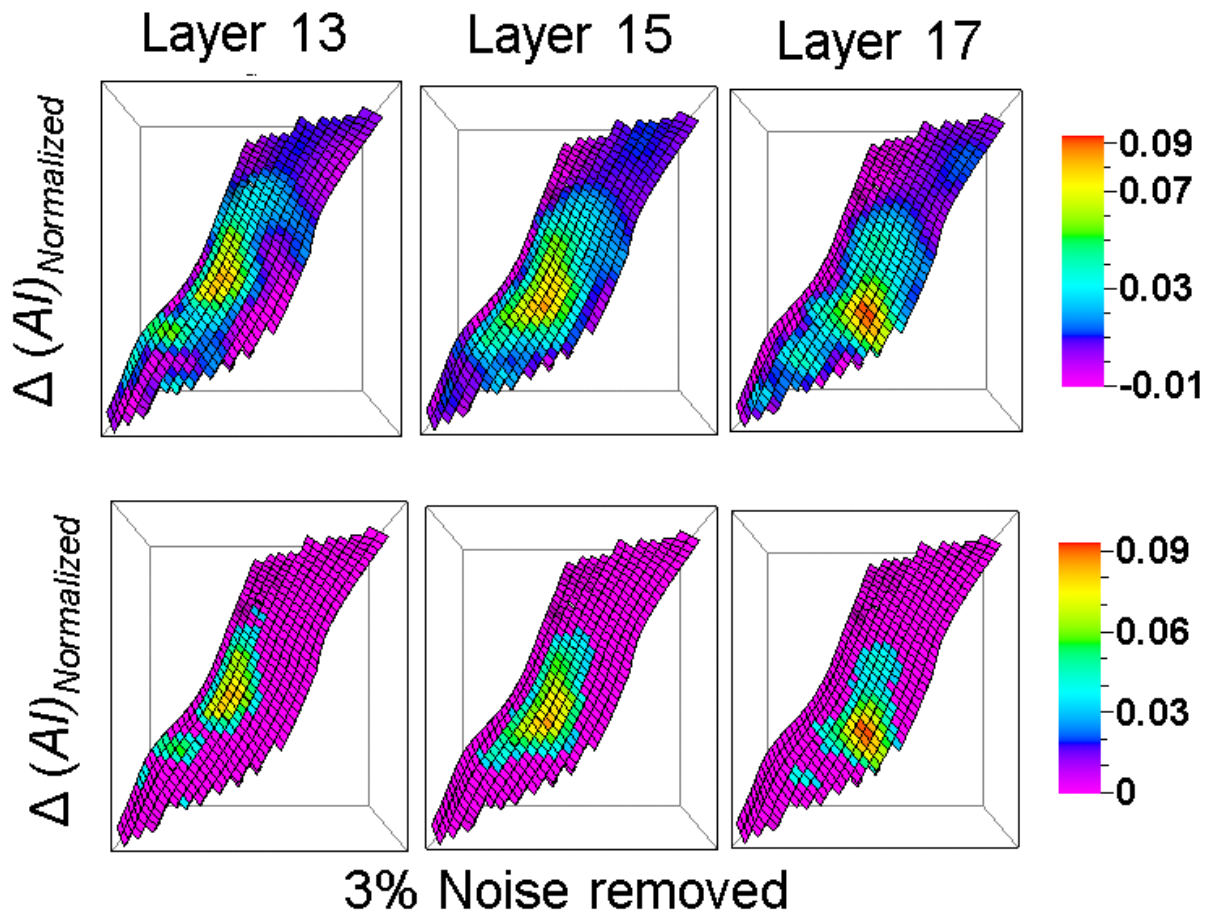


Figure 6.11: Observed time-lapse seismic data in the Norne field (Normalized P-wave impedance change from 2001 to 2004), On the top normalized P-wave impedance change from 2001 to 2004 in layers 13,15 and 17, On the bottom normalized P-wave impedance change from 2001 to 2004 after 3% noise is removed

Using the impedance change between 2001 and 2004, normalized P-wave impedance change in the segment E of Norne field is obtained. The dimensions of flow simulation grids are 100 meters in x and y direction and 3 meters in the z direction. The impedance from seismic grid is interpolated over reservoir grid using the method of median averaging. This normalized change in the P-wave impedance from 2001 to 2004 is taken as the observed time-lapse seismic data to be used in the joint inversion process. It is observed that mostly there is an increase in impedance from 2001 to 2004. The magnitude of decrease in impedance is very less and nearly at the same scale of noise. The increase in the impedance mostly takes place between layer 13 and 18 of the segment E of the Norne field. The increase in the impedance is supported by the fact that water is being injected, and oil and gas are being produced from the reservoir. As oil and gas present in the reservoir are replaced by the water, impedance of the swept region is increased. There is a very slight decrease (close to 1%) in the impedance due to increase in the pore pressure inside the reservoir. We filter 3% absolute change in the impedance to remove noise and keep only the significant changes. Figure 6.11 shows the normalized impedance change between 2001 and 2004 in the layers 13, 15 and 17. On top, the actual impedance changes are shown while at the bottom filtered impedance changes are shown. The filtered normalized impedance change (3% noise removed) from 2001 to 2004 is considered as the observed time-lapse seismic.

$$\Delta(AI)_{normalized} = \frac{AI_{2004} - AI_{2001}}{AI_{2001}} \quad (5.25)$$

## 6.2.2 Dimensionality Reduction

The high dimension of porosity model is reduced by following the methodology described in Section 5.5. The logit transformation is used in combination with principal component analysis to reduce the model space. The reservoir model consists of 22 different zones in the vertical direction. Since porosity models have been generated using different variogram for each zone, dimensional reduction is performed for each zone. The number of PCA coefficients is same for each zone, only the PCA vectors are different. Figures 6.12 and 6.13 show that seventy

PCA coefficients are enough to capture the 60% of variance present in the prior reservoir models of Norne field.

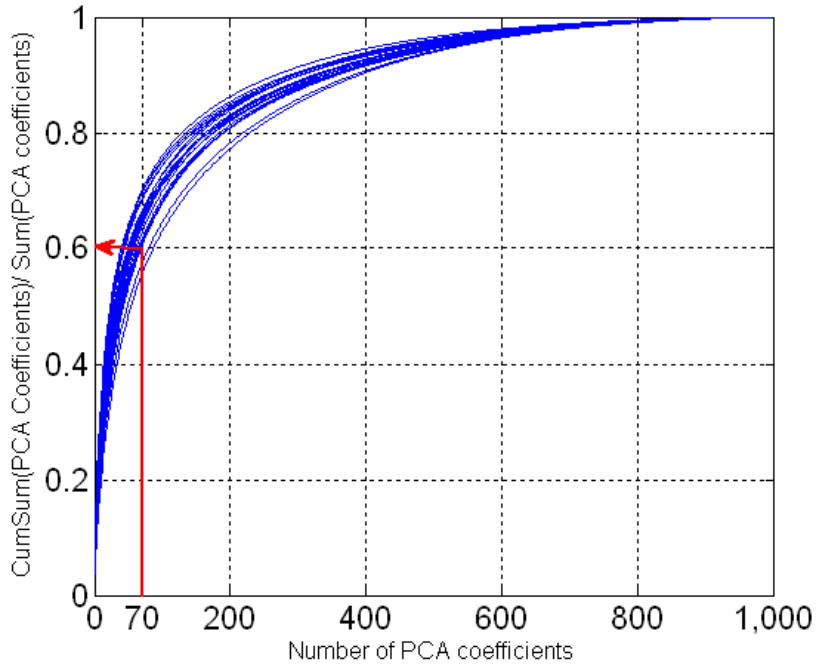


Figure 6.12: The ratio of cumulative sum of PCA coefficients and sum of PCA coefficients are plotted against the number of PCA coefficients. There are 22 blue curves, one for each of the 22 horizontal layers present in the reservoir model of the Norne field. Red line indicates that 70 PCA coefficients are required to capture the 60% variance present in the prior models of the Norne field.

### 6.2.3 Sensitive Parameters

In the previous chapters, we already established that coordination number, porosity models, relative permeability, clay content, fluid mixing and pore compressibility are the sensitive parameters in joint inversion of production and time-lapse seismic data. These parameters are varied in the optimization during joint inversion of production and time-lapse seismic data of Norne field. Porosity model is varied by varying the 70 PCA coefficients as discussed previously. Clay content is varied from 0.1 to 0.4, and it is consistent with what is observed in the Norne field. Similarly coordination number is varied between 5 and 9. Five sets of relative permeability curves are selected for variations (Figure 6.14). These five sets of relative permeability curves capture the range of variations of relative permeability curves present in the Norne field. Pore compressibility is varied between  $1.5E-10 \text{ Pa}^{-1}$  and  $3E-10 \text{ Pa}^{-1}$ .

Uniform or patchy saturation distribution is considered for the fluid mixing. The effective fluid bulk moduli are different for uniform and patchy saturation distribution. The harmonic average of the individual fluid bulk moduli is used for the case of uniform fluid distribution while the arithmetic average is used for the patchy distribution.

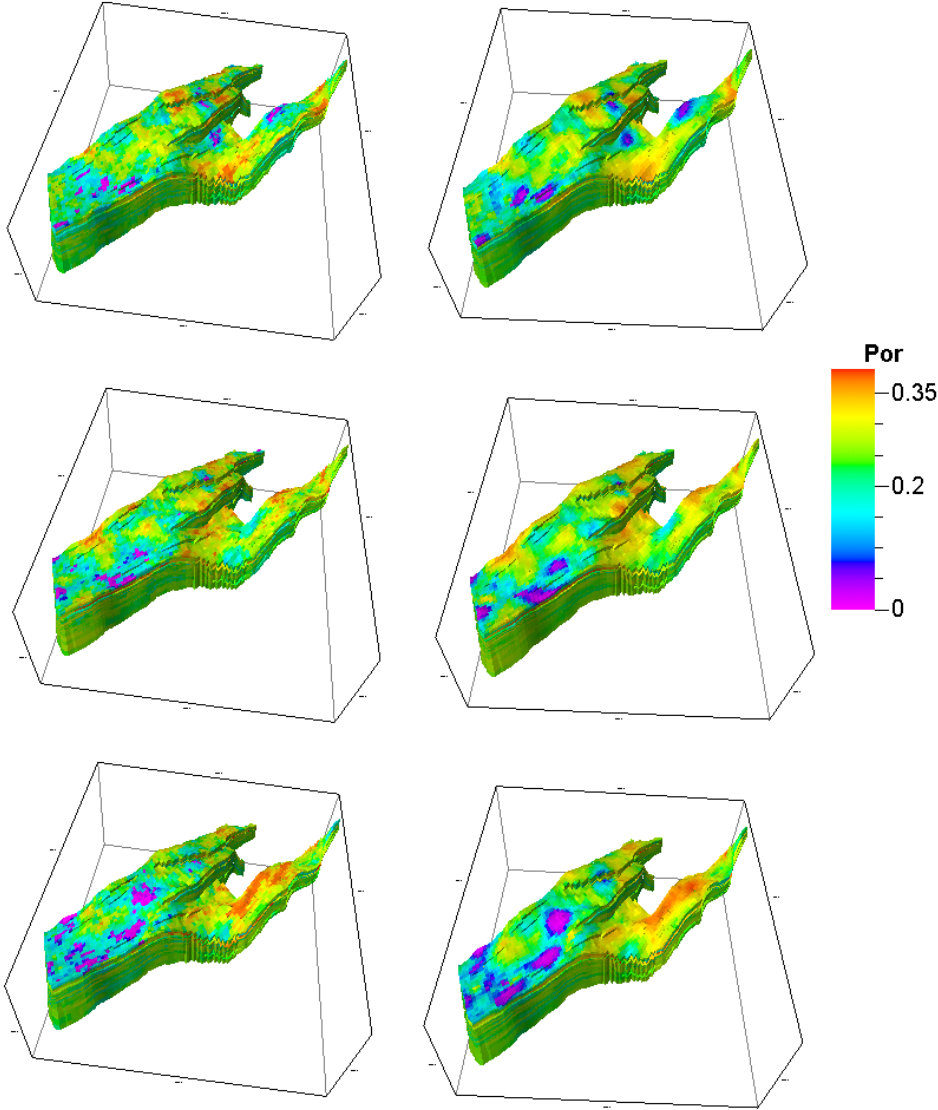


Figure 6.13: Norne reservoir porosity model and porosity models constructed using PCA are compared. On left three original porosity models for Norne field and on right three corresponding porosity models of Norne constructed using PCA coefficients. Clearly 70 PCA coefficients are successful in capturing much of the heterogeneity present in the original porosity models.

The use of the arithmetic average is an approximation and gives an upper bound (Mavko and Mukerji, 1998). Overall seventy five parameters are optimized in the joint inversion process such that simulated production and time-lapse seismic response of these parameters provide a satisfactory match with the observed production and time-lapse seismic data of Norne field.

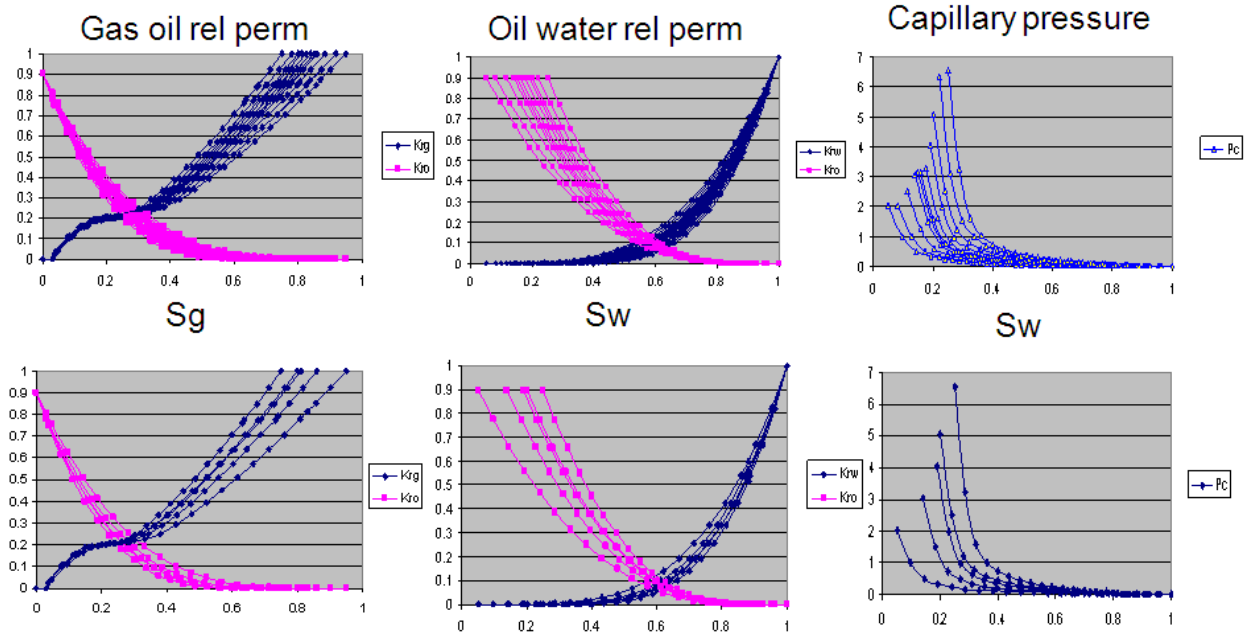


Figure 6.14: Relative permeability curves present in the Norne field. On the top all of the relative permeability curves present in the Norne field (from left to right: Gas oil relative permeability curves, Oil water relative permeability curves and capillary pressure curves). At the bottom five sets of relative permeability curves selected to be used for joint inversion (These five sets capture the range of variations present in all of the relative permeability curves).

### 6.2.4 Methodology

As described in the previous chapter, a family of particle swarm optimizers is used in combination with principal component analysis for the joint inversion of production and time-lapse seismic data. The same methodology is applied for joint inversion of production and time-lapse seismic data of Norne field. Figure 6.15 describes the methodology used for joint inversion or history matching of observed data in the Norne field. As mentioned earlier, seventy five optimization variables are initialized with an initial guess, and perturbed using particle swarm optimizers such that responses of these parameters provide a satisfactory match with the observed data. The ranges of PCA coefficients are obtained by projecting the prior reservoir

models in the PCA space. The goal of the joint inversion or history matching process is to match the observed oil, gas, water rates and bottom hole pressure in the wells E-2H, E-3H and E-3AH from 1997 to 2004, as well as the 4D seismic data: the normalized impedance change in the reservoir from 2001 to 2004 (impedance change in layers 13, 15 and 17 of the Segment E). This is achieved by perturbing the seventy five optimization variables defined in the previous sections.

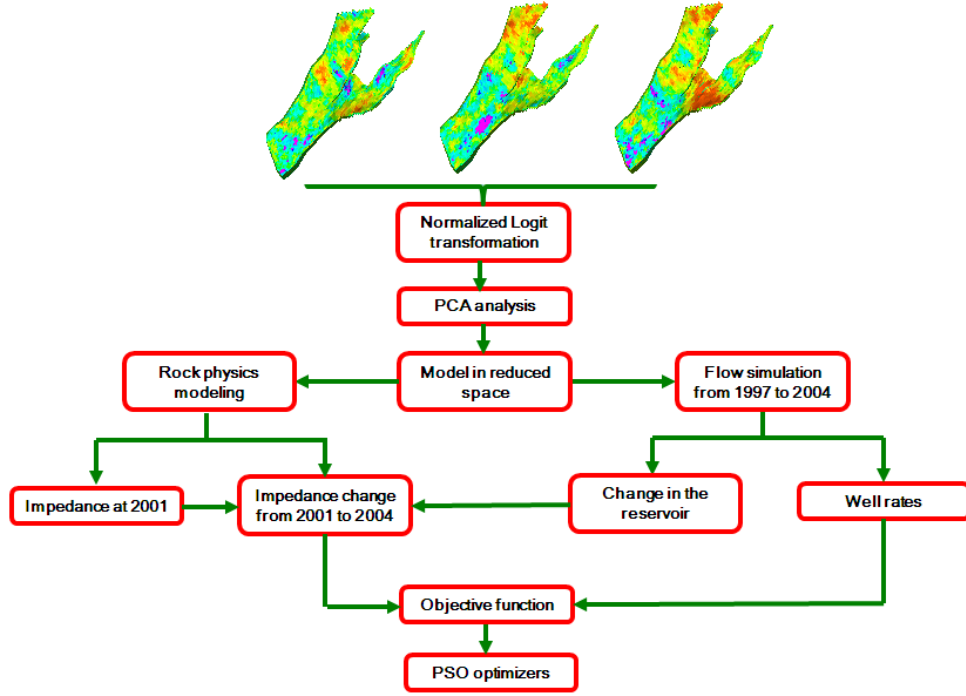


Figure 6.15: Workflow for joint inversion of production and time-lapse seismic data of Norne field. A family of particle swarm optimizers is used in combination with principal component analysis with variations in the sensitive parameters

The objective function used for the history matching process is defined as following:

$$\begin{aligned}
 O = \sum_{i=1}^N & \left[ \frac{\|P_{oil}^{obs} - P_{oil}^{sim}\|_2^2}{\|P_{oil}^{obs}\|_2^2} + \frac{\|P_{water}^{obs} - P_{water}^{sim}\|_2^2}{\|P_{water}^{obs}\|_2^2} + \frac{\|P_{gas}^{obs} - P_{gas}^{sim}\|_2^2}{\|P_{gas}^{obs}\|_2^2} \right. \\
 & \left. + \frac{\|W_{bhp}^{obs} - W_{bhp}^{sim}\|_2^2}{\|W_{bhp}^{obs}\|_2^2} \right] + \frac{\|(\Delta AI)_{norm}^{obs} - (\Delta AI)_{norm}^{sim}\|_2^2}{\|(\Delta AI)_{norm}^{obs}\|_2^2}
 \end{aligned} \tag{5.26}$$

where  $N$  is the number of wells (3 wells in this case: E-2H, E-3H and E-3AH);  $P_{oil}^{obs}$ ,  $P_{water}^{obs}$ ,  $P_{gas}^{obs}$  and  $W_{bhp}^{obs}$  are the historical oil, gas, water production rates and bottom hole pressure;  $P_{oil}^{sim}$ ,  $P_{water}^{sim}$ ,  $P_{gas}^{sim}$  and  $W_{bhp}^{sim}$  are the simulated oil, gas, water production rates and bottom hole pressure;  $(\Delta AI)_{norm}^{obs}$  is the observed normalized impedance change from 2001 to 2004;  $(\Delta AI)_{norm}^{sim}$  is the simulated normalized impedance change from 2001 to 2004.

Production response of the reservoir model is obtained by running flow simulations. Time-lapse seismic response (normalized impedance change from 2001 to 2004) of the reservoir model is obtained by performing a forward time-lapse seismic modeling.

### 6.2.5 Flow Simulations and Forward Time-lapse Seismic Modeling

Flow simulations are performed to obtain production response from the wells as well as changes in the reservoir condition (change in pressure and saturation). The changes in the reservoir conditions are used to model the time-lapse seismic response. The flow simulation model used for this study is described in Section 3.4. As previously mentioned, the producers are controlled using reservoir fluid volume rate calculated from observed phase flow rates. Reservoir fluid volume is the volume occupied by the produced fluid at reservoir conditions.

Forward seismic modeling is performed to obtain time-lapse seismic response of Norne field. As previously mentioned, the simulated time-lapse seismic response in this study is the normalized P-wave impedance change from 2001 to 2004. To obtain time-lapse seismic response, rock physics modeling is performed as described in Section 4.2. As discussed previously, segment E of Norne field consists of three facies (sand, shaly sand and shale), but it has been observed that the presence of shaly sand and shale facies in the field are very limited. They are only present in the NOT formation which acts as a cap rock (permeability barrier). Modeling and matching of time-lapse seismic response in the NOT formation is not considered in this study. Thus, segment E of the Norne field is modeled as sand facies with varying clay content and coordination number.

Following the workflow described in Section 4.2, constant cement model is used to obtain initial seismic velocities,  $V_P$  and  $V_S$  and thus initial P-wave seismic impedance (at 2001). As described in 4.3.2, time-lapse seismic modeling is performed by taking in to account the effect of change in pressure and saturations, to obtain the P-wave impedance in 2004. The values of P-wave impedance in 2001 and 2004 are used to obtain the simulated normalized change in P-wave impedance from 2001 to 2004.

### 6.3 History Matching Results

Following the proposed workflow described in 6.2.4; variants of particle swarm optimization are used for joint inversion of production and time-lapse seismic data of Norne field. The family of particle swarm optimization consists of CC-PSO, CP-PSO, PP-PSO, GPSO and RR-PSO. These variants are already described in the Section 5.3.

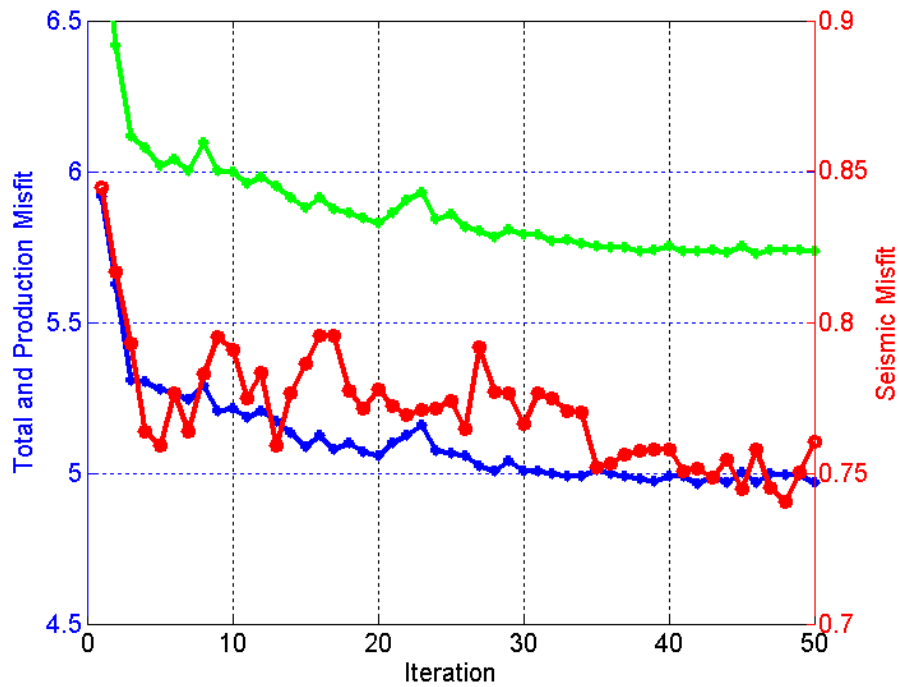


Figure 6.16: The decrease in median of the production misfits, time-lapse seismic misfits and total misfits with increase in number of iterations while using CC-PSO. Production misfit, time-lapse seismic misfit and total misfit are shown by blue, red and green curves respectively.

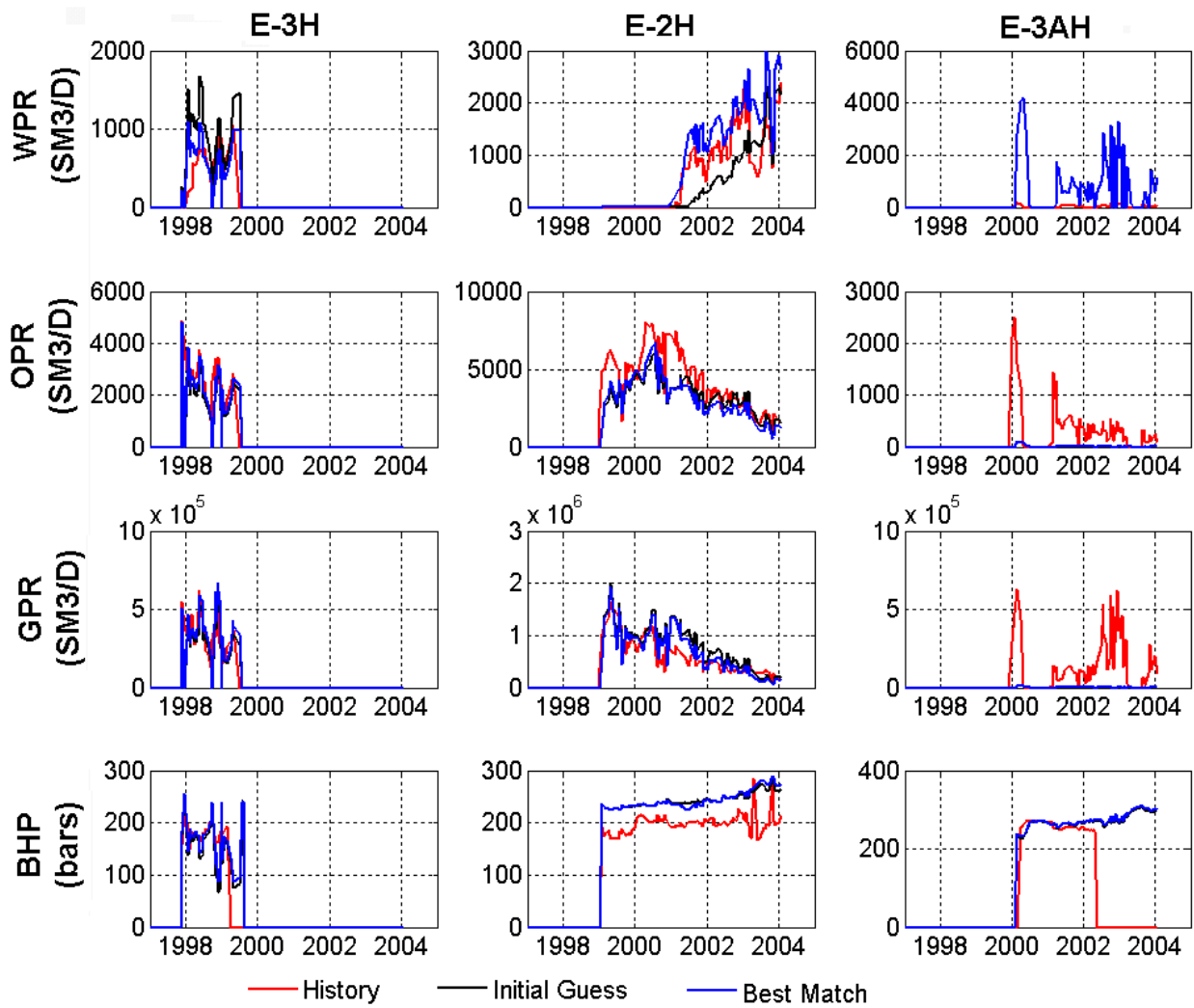


Figure 6.17: History matching results for matching production data using CC-PSO. Simulated production response of initial guess model, simulated production response of best model and history are shown by black, blue and red curves respectively. Matching of water, oil, gas rates and bottom hole pressure are shown in a column for each well

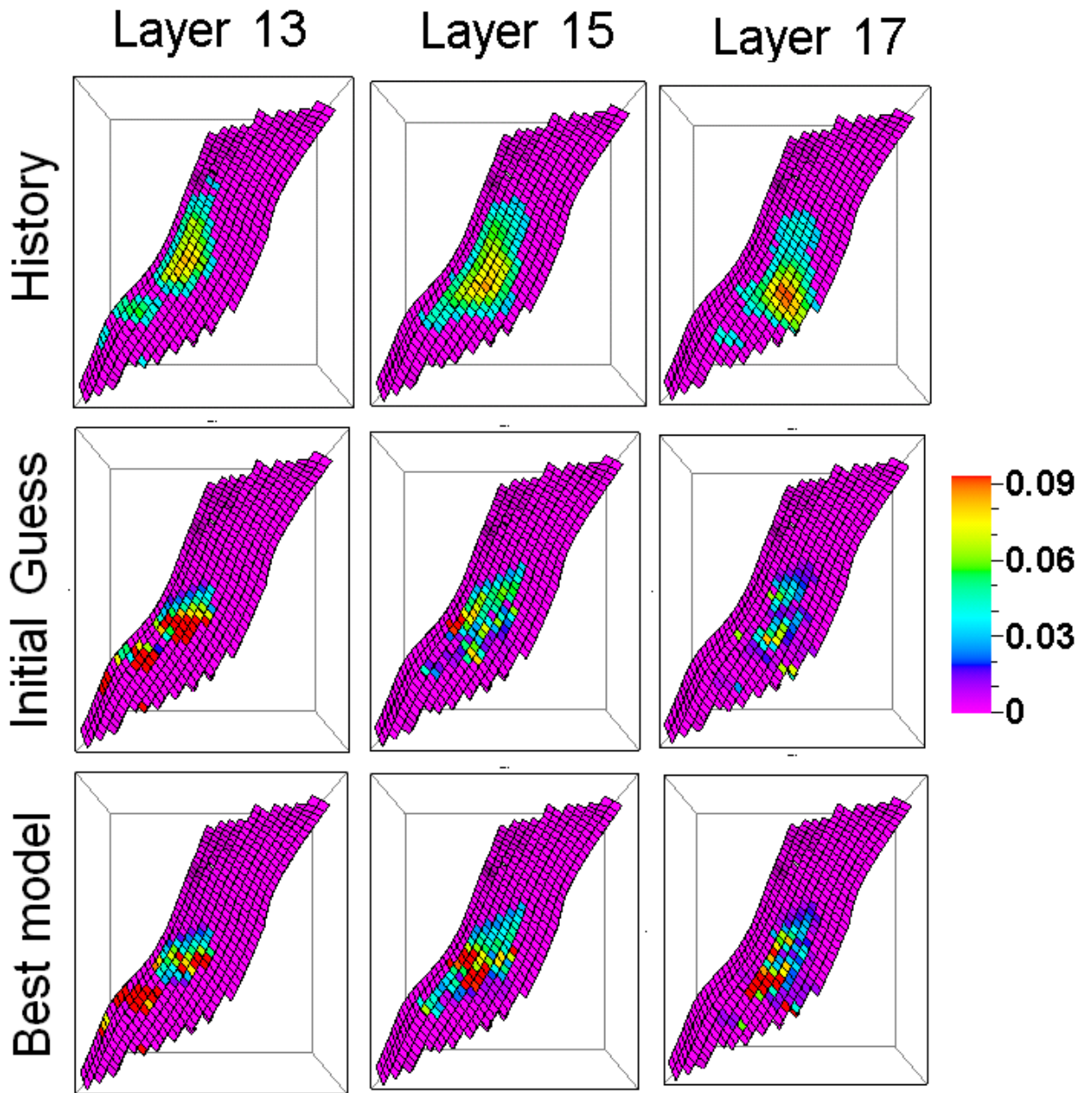


Figure 6.18: History matching results for matching time-lapse seismic data using CC-PSO. History, simulated time-lapse seismic response of initial guess model and simulated time-lapse seismic response of best model are shown from top to bottom for layers 13, 15 and 17.

The sensitive parameters mentioned in Section 6.2.3 are varied with in a range (lower limit and upper limit for each sensitive parameter is provided) to provide a set of properties whose

production and time-lapse seismic response have a satisfactory match with the observed production and time-lapse seismic data. The swarm size and number of iterations should be chosen based on the available computational resources, since a high number of simulations for production and time-lapse seismic responses are required with the increase in swarm size and number of iterations. In this study the swarm size for particle swarm optimization is 20. The number of iterations performed for each of the variant of particle swarm optimization is 50. These numbers are chosen based on the available computational resources.

Figure 6.16 shows the decrease in production misfit, time-lapse seismic misfit and total misfit with increase in the number of iterations while using CC-PSO. The production misfit, time-lapse seismic misfit and total misfit for each particle in the swarm (swarm size 20) are evaluated. The median of the distribution of misfits is plotted with the increase in number of iterations. The decrease in production misfit is 17% while the decrease in time-lapse seismic mismatch is 12% over the 50 iterations. It is observed that production misfit has converged faster than time-lapse seismic misfit.

Figure 6.17 shows the history matching results of production data in the case of CC-PSO. The history and production responses of initial guess model and best model are shown. As mentioned earlier production response consist of water, oil, gas production rate and bottom hole pressure in wells E-2H, E-3H and E-3AH. The history, production responses of initial guess model and best model are shown in red, black and blue curves respectively. It is clear that a satisfactory history matching of production data is achieved in wells E-2H and E-3H. The production response of the best model shows improvement over the production response of initial guess model. The history matching of production data in the well E-3AH is unsatisfactory.

Figure 6.18 shows the history matching result of time-lapse seismic data in the case of CC-PSO. A satisfactory match of time-lapse seismic data is achieved in the layers 13 and 15, whereas the match is unsatisfactory in the layer 17. We also observe that, in some layers the time-lapse seismic response of the best model has improved from the time-lapse seismic response of the initial guess model.

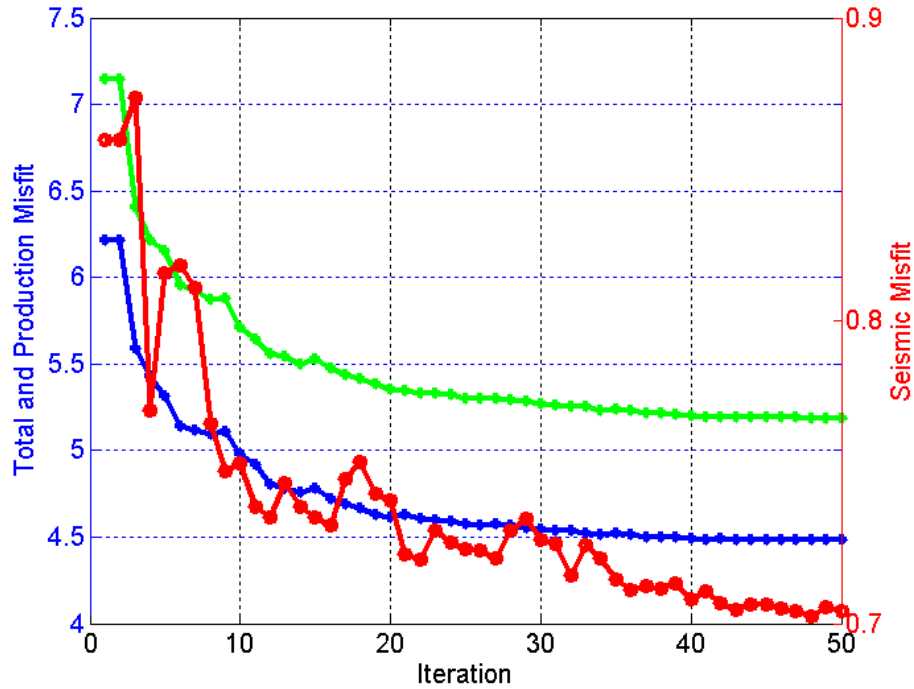


Figure 6.19: The decrease in median of the production misfits, time-lapse seismic misfits and total misfits with increase in number of iterations while using CP-PSO. Production misfit, time-lapse seismic misfit and total misfit are shown by blue, red and green curves respectively.

Figure 6.19 shows the decrease in the median of production misfits, total misfits and time-lapse seismic misfits with the increase in number of iterations while in the case of CP-PSO. The production misfit is decreased by 28%, and time-lapse seismic misfit is decreased by 21% over 50 iterations. Again it is observed that production misfit converged faster than time-lapse seismic misfit. The percentage of decrease in production and seismic misfit indicates that CP-PSO has performed better than CC-PSO.

Figure 6.20 shows the history matching results for production data using CP-PSO. The history, production response of initial guess model and best model are shown in the red, black and blue curves respectively. A satisfactory history match of the oil, gas, water production rate and bottom hole pressure is achieved in the wells E-3H and E-2H. The production response of initial guess model has improved to the production response of the best model. A satisfactory history match of gas production rate has achieved in the well E-3AH, having significant improvement from the production response of initial guess model. A significant improvement

over the simulated water production rate of initial guess model is achieved in the well E-3AH, but history matching of oil and gas rates in the well E-3AH is unsatisfactory.

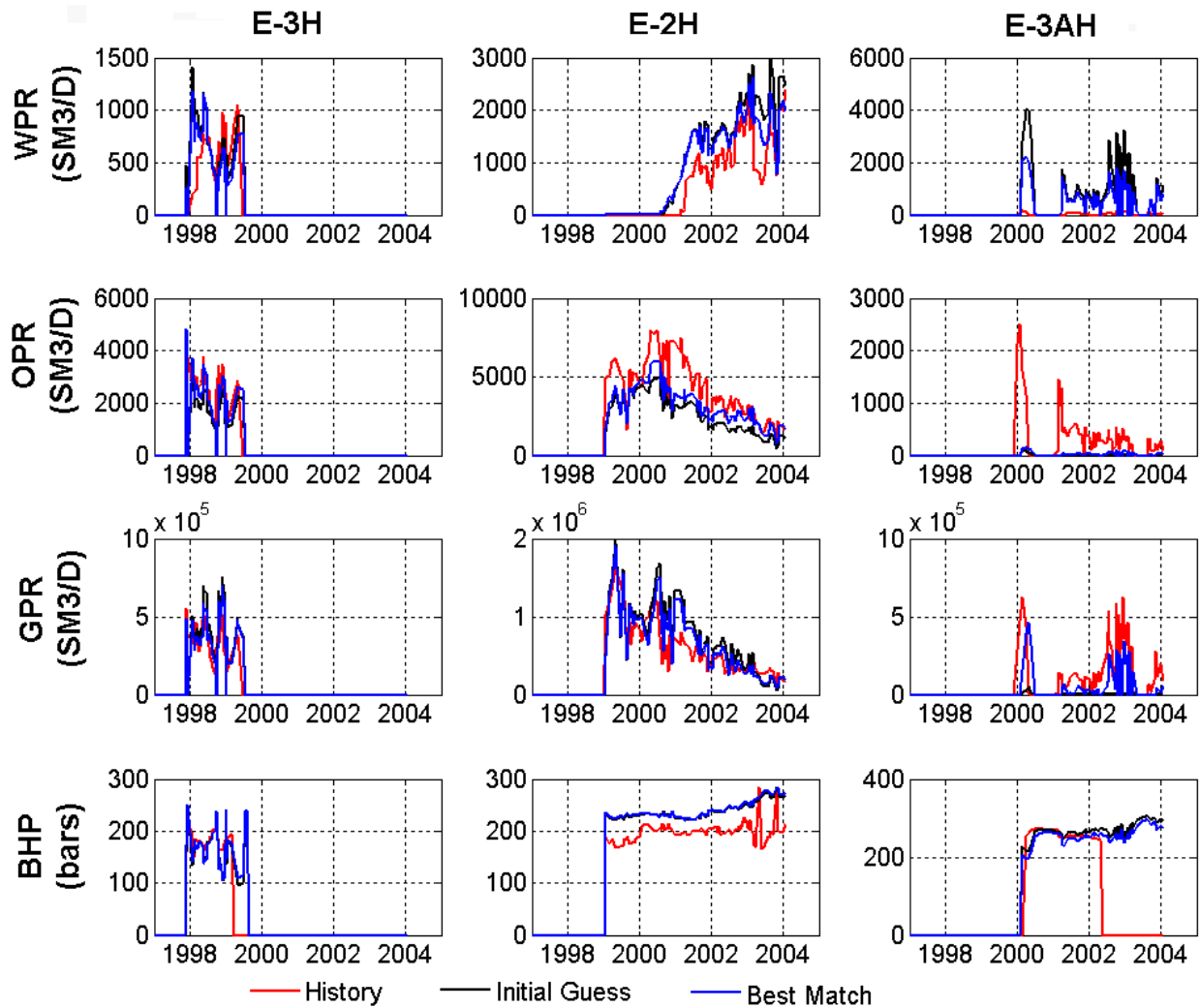


Figure 6.20: History matching results for matching production data using CP-PSO. Simulated production response of initial guess model, simulated production response of best model and history are shown by black, blue and red curves respectively. Matching of water, oil, gas rates and bottom hole pressure are shown in a column for each well

Figure 6.21 shows the history matching results for time-lapse seismic data using CP-PSO. In some areas, the simulated time-lapse seismic response of initial guess model has improved to the time-lapse seismic response of the best model. The history match of time-lapse seismic data in layer 17 is unsatisfactory.

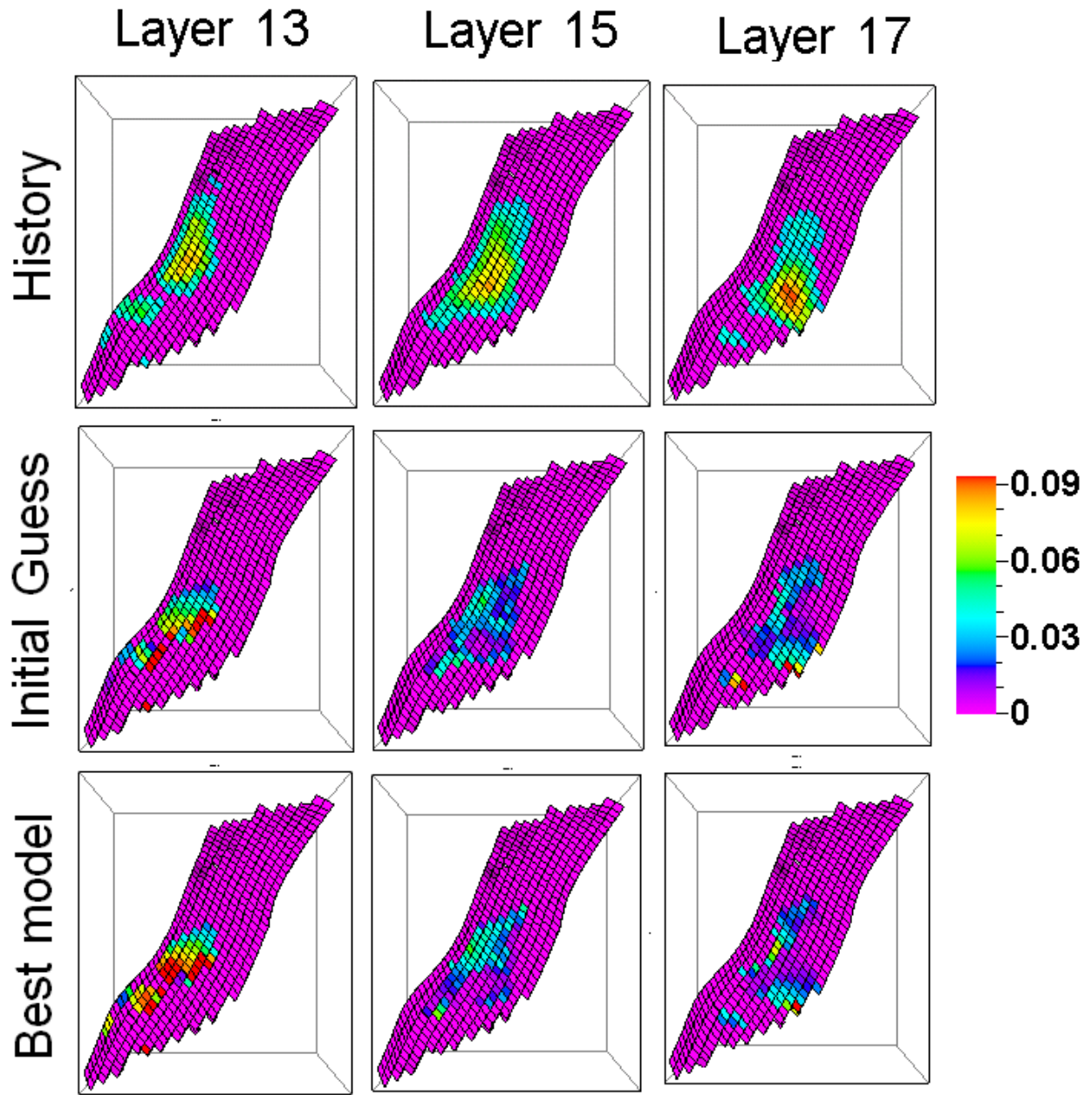


Figure 6.21: History matching results for matching time-lapse seismic data using CP-PSO. History, simulated time-lapse seismic response of initial guess model and simulated time-lapse seismic response of best model are shown from top to bottom for layers 13, 15 and 17.

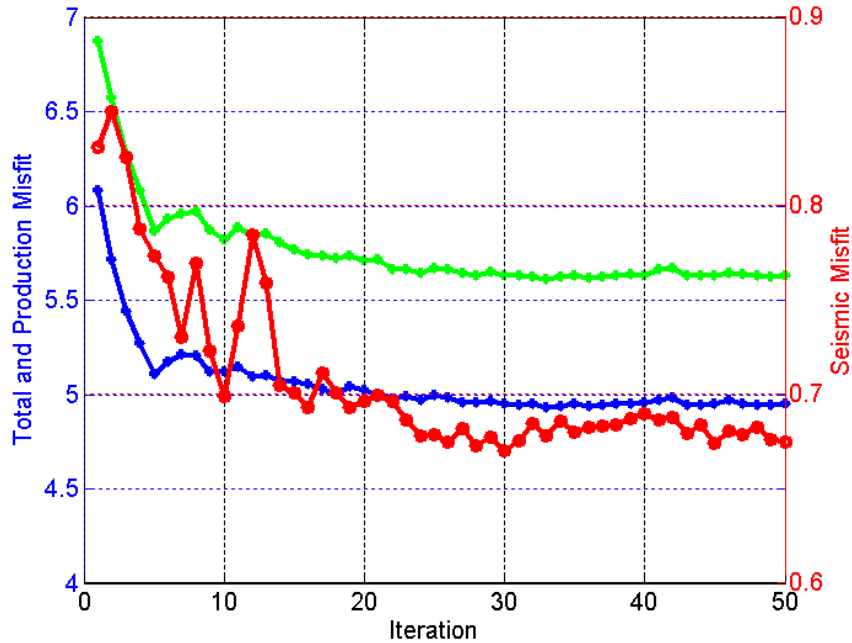


Figure 6.22: The decrease in median of the production misfits, time-lapse seismic misfits and total misfits with increase in number of iterations while using GPSO. Production misfit, time-lapse seismic misfit and total misfit are shown by blue, red and green curves respectively.

Figure 6.22 shows the decrease in the median of production misfits, time-lapse seismic misfits and total misfits with the increase in number of iterations in the case of GPSO. The production misfit is decreased by 20%, and time-lapse seismic misfit is decreased by 22%. The production misfit is converged after 20 iterations. The production mismatch is converged faster than the time-lapse seismic mismatch.

Figure 6.23 shows the history matching results for matching production data using GPSO. Red, black and blue curves represent history and simulated response of initial and best model respectively. A satisfactory history matching of production data is achieved in the wells E-3H and E-3H. The simulated production response of initial guess model is significantly improved using GPSO. It is clear from the difference in the simulated responses of initial guess model and best model in the well E-2H. There is a significant improvement in the simulated water and oil rate of initial guess model in the well E-2H. The history matching of production data is unsatisfactory in the well E-3AH.

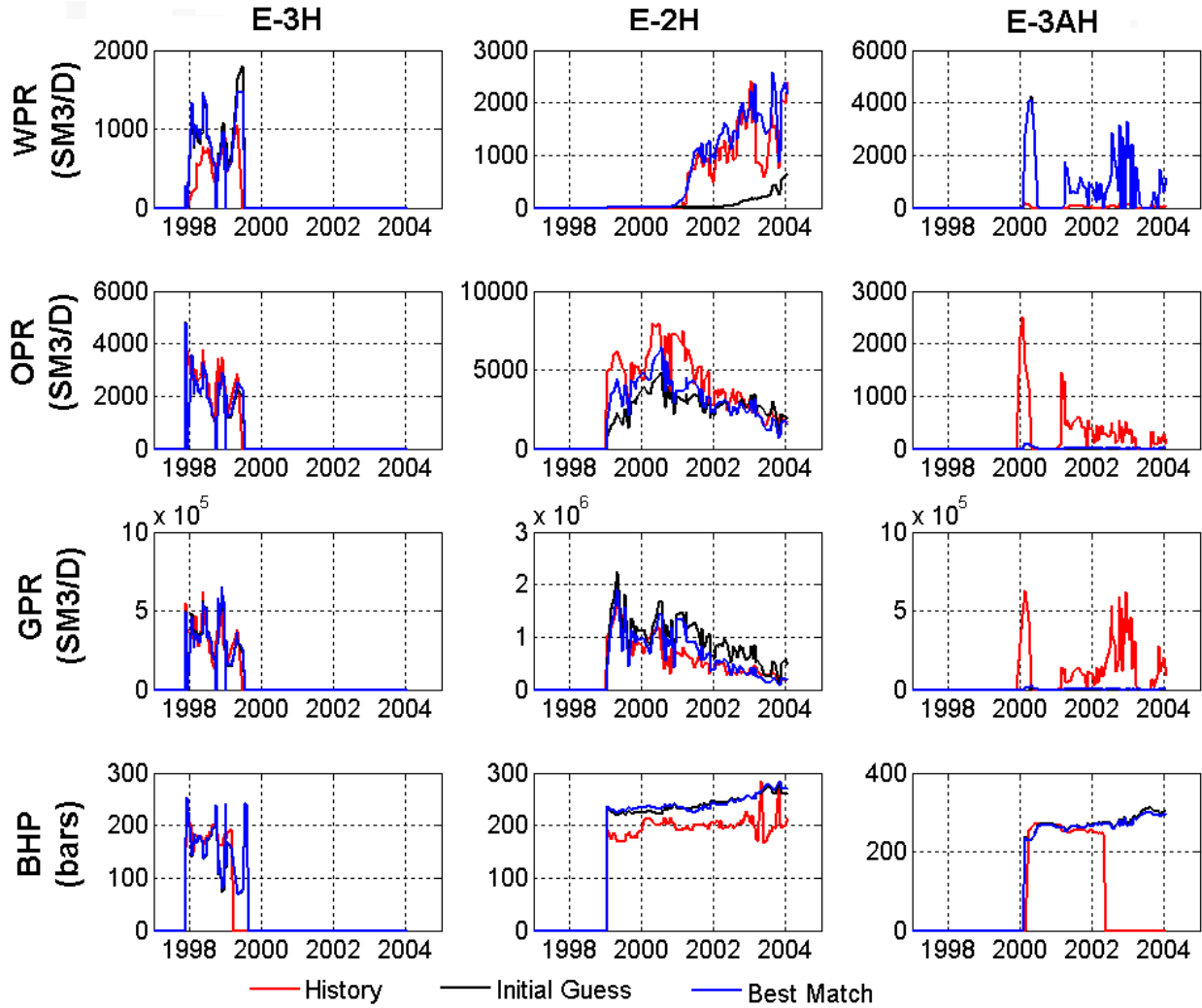


Figure 6.23: History matching results for matching production data using GPSO. Simulated production response of initial guess model, simulated production response of best model and history are shown by black, blue and red curves respectively. Matching of water, oil, gas rates and bottom hole pressure are shown in a column for each well

The history matching results for matching time-lapse seismic data using GPSO are shown in the Figure 6.24. There is a significant improvement in the simulated time-lapse seismic response of initial guess model in the layers 15 and 17. It is clear by comparing the simulated time-lapse seismic responses of the initial guess model and best model. There is no significant improvement in the simulated time-lapse seismic response of the initial guess model in layer 13.

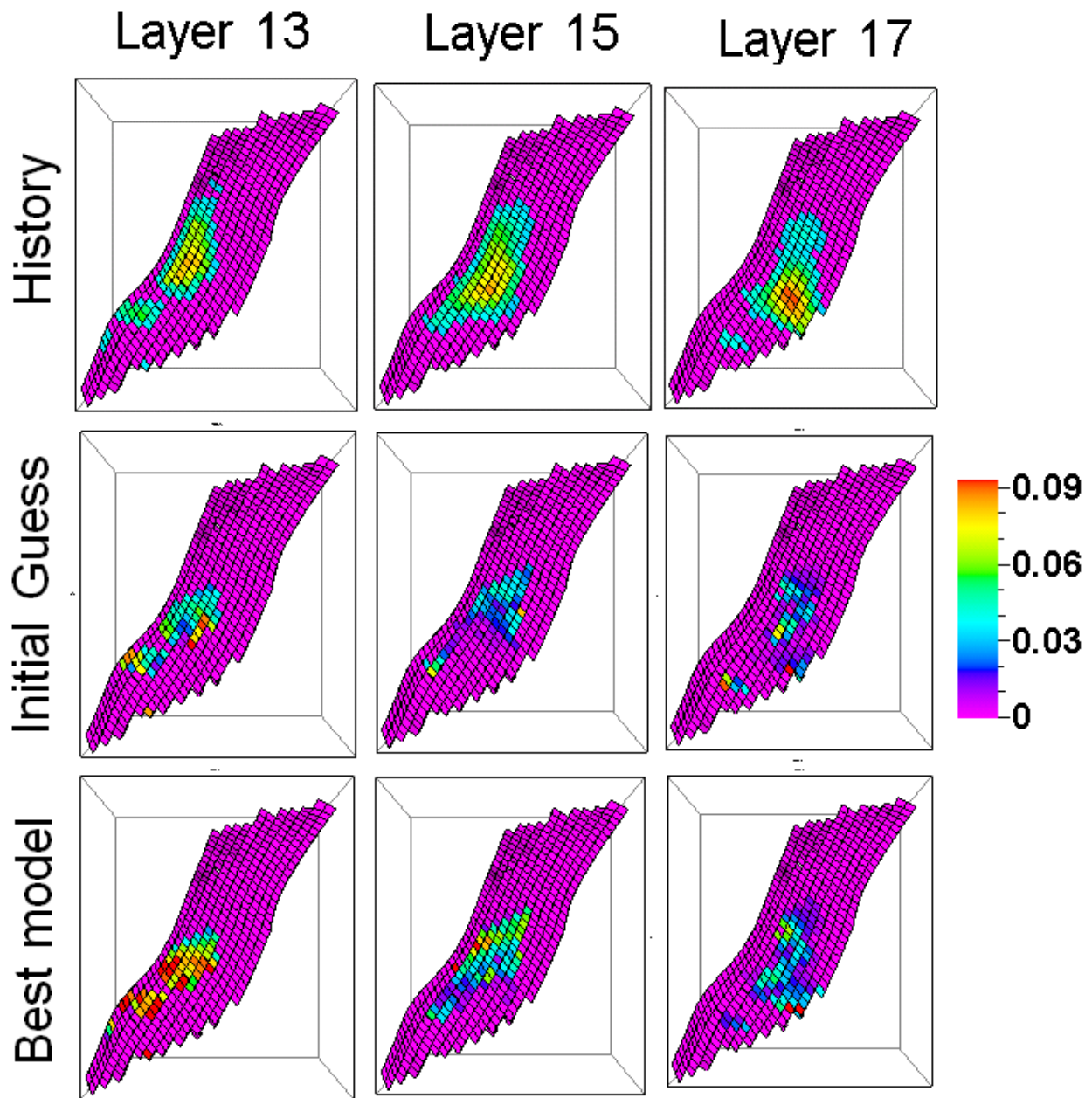


Figure 6.24: History matching results for matching time-lapse seismic data using GPSO. History, simulated time-lapse seismic response of initial guess model and simulated time-lapse seismic response of best model are shown from top to bottom for layers 13, 15 and 17.

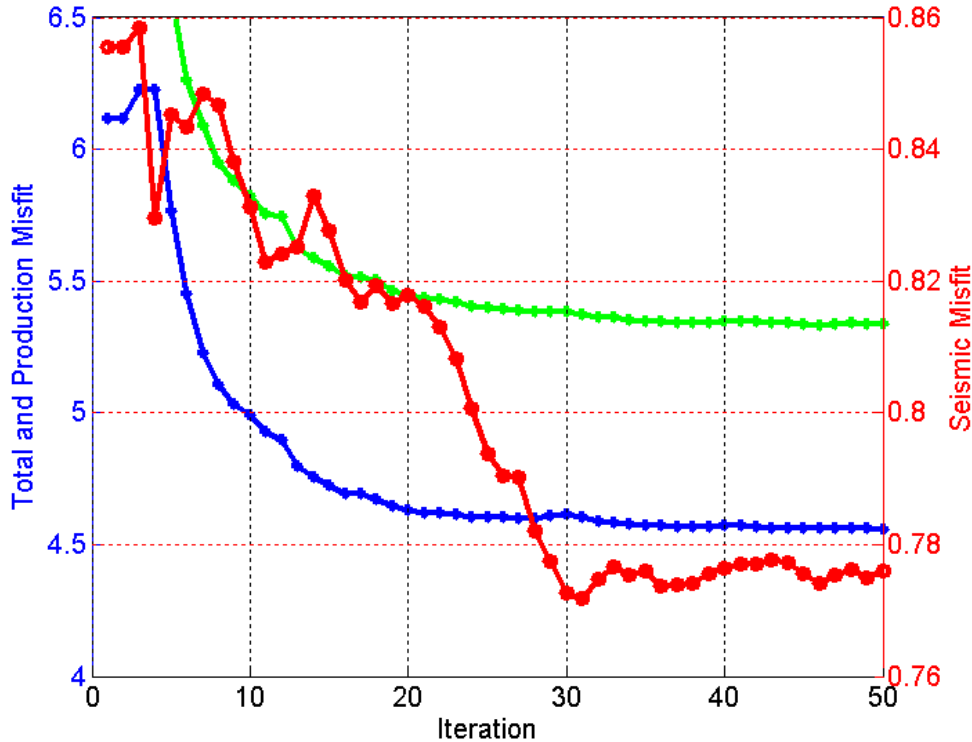


Figure 6.25: The decrease in median of the production misfits, time-lapse seismic misfits and total misfits with increase in number of iterations while using PP-PSO. Production misfit, time-lapse seismic misfit and total misfit are shown by blue, red and green curves respectively.

Figure 6.25 shows the decrease in the median of production misfits, time-lapse seismic misfits and total misfits with an increase in number of iterations while using PP-PSO. The production misfit is decreased by 25%, whereas time-lapse seismic misfit is decreased by 9% over 50 iterations. Again the production misfit converged faster than time-lapse seismic misfit. The production misfit is almost converged after only 20 iterations.

Figure 6.26 shows the results of history matching of production data using PP-PSO. A satisfactory history match is achieved for the production data in the wells E-2H and E-3H. It is confirmed by a significant improvement in the simulated production response of initial guess model for wells E-2H and E-3H. We also obtained a satisfactory history match for gas production rates in the well E-3AH. The history match achieved for oil and water production rates in the well E-3AH is unsatisfactory.

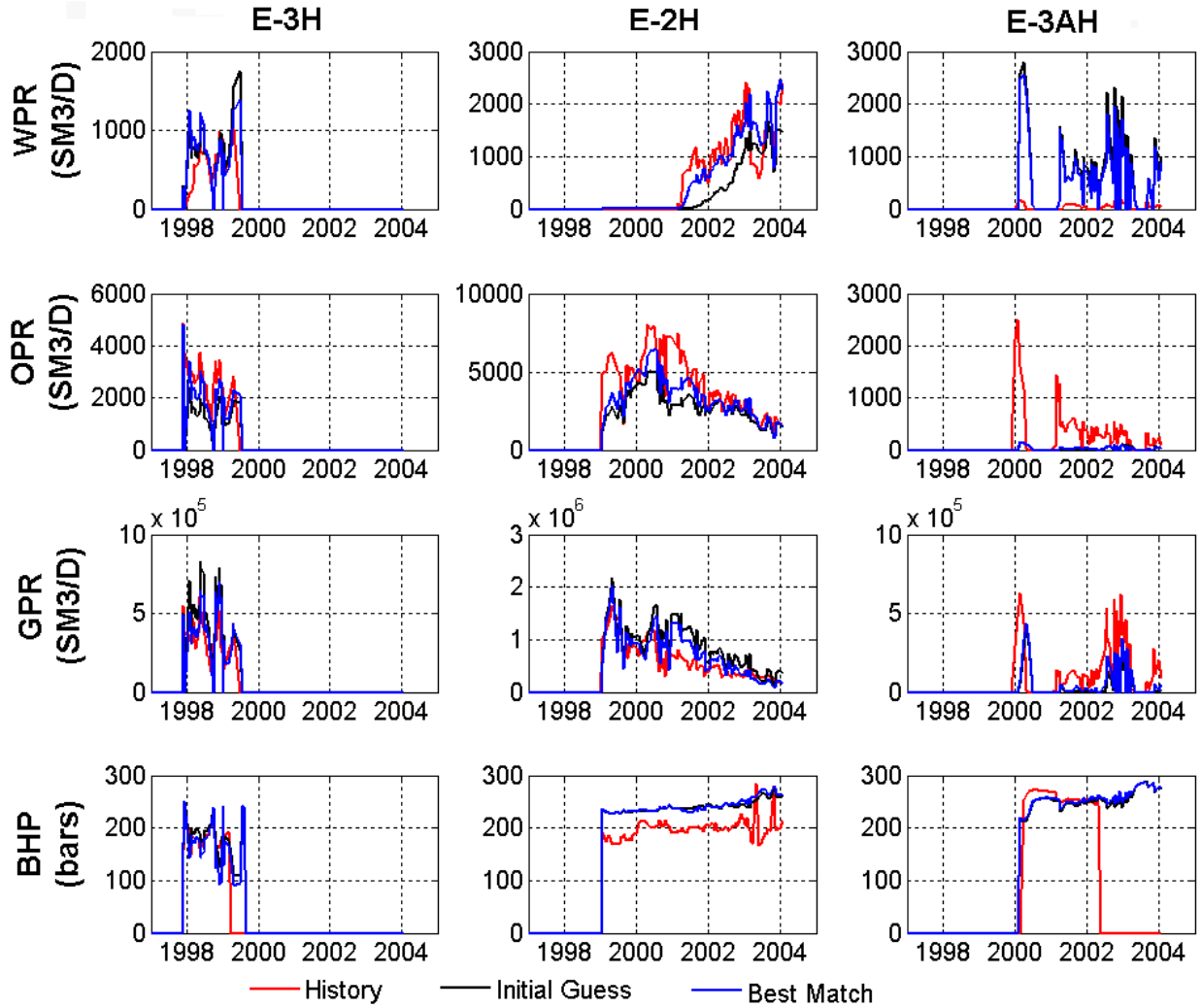


Figure 6.26: History matching results for matching production data using PP-PSO. Simulated production response of initial guess model, simulated production response of best model and history are shown by black, blue and red curves respectively. Matching of water, oil, gas rates and bottom hole pressure are shown in a column for each well

Figure 6.27 shows the history matching results of matching time-lapse seismic data while using PP-PSO. There is an improvement in the simulated time-lapse seismic response of initial guess model in the layer 15. The improvements in the simulated time-lapse seismic response of initial guess model after history matching are very minor in the layers 13 and 17.

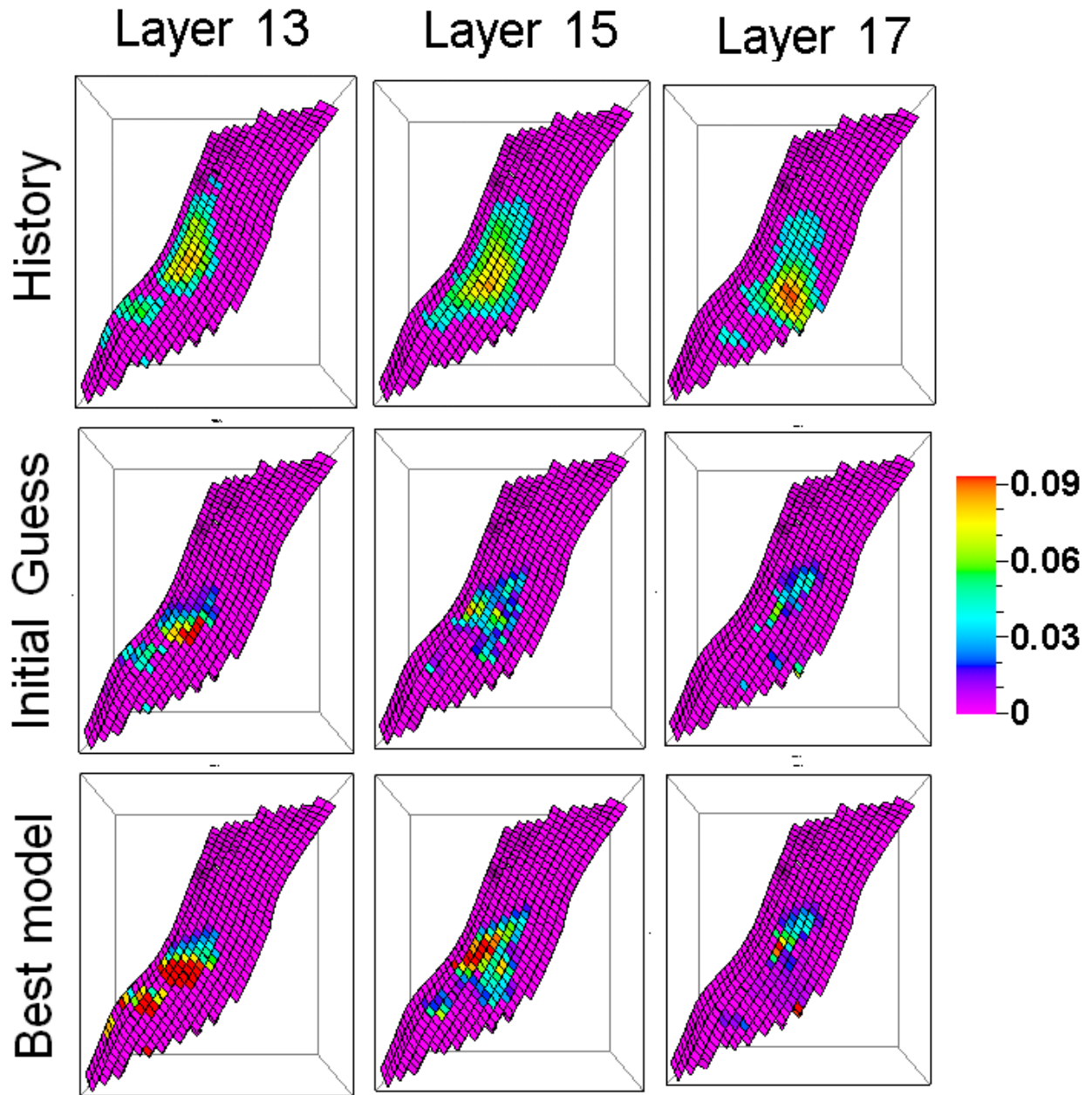


Figure 6.27: History matching results for matching time-lapse seismic data using PP-PSO. History, simulated time-lapse seismic response of initial guess model and simulated time-lapse seismic response of best model are shown from top to bottom for layers 13, 15 and 17.

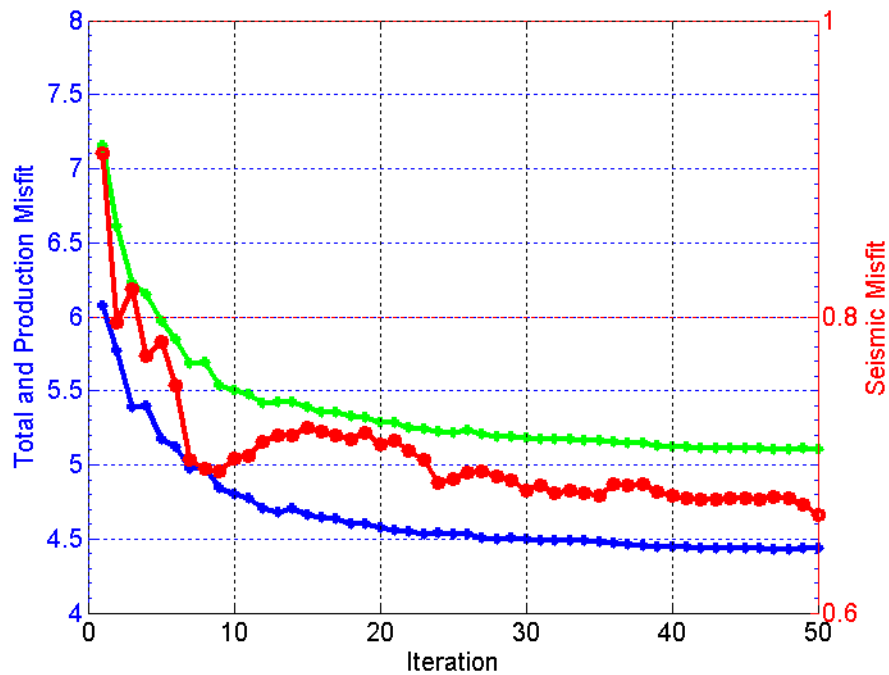


Figure 6.28: The decrease in median of the production misfits, time-lapse seismic misfits and total misfits with increase in number of iterations while using RR-PSO. Production misfit, time-lapse seismic misfit and total misfit are shown by blue, red and green curves respectively.

Figure 6.28 shows the decrease in median production misfits, time-lapse seismic misfits and total misfits with the increase in number of iterations while using RR-PSO. The production misfit is decreased by 25%, whereas time-lapse seismic misfit is decreased by 28% over 50 iterations. The production misfit is converged faster than time-lapse seismic misfit. The RR-PSO has provided the lowest time-lapse seismic misfit among all PSO family members.

The results of history matching of production data using RR-PSO are shown in the Figure 6.29. A satisfactory history matching of production data is achieved in the wells E-3H and E-2H. The simulated production response of initial guess model has improved significantly in the history matching process. A satisfactory history match of gas production rates in E-3AH well is also achieved. It is only achieved while using CP-PSO, PP-PSO and RR-PSO. There is an improvement in the simulated water production rates of initial guess model, but history matching of the water production rate is unsatisfactory.

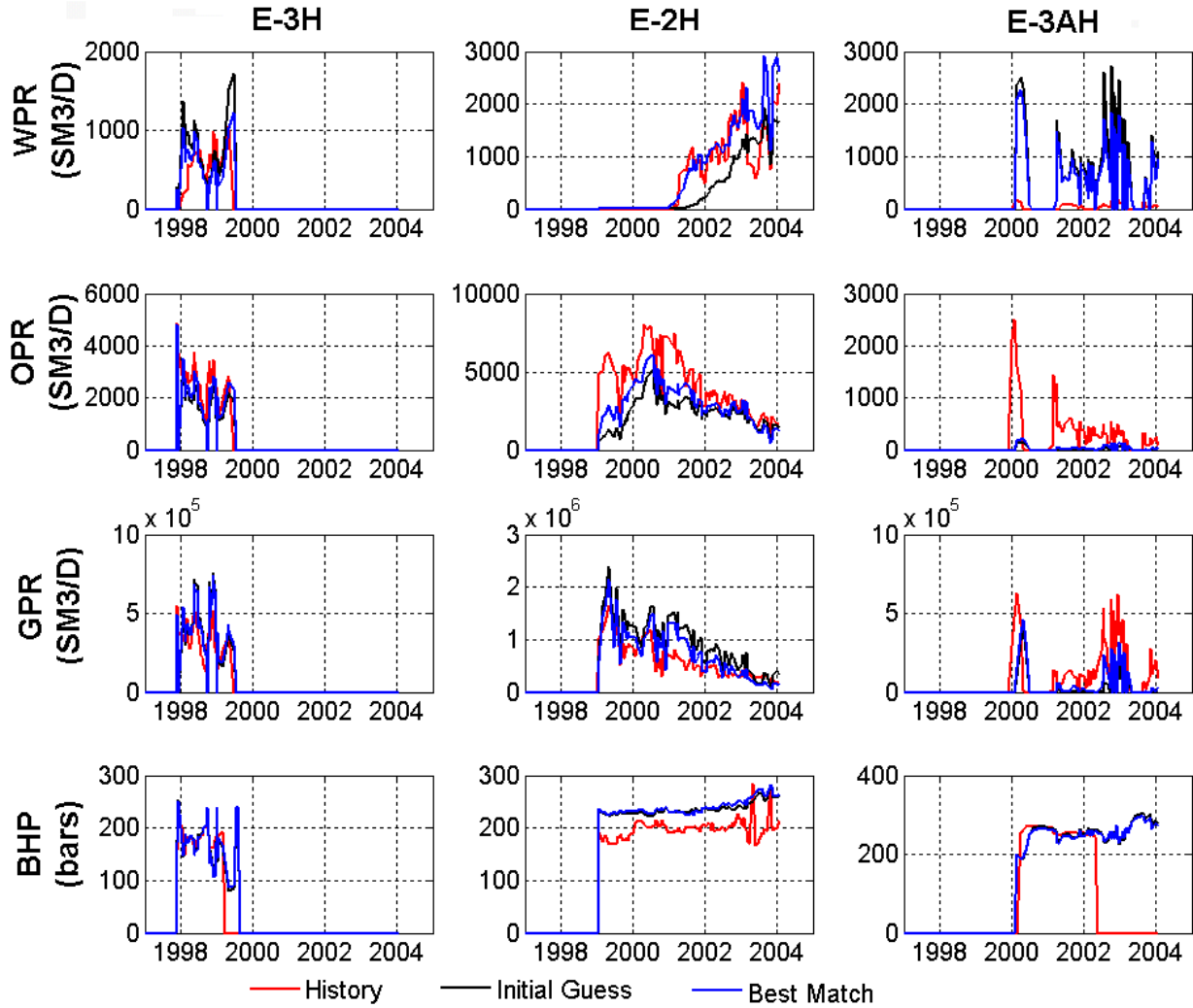


Figure 6.29: History matching results for matching production data using RR-PSO. Simulated production response of initial guess model, simulated production response of best model and history are shown by black, blue and red curves respectively. Matching of water, oil, gas rates and bottom hole pressure are shown in a column for each well

Figure 6.30 shows the history matching results for matching time-lapse seismic response while using RR-PSO. A satisfactory history match of time-lapse seismic data is achieved for layer 13. There is a significant and clear improvement in the simulated time-lapse seismic response of initial guess model in layer 13. There is an improvement in the simulated time-lapse seismic response of initial guess model in the layers 15 and 17 but history matching is unsatisfactory in these two layers.

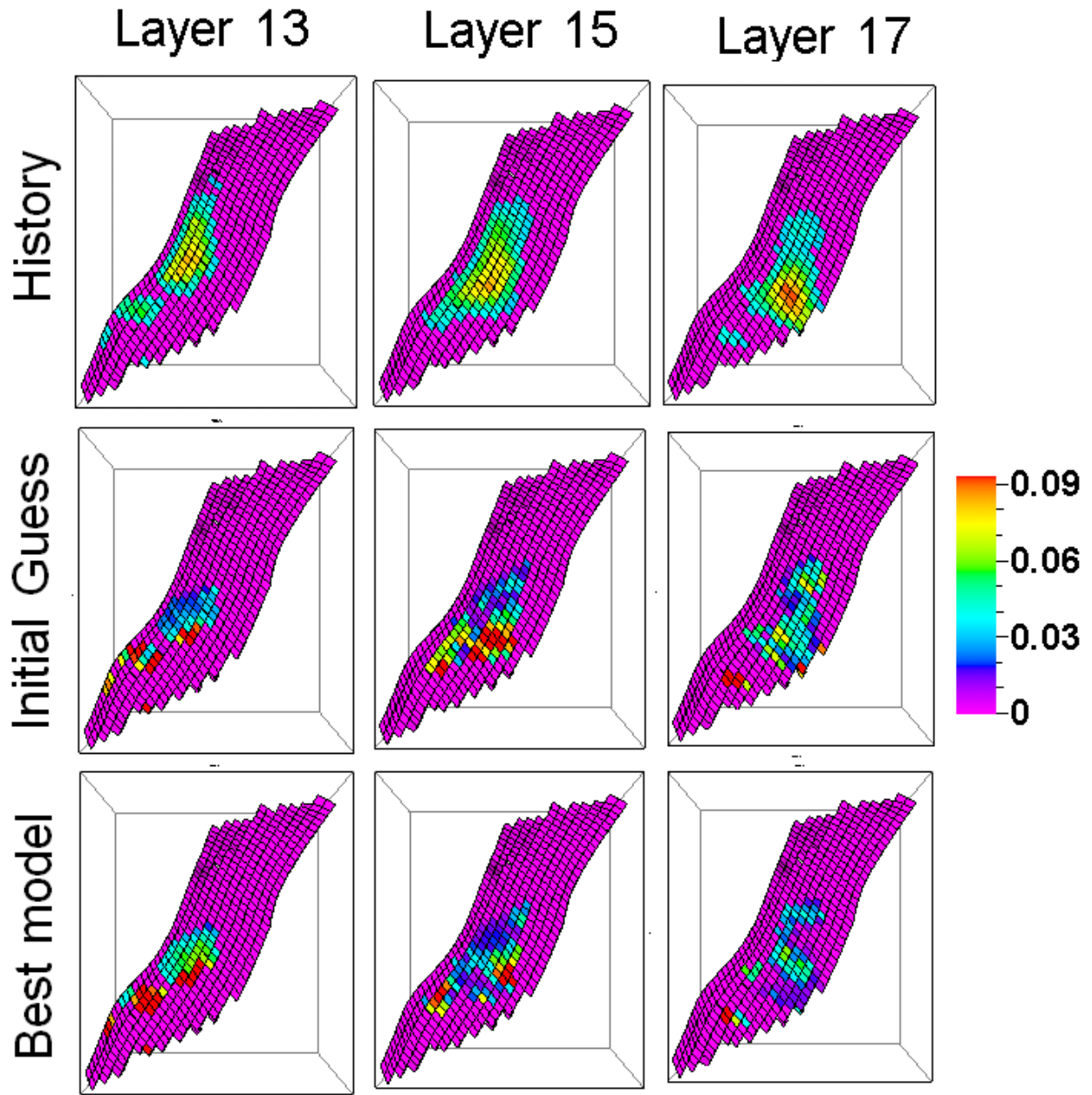


Figure 6.30: History matching results for matching time-lapse seismic data using RR-PSO. History, simulated time-lapse seismic response of initial guess model and simulated time-lapse seismic response of best model are shown from top to bottom for layers 13, 15 and 17.

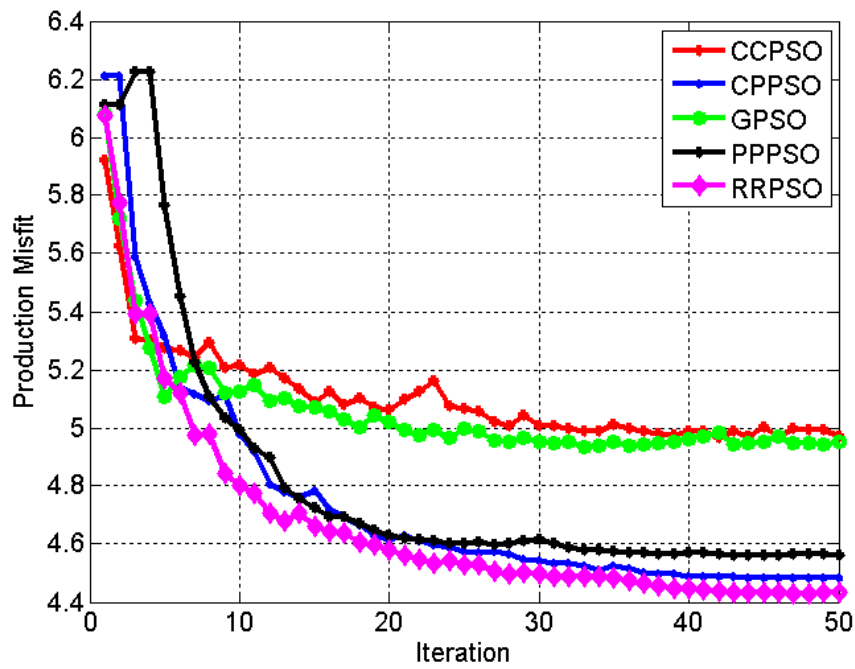


Figure 6.31: The decrease in median of the production misfits with increase in number of iterations for different PSO family members.

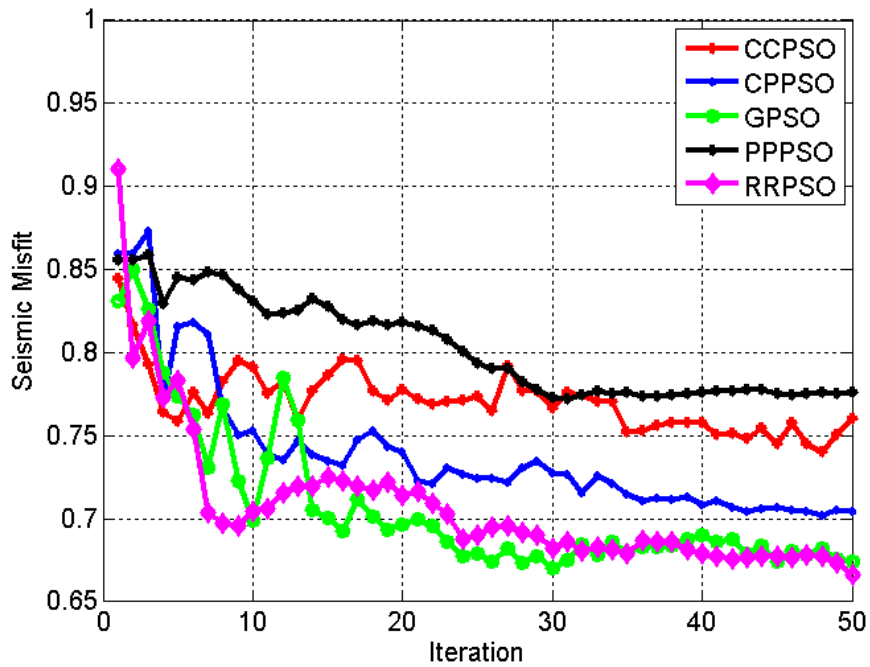


Figure 6.32: The decrease in median of the time-lapse seismic misfits with increase in number of iterations for different PSO family members.

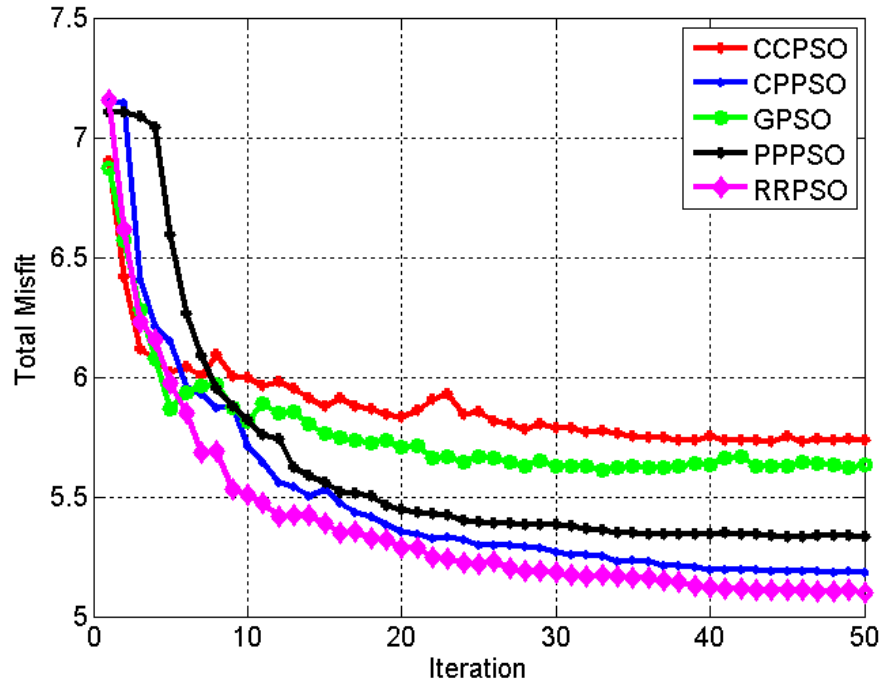


Figure 6.33: The decrease in median of the total misfits with increase in number of iterations for different PSO family members.

Figures 6.31, 6.32 and 6.33 show the decrease in production misfits, time-lapse seismic misfits and total misfits with the increase in iterations for all of the PSO family members respectively. RR-PSO has provided lowest production misfit, seismic misfit as well as lowest total misfit among all of the PSO family members. CP-PSO, PP-PSO and RR-PSO have performed better in history matching of production data and provided lower production misfits as compared to CC-PSO and GPSO. CP-PSO, PP-PSO and RR-PSO have provided satisfactory history match for gas production rate in well E-3AH, whereas CC-PSO and GPSO have failed to do so. Similarly, RR-PSO and GPSO have performed better in history matching of time-lapse seismic data and provided lower time-lapse seismic misfit as compared to CC-PSO, CP-PSO and PP-PSO. RR-PSO, CP-PSO and PP-PSO have performed better in minimizing the total misfit as compared to CC-PSO and GPSO. Initial and best porosity models obtained using different particle swarm optimizers are shown in the Figures 6.34 and 6.35. The parameters for initial and best models for different particle swarm optimizers are shown in the tables 6.1, 6.2, 6.3, 6.4, 6.5 and 6.6. The best model parameters obtained for different particle swarm optimizers are significantly different from each other.

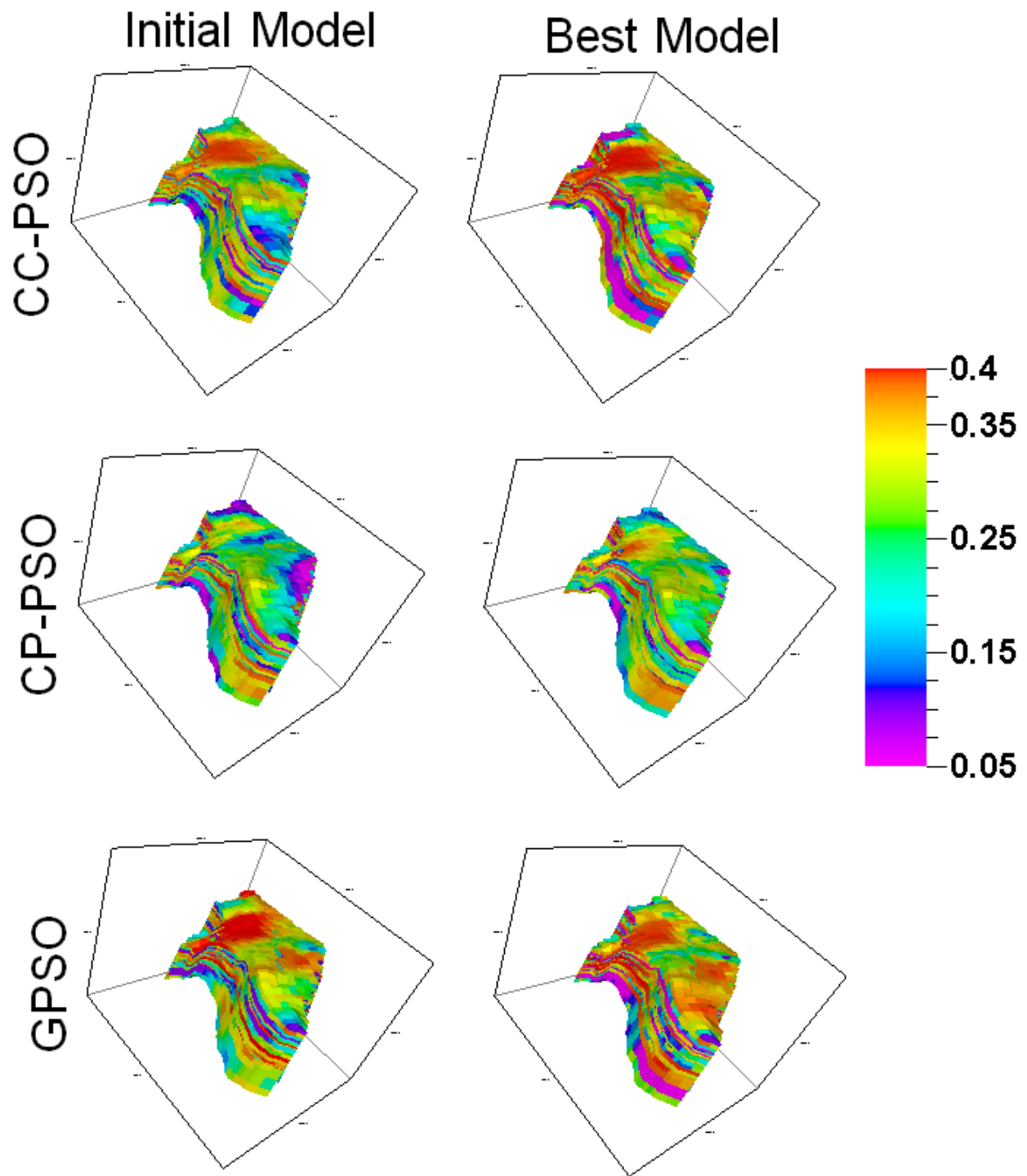


Figure 6.34: Initial and best porosity models obtained using CC-PSO, CP-PSO and GPSO. Initial and best porosity models are shown in left and right respectively.

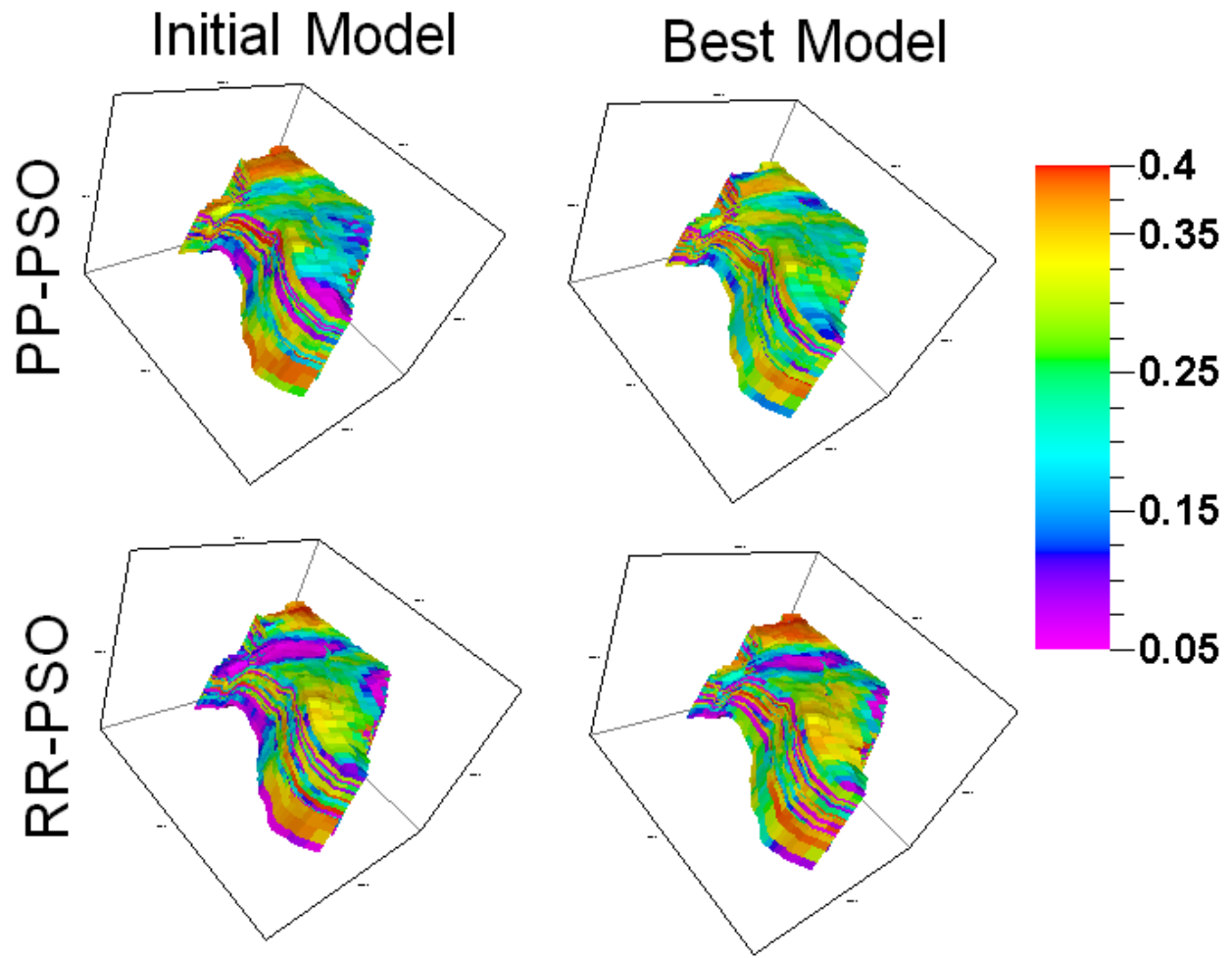


Figure 6.35: Initial and best porosity models obtained using PP-PSO and RR-PSO. Initial and best porosity models are shown in left and right respectively.

CC PSO	Relative Permeability	Clay Content	Coordination Number	Fluid Mixing	Pore Compressibility
Initial Model	Curve 3	0.35	5.66	Patchy	1.73e-10
Best Model	Curve 5	0.4	5	Patchy	1.5e-10

Table 6.1: The parameters corresponding to initial and best models obtained using CC-PSO

<b>CP PSO</b>	<b>Relative Permeability</b>	<b>Clay Content</b>	<b>Coordination Number</b>	<b>Fluid Mixing</b>	<b>Pore Compressibility</b>
<b>Initial Model</b>	Curve 1	0.21	6.75	Uniform	2.86e-10
<b>Best Model</b>	Curve 2	0.26	6.98	Uniform	2.16e-10

Table 6.2: The parameters corresponding to initial and best models obtained using CP-PSO

<b>GPSO</b>	<b>Relative Permeability</b>	<b>Clay Content</b>	<b>Coordination Number</b>	<b>Fluid Mixing</b>	<b>Pore Compressibility</b>
<b>Initial Model</b>	Curve 3	0.12	6.68	Uniform	2.34e-10
<b>Best Model</b>	Curve 5	0.1	5	Uniform	3e-10

Table 6.3: The parameters corresponding to initial and best models obtained using GPSO

<b>PP PSO</b>	<b>Relative Permeability</b>	<b>Clay Content</b>	<b>Coordination Number</b>	<b>Fluid Mixing</b>	<b>Pore Compressibility</b>
<b>Initial Model</b>	Curve 3	0.14	8.45	Patchy	1.99e-10
<b>Best Model</b>	Curve 4	0.26	5.02	Patchy	2.1e-10

Table 6.4: The parameters corresponding to initial and best models obtained using PP-PSO

<b>RR PSO</b>	<b>Relative Permeability</b>	<b>Clay Content</b>	<b>Coordination Number</b>	<b>Fluid Mixing</b>	<b>Pore Compressibility</b>
<b>Initial Model</b>	Curve 2	0.19	6.41	Uniform	2.1e-10
<b>Best Model</b>	Curve 3	0.3	8.13	Uniform	2.73e-10

Table 6.5: The parameters corresponding to initial and best models obtained using RR-PSO

## 6.4 Model Sampling

Following the procedure described in Section 5.9 , a number of history matched models can be obtained. The simulated production and time-lapse seismic responses of these models can provide satisfactory match with the observed production and time-lapse seismic data of the Norne field. The models are selected based on the tolerance value of 5.5 on total misfit. The above method is applied on the results of RR-PSO, and we believe that it can be applied on other members of particle swarm optimizers.

The process starts with the selection of models having total misfit value of 5.5 or less. Next all of the model parameters (There are 75 parameters in one model) are assigned in one vector. Since first seventy elements of the vector are only for the porosity, so to differentiate the effect of model parameters, each of the elements responsible for porosity model is weighted by the number of elements used for porosity model (70 in this case). Figure 6.36 shows the two history matched models obtained after model sampling on the results of RR-PSO.

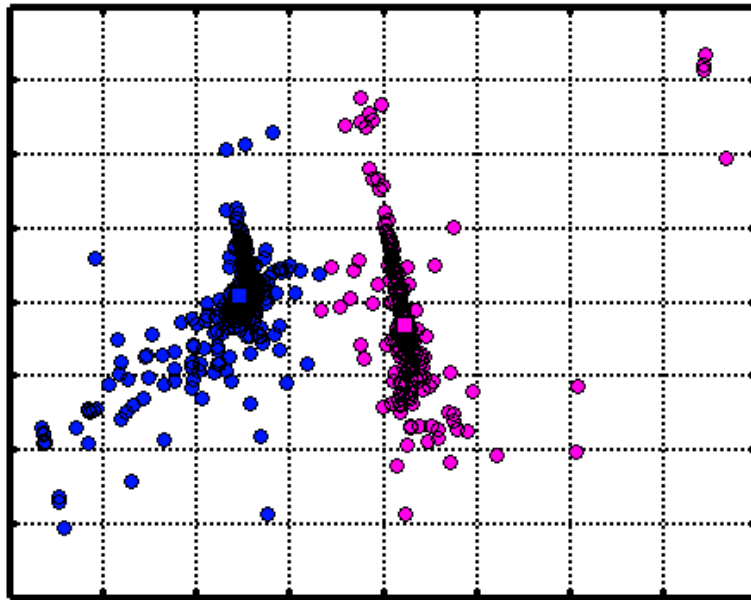


Figure 6.36: Two history matched models are obtained after the kernel k-medoid clustering. Model sampling is applied on the results of RR-PSO. History matched models are the centroid of clusters (shown in the red and blue square), all other models are shown in red and blue circles

Two history matched porosity models obtained after model sampling on the results of RR-PSO are shown in the Figure 6.37. Other parameters for the history matched models are shown in the Table 6.6. The differences between porosity models are highlighted using black circles. The coordination numbers, clay contents and pore compressibilities for these two models are different, whereas relative permeability curves and fluid mixing values are the same. Similarly, a number of history matched models can be obtained using the method described above.

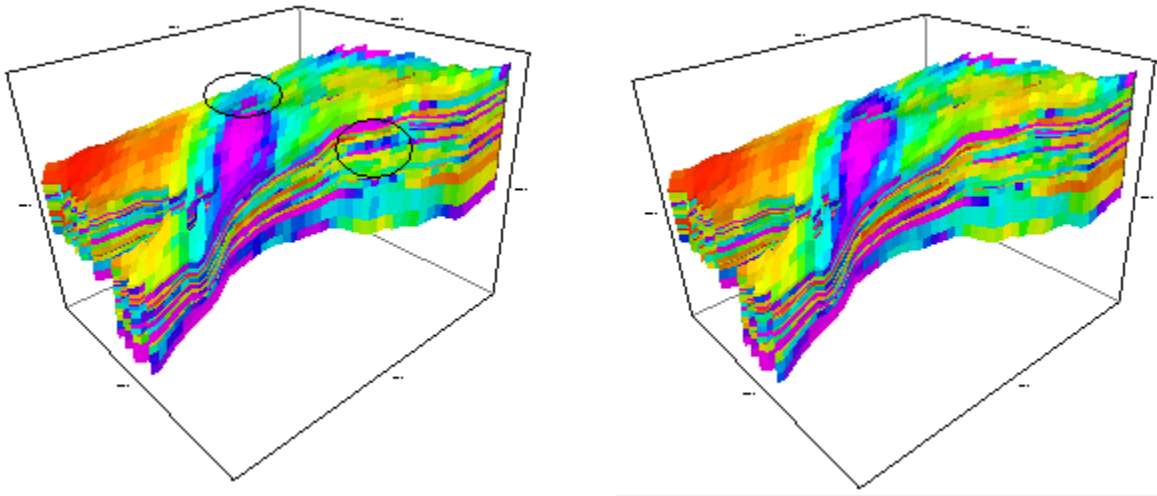


Figure 6.37: Two history matched porosity models obtained after model sampling using the results of RR-PSO. The differences between two models are highlighted by the black circles.

<b>RR PSO</b>	<b>Relative Permeability</b>	<b>Clay Content</b>	<b>Coordination Number</b>	<b>Fluid Mixing</b>	<b>Pore Compressibility</b>
<b>Model 1</b>	Curve 3	0.24	7.74	Uniform	2.48e-10
<b>Model 2</b>	Curve 3	0.31	8.13	Uniform	2.66e-10

Table 6.6: Parameters for the two history matched models after model sampling on the results of RR-PSO

## 6.5 Conclusions

We successfully applied particle swarm optimizers for joint inversion of production and time-lapse seismic data of the Segment-E of the Norne field. RR-PSO has performed best in minimizing the production misfit, time-lapse seismic misfit and total misfit. A satisfactory history match of oil, water and gas rate and bottom hole pressure in the wells E-2H and E-3H are achieved whereas the large mismatch of production data in the well E-3AH still needs to be further investigated. A satisfactory history match of time-lapse seismic data is achieved in some layers, but mismatch in matching whole pattern is still needs to be investigated. Overall RR-PSO has very strong potential for joint inversion of time-lapse seismic and production data of any real field. The best models obtained for each particle swarm optimizer is significantly different from each other. So particle swarm optimizers can also be used in combination to obtain a set of history matched models.

RR-PSO, PP-PSO and CP-PSO have performed better than CC-PSO and GPSO in terms of lowering the total misfit in joint inversion of production and time-lapse seismic data of Norne field. It is also observed that, behavior is similar for lowering the misfit in production data. CC-PSO and RR-PSO have performed better than CP-PSO, PP-PSO and CC-PSO in lowering the time-lapse seismic misfit. Time-lapse seismic misfit is a part of the objective function used for calculation of total misfit. Particle swarm optimizers are focused on to minimize the total misfit. At the same time particle swarm optimizers are exploratory in nature. This explains the behavior of CP-PSO; it has matched production data satisfactorily but provided unsatisfactory match of time-lapse seismic data in some layers. Similarly, for the same reason CC-PSO has performed better in minimizing the time-lapse seismic misfit as compared to production misfit.

# Chapter 7

## **CONCLUSIONS AND FUTURE RESEARCH**

Reservoir models include static and dynamic information about the reservoir and are extensively used in the petroleum industry. Reservoir modeling involves integration of a wide variety of geological, geophysical and production data. During the exploration stage of the reservoir, reservoir models are developed using static information available for the reservoir. As the reservoir is produced, more dynamic data become available, including production and time-lapse seismic data. These dynamic data are intergraded into the reservoir model for better management of the reservoir and thus better reservoir forecasting. Dynamic data are integrated in to the reservoir model using joint inversion or the history matching process. In recent years, time-lapse seismic (4D seismic) has started playing an important role in the joint inversion process. It can provide information on the dynamics of fluids in the reservoir based on the relation between variations of seismic signals and movement of hydrocarbons and changes in formation pressure. Movement of fluids and changes in pore pressure depends on the petrophysical properties of the reservoir rock.

However joint inversion of production and time-lapse seismic is complex and challenging. In this dissertation we have looked several aspects of joint inversion of production and time-lapse seismic while keeping a practical approach by including the real field data of Norne field. The important conclusions of this research are following:

The general practice of history matching of time-lapse seismic and production data is to update the porosity or/and permeability model until a minimum mismatch between observed and modeled data is achieved. In this process the parameters for reservoir and seismic simulator are considered as fixed, but in reality there are uncertainties attached with these parameters and ignoring them can give misleading results. Thus, it is necessary to rank the sensitive parameters both in the reservoir simulator and as well as in the seismic simulator for better joint inversion of time-lapse seismic and production data. So we have identified sensitive parameters and ranked them in modeling the production and time-lapse seismic response of the Norne field. This sensitivity workflow can also be applied for the joint inversion of production and time-lapse seismic data of other fields. It is shown that rock physics model is the most important parameter among the parameters considered for time-lapse seismic modeling of the Norne field. Presence or absence of cement in the rock has a strong impact on the sensitivity of velocity to fluid saturation changes. Relative permeability and porosity/permeability model are the second and third most sensitivity parameter for time-lapse seismic modeling of Norne field. Pore compressibility is the least sensitive parameter for time-lapse seismic modeling of Norne field. We also found that relative permeability curve is the most important parameter for modeling of flow response of Norne field. Porosity/Permeability models are the second most sensitive parameter for modeling of flow response.

It is obvious that rock physics model is the most important parameter for modeling time-lapse seismic response of the Norne field. Thus in the next step, we studied the sensitive rock physics parameter for modeling time-lapse seismic response of Norne field. At first we investigated sensitive parameters in the Gassmann's equation to generate the initial seismic velocity. It is found that clay content is the most sensitive parameter in fluid substitution for calculating seismic velocities in Norne field. Salinity and pore pressure have the minimal impact

on fluid substitution. Next we identified sensitive rock physics parameters in modeling the time-lapse seismic response. Among the parameters investigated, Coordination number is the most sensitive parameter in modeling the time-lapse seismic signature of Norne field. Clay content and fluid mixing are the second and third most sensitive parameter for modeling time-lapse seismic signature. The Results of sensitivity study are used in joint inversion of time-lapse seismic and production data of Norne field. This method can also be used to identify and compare sensitive rock physics parameters in modeling the time-lapse seismic response of any field.

Joint inversion of seismic and flow data for reservoir parameter is highly non-linear and complex. Local optimization methods may fail to obtain multiple models that fit the observed seismic and production data. Stochastic optimization based inversion has shown very good results in integration of time-lapse seismic and production data in reservoir history matching. Also, high dimensionality of the inverse problem makes the joint inversion of both data sets computationally expensive. High dimensionality of the inverse problem can be solved by using principal component basis derived from the prior. We developed a workflow and used a family of particle swarm optimizers in combination with principal component base for joint inversion of production and time-lapse seismic data of a synthetic field. We demonstrated that all of the members of PSO family performed well in joint inversion of production and time-lapse seismic data of a synthetic field. RR-PSO, CP-PSO and PP-PSO have performed better than CC-PSO and GPSO in matching the production and as well as time-lapse seismic data. RR-PSO has performed best among all of the PSO family members in lowering the production misfit, time-lapse seismic misfit and total misfit. It also has the highest convergence rate as compared to all of the other PSO family members. RR-PSO has the strong potential in providing good results for joint inversion of production and time-lapse seismic data of a field. Also, all of the members of PSO family can be used in combination to obtain different sets of history matched models. We also developed a method to obtain a set of history matched models using PSO in combination with MDS and kernel k-medoid clustering.

We successfully performed the joint inversion of production and time-lapse seismic data of Norne field using a family of particle swarm optimizers and by varying sensitive parameters that have been identified previously. A satisfactory history match of oil, water and gas rate and bottom hole pressure in the wells E-2H and E-3H are achieved whereas the large mismatch of production data in the well E-3AH still needs to be further investigated. A satisfactory history match of time-lapse seismic data is achieved in some layers, but mismatch in matching whole pattern is still needs to be investigated. All of the PSO family members minimized the simulated production and time-lapse seismic response of initial guess model. RR-PSO, PP-PSO and CP-PSO have performed better than CC-PSO and GPSO in terms of lowering the total misfit in joint inversion of production and time-lapse seismic data of Norne field. It is also observed that, behavior is similar for lowering the misfit in production data. CC-PSO and RR-PSO have performed better than CP-PSO, PP-PSO and CC-PSO in lowering the time-lapse seismic misfit. RR-PSO has performed best in minimizing the production misfit, time-lapse seismic misfit and total misfit. Overall RR-PSO has very strong potential for joint inversion of time-lapse seismic and production data of any real field.

Overall we have shown that it is not only the porosity or permeability models that are important in joint inversion of production and time-lapse seismic data of a field, rather porosity or permeability model are a subset of parameters that need to be varied for a successful joint inversion. We also successfully applied and compared different particle swarm optimizers for the joint inversion of production and time-lapse seismic data of Norne field. The contribution from this research is a systematic workflow for joint inversion of seismic time-lapse and production data that can be and has been practically applied to a real field.

## **Future Research Directions**

- In this research normalized changes in P-wave seismic impedance from 2001 to 2004, have been used in joint inversion of production and time-lapse seismic data of the Norne field. A significant area of research would be to identify the type of time-lapse seismic data that is used in the joint inversion process. In other words, what type of time-lapse seismic data should be used for joint inversion?

- Scales of the models are significantly different in reservoir model, seismic grid and flow simulation model. The scale of the model increases from the static model to flow simulation model. The scale used in the joint inversion of production and time-lapse seismic data is an interesting and challenging area of research.
- We have used principal component analysis for the dimensionality reduction. There are several other methods for the dimensionality reduction. A comparison of all dimensionality reduction methods for joint inversion of time-lapse and production data is a potential area of research.
- We have not looked at the effect of uncertainties in variogram ranges, fluid contacts and fault transmissibilities on joint inversion of production and time-lapse seismic data. These parameters should be investigated for their sensitivity towards the joint inversion of production and time-lapse seismic data.
- Another area of research is to model the geomechanical effects and how they impact time-lapse seismic response of a field. Joint inversion of geomechanical data, production data and time-lapse seismic data is also an interesting area of research.
- The general equation of the objective function in the joint inversion consists of the sum of the norm of differences in the modeled and observed production and seismic data. What should be the equation of the objective function in joint inversion? What are the effects of using different objection functions on the joint inversion of production and time-lapse seismic data?
- Recently distance and kernel based methods (Scheidt and Caers, 2009a, b, c) have been used for joint conditioning of static and dynamic data. It has shown potential for assessment of uncertainties associated with the reservoir model updating. . Thus, application of this method in assessment of uncertainties associated with joint inversion of time-lapse seismic and production data is an interesting area of

research. An important step of this method is to choose an appropriate distance such that different models can be correlated based on their target response. How to choose distances for joint inversion of time-lapse seismic and production data? Can this method be used for assessment of uncertainties associated with joint inversion of time-lapse seismic and production data?

- Time-lapse seismic data of the Norne field, acquired in 2001 and 2004 have been used in this research for joint inversion process. Time-lapse seismic data in the Norne field consists of near, mid, far and full stacks of 3D seismic at four different years (2001, 2003, 2004 and 2006). The use of near and far stacks of 3D seismic data in joint inversion process is a potential area of research.

# BIBLIOGRAPHY

- Arenas E., Kruijsdijk C. and Oldenziel T., 2001, Semi-Automatic history matching using the pilot point method including time-lapse seismic data, SPE 71634, SPE Annual Technical Conference and Exhibition, New Orleans, USA, Sep 30- Oct 3
- Avseth, P., Mukerji, T., and Mavko, G., 2005, Quantitative Seismic Interpretation, Cambridge.
- Batzle M., and Z. Wang, 1992, Seismic properties of pore fluids, *Geophysics*, 57, 1396-1408.
- Begum N., 2009, Reservoir parameter estimation for reservoir simulation using ensemble kalman filter (EnKF), M. Sc. thesis, NTNU, Norway
- Borg, I. and Groenen, P.J.F. (2005). Modern multidimensional scaling. 2nd edition. New York: Springer
- Carlisle, A., and G. Dozier, 2001. An off-the-shelf PSO. In proceedings of The Workshop On particle Swarm Optimization, Indianapolis, IN, 1-6.
- Castro S. ,2007, A probabilistic approach to jointly integrate 3D/4D seismic, production data and geological information for building reservoir models, Ph.D. dissertation, Stanford University
- Clerc, M., and J. Kennedy, 2002, The particle swarm--explosion, stability, and convergence in a multidimensional complex space, *IEEE Transactions on Evolutionary Computation* 6, 58-73.
- Cramer, J. S., 2003, Logit models from economics and other fields, Cambridge university press
- Dadashpour M., 2009, Reservoir Characterization Using Production Data and Time-Lapse Seismic Data, Doctoral theses at NTNU, 2009: 195.

- Deutsch C, Journel A, 1998, GSLIB: geostatistical software library and user's guide, 2nd edn. Oxford University Press, New York, 384 p
- Dutta, N. C., and H. Ode, 1979a, Attenuation and dispersion of compressional-waves in fluid-filled rocks with partial gas saturation, *Geophysics*, 44, 1777–1805.
- Dvorkin, J., A. Nur, and H. Yin, 1994, Effective properties of cemented granular materials: *Mechanics of Materials*, 18, no. 4, 351–366, doi: 10.1016/0167-6636(94)90044-2.
- Dvorkin J., and Nur A., 1996, Elasticity of high-porosity sandstones: Theory for two North Sea datasets, *Geophysics*, 61, 1363-1370
- Echeverría, D., and T. Mukerji, 2009, A robust scheme for spatio-temporal modeling of oil reservoirs, in Anderssen, R.S., R.D. Braddock and L.T.H. Newham, eds., World IMACS Congress and MODSIM09 International Congress on Modelling and Simulation, Modelling and Simulation Society of Australia and New Zealand and International Association for Mathematics and Computers in Simulation, Cairns, Australia, 4206-4212 [www.mssanz.org.au/modsim09/J1/echeverria.pdf](http://www.mssanz.org.au/modsim09/J1/echeverria.pdf)
- Echeverría, D., T. Mukerji and E.T.F. Santos, 2009, Robust scheme for inversion of seismic and production data for reservoir facies modeling, *SEG Expanded Abstracts*, 28, 2432-2436.
- Fanchi R. J., 1999, Predicting 4D seismic performance using an integrated flow model, *ATCE, SPE*
- Fernández-Alvarez, J. P., J.L. Fernández-Martínez, and C.O. Menéndez Pérez, 2008, Feasibility analysis of the use of binary genetic algorithms as importance samplers: application to a geoelectrical VES inverse problem, *Mathematical Geosciences*, 40, 375-408.
- Fernández-Martínez, J. L., E. García-Gonzalo and J.P. Fernández-Alvarez, 2008a, Theoretical analysis of Particle Swarm trajectories through a mechanical analogy, *International Journal of Computational Intelligence Research*, 4, 93-104.
- Fernández-Martínez, J. L., J.P. Fernández-Álvarez, E. García-Gonzalo, C.O. Menéndez-Pérez and H.A. Kuzma, 2008b, Particle Swarm Optimization (PSO): a simple and powerful algorithm family for geophysical inversion. *SEG Expanded Abstracts*, 27, 3568-3571.
- Fernández-Martínez, J. L., and E. García-Gonzalo, 2009, The PSO family: deduction, stochastic analysis and comparison, *Swarm Intelligence*, 3, 245-273.
- Fernández-Martínez J.L., Mukerji T., García Gonzalo E. and Suman A. 2010, Reservoir characterization and inversion uncertainty via a family of Particle Swarm Optimizers. Application to the synthetic Stanford VI reservoir. 80th SEG meeting, Denver , Colorado , USA , Expanded Abstracts.

- Fernández-Martínez J. L., García-Gonzalo E., Álvarez J. P. F., Kuzma H. A. and Menéndez-Pérez C. O., 2010a, PSO: A Powerful Algorithm to Solve Geophysical Inverse Problems. Application to a 1D-DC Resistivity Case. *Journal of Applied Geophysics*. Accepted for publication.
- Fernández-Martínez J. L., García-Gonzalo E. and Naudet V. 2010b, Particle Swarm Optimization applied to the solving and appraisal of the Streaming Potential inverse problem. *Geophysics. Hydrogeophysics Special Issue*. Accepted for publication.
- Fernández-Martínez J. L., García-Gonzalo E., and Mukerji T., 2010c, How to design a powerful family of Particle Swarm Optimizers for inverse modelling. *Transactions of the Institute of Measurement and Control. New trends in bio-inspired computation*. To be published.
- Fernandez-Martinez Juan, Mariethoz G., Garcia-Gonzalo E., Fernandez M. , Mukerji T., Tompkins M. ,2010d. Particle Swarm Optimization (PSO) and model reduction techniques. Application to hydro-geological inverse problems. *Proceedings of IAHR International Groundwater Symposium, Valencia, 22 - 24 September 2010*
- Fernández-Martínez, J. L., E. García-Gonzalo, and T. Mukerji, 2011, How to design a powerful family of Particle Swarm Optimizers for inverse modelling, *Transactions of the Institute of Measurement and Control, New trends in bio-inspired computation*, 0(0), 1-15, doi: 10.1177/0142331211402900.
- Gassmann F., 1951, Über die Elastizität poroser Medien, *Vierteljahrsschrift der Naturforschenden Gesellschaft in Zürich*, 96, 1-23.
- Goldberg, D.E., 1989, *Genetic algorithms in search, optimization and machine learning*, Addison-Wesley, 412 p.
- García-Gonzalo E., and Fernández-Martínez J. L., 2009, Design of a simple and powerful Particle Swarm optimizer: *Proceedings of the International Conference on Computational and Mathematical Methods in Science and Engineering, CMMSE2009, Gijón, Spain*.
- Hashin Z. and Shtrikman S., 1965, *J. mech. phys. solids* 13, 119
- Haverl M. C., Aga M. and Reiso E., 2005, Integrated workflow for quantitative use of time-lapse seismic data in history matching : A North sea field case, *SPE 94453, SPE Europe Annual Conference, Madrid, Spain, June 13-16*
- Holland, J. H., 1992, *Adaptation in natural and artificial systems*, MIT Press, 228 p.
- Huang X., Meister L. and Workman R., 1997, Reservoir characterization by integration of time-lapse seismic and production data, *SPE 38695, SPE Annual Technical Conference and Exhibition, San Antonio USA, Oct 5-8*

- Huang X., Meister L. and Workman R. ,1998 Improving production history matching using time-lapse seismic data, *The Leading Edge*, 17 1430-1434
- Jin et al. Stochastic inversion for reservoir properties using parallel learning based VFSA and pilot point parameterization, 2009, SPE Reservoir simulation symposium, woodland, Texas
- Kennedy, J. and R.C. Eberhart, 1995, Particle swarm optimization, *Proceedings IEEE International Conference on Neural Networks*, 4, 1942-1948.
- Kirkpatrick, S., C.D. Gelatt and M.P. Vecchi, 1983, Optimization by Simulated Annealing, *Science*, 220, 671-680.
- Landa J. L. ,1997, Reservoir parameter estimation constrained to pressure transients, performance history and distributed saturation data , Ph.D. dissertation, Stanford University
- Landro M. ,2001 Discrimination between pressure and fluid saturation changes from time-lapse seismic data, *Geophysics*, 66 836-844
- Ma, X.Q, 2002, Simultaneous inversion of prestack seismic data for rock properties using simulated annealing, *Geophysics*, 67, 1877-1885.
- Mantica S., Cominelli A. and Mantica G., 2001 Combining global and local optimization techniques for automatic history matching production and seismic data, SPE 66355, SPE Reservoir Simulation Symposium, Houston, Texas, Feb 11-14
- Mavko, G., and Mukerji, T., 1998, Bounds on low frequency seismic velocities in partially saturated rocks, *Geophysics*, 63, 918-924
- Mindlin, R.D., 1949, Compliance of elastic bodies in contact, *Trans. ASME*, 71, A-259.
- Naudet, V., J.L. Fernández-Martínez, E. García-Gonzalo and J.P. Álvarez-Fernández, 2008, Estimation of water table from self-potential data using particle swarm optimization (PSO), *SEG Expanded Abstracts*, 27, 1203-1207.
- Oliver D. S., Alberto C., Stanislas V. D. B. and Sudip D. C. ,2000, A gradient base approach for history matching of production and 4D seismic data, 7th European conference on the mathematics of oil recovery, Baveno, Italy, Sept 5-8
- Onwunalu, J.E., and L.J. Durlofsky, 2009, Application of a particle swarm optimization algorithm for determining optimum well location and type, *Computational Geosciences*, 14, 183-198.

- Ozcan, E. and C.K. Mohan, 1999, Particle swarm optimization: surfing the waves, Proceedings of the IEEE Congress on Evolutionary Computation (CEC '99), Washington DC, 3, 1939-1944.
- Osdal, B., O. Husby, H. A. Aronsen, N. Chen, and T. Alsos, 2006, Mapping the fluid front and pressure buildup using 4D data on Norne Field: The Leading Edge, 25, 1134–1141.
- Pearson, K., 1901, Principal components analysis, The London, Edinburgh and Dublin Philosophical Magazine and Journal, 6, 566.
- Poli, R., 2008b, Analysis of the Publications on the Applications of Particle Swarm Optimisation, Journal of Artificial Evolution and Applications, 685175, 10 p. doi: 10.1155/2008/685175.
- Portella R. C. M. and Emerick A. A., 2005, Use of quantitative 4D seismic data in automatic history match, SPE 94650, SPE latin American and Caribbean petroleum engineering conference, Rio de Janeiro, Brazil, June 20-23
- Reynolds, A. C., N. He, L. Chu, and D. S. Oliver, 1996, Reparameterization techniques for generating reservoir descriptions conditioned to variograms and well-test pressure data, SPE Journal, 1, 4, 413-426.
- Romary, T., 2009a, Integrating production data under uncertainty by parallel interacting Markov chains on a reduced dimensional space, Computational Geosciences, 13, 103-122.
- Romary, T., 2009b, History matching of approximated lithofacies models under uncertainty, Computational Geosciences, 14, 343-355.
- Rotondi et al.2006, Hydrocarbon production forecast and uncertainty quantification: A field application, ATCE, SPE
- Sarma, P., L.J. Durlofsky, K. Aziz and W.H. Chen, 2006, Efficient real-time reservoir management using adjoint-based optimal control and model updating, Computational Geosciences, 10, 3–36.
- Scheidt C., Caers J., 2009a, Bootstrap confidence intervals for reservoir model selection techniques. Comput Geosci. doi: 10.1007/s10596009-9156-8
- Scheidt C., Caers J. ,2009b, Uncertainty quantification in reservoir performance using distances and kernel methods – application to a West-Africa deepwater turbidite reservoir. SPEJ 118740-PA, Online First
- Schoelkopf, B., & Smola, A. (2002). Learning with kernels. Cambridge, MA: MIT Press.

- Sen, M., Stoffa, P.L., 1996, Bayesian inference, Gibb's sampler and uncertainty estimation in geophysical inversion : *Geophysical Prospecting*, 44(2),313-350
- Sengupta M., 2000, Integrating rock physics and flow simulation to reduce uncertainties in seismic reservoir monitoring, Ph.D. dissertation, Stanford University
- Sena, A., M. Sen, P. Stoffa, R. Seif and L. Jin, 2009a, Joint inversion of time-lapse seismic and production data using VFSA with Local Thermal Regulation and pilot point parameterization, *SEG Expanded Abstracts*, 28, 1810-1814.
- Sena, A., P. Stoffa, M. Sen and R. Seif, 2009b, Assessing the value of time-lapse seismic data in joint inversion for reservoir parameter estimation in an oil reservoir subjected to water flooding recovery: a synthetic example, *SEG Expanded Abstracts*, 28, 3904-3908.
- Steffensen, I. and P. I. Karstad, 1995, Norne field development: Fast track from discovery to production, *SPE*.
- Sambridge, M., 1999, Geophysical Inversion with a Neighbourhood Algorithm –II. Appraising the ensemble, *Geophysical Journal International*, 138, 727-746.
- Sambridge, M., and G. Drijkoningen, 1992, Genetic algorithms in seismic waveform inversion, *Geophysical Journal International*, 109, 323-342.
- Sen, M.K. and P.L. Stoffa, 1995, *Global Optimization Methods in Geophysical Inversion*, as part of *Advances in Exploration Geophysics series*, Elsevier Publishing, Co.
- Shaw, R. and S. Srivastava, 2007, Particle swarm optimization: A new tool to invert geophysical data, *Geophysics*, 72, F75-F83.
- Stephen et al, 2005, Multiple model seismic and production history matching: A case study , *EAGE Annual conference* , Spain
- Storn, R. and K. Price, 1997, Differential Evolution - A Simple and Efficient Heuristic for global Optimization over Continuous Spaces, *Journal of Global Optimization*, 11, 341-359.
- Suman A. and T. Mukerji, 2008, Uncertainties in rock properties and effects on seismic history matching, *Stanford Center for Reservoir Forecasting (SCRF), Annual Report*.
- Trelea, I., 2003, The particle swarm optimization algorithm: convergence analysis and parameter selection, *Information Processing Letters*, 85, 317--325.
- Van D., Oldenziel R. T., and Van K., 2001, Geological parameterization of a reservoir model for history matching incorporating time-lapse seismic based on a case study of the statfjord field,

SPE 71318, SPE Annual Technical Conference and Exhibition, New Orleans, Louisiana, 30 Sept – 3 Oct

Van den Bergh, F. and A. Engelbrecht, 2006, A study of particle swarm optimization particle trajectories, *Information Sciences*, 176, 937-971.

Vasco D. W., Datta-Gupta A. and He Z., 2003, Reconciling time-lapse seismic and production data using streamline models: The Bay Marchand field, Gulf of Mexico, SPE 84568

Verlo S. B. and Hetland, M., 2008, Development of a field case with real production and 4D data from the Norne Field as a benchmark case for future reservoir simulation models testing, Masters Thesis, NTNU, Norway

Walker G. J. and Lane H. S., 2007 Assessing the accuracy of history-match predictions and the impact of time-lapse seismic data: A case study for the Harding reservoir, SPE 106019, Reservoir simulation symposium, Houston, Feb 26-28

White, J.E. 1975. Computed seismic speeds and attenuation in rocks with partial gas saturation. *Geophysics* 40:224–232.

Wu J., Mukerji T. and Journel A., G 2005 Improving water saturation prediction with 4D seismic, SPE 95125, SPE Annual Technical Conference and Exhibition, Dallas, Texas, USA, Oct 9-12

Zimmerman, R. W., 1991, *Compressibility of Sandstones*, Elsevier Science Publishers, Amsterdam, Netherlands.

Zimmer, M., M. Prasad and G. Mavko, 2002, Pressure and porosity influences on VP-VS ratio in unconsolidated sands, SEG expanded abstracts.

Zheng, Y.L., L.H. Ma, L.Y. Zhang and J.X. Qian, 2003, On the convergence analysis and parameter selection in particle swarm optimization, *International Conference on Machine Learning and Cybernetics (ICMLC '03)*, 3, 1802-1807.